EFFECT OF METAL ION ADDITIVES ON THE THERMAL DECOMPOSITION KINETICS AND MECHANISM OF ZINC OXALATE DIHYDRATE

Thesis submitted to the
University of Calicut in partial fulfillment of the
requirements for the award of the degree of

Doctor of Philosophy in Chemistry

By

SABIRA K.

DEPARTMENT OF CHEMISTRY
UNIVERSITY OF CALICUT
KERALA-673635
NOVEMBER 2020

CERTIFICATE

Certified that the research work embodied in the thesis entitled **"EFFECT OF METAL ION ADDITIVES ON THE THERMAL DECOMPOSITION KINETICS AND MECHANISM OF ZINC OXALATE DIHYDRATE"** has been carried out by **Sabira K.** under my supervision at the Department of Chemistry, University of Calicut, Kerala and the same has not been submitted elsewhere previously for the award of any other degree or diploma.

University of Calicut

Dr. K. Muraleedharan
Professor
Department of Chemistry
University of Calicut
Kerala

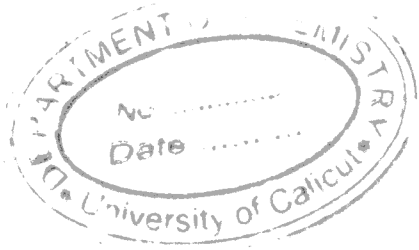

CERTIFICATE

Certified that the research work embodied in the thesis entitled **"EFFECT OF METAL ION ADDITIVES ON THE THERMAL DECOMPOSITION KINETICS AND MECHANISM OF ZINC OXALATE DIHYDRATE"** has been carried out by **Sabira K.** under my supervision at the Department of Chemistry, University of Calicut, Kerala and the same has not been submitted elsewhere previously for the award of any other degree or diploma. The suggestions/ corrections/ recommendations/observations made by the adjudicators have been included in the revised thesis.

University of Calicut
15th July 2021

Dr. K. Muraleedharan
Professor
Department of Chemistry
University of Calicut
Kerala

DECLARATION

I hereby declare that the research work embodied in the thesis entitled **"EFFECT OF METAL ION ADDITIVES ON THE THERMAL DECOMPOSITION KINETICS AND MECHANISM OF ZINC OXALATE DIHYDRATE"**, submitted to the University of Calicut is a bonafide record of research work done by me during the period 2016-2020 under the supervision and guidance of Dr. K. Muraleedharan, Professor, Department of Chemistry, University of Calicut. The same has not been submitted elsewhere for any degree or diploma.

University of Calicut **Sabira K.**

ACKNOWLEDGEMENT

It is my proud privilege to express deep sense of gratitude and respect to my esteemed supervisor ***Dr. K. Muraleedharan****, Professor, Department of Chemistry, University of Calicut, for giving me an opportunity to join his research team. His constant encouragement, support and valuable suggestions throughout the period of research enabled me to complete this study successfully.*

I am extremely grateful to ***Dr. A. I. Yahya****, Head of the Department of Chemistry and also to the former HOD,* ***Dr. P. Raveendran****, for providing research facilities in the department.*

I also take this opportunity to express my sincere gratitude to ***Dr. Abraham Joseph, Dr. N. K. Renuka,, Dr. P. Pradeepan, Dr. M. T. Ramesan, Dr. V. M. Abdul Mujeeb, Dr. Suresh Babu*** *and other Guest faculty for their timely intervention, encouragement and motivation. I would like to acknowledge all the technical and ministerial staff in the department of Chemistry for the help and support rendered by them.*

I would like to express my special thanks to ***Dr. D. Bahulayan, Dr. K. Aravindakshan, Dr. Purushothaman, Dr. P. Muhammad Shafi, Dr. Ganga Devi*** *and* ***all other teachers*** *from my first class onwards, for the encouragement, affection and support given to me that help me a lot to achieve in my life.*

I gratefully acknowledge CSIR for financial assistance. Also, I would like to express my sincere thanks to the University of Calicut and CSIF for SEM-EDS analysis, and providing the computational facility, Department of Physics for XRD analysis, STIC CUSAT for HR-TEM

analysis, PSG Coimbatore for SEM-EDAX analysis, and TEM facility, funded by a TPF Nanomission, GOI project at Centre for Nano and Soft Matter Sciences, Bengaluru.

I am also obliged to Principal, ***V. Balakrishnan Sir****, GHSS Kuttiadi for allowing me to continue research in part time mode. I am also indebted to my Colleagues at GHSS Kuttiadi for their support, encouraging approach, motivation and continuous cooperation wherever I needed.*

I am deeply indebted to my parents, family members, for their care, prayer and support that make my journey easy.

I express my immense gratitude to my husband, ***Mr. Sakkeer Husain B. and daughters Haza B.*** *and* ***Hamdiya Haneen B.*** *for their support, help, motivation, encouragement, prayers and patience all along the research programme. They have to adjust a lot during my research tenure and had to forego many things in life for helping me to complete my research.*

I would also like to express gratefulness to all the past and present research scholars of our group Dr. Sarada K., Dr. Sindhu N.V., Dr. Nusrath, K., Dr. Vijisha K. Rajan, Ms. Jaseela M.A., Ms. Shameera Ahamed T. K., Mr. Sivanandan C.K., Ms. Sumayya P.C., Ms. Jalala V.K., Ms. Vinduja P., Ms. Neenu Krishna P.U., Ms. Swathi Krishna and friends from different research groups for their immense support.

Above all, I bow to the God Almighty (Allah), the most merciful and beneficent for all the blessings. By the grace of Him I could reach upto this level.

Sabira K.

Dedicated to My Family

ABBREVIATIONS

CNT	-	Carbon nanotube
GLN	-	Graphene-like 2D layered nanomaterial
MOS	-	Metal oxide semiconductor
MMO	-	Mixed metal oxide
TGA	-	Thermogravimetric analysis
DTA	-	Differential thermal analysis
DSC	-	Differential scanning calorimetry
E_a	-	Activation energy
A	-	Arrhenius pre-exponential factor
FWO	-	Flynn-Wall-Ozawa
KAS	-	Kissinger-Akahira-Sunose
ZnO-NPs	-	ZnO-nanoparticles
PL	-	Photoluminescence
UV	-	Ultraviolet
EGA	-	Evolved gas analysis
α	-	Conversion function
T	-	Temperature
DTG	-	Derivative thermogravimetry
FTIR	-	Fourier transform infrared spectroscopy
DFT	-	Density functional theory
QTAIM	-	Quantum theory of atoms in molecules

SCF	-	Self consistent field
E_g	-	Optical band gap
XRD	-	X-ray diffraction
FESEM	-	Field emission scanning electron microscopic
EDAX	-	Energy-dispersive X-ray spectroscopy/analysis
HR-TEM	-	High resolution transmission electron microscopic
SAED	-	Selected area (electron) diffraction
HOMO	-	Highest occupied molecular orbital
LUMO	-	Lowest unoccupied molecular orbital
UV-DRS	-	Ultraviolet- Diffuse reflectance spectrum
ZnOx	-	Zinc oxalate
Ce-ZnOx	-	Cerium-zinc oxalate
$SZ_{0.1}$	-	Strontium zinc oxalate with Sr concentration 0.1
SZ_1	-	Strontium zinc oxalate with Sr concentration 1 mol%
SZ_2	-	Strontium zinc oxalate with Sr concentration 2 mol%
SZ_5	-	Strontium zinc oxalate with Sr concentration 5 mol%
ZO	-	Zinc oxide
$SZO_{0.1}$	-	Strontium zinc oxide with Sr concentration 0.1 mol%
SZO_1	-	Strontium zinc oxide with Sr concentration 1 mol%
SZO_2	-	Strontium zinc oxide with Sr concentration 2 mol%
SZO_5	-	Strontium zinc oxide with Sr concentration 5 mol%
Ba-ZnOx	-	Barium zinc oxalate
$BZOx_2$	-	Barium zinc oxalate with Ba concentration 2 mol%

$BZOx_3$	-	Barium zinc oxalate with Ba concentration 3 mol%
$BZOx_4$	-	Barium zinc oxalate with Ba concentration 4 mol%
$BZOx_5$	-	Barium zinc oxalate with Ba concentration 5 mol%
BZO_2	-	Barium zinc oxide with Ba concentration 2 mol%
BZO_3	-	Barium zinc oxide with Ba concentration 3 mol%
BZO_4	-	Barium zinc oxide with Ba concentration 4 mol%
BZO_5	-	Barium zinc oxide with Ba concentration 5 mol%

CONTENTS

PREFACE

Zinc oxalate is an important derivative of oxalic acid. It is used in metal treatment industry and pharmaceutical applications. Zinc oxalate have antiseptic properties and ability to kill bacteria. The thermal decomposition of zinc oxalate yield zinc oxide which is an excellent multifunctional material. It used as a sunscreen ingredient. Zinc oxide (ZnO) is a better photocatalyst than TiO_2 for the degradation of organic pollutants. It has interesting biological properties like cytotoxic activities, antibacterial activities, *etc*. ZnO is also used in today's technology as semiconductor material, gas sensor, piezoelectric sensor, electro-luminescent material, magnetic material, actuator and cosmetic ingredients. Doping ZnO nanostructures with metal ions result in the modification of the electronic and optical performance and improve its applications.

The decomposition study serves as the most useful tool to get insight into the mechanism of solid-state decomposition of oxalate based materials leading to metal oxides. The thesis deals with the elucidation of kinetics of thermal decomposition of zinc oxalate dihydrate up to the formation of zinc oxide nanostructures and the effect of some additives like Ce, Sr and Ba of different molar concentrations using model-free isoconversional methods in non-isothermal condition using two thermal analyses techniques, Differential Scanning Calorimetry (DSC) (in nitrogen atmosphere) and Thermogravimetry (TG) (in static air). The thesis is divided into 6 chapters.

Chapter 1 deals with general introduction emphasizing importance of solid state reaction kinetics and the methods used for the

thermal analysis. This chapter also includes the importance of zinc oxide nanomaterials and the metal ions modified zinc oxide nanomaterials. Computational aspects of thermal decomposition of metal oxalates is also incorporated in this chapter.

Chapter 2 deals with the examination of the dehydration of zinc oxalate dihydrate and the thermal decomposition behavior of anhydrous zinc oxalate by experimental techniques by non- isothermal DSC technique in flowing N_2 atmosphere and by a theoretical examination of the electronic structure and bonding properties in view of the DFT strategy utilizing Gaussian09W simulation package. Chapter 3 focuses on the consequences of Ce^{3+} additives with cerium concentrations 0.1, 1, and 5 mol% on the kinetics of thermal dehydration and decomposition reactions of zinc oxalate dihydrate in two different atmospheres, nitrogen and air using DSC and TGA techniques. Chapter 4 introduces the kinetics of thermal decomposition of strontium added zinc oxalate of different strontium concentration 0.1, 1, 2, and 5 mol% using DSC technique in N_2 atmosphere. Chapter 5 discusses the synthesis and characterization of Ba doped zinc oxide nanoparticles with four different concentrations of barium, 2, 3, 4, and 5 mol % and the examination of the kinetics of the thermal decomposition of the formation of ZnO and Ba-ZnO nanoparticles from their oxalates precursors by non-isothermal TG in the air and DSC in N_2 with a view of obtaining the kinetic parameters and also to study the effect of barium doping on the kinetics of dehydration and decomposition of zinc oxalate dihydrate, the knowledge of which helps in the modification of the decomposition products by suitably altering the oxalate precursor. Chapter 6 includes the summary of findings obtained in the present work and a brief mention of the future perspective.

GENERAL INTRODUCTION

1.1. General introduction

Solid state chemistry, sometimes also termed as materials chemistry, deals with the synthesis, structure, and properties of solid-phase materials. The solid state chemistry focussed on the synthesis of novel materials and it has a strong overlap with solid state physics, mineralogy, crystallography, ceramics, metallurgy, thermodynamics, materials sciences, and electronics. Solid state chemistry continues to play an expanding role in several astounding arrays of disciplines. As the invention of new physical phenomena has always relied on the invention of novel materials, the synthesis of new solid state materials and kinetically stable composites with optimized properties is of great importance. The growing interest in solid state materials provides room for positive materials with tunable properties and these novel materials can be used in different areas like energy storage, catalysis, electronics, sensors, and separation technology.

The discovery of nanomaterials has revolutionized the world and has brought material chemistry to new levels. Today's research is more focussed on this 'fascinating materials' because of their amazing properties. The advancement of nanotechnology and nanophase engineering expands the manipulation of mechanical, catalytic, electric, magnetic, optical, and electronic properties of materials. The synthesis of nanomaterials is now an important field of research because of their superior properties such as mechanical strength, thermal stability,

photocatalytic activity, electrical conductivity, magnetic properties, and optical properties than that of the bulk properties. At the nanometer length scale, chemical reactivity of the materials enhances, affects their strength, and also quantum effects can begin to dominate and results in the intensification of novel properties like physical, chemical, biological, etc. Due to the large and reactive surface area of nanomaterials, they possess unique physical and chemical properties compared to their bulk materials. These nanomaterials are extensively used in several fields such as chemistry, electronics, photochemistry and biomedicine [1,2]. Nanomaterials are the most enticing and promising multifunctional molecules of today's world.

In many developing countries, population boom, rapid urbanization, industrialization, and paucity of wastewater treatment systems have exacerbated water shortages and a deterioration in water quality. The heavy metal contamination of water is one of the most crucial issues relating to water faced by the people worldwide because of the toxicity and carcinogenicity. The large surface area of nanomaterials as compared to their bulk counterparts make this material efficacious adsorbents in the processes of pollution remediation [3]. Due to the excellent mobility, high reactivity, low toxicity, controlled particle size, and abundant surface active sites of nanoscale zero-valent irons make them environmentally friendly materials and they can be used as effective adsorbents for the complete elimination of heavy metal ions [4]. Even though water is ubiquitous, just a tiny portion of it can be used for drinking purposes, since less than 1 percent of the earth's

surface water is freshwater, and remaining is found in the oceans. This small fraction of freshwater is also decreasing due to human interference on the earth and in the near future, people should use ocean water for their daily life activities, and here comes the importance of desalination of seawater. The introduction of carbon nanotubes (CNT), graphene, zeolites, and aquaporin with novel properties contribute a significant potential breakthrough in water desalination [5].

graphene-like 2D layered nanomaterials (GLN) including boron nitride nanosheets, graphitic-carbon nitride nanosheets, and transition metal dichalcogenides have been one of the most desirable fields of research from physics and chemistry to biology and engineering, enjoying unusual properties (e.g., heavy mechanical strength, high surface area, unparalleled thermal conductivity, remarkable biocompatibility and ease of functionalization). These 2D-layered nanomaterials have demonstrated great biochemical and biomedical potential [6].

The air pollution caused by the rapid industrialization resulting in ecological imbalance and global warming and the requirement for gas-sensing devices seems to be very high and is a hot research topic due to the serious health, safety, and environmental concerns. Conductometric metal oxide semiconductor (MOS) gas sensors are considered as being the most desirable gas sensors for sophisticated technologies in the automobile, pharmaceutical, safety, and environmental sectors due to their high sensitivity, reduced size, and low cost. The composite nanostructures, MOS gas sensors based on

metal@metal oxide core-shell nanostructures where certain noble metals (e.g., Ag, Pd) as the core and metal oxides (e.g., SnO_2) as the shell structure, integrated into a single nanostructure introduce unique synergetic features compared to single-component materials [7]. Multiple researchers have explored hybrid architectures developed by integrating metal oxide nanoparticles with graphene or its derivatives, which have shown superior fuel sensing capability, in particular, sensitivity and selectivity at room temperature, and these gas sensors can be used to detect gas molecules such as mono-nitrogen oxides (nitric oxide, NO), nitrogen dioxide (NO_2), ammonia (NH_3), carbon monoxide (CO) [8].

The increased interest behind the nanoscience and nanotechnology research is that nanotechnology facilitates the controlled synthesis of material products where at least one dimension of the structure is < 100 nm. This ultra-small size is comparable to the proteins and biomolecules that occur naturally in the cell [9] and is considerably lower than the typical diameter (~7 μm) of many human cells. Reducing materials to the nanoscale can frequently alter their electrical, magnetic, structural, morphological, and chemical properties, incentivizing them to interact with cell biomolecules in a peculiar way and allow their physical transportation into the cell by appropriate engineering design. The potential use of ZnO and many other metal oxide nanoparticles in biomedical and cancer applications are gaining considerable attention in medical and scientific communities [10].

Owing to the special qualities and promising applications of nanosized transition metals and metal oxides become one of the hottest topics in material science. Transition metal oxides are the functional components used in catalysis in a wide variety of processes to convert hydrocarbons to other chemicals which is a highly economically important process, used as electrode materials in electrochemical reactions, used in the electronic industry to make conductors in the film [11]. They exhibit fascinating optical, magnetic, and electrical properties or they show metallic, insulating, semiconducting and ferro, ferri, or antiferro magnetic behavior. Some metal oxides exhibit superconducting behavior also. They are used in many devices like energy storage, energy conversion, gas sensing, catalysis, magnetic storage, etc. [12–15]. Various physical and chemical synthetic approaches have been developed for the synthesis of transition metal oxide micro or nanoparticles which include dividing a bulk solid through mechanical abrasion (crushing), electrical or thermal erosion (laser ablation), vapour phase oxidation, thermal vapour transport and condensing ions or molecules, chemical vapour deposition [16–20]. These methods should be carried out at relatively high temperatures (500-1500 ^{0}C) to grow crystalline particles [20]. Transition metal oxides can also be prepared by a variety of methods using chemical precursors, intercalation, ion exchange, alkali flux, electrochemical, sol-gel, high pressure, and arc techniques [21]. Precipitation and coprecipitation of ions from solution have been used for many years for the synthesis of fine powders. Metal oxides are usually synthesized by the thermal decomposition of precursor compounds, metal nitrates, bicarbonates,

carbonates, hydroxides, and oxalates that decompose at low temperatures and minimize the sintering of the resulting oxide and having minimum interfering side reactions. The precursors used for the synthesis of transition metal oxides have been extensively studied because they can often be configured structurally. Some precursors are recognized that they can be transformed into respective nano-metal oxides with a high degree of retention of shape or similarities. Among the different synthetic pathways and precursors for the synthesis of metal oxide or mixed metal oxides, thermal decomposition of metal-organic complexes at relatively low temperature become increasingly important due to the easy control of process condition, purity, phase, composition, and microstructure of the resulting product [22–24]. Thermal decomposition of the metal complexes with oxalate ligand serves as a wide and convenient source of oxide with controlled stoichiometry, high homogeneity, and reduced particle size. Transition metal oxalates, where oxalate ($C_2O_4^{2-}$) is the simplest dicarboxylate, are representative of transition metal oxide precursors due to the significant advantages in terms of minimum cost, diverse preparation strategies, comparatively low temperature and easy modification of the precursor [25,26]. Transition metal oxalates have been successfully synthesized using a variety of methods, including reverse micellar route, precipitation, microemulsion, and sol-gel, *etc* [27]. Mixed metal oxide (MMO) nanoparticles or heterometal oxide nanoparticles can play important roles in several areas of chemistry and physics. The special electronic and magnetic properties acquired when two metals were mixed in an oxide matrix were well explored. However, the other most

common use for MMOs is in the catalysis field. Mixed metal oxide nanoparticles can be synthesized by sol-gel method, solvothermal method, hydrothermal method, flame spray pyrolysis, the co-precipitation method using suitable metal oxalate as the precursor and followed by its thermal decomposition [27–30].

The decomposition study serves as the most useful tool to get insight into the mechanism of solid-state decomposition of oxalate based materials leading to metal oxides.

Studies regarding solid state have three dimensions: the phenomenological, the thermodynamic, and the kinetic. Qualitative and semi qualitative observation of a phenomenon that occurs during a reaction is coming under the aspect of the phenomenological study. The thermodynamic aspects of solid state study involve the initial, final, and equilibrium states of the system and the inducing force behind the transformation. The kinetic part includes the rates of transformation of the reactant to the product. Most of the solid state reactions are assumed to be of diffusion controlled.

Factors like morphology, reaction interface geometry, diffusion of reaction species, the possibility of the nucleation, and crystallite anisotropy influence the reaction rate [31]. The starting material is solid at the commencement of so many manufacturing processes and most studies of thermal analysis. After, probably either during or due to the heat treatment, a transformation to a liquid or gas phase may happen in

whole or in part or it seems essential to understand this special position of the solid phase. There are several possibilities;

A (solid) → A (liquid) → B (solid) + gas/gases

A (solid) → B (solid) + gas/gases

A (solid) → A (liquid) → gas/gases

A (solid) → gas (gases)

A (solid) → B (liquid) + gas/gases

A (solid) + gas →B gas/gases [32].

Or the solid state reactions can be classified into 4 categories,

1. Solid-solid reaction
2. Solid-liquid reaction
3. Solid-gas reaction
4. Reactions of a single solid (e.g., solid state decomposition)

And among these, this work is concerned only with solid state decomposition reactions of the type;

A (solid) → B (solid) + C (gas/gases)

1.1.1. Solid state reaction kinetics

The kinetic data of solid state reactions are of practical importance to the large and increasing number of technologically

important processes. Understanding of kinetic parameters, such as the reaction rate and energy of activation of the thermal decomposition reaction has been one of the keys for assessing the mechanisms of reaction in the solid phase. There are also more practical reasons behind the study of reaction rates and the dependence of temperature. Whenever variations are found in the mechanisms of reaction, it may lead to a particular feature and therefore a thorough understanding of the materials. For the accurate design of installations and treatment conditions, the industry requires estimations of the kinetic parameters, because increasing temperature or lengthening reaction time means more cost. The thermo-analytical experiments can be implemented for the modeling of industrial thermal processes by using a correct mathematical relationship. The outcomes of the kinetic investigation of thermo-analytical reactions in the solid state can also be applied to various problems like useful lifetime of some materials, oxidative, thermal and chemical stability, and quality management.

Chemical kinetics offers mathematical models to describe and predict the transformation rate of chemical reactions. The basic principle of chemical kinetics is based on the law of mass action developed during mid - nineteenth century by Cato M. Guldberg (1836-1902) and Peter Waage (1833-1900), in which equilibrium constant was generated in terms of kinetic data and rate equations. Over the last few years, heterogeneous kinetics or solid state kinetics have been one of the most challenging and demanding research areas. Solid state kinetics can be studied by utilizing different methods. In 1925, Kujirai and Akahira

completed their first work in the solid state kinetics on the topic 'Influence of temperature on the degradation of fibrous industrial materials' [33]. The solid state kinetics can be well studied by using data obtained from thermogravimetric analysis (TG), differential thermal analysis (DTA), and differential scanning calorimetry (DSC) in addition to a variety of other methods.

Kinetic analysis of thermal decomposition reactions can be a valuable study for predicting the characteristics of intermediate products and products of thermal decomposition [34]. Numerous analytical methods were established for the determination of kinetic parameters for solid state decomposition reactions [35–37]. Many of the existing kinetic methods available vary from one another simply because of their respective different approximations of the temperature-containing integral. Due to the inherent advantages of integral methods, the experimental kinetic data were usually analyzed by employing integral methods [38].

The prime objective of the kinetic analysis is to identify the rate equation that provides the most appropriate description of the experimental conversion function versus temperature. This can be accomplished by analyzing the precise mathematical fit of the experimental data with the relation between conversion function and temperature needed by the models to represent the data satisfactorily. In solid state kinetics, mechanistic portrayals generally involve recognizing a reasonable reaction model, as it is often hard to find information about individual reaction steps. A model can represent a

particular type of reaction and translate mathematically into a rate equation. Many models are constructed according to certain mathematical presumptions. Mechanistically, solid state kinetic reactions may be categorized as nucleation, diffusion, and reaction order models. Two methods are used for studying the kinetics of solid state reaction; model-fitting method and model-free method.

1.1.1.1.The model-fitting method of thermal analysis

The model-fitting methods were widely used because of their ability to directly determine the kinetic triplet, activation energy (E_a), Arrhenius pre-exponential factor (A), and reaction model $f(\alpha)$.

The equation used for non-isothermal data is

$$ln\ (g(\alpha)/T^2) = ln\ (AR/\beta) - E/(RT) \quad (1)$$

The most probable kinetic function and the corresponding kinetic parameters, namely the activation energy, are determined by plotting $ln\ (g(\alpha)/T^2)$ *versus* $1/T$. Thus, a plot of $ln\ (g(\alpha)/T^2)$ *vs.* $1/T$ must be a straight line for the correct mechanism and non-linear for an incorrect mechanism. Hence, by calculating the value of $ln\ (g(\alpha)/T^2)$ using the non-isothermal data for the various reaction models enough to explain the kinetics of reaction and plotting them *vs.* $1/T$, the most probable mechanism corresponding to the linear plot can be determined. The model giving the best fit *i.e.*, maximum correlation coefficient (R^2 approximately to unity) is taken as the best model describing the mechanism of the reaction. From the slope of the line, activation energy

can be calculated and the frequency factor can be calculated from the intercept of the linear equation. This method is called the Coats Redfern method [39].

The different reaction models *f(α)* commonly used to describe the reaction kinetics and their integrated forms *g(α)* are given in **Table 1.** below,

$$g(\alpha) = \int_0^{\alpha} \frac{1}{f(\alpha)} d\alpha \qquad (2)$$

Table 1. Different reaction models used to describe the reaction kinetics

No.	Code	Reaction model	*f(α)*	Function *g(α)*
1	P4	Power law	$4\alpha^{3/4}$	$\alpha^{1/4}$
2	P3	Power law	$3\alpha^{2/3}$	$\alpha^{1/3}$
3	P2	Power law	$2\alpha^{1/2}$	$\alpha^{1/2}$
4	P2/3	Power law	$2/3\alpha^{-1/2}$	$\alpha^{3/2}$
5	D1	One-dimensional diffusion	$1/2\alpha^{-1}$	α^2
6	F1	Mampel (first-order)	$1-\alpha$	$-\ln(1-\alpha)$
7	A4	Avrami–Erofeev	$4(1-\alpha)[-\ln(1-\alpha)]^{3/4}$	$(-\ln(1-\alpha))^{1/4}$
8	A3	Avrami–Erofeev	$3(1-\alpha)[-\ln(1-\alpha)]^{2/3}$	$(-\ln(1-\alpha))^{1/3}$
9	A2	Avrami–Erofeev	$2(1-\alpha)[-\ln(1-\alpha)]^{1/2}$	$(-\ln(1-\alpha))^{1/2}$
10	D3	Three-dimensional diffusion	$3/2(1-\alpha)^{2/3}[1-(1-\alpha)^{1/3}]^{-1}$	$(1-(1-\alpha)^{1/3})^2$
11	R3	Contracting sphere	$3(1-\alpha)^{2/3}$	$1-(1-\alpha)^{1/3}$
12	R2	Contracting cylinder	$2(1-\alpha)^{1/2}$	$1-(1-\alpha)^{1/2}$
13	F2	Second-order	$(1-\alpha)^2$	$(1-\alpha)^{-1}-1$

1.1.1.2. Model-free and Isoconversional methods of thermal analysis

The most dependable method for calculating the activation energy of thermally activated processes is model-free methods. Model-free methods calculate the activation energy of solid state reaction without modelistic assumptions. Model-free methods, therefore, report activation energy only. Isoconversional methods are model-free methods that assess the kinetic parameter, namely activation energy at different conversion value, α. Isoconversional methods are also called multi-curve methods since these methods require several kinetic curves to perform the analysis. The word isoconversional is used because the calculations are performed at the same value of conversion α from several curves at different heating rates. The reaction rate is supposed to be a function of temperature only. These methods, therefore, calculate the activation energy for each conversion point, resulting in an isoconversional plot; E_a *vs* α. Isoconversion methods based on multiple heating programs seem to be the most popular method for finding the kinetics of thermal decomposition reactions of solids. The words model-free and isoconversional methods are often used synonymously, but not all model-free methods are isoconversional. Solid state kinetics can be studied *via* either isothermal or non-isothermal experimental condition and isoconversional methods can be used for the interpretation of both isothermal and non-isothermal data. Among these, the non-isothermal method is more preferred over isothermal because all interesting information can be obtained from a single experimental run [40–42]. The rate of transformation of a solid state reaction under non-isothermal

conditions is assumed to be the product of two functions, one temperature-dependent, and the other conversion-dependent.

The kinetic parameters of solid state decomposition reaction proceeding in non-isothermal conditions can be studied using the differential form of the kinetic equation;

$$d\alpha / dt = k(T) f(\alpha) \quad (3)$$

where $f(\alpha)$ is a function of α depending on reaction model and

$$k(T) = Ae^{-E_a/RT} \quad (4)$$

where E_a is the activation energy and A is the pre-exponential factor. Arrhenius parameters can be determined only if $k(T)$ and $f(\alpha)$ are separated. The variation in the rate of reaction at different heating rates can be used to determine the activation energy of the reaction. Activation energy is constant throughout the conversion for a single-stage reaction while it varies for complex reactions. The mechanism of the reaction can be explained by studying the variation of activation energy with α. M.J. Starink compared the accuracy of different isoconversional methods in the determination of activation energy from linear heating rate experiments [42].

Combining equations (3) and (4)

$$d\alpha / dt = Ae^{-E_a/RT} f(\alpha) \quad (5)$$

At non-isothermal conditions, the temperature is increasing with time at the constant heating rate. Integration of Eq. (5) involves solving the temperature integral, *I(E, T)*

$$g\ (\alpha) = A/\beta \int_0^{Tx} e^{-E_a/RT} dt = A/\beta I\left(E,T\right) \tag{6}$$

this equation has an ineffectual analytical solution. Some approximations or numerical integration is used to solve the equation. All of the approximations lead to a direct isoconversional method in the form:

$$ln\ \left(\beta / T^K\right)\ =\ C - E_a / RT \tag{7}$$

for a selected degree of conversion function, α, a corresponding $T_{\alpha i}$ and heating rate β are used to plot $ln(\beta/T^K)$ against $1/T_{\alpha i}$, where K is a constant. The activation energy is then determined from the regression slope [43].

Some of the commonly used isoconversional methods are Flynn-Wall-Ozawa (FWO), Kissinger-Akahira-Sunose (KAS) , Tang, Starink, Boswell, and Friedman.

1.1.1.2.1. Flynn-Wall-Ozawa (FWO) Method [44,45]

The equation based on the FWO method is:

$$ln\beta =\ ln\left(AE / g\left(\alpha\right)R\right) - 5.331 - 1.052E_\alpha / RT_{\alpha i} \tag{8}$$

where α is the conversion function. From the slope of the graph $ln\beta$ *vs* $1/T_{\alpha i}$, E_a can be calculated.

1.1.1.2.2. Kissinger-Akahira-Sunose (KAS) Method [46]

KAS is also an integer isoconversional method similar to FWO.

$$ln\beta / T^2 = ln\left(AR / E_a g(\alpha)\right) - E_a / RT \quad (9)$$

E_a can be obtained from the slope of the straight-line graph $\ln\beta/T^2$ against 1/T.

1.1.1.2.3. **Tang Method** [47]

$$ln\left(\beta / T^{1.894661}\right) = ln\left(AE_a / Rg(\alpha)\right) + 3.635041 - 1.894661 ln\, E_a - 1.00145033 E_a / RT \quad (10)$$

E_a can be obtained from the slope of the straight-line plot of $ln(\beta/T^{1.894661})$ *vs* $1/T$.

1.1.1.2.4. Starink Method [48,49]

$$ln\beta / T^{1.95} = C^{1.95}(\alpha) - E_a / RT \quad (11)$$

$$ln\beta / T^{1.92} = C^{1.92}(\alpha) - 1.0008 E_a / RT \quad (12)$$

1.1.1.2.5. Boswell Method

$$ln\beta / T = C(\alpha) - E_a / RT_{\alpha i} \quad (13)$$

1.1.1.2.6. Friedman Method

$$ln(d\alpha / dt) = ln(A / f(\alpha)) - E_a / RT \quad (14)$$

In this method, $ln(d\alpha / dt)$ is plotted against *1/T*. From the values of slope, E_a can be calculated.

1.1.2. Why zinc oxalate as the material for study?

ZnO is an n-type semiconductor with a bandgap of 3.37 eV and exciton binding energy of 60 M eV [50]. ZnO is an excellent, multifunctional compound. ZnO nanoparticles (ZnO-NPs) are used in several fields today. Owing to its high quantum efficiency, several researchers confirmed that it is a better photocatalyst for the degradation of organic pollutants over TiO_2 [51–53]. The biggest advantage of ZnO is that it absorbs over a larger fraction of the solar spectrum than TiO_2. For this reason, ZnO photocatalyst is the most suitable for photocatalytic degradation in the presence of sunlight. ZnO nanoparticles possess multiple interesting properties for biomedical applications, such as preferable bandgap, electrostatic charge, surface chemistry, and redox cycling cascade potentiation. Especially, ZnO nanoparticles seem to have innate cytotoxicity initiatives without causing harmful systemic pro-inflammatory effects [10]. ZnO-NPs have alluring antibacterial properties caused by their increased specific surface area because of the reduced particle size, which leads to better particle surface reactivity. In the food packaging industry, one practical application of ZnO antibacterial bioactivity was explored, where ZnO-NPs was used as an

antibacterial agent for foodborne diseases. Proper inclusion of ZnO-NPs in packaging materials may allow the interaction with pathogenic bacteria and thus release zinc oxide NPs on the surface of the food where they come into direct contact with harmful bacteria and cause bacterial death and/or inhibition [54].

ZnO nanomaterials were also employed for the fabrication of efficient gas sensors for detecting numerous toxic and dangerous gasses [55]. ZnO NPs demonstrated the potential for seed germination and plant growth stimulation, along with disease suppression and plant safety through its antimicrobial properties [56]. Zinc Oxide (ZnO) is investigated as a technologically notable material with a wide range of applications such as semiconductor, gas sensor, piezoelectric sensor, electro-luminescent material, magnetic material, actuator and cosmetic ingredients [57].

Doping ZnO nanostructures with metal ions is a strategy to modify their electronic and optical performance and improve their applications. Iron and cobalt doped zinc oxide nanoparticles characterized and used for the first time as anode material for lithium-ion batteries [58]. Manganese doped ZnO exhibits excellent antibacterial activity against *Escherichia coli, Klebsiella pneumoniae, Shigella dysenteriae, Salmonella typhi, Pseudomonas aeruginosa, Bacillus subtilis, and Staphylococcus aureus* than pure ZnO [59]. Strontium-doped zinc oxide nanoparticles synthesized through a sol-gel process display enhancement in photocatalytic activity for methylene blue degradation compared to pure ZnO up to an optimum concentration

[60]. The optical bandgap of ZnO nanoparticles raised from 3.16 to 3.20 eV when the aluminum concentration is increased to 10 mol percent in solution [61]. The research work on the optical properties of nickel doped ZnO synthesized through the auto-combustion method showed that bandgap energy declines from 3.21 eV to 3.17 eV, photoluminescence (PL) spectra of the as-prepared samples under room temperature exhibits strong ultraviolet (UV) and blue emission peaks [62].

Recent studies show that the addition of transition and noble metals like gold, silver, and platinum accelerate the charge transfer process and thereby increasing the photodegradation process [27,29,63]. Lanthanide-doped ZnO nanocrystals are one of the new classes of luminescent materials for advanced display and lighting applications. La, Ce-co-doped ZnO nanoparticles show prominent large red-shift in the ultraviolet region which makes them good prospects for use in visible high-efficiency luminescent flat displays and excellent solar light-activated photocatalysts [64]. Doping with Ce ion enhances the photocatalytic activity against various organic pollutants which can be due to the increased surface oxygen vacancies, higher adsorption capacity, and better separation of electron-hole pairs in nanostructured photocatalyst [65]. Ce-doped ZnO nanorods have been reported as an efficient electron mediator for the fabrication of hydroquinone chemical sensors [66].

Sr doped ZnO show enhancement in gas sensing properties and this nanostructure is a propitious material for the designing of sensor

devices for monitoring indoor air quality [67]. Recent studies have shown that Sr doped ZnO nanostructures exhibit an increase in photocatalytic activity [60,68,69].

Effects of barium doping on structural, optical, and ferroelectric properties of ZnO nanoparticles prepared by a low-cost thermal decomposition method are presented by Gunjan Srinet *et al.* and they observed that some structural transformation in the morphology of nanostructure has occurred with Ba doping. The doping of Ba also causes redshift in the UV-visible spectra, a high value of dielectric constant, transition temperature, a high value of remnant polarization, and low value of the coercive field which can be useful for potential applications [70]. S. D. Bukkitgar *et al.* studied the mefenamic acid-sensing properties of 5% barium doped ZnO nanoparticles using glassy carbon electrodes and the developed method was used in the in-vitro analysis of mefenamic acid in pharmaceutical formulations and spiked human urine samples [71]. Ba-doped ZnO nanospheres show superior photocatalytic efficiency compared to pure ZnO and commercial TiO_2 [72]. The doping of Ba on ZnO nanoparticles causes changes in the optical, mechanical, photocatalytic, and electric properties of ZnO, so it is very important to study the effect of Ba doping on the kinetics of formation of ZnO nanoparticles.

zinc oxides can be synthesized by a variety of methods like reverse micellar route, precipitation, chemical vapour synthesis, microemulsion, and sol-gel using different starting compounds and all have their advantages and disadvantages [73–77]. Thermal

decomposition of many precursors like zinc oxalate, zinc nitrate, zinc hydroxide, zinc carbonate, or zinc acetate is successful in the production of zinc oxide nanoparticles [78,79]. The thermal decomposition of zinc oxalate has been used to produce very pure fine-grain ZnO powder and these ZnO nanoparticles are used for many important applications [80–82].

Oxalate $(C_2O_4)^{2-}$ is the dianion of the parent acid oxalic acid ($H_2C_2O_4$). It is an excellent bidentate ligand and can very easily coordinate with transition and nontransition metals. Transition metal oxalates are insoluble in water and this enables for the quantitative precipitation of many ions. The metal oxalates prepared in aqueous medium are crystallized in the form of their hydrates. At a specific temperature, hydrated salts have a fixed composition. The oxalates typically lose their water of crystallization below 473 K and their anhydrous salts are formed. Most anhydrous oxalates face thermal decomposition before melting. The products produced during the thermal decomposition reaction depend on the temperature, pressure, the atmosphere in which the decomposition occurs, and, above everything, on the nature of the oxalate being studied.

1.2. Review of Literature

Studies of thermal decomposition of oxalates are quite an important topic because they have industrial applications, numerous analytical applications and because of their thermal stability and decomposition in many ways serve as examples for the decomposition

of several other oxysalts. The processes of thermal decomposition of metal oxalates are relatively complex due to the reduction property of oxalate ion $(C_2O_4)^{2-}$. Therefore their thermal studies have always been in the spotlight. A review of the thermal decomposition of some solid oxalates has been given by Harris and co-workers [83]. The atmosphere of decomposition, crystal shape, size, presence of defects, and different pretreatments, including irradiation, mechanical grinding, doping, *etc*., play a pivotal role in the decomposition process, particularly in determining the kinetics of oxalate decomposition. Irradiation and mechanical grinding usually raise the rate of decomposition and dehydration reactions and lower the temperature for decomposition and dehydration reactions. In certain cases, even just the treatment itself results in dehydration and decomposition reaction. The effect of doping depends on the type and nature of dopants.

Dollimore and Griffiths performed a comparative differential thermal analysis (DTA) investigation of 25 oxalates in an environment of N_2 and O_2 [84]. The onset temperatures of dehydration and decomposition reactions are disclosed and environmental role on temperatures of reaction as well as decomposition products has been explained. The particle size of the sample also plays a crucial role in deciding the temperature of decomposition of the substance under investigation. In general, it is observed that the decomposition temperature is lowered with a decline of particle size. The activation energy of decomposition is observed to vary greatly with the temperature of decomposition. In certain situations, activation energy

relies on the mass of the sample and the environment in which decomposition occurs. The process of mixing one oxalate with another eventually changes the reaction mechanism. Padmanabhan *et al.* have reported the thermal decomposition of thorium, lanthanum, and uranium oxalates from thermogravimetry (TG) and differential thermal analysis (DTA) [84]. Dollimore and Nicholson explored the occurrence of variations in the surface area of the solid products when heavy metal oxalates like aluminium, manganese, iron, cobalt, nickel, zinc, chromium, copper, are heated at different temperatures [85]. Dollimore *et al.* studied the thermogravimetric (TG) analysis of several oxalates such as aluminium, manganese, iron, cobalt, nickel, zinc, chromium, copper, cadmium, stannous, lead and thorium in air and nitrogen atmospheres [86]. Dollimore reviewed the thermal decomposition and stability of several oxalates in terms of their characteristics [87]. The thermal decomposition of oxalates is observed to be associated with a substantial induction period especially at low temperatures [88,89]. The heating rate is the key factor in determining the temperature of the decomposition reaction in the non-isothermal analysis. Boris V. L'vov made an excellent review of the physical approach to the interpretation of the kinetics and mechanism of thermal decomposition of solids [90]. The physical approach helps for the quantitative interpretation of the features of the crystolysis reactions like the mechanism of nucleation, the effect of self-cooling in the measurement of kinetic parameters, investigation of kinetics and mechanism of decomposition reactions of molecular, ionic, covalent and metallic crystals.

The oxalates of iron, potassium, strontium, barium, calcium, *etc*., exhibit the phenomenon of allotropy during heating before decomposition. Oxalate decomposition requires the cleavage of the C-C bond since the products are CO and CO_2 each of which possesses only one carbon atom. For most cases in thermal decomposition reaction, the breaking of the C-C bond is the rate-determining step. The cleavage of the C-C bond may be heterolytic or homolytic and these cleavages produce CO_2 and $(CO_2)^{2-}$ or two CO_2^- anions respectively [91].

Boldyrev *et al.* [92–96] suggested three possible pathways for the thermal decomposition of oxalates.

1. The first category includes oxalates that break into the corresponding carbonate as the solid product and carbon monoxide as the gaseous product.

$$MC_2O_4 \rightarrow MCO_3 + CO \qquad (15)$$

2. The second group comprised of oxalates that normally decompose to form the metal oxide as the solid product and a mixture of carbon monoxide and carbon dioxide as the gaseous products.

$$MC_2O_4 \rightarrow MO + CO + CO_2 \qquad (16)$$

3. The third group contains those oxalates which produce metal as the solid product and carbon dioxide as the gaseous product during thermal decomposition.

$$MC_2O_4 \rightarrow M + 2CO_2 \quad (17)$$

The mechanism of thermal decomposition and dehydration is quite well defined for many oxalates. These are therefore usually used as standards to verify the accuracy of the theoretically proposed model and the equation of solid state thermal decomposition reactions.

1.2.1. Thermal decomposition of zinc oxalate

Zinc oxalate dihydrate undergoes dehydration as,

$$ZnC_2O_4.2\ H_2O \rightarrow ZnC_2O_4 + 2H_2O \quad (18)$$

The decomposition of zinc oxalate in air has been studied by Dollimore *et al.* who found that the power-law is applicable during the acceleratory region with the value of *n* varying in between 1.5 and 1.8 [32].

Yankwich *et al*. reported the decomposition of anhydrous zinc oxalate (in the region 573 to 643 K) in which zinc oxide as the solid product and carbon monoxide and carbon dioxide as the gaseous products.

$$ZnC_2O_4(s) \rightarrow ZnO(s) + CO\ (g) + CO_2\ (g) \quad (19)$$

In this sequence of the decomposition reaction, carbon dioxide is formed in slight excess (the CO_2/CO ratio is about 1.09), but no zinc metal was detected. The kinetic analysis showed that there are three phases in the decomposition: (a) The initial acceleratory step ($\alpha < 0.04$) during which the reaction is predominantly due to the growth of nuclei formed during

the dehydration of the $ZnC_2O_4.2H_20$ from which the anhydrous starting material is prepared; (b) an intermediate acceleratory period ($0.04 < \alpha < 0.4$) during which original nucleic growth predominates at the beginning and reaction due to randomly generated nuclei predominates at the end, and (c) a decay period ($\alpha > 0.4$) during which the decomposition progresses entirely by random nucleation and followed by a very fast reaction. The findings indicate that the same elementary processes are connected with the nucleation and growth of the nucleus [97]. Yankwich *et al*. synthesized zinc oxalate in a vacuum from the dihydrate just before the pyrolysis were initiated. Yankwich got sigmoidal *α-t* curves for all the experiments carried out which indicates the thermal decomposition exhibits an initial acceleratory phase and a final deceleratory phase. Although there was an acceleratory process ($\alpha < 0.4$) which obeys a power law with n = 1 to 2, the isothermal *α versus t* curves were predominantly deceleratory with an E_a value of 210 kJ mol^{-1}.

Palanisamy *et al.* investigated the thermal decomposition kinetics of zinc oxalate by isothermal and non-isothermal thermogravimetry in air [98]. The isothermal kinetic results indicate that the mechanism of zinc oxalate decomposition comprises of rapid nucleation, accompanied by two dimensional growth in the acceleratory region [98]. The activation energy and the frequency factor procured from TG curves are in full conformity with those acquired from the isothermal method. The decomposition of zinc oxalate in air in the temperature range 613-643 K is found to obey the simple power-law

with n = 2 to 2.2 in the region 0.05 < α <0.65 and a unimolecular law towards the final stages of the reaction (0.8 < α <1.0). The intermediate region (0.65 < α <0.8) could not be analyzed satisfactorily by any single kinetic expression. This may be attributed to the fact that a combination of various kinetic laws may be operative in this region. A value of n = 2 in power-law can be viewed in two different ways; either that is attributed to random nucleation preceded by one-dimensional growth or to incredibly rapid nucleation accompanied by two-dimensional growth. One dimensional growth of nuclei seems to be a very hard process of spreading the reaction in a three-dimensional solid matrix, in the current context, the reaction is likely to be due to relatively fast random nucleation accompanied by two-dimensional growth. In general, the reactant-product interface is of complex shape towards the end of the reaction. Due to the strain generated at the reactant-product interface, the reactant breaks into smaller pieces of it which do not contain any nuclei of its own. So every molecule has got equal opportunities for decomposition in these chunks. The final stage of the reaction thus obeys unimolecular law. The findings of Palanisamy *et al.* are in good agreement with the results of Yankwich *et al*. The activation energies for zinc oxalate decomposition from the TG curves by the methods of Coats and Redfern and Zsako are in satisfactory agreement with the value obtained by the isothermal method. The activation energy obtained for the dehydration of two molecules of water from the dihydrate of zinc was found that 17 kcal mol^{-1} in the temperature range 150-220 ^{0}C.

The thermal decomposition of zinc oxalate was investigated by Majumdar *et al.* [99] from a fresh experimental approach. DTA and TG were performed in air using sample cells composed of various materials (Pt, Al, Al_2O_3, and Ni). The results indicate that there are two corroborating steps, dehydration and decarboxylation and the end product is always ZnO. The first DTA peak was always endothermic, regardless of the building material of the sample cell, but the second DTA signal was exothermic only when the sample cell was constructed with Pt or when a few bits of Pt-foil was mixed with zinc oxalate in the aluminium sample cell. Ditte's test always responded positively, that is CO was evolved on heating $ZnOx.2H_2O$ in air/CO_2/N_2 when the sample was not in contact with Pt. All information suggests that Pt catalyzes the oxidation of CO liberated by ZnOx. Based on standard heats of formation of ZnC_2O_4 and other components, thermochemical calculations indicate that the two possible decomposition reactions, namely

$$\text{(i) } ZnC_2O_4 \rightarrow Zn + 2CO_2 \qquad \Delta H_1° = +201.66 \text{ kJ} \quad (20)$$

$$\text{(ii) } ZnC_2O_4 \rightarrow ZnO + CO + CO_2 \qquad \Delta H_2° = +136.73 \text{ kJ} \quad (21)$$

should be endothermic. Secondary in situ oxidation of either metallic zinc (ΔH = - 347.98 kJ mol^{-1}) or carbon monoxide (ΔH = -283.05 kJ mol^{-1}) would result in an overall exothermic effect. As the final product of decomposition of zinc oxalate in oxygen-free nitrogen [100] and the NH_3-N atmosphere is zinc oxide, and as CO is evolved in both, it is very sure that the decomposition proceeds primarily *via* reaction (2) under all

conditions. The lack of CO in evolved gases from Zn-oxalate in contact with Pt with a sufficient supply of air and the exothermic nature of the second DTA signal under these conditions can therefore only be described in terms of low-temperature oxidation of CO, catalyzed by Pt and not by the product ZnO.

The thermal decomposition of ZnC_2O_4 in the helium atmosphere was examined by Barbara Małecka *et al*. in isothermal and non-isothermal conditions and it was found to be a one-stage process with ZnO as a solid product [101]. Thermal decomposition was conducted with a system allowing simultaneous recording of both TGA and DTA signals. This device was linked online with a quadruple mass spectrometer so that evolved gas analysis (EGA) can be performed in parallel for detecting gaseous reaction products. From the mass loss studies, it is found that some water remained in occlusions in the oxalate structure. The X-ray diffraction pattern of the sample after dehydration indicated the presence of α-ZnC_2O_4. The decomposition stage begins around 600 K. The shape of the endothermic DTA signal indicates that decomposition is a single-stage process. Signals from EGA show CO and CO_2 evolve concurrently with the same rate during decomposition. The molar ratio CO: CO_2 determined from EGA signals is 1 and the only solid decomposition product identified through XRD analysis is ZnO. The sigmoidal shaped $\alpha - T$ curve suggests the existence of an induction period connected with the nucleation of a new phase and Avrami-Erofeev equation gave the best fit to the experimental data. At the beginning of the reaction, the rate of decomposition is determined by the

nucleation of a new phase. The activation energy is increased with an increase in heating rate. The kinetics of decomposition in the range of conversion $0.2 < \alpha < 0.85$ were described in terms of the Avrami-Erofeev equation with the same parameter $n \approx 2$ for isothermal and nonisothermal measurements that clearly indicates that the reaction rate is influenced by the two-dimensional growth of nuclei. The activation energy value for the non-isothermal and isothermal conditions was 181.4−186.5 and 190.8 kJ mol^{-1} respectively. The study concluded that kinetics of decomposition of ZnC_2O_4 proceeds with the same mechanism in isothermal and non-isothermal conditions.

The thermal decomposition of ZnC_2O_4 was studied in air, nitrogen, hydrogen, and carbon dioxide atmospheres in nonisothermal condition [102] by Mohamed *et al.* using Derivative thermogravimetry (DTG) and differential scanning calorimetry (DSC) to determine the reactivities and to characterize the factors that control the relative stabilities of a set of chemically related compounds. In the inert and reducing atmospheres, the decomposition temperature increased with a rise in enthalpy of formation of the divalent transition metal oxide, and it is also concluded that the rupture of the cation-oxygen (oxalate) bond (metal-oxygen bond) is the parameter that determines the stability of the salt. Apart from the small influence of CO_2, the decomposition of zinc oxalate was independent of the presence of gases like oxygen, nitrogen, hydrogen. The present observations detected no perceptible influence of O_2 on zinc oxalate decomposition. The reaction temperature is consistent with previous studies [97,103] in which reaction yielded ZnO

without the intervention of the carbonate. The largest enthalpies of reaction and highest reaction temperatures are associated with the oxide-forming reactions (MnO, ZnO, FeO) and lower for Ni and Co, where reaction conditions determine whether oxide or metal.

Nicholas D. Cooper [104] studied the complete kinetic and mechanistic decomposition of zinc oxalate with the characterization of intermediates and final oxide using thermogravimetric analysis in alumina crucibles at different heating rates; 1, 2, 5, 10 15, 20, 25, 30, and 40 K min^{-1} in an atmosphere of flowing nitrogen at a flow rate of 50 ml min^{-1}. Sample sizes of 1 mg, 5 mg, and 10 mg were carried out to determine the effect of sample size on the apparent activation energies. Isothermal kinetics were also done by heating the sample to the desired temperature at 20 K min^{-1} and allowing it to remain there for 60 minutes. The atmosphere was the same as those used for the non-isothermal measurements. The main conclusions arrived by Nicholas D. Cooper are both isoconversional kinetic analysis and the Evolved gas analysis-Fourier transform IR spectroscopy (EGA-FTIR) of the initial decomposition region indicate that the thermal decomposition of zinc oxalate follows a multi-step mechanism. EGA-FTIR indicates that the gaseous products, CO and CO_2, are produced at different rates supporting the conclusion from the isoconversional investigations and also observed that CO is formed in excess initially. These findings are in line with Boldyrev's proposed mechanism [105].

Yankwich and Zavitsanos [97] determined the decomposition was a four step process with an activation energy of ~ 200 kJ mol^{-1} for

each step, later researchers have favored this decomposition being a single step process [101,103,106,107]. Since the consensus is that zinc oxalate decomposes in one step without complete melting to produce zinc oxide, carbon dioxide, and carbon monoxide at most pressures in inert atmospheres, Aggarwal and Dollimore [106] recommend using it as a thermal decomposition reference standard to calibrate thermal analysis instruments. However, the value determined for the activation energy of this decomposition has not been established with certainty. The value determined for the activation energy (300 kJ mol^{-1}) by Aggarwal and Dollimore [106] is ~100 kJ mol^{-1} larger than the value reported by Yankwich and Zavitsanos, or by Danforth and Dix [103]. The most complete investigation done to date by Malecka, Drozdz-Ciesla, and Malecki [103] was analyzed using the Avrami–Erofe'ev equation with $n \approx 2$ giving activation energy between 181.4-186.5 kJ mol^{-1} for $0.2 < \alpha < 0.8$. A recent model-free analysis by Chengcheng Hu *et al.* [107] reported an activation energy of ~120 kJ mol^{-1} for this decomposition. Boldyrev has established that the thermal decomposition of metal oxalates fall into three classifications:

A. Those decomposing to produce the metal carbonate and CO

B. Those decomposing to produce the metal oxide, CO and CO_2

C. Those decomposing to produce the metal and CO_2.

The decomposition of zinc oxalate is a member of category B with growing evidence that it follows the mechanism for category A. Boldyrev suggested that the first step in the decomposition of each

classification was the breaking of the C-C bond to produce two CO^{2-} anions, which could recombine to produce carbonyl carbonate [$CO_3CO_2^-$]. While electron transfer complicates the mechanism for category C, this could also be a viable mechanism for category B. However, DFT (Density functional theory) calculations done for zinc oxalate by Kolezynski and Malecki [108] suggest this may not be the case. Their calculations indicate that one of the zinc oxide bonds breaks first leaving a partially anchored oxalate ion. The C-C bond then breaks to produce a CO_2 molecule and the CO_2^{2-} anion which rapidly decomposes to give zinc oxide and CO. Cooper gave particular attention to the initial decomposition region ($0.2 < \alpha$) that was largely ignored in the previous investigations to determine if this region offered additional clues about the decomposition mechanism. These measurements indicated that the apparent activation energy was a function of both the sample mass and the extent of reaction indicating that the reaction followed a multiple-step mechanism. EGA-FTIR studies indicated that there is a slight excess of CO during the initial reaction, supporting the possibility that carbonyl carbonate is an intermediate in the decomposition of classification B compounds. However, no evidence of this intermediate was observed in neither the IR nor the XRD of the solids formed during the decomposition. This result does not support the conclusion that CO_2 is produced initially as indicated by the DFT calculations.

Chengcheng Hu *et al.* [107] carried out the thermal decomposition studies of zinc oxalate by thermogravimetry (TG),

derivative thermogravimetric (DTG), and differential thermal analysis (DTA). The zinc oxalate dihydrate was synthesized by using oxalic acid and zinc acetate by mechanical mixing and homogenized in a planetary ball mill for 2 h and then dried in an oven at 80 ^{0}C for about 12 h. The results show that the thermal decomposition reaction includes two stages: dehydration and decomposition, with nanostructured ZnO as the final solid product [107]. The TG curves of zinc oxalate dihydrate have two mass loss stages. The first mass loss appears from 90 to 171 ^{0}C, accompanied by a large endothermic DTA peak at 152 ^{0}C with a slight shoulder on its low-temperature side (at 130 ^{0}C). The calculated mass loss agrees with the evolution of 2 mol water per mole of zinc oxalate dihydrate. The second mass loss of 37.2 % (theoretical mass loss 38.03 %) appears between 300 and 400 ^{0}C, which is accompanied by a sharp endothermic peak at 402 ^{0}C corresponding to the ZnC_2O_4 decomposition reaction. The total mass loss is 56.9 %, which is in good agreement with the calculated value of 57.1 % that can be calculated if it is assumed that the $ZnC_2O_4.2H_2O$ is completely transformed into ZnO. It is found from the DTA curves that, the peak temperature of the first stage gradually shifts to the higher with the increase of heating rate and for the second stage, the decomposition temperature shift to the higher linearly and the peaks become sharper and sharper. Kinetic model and kinetic parameters of the thermal decomposition stage of zinc oxalate have been determined by utilizing Ozawa integral method along with Coats–Redfern integral method. From the kinetic analysis, Chengcheng Hu *et al.* concluded that the decomposition conforms to the nucleation and growth of the nuclei model. The value of activation energy and the

kinetic reaction model are delineated to be 119.7 kJ mol^{-1} and $G(\alpha) = -\ln(1 - \alpha)^{1/2}$, respectively. The main conclusion reached is reaction starts at separated points on the crystal surface, where the lattice defects existed. The core of a new phase is formed by these adjacent decomposition products; afterward, the interface reaction of perinuclear molecules occurs on the nucleus. The growth and extension of the new phase are accompanied by the disappearance of the old phase until the whole solid phase has decomposed completely. The nucleus would be able to grow and expand quickly once it is formed since the activation energy for the formation of the nucleus is larger than the activation energy for the growth of the nucleus [109].

A flexible method has been developed for the preparation of zinc oxalate dihydrate nanorods using reverse micelles [109]. The oxalate crystals thus obtained were smooth and its average dimensions were 120 μm in diameter and 600 nm in length. Nanoparticles of zinc oxide obtained successfully by the thermal decomposition of zinc oxalate rods were ≈ 55 nm in diameter.

A method of multiple rates isotemperature is proposed to define the most possible mechanism, $g(\alpha)$, of thermal decomposition of zinc oxalate; the iterative isoconversional procedure has been employed to estimate apparent activation energy, E_a [110]. The preexponential factor A is obtained based on E_a and $g(\alpha)$. By this new method, the kinetic triplet of dehydration of zinc oxalate dihydrate is determined, and it is reported that the most probable mechanism for dehydration belongs to random nucleation and growth.

Kolezynski and Malecki [108] presented the results of first-principles calculations of band structure, the density of states, and electron density topology of ZnC_2O_4 crystal performed using WIEN2k FP LAPW ab initio package. The calculations are performed by selecting 500 k-points (7×7×8 mesh within the irreducible Brillouin zone), cut-off parameter Rk_{max}=7.5, and GGA-PBE exchange-correlation potential. The self-consistent field (SCF) electron density obtained was used in estimation of Bader's QTAIM (quantum theory of atoms in molecules), topological features of the electron density in crystal. Ample calculations of bond orders (Pauling, Bader, Cioslowski, and Mixon) and bond valences were carried out according to the bond valence model. The band structure and density of states calculated for zinc oxalate suggest, that zinc atom is almost entirely interacting with oxygen atoms, and the two symmetrically inequivalent O_1 and O_2 oxygen atoms, are experiencing the different influence of the surroundings, and therefore different bonding properties. Bader's QTAIM analysis of electron density topology results show that the value of electron density in bond critical points (BCP) is largest for C_1–O_1 bond, then smaller but comparable in value for C1 –O_2^i and C_1–C_2 bonds and much smaller for zinc oxygen bonds, but again greater for Zn–O_1 and smaller for both Zn–O_2 bonds. Thus the C_1–O_1 bond is the strongest one, the strength of C_1–O_2^i and C_1–C_1 bonds are similar and the weakest bonds are created by zinc and oxygen atoms. Therefore during the thermal decomposition process, one of the two longest Zn–O_2^{ii} bonds will be broken initially. After the breaking of Zn–O_2^{ii} bonds, there is a possibility of significant structure rebuilding. After the breaking of Zn–O_2^{ii} bond, Zn–O_1 (O_1 from neighbouring octahedron, bonded to C_1 from analyzed octahedron) and C_1–C_2 are sequentially broken and free CO_2

molecule is evolved. From the bond order calculation also concluded that in the C_1–O_1 bond is strongest, then much weaker are C_1–O_2^i and C_1–C_2 bonds (the latter one is little stronger) and the weakest are Zn–O bonds. Again this allows us to suppose that in the process of thermal decomposition, the above-mentioned bond-breaking sequence, leading to freeing of CO_2 molecule, will take place. In the next steps of decomposition process bond orders of C_1–O_2^i, Zn–O_1 and Zn–O_2^i are comparable and the Zn–O bonds orders are even greater than the one for C_1–O_2^i, thus it is supposed that as next ones, the C_1–O_2^i, than Zn–O_1 bonds will be broken, leaving Zn–O_2^i and C_1–O_1 bonds unbroken. Eventually, this process will lead to the decomposition of the anhydrous zinc oxalate to ZnO+CO+CO_2, in agreement with the experiment.

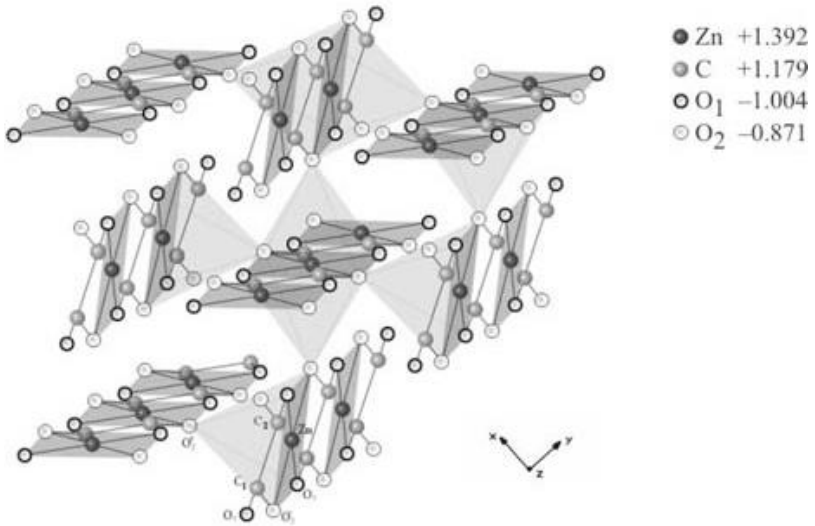

Fig. 1. Anhydrous zinc oxalate crystal structure. Calculated Bader's QTAIM total charges for the atoms are presented in the upper right corner of the figure.

The obtained results are analyzed for the thermal decomposition process, and this analysis indicates, that most probably this compound should decompose to the metal oxide, carbon monoxide, and carbon dioxide, in agreement with the experiment [107].

1.2.2. Computational aspects of thermal decomposition of metal oxalates

Since there is still lack of consistent description and explanation of the origin and thermal decomposition path of metal oxalates, the theoretical analysis of the electronic properties based on the ab-initio calculations have been carried out, which can give additional insight into the thermal decomposition process and help not only to explain thermal decomposition path in given oxalate but also to predict such most probable path for the compound for which experimental results are unavailable. Koleżyński *et al.* present the results of the theoretical studies undertaken for anhydrous zinc oxalate [108]. The obtained results of the ab-initio electronic structure calculations, bond orders, and bond valences of zinc oxalate are discussed in the light of the thermal decomposition process. The computations were done using WIEN2k FP LAPW ab-initio program. The obtained results were analyzed for the thermal decomposition process, and this analysis indicates, that most probably zinc oxalate should decompose to the metal oxide, carbon monooxide, and carbon dioxide, in agreement with the experiment [108].

Theoretical study of the characteristics of crystal structure and bonding in the thermal decomposition process is addressed in the selected anhydrous metal oxalates (Cd, Co, Zn) [111]. The overall findings encourage to conclude that these methods make possible to define and analyse the crystal structure and bonding properties when used simultaneously, and provide greater insights into its actions during the thermal decomposition process. The proposed theoretical strategy has been regarded as an effective and accurate method for theoretical research, enabling for the description and prediction of the properties of the structure and bonding and, thus, the most plausible form of thermal decomposition in these structures [111].

1.3. Aim and scope of the work

The doping and mixing of metal into metal oxide nanoparticles lead to the modification of most of the properties like electrical, mechanical, catalytic, and optical and hence their formation is also an important research topic. This thesis includes the synthesis and characterization of zinc oxalate and zinc oxalate doped with some metals, Ce, Sr, and Ba and the study of the effect of doping on the kinetics of formation of ZnO nanoparticles by the addition of the dopants Ce, Sr, and Ba using model-free isoconversional methods in non-isothermal condition using two thermal analyses techniques, Differential Scanning Calorimetry (DSC) (in nitrogen atmosphere) and Thermogravimetry (TG) (in static air). Until now, nobody seems to have reported the thermal behavior of coprecipitated binary oxalate mixtures of zinc with cerium, strontium, and barium. Neither the activation

energy nor the decomposition pathway has been established unequivocally for zinc oxalate. Since better knowledge of these could lead to more efficient processes for manufacturing ZnO, the newer more accurate isoconversional methods were used to investigate the decomposition process. Even the thermal decomposition of $ZnC_2O_4.2H_2O$ has been the subject of several studies, the mechanism and reaction kinetics of this transformation remains poorly understood. Even after numerous experimental results, there is still a lack of reliable description and interpretation of the origin and thermal decomposition route in the oxalates, but it can be expected that the primary reasons for disparities in the behavior of oxalates during thermal decomposition are the differences in the types of chemical bonds in oxalates depending on the type of metal atom and the structure of crystals. Hence the theoretical investigation was performed through density functional theory to understand the decomposition pathway of zinc oxalate. The study also includes a comparison of the thermal decomposition reaction of zinc oxalate and the Ce, Sr, and Ba added zinc oxalate in two different atmospheres, nitrogen and air.

1.4. References

[1] R. Hao, R. Xing, Z. Xu, Y. Hou, S. Gao, S. Sun, Synthesis, Functionalization, and Biomedical Applications of Multifunctional Magnetic Nanoparticles, Adv. Mater. 22 (2010) 2729–2742.

[2] M. Abhilash, et al, Potential applications of Nanoparticles, Int. J. Pharma Bio Sci. 1 (2010) 1–12.

[3] G.K. Sarma, S. Sen Gupta, K.G. Bhattacharyya, Nanomaterials as versatile adsorbents for heavy metal ions in water: a review, Environ. Sci. Pollut. Res. 26 (2019) 6245–6278.

[4] Y. Wu, H. Pang, Y. Liu, X. Wang, S. Yu, D. Fu, J. Chen, X. Wang, Environmental remediation of heavy metal ions by novel-nanomaterials: A review, Environ. Pollut. 246 (2019) 608–620.

[5] Y.H. Teow, A.W. Mohammad, New generation nanomaterials for water desalination: A review, Desalination. 451 (2019) 2–17.

[6] G. Yang, C. Zhu, D. Du, J. Zhu, Y. Lin, Graphene-like two-dimensional layered nanomaterials: applications in biosensors and nanomedicine, Nanoscale. 7 (2015) 14217–14231.

[7] A. Mirzaei, K. Janghorban, B. Hashemi, G. Neri, Metal-core@metal oxide-shell nanomaterials for gas-sensing applications: a review, J. Nanoparticle Res. 17 (2015) 371.doi.10.1007/s11051-015-3164-5.

[8] S. Gupta Chatterjee, S. Chatterjee, A.K. Ray, A.K. Chakraborty, Graphene–metal oxide nanohybrids for toxic gas sensor: A review, Sensors Actuators B Chem. 221 (2015) 1170–1181.

[9] S.E. McNeil, Nanotechnology for the biologist, J. Leukoc. Biol. 78 (2005) 585–594.

[10] J.W. Rasmussen, E. Martinez, P. Louka, D.G. Wingett, Zinc oxide nanoparticles for selective destruction of tumor cells and potential for drug delivery applications, Expert Opin. Drug Deliv. 7 (2010) 1063–1077.

[11] H.H. Kung, Transition metal oxides: surface chemistry and catalysis, Elsevier, 1989.

[12] G. Eranna, B.C. Joshi, D.P. Runthala, R.P. Gupta, Oxide Materials for Development of Integrated Gas Sensors—A Comprehensive Review, Crit. Rev. Solid State Mater. Sci. 29 (2004) 111–188.

[13] A.S. Aric, P. Bruce, B. Scrosati, J.-M. Tarascon, W. Van Schalkwijk, Nanostructured materials for advanced energy conversion and storage devices, in: Mater. Sustain. Energy, 2010, 148–159. doi.10.1142/9789814317665-0022.

[14] M.M. Thackeray, C.S. Johnson, J.T. Vaughey, N. Li, S.A. Hackney, Advances in manganese-oxide 'composite' electrodes for lithium-ion batteries, J. Mater. Chem. 15 (2005) 2257–2267.

[15] M. Winter, R.J. Brodd, What Are Batteries, Fuel Cells, and Supercapacitors?, Chem. Rev. 104 (2004) 4245–4270.

[16] J.Y. Lao, J.G. Wen, Z.F. Ren, Hierarchical ZnO Nanostructures, Nano Lett. 2 (2002) 1287–1291.

[17] J.-J. Wu, S.-C. Liu, Catalyst-Free Growth and Characterization of ZnO Nanorods, J. Phys. Chem. B. 106 (2002) 9546–9551.

[18] J.Y. Lao, J.Y. Huang, D.Z. Wang, Z.F. Ren, ZnO Nanobridges and Nanonails, Nano Lett. 3 (2003) 235–238.

[19] J.Q. Hu, Q. Li, N.B. Wong, C.S. Lee, S.T. Lee, Synthesis of Uniform Hexagonal Prismatic ZnO Whiskers, Chem. Mater. 14 (2002) 1216–1219.

[20] M.L. Kahn, A. Glaria, C. Pages, M. Monge, L. Saint Macary, A. Maisonnat, B. Chaudret, Organometallic chemistry: an alternative approach towards metal oxide nanoparticles, J. Mater. Chem. 19 (2009) 4044–4060.

[21] A.R. Barron, C. N. R. Rao and B. Raveau. Transition metal oxides. VCH, New York, 1995, ISBN 1-56081-647-3, 338 pp., Adv. Mater. Opt. Electron. 5 (1995) 286.

doi.10.1002/amo.860050510.

[22] S. Chaianansutcharit, O. Mekasuwandumrong, P. Praserthdam, Synthesis of Fe_2O_3 nanoparticles in different reaction media, Ceram. Int. 33 (2007) 697–699.

[23] N. Pinna, G. Garnweitner, M. Antonietti, M. Niederberger, A General Nonaqueous Route to Binary Metal Oxide Nanocrystals Involving a C−C Bond Cleavage, J. Am. Chem. Soc. 127 (2005) 5608–5612.

[24] Y.C. Zhang, J.Y. Tang, X.Y. Hu, Controllable synthesis and magnetic properties of pure hematite and maghemite nanocrystals from a molecular precursor, J. Alloys Compd. 462 (2008) 24–28.

[25] D. Wang, Q. Wang, T. Wang, Morphology-Controllable Synthesis of Cobalt Oxalates and Their Conversion to Mesoporous Co_3O_4 Nanostructures for Application in Supercapacitors, Inorg. Chem. 50 (2011) 6482–6492.

[26] Z. Jia, D. Ren, L. Xu, Generalized preparation of metal oxalate nano/submicro-rods by facile solvothermal method and their calcined products, Mater. Lett. 76 (2012) 194–197.

[27] P. Pawinrat, O. Mekasuwandumrong, J. Panpranot, Synthesis of Au–ZnO and Pt–ZnO nanocomposites by one-step flame spray pyrolysis and its application for photocatalytic degradation of dyes, Catal. Commun. 10 (2009) 1380–1385.

[28] O. Bechambi, M. Chalbi, W. Najjar, S. Sayadi, Photocatalytic activity of ZnO doped with Ag on the degradation of endocrine disrupting under UV irradiation and the investigation of its antibacterial activity, 347 (2015) 414-420.

[29] B. Subash, B. Krishnakumar, V. Pandiyan, M. Swaminathan, M. Shanthi, Synthesis and characterization of novel WO_3 loaded Ag–ZnO and its photocatalytic activity, Mater. Res. Bull. 48 (2013) 63–69.

[30] B. Krishnakumar, B. Subash, M. Swaminathan, AgBr–ZnO–An efficient nano-photocatalyst for the mineralization of Acid Black

1 with UV light, Sep. Purif. Technol. 85 (2012) 35–44.

[31] R.C. Ropp, Solid state chemistry, Elsevier, 2003.

[32] D. Dollimore, The application of thermal analysis in studying the thermal decomposition of solids, Thermochim. Acta. 203 (1992) 7–23.

[33] T. Kujirai, T. Akahira, Effect of temperature on the deterioration of fibrous insulating materials, Sci. Pap. Inst. Phys. Chem. Res. 2 (1925) 223-252.

[34] L. Findoráková, R. Svoboda, Kinetic analysis of the thermal decomposition of Zn(II) 2-chlorobenzoate complex with caffeine, Thermochim. Acta. 543 (2012) 113–117.

[35] A. Perejón, P.E. Sánchez-Jiménez, J.M. Criado, L.A. Pérez-Maqueda, Kinetic Analysis of Complex Solid-State Reactions. A New Deconvolution Procedure, J. Phys. Chem. B. 115 (2011) 1780–1791.

[36] R. Svoboda, J. Málek, Applicability of Fraser–Suzuki function in kinetic analysis of complex crystallization processes, J. Therm. Anal. Calorim. 111 (2013) 1045–1056.

[37] J.A.F.F. Rocco, J.E.S. Lima, A.G. Frutuoso, K. Iha, M. Ionashiro, J.R. Matos, M.E. V Suárez-Iha, Thermal degradation of a composite solid propellant examined by DSC, J. Therm. Anal. Calorim. 75 (2004) 551–557.

[38] C. Deng, J. Cai, R. Liu, Kinetic analysis of solid-state reactions: Evaluation of approximations to temperature integral and their applications, Solid State Sci. 11 (2009) 1375–1379.

[39] A.W. Coats, J.P. Redfern, Kinetic Parameters from Thermogravimetric Data, Nature. 201 (1964) 68–69.

[40] T. Tang, M. Chaudhri, Analysis of isothermal kinetic data from solid-state reactions, J. Therm. Anal. Calorim. 17 (1979) 359–370.

[41] T.B. Tang, M.M. Chaudhri, Analysis of dynamic kinetic data from solid-state reactions, J. Therm. Anal. Calorim. 18 (2005) 247–261.

[42] J. Sestak, V. Satava, W.M. Wendlandt, The study of heterogeneous processes by thermal analysis, Chem. Informations. 5 (1974).

[43] K. Sarada, K. Muraleedharan, Effect of addition of silver on the thermal decomposition kinetics of copper oxalate, J. Therm. Anal. Calorim. 123 (2016) 643–651.

[44] J.H. Flynn, L.A. Wall, A quick, direct method for the determination of activation energy from thermogravimetric data, J. Polym. Sci. Part B Polym. Lett. 4 (1966) 323–328.

[45] T. Ozawa, A New Method of Analyzing Thermogravimetric Data, Bull. Chem. Soc. Jpn. 38 (1965) 1881–1886.

[46] H.E. Kissinger, Reaction Kinetics in Differential Thermal Analysis, Anal. Chem. 29 (1957) 1702–1706.

[47] T. Wanjun, C. Donghua, New approximate formula for the generalized temperature integral, J. Therm. Anal. Calorim. 98 (2009) 437-440.

[48] M.J. Starink, Activation energy determination for linear heating experiments: deviations due to neglecting the low temperature end of the temperature integral, J. Mater. Sci. 42 (2007) 483–489.

[49] M.J. Starink, The determination of activation energy from linear heating rate experiments: a comparison of the accuracy of isoconversion methods, Thermochim. Acta. 404 (2003) 163–176.

[50] S.K. Kansal, M. Singh, D. Sud, Studies on photodegradation of two commercial dyes in aqueous phase using different photocatalysts, J. Hazard. Mater. 141 (2007) 581–590.

[51] C.A.K. Gouvêa, F. Wypych, S.G. Moraes, N. Durán, N. Nagata, P. Peralta-Zamora, Semiconductor-assisted photocatalytic degradation of reactive dyes in aqueous solution, Chemosphere. 40 (2000) 433–440.

[52] M. Muruganandham, I.S. Chen, J.J. Wu, Effect of temperature on the formation of macroporous ZnO bundles and its application in photocatalysis, J. Hazard. Mater. 172 (2009) 700–706.

[53] S. Sakthivel, B. Neppolian, M. V Shankar, B. Arabindoo, M. Palanichamy, V. Murugesan, Solar photocatalytic degradation of azo dye: comparison of photocatalytic efficiency of ZnO and TiO_2, Sol. Energy Mater. Sol. Cells. 77 (2003) 65–82.

[54] A. Sirelkhatim, S. Mahmud, A. Seeni, N.H.M. Kaus, L.C. Ann, S.K.M. Bakhori, H. Hasan, D. Mohamad, Review on Zinc Oxide Nanoparticles: Antibacterial Activity and Toxicity Mechanism, Nano-Micro Lett. 7 (2015) 219–242.

[55] R. Kumar, O. Al-Dossary, G. Kumar, A. Umar, Zinc Oxide Nanostructures for NO_2 Gas–Sensor Applications: A Review, Nano-Micro Lett. 7 (2015) 97–120.

[56] A. Singh, N.B. Singh, S. Afzal, T. Singh, I. Hussain, Zinc oxide nanoparticles: a review of their biological synthesis, antimicrobial activity, uptake, translocation and biotransformation in plants, J. Mater. Sci. 53 (2018) 185–201.

[57] M. Hasanpoor, M. Aliofkhazraei, H. Delavari H., In-situ study of mass and current density for electrophoretic deposition of zinc oxide nanoparticles, Ceram. Int. 42 (2016) 6906–6913.

[58] D. Bresser, F. Mueller, M. Fiedler, S. Krueger, R. Kloepsch, D. Baither, M. Winter, E. Paillard, S. Passerini, Transition-Metal-Doped Zinc Oxide Nanoparticles as a New Lithium-Ion Anode Material, Chem. Mater. 25 (2013) 4977–4985.

[59] K. Rekha, M. Nirmala, M.G. Nair, A. Anukaliani, Structural, optical, photocatalytic and antibacterial activity of zinc oxide and manganese doped zinc oxide nanoparticles, Phys. B Condens. Matter. 405 (2010) 3180–3185.

[60] R. Yousefi, F. Jamali-Sheini, M. Cheraghizade, S. Khosravi-Gandomani, A. Sáaedi, N.M. Huang, W.J. Basirun, M. Azarang, Enhanced visible-light photocatalytic activity of strontium-doped zinc oxide nanoparticles, Mater. Sci. Semicond. Process. 32 (2015) 152–159.

[61] S. Suwanboon, P. Amornpitoksuk, A. Haidoux, J.C. Tedenac, Structural and optical properties of undoped and aluminium doped zinc oxide nanoparticles via precipitation method at low temperature, J. Alloys Compd. 462 (2008) 335–339.

[62] R. Elilarassi, G. Chandrasekaran, Synthesis and optical properties of Ni-doped zinc oxide nanoparticles for optoelectronic applications, Optoelectron. Lett. 6 (2010) 6–10.

[63] O. Bechambi, M. Chalbi, W. Najjar, S. Sayadi, Photocatalytic activity of ZnO doped with Ag on the degradation of endocrine disrupting under UV irradiation and the investigation of its antibacterial activity, App. Surf. Sci. 347 (2015) 414-420.

[64] J. Iqbal, X. Liu, H. Zhu, Z.B. Wu, Y. Zhang, D. Yu, R. Yu, Raman and highly ultraviolet red-shifted near band-edge properties of LaCe-co-doped ZnO nanoparticles, Acta Mater. 57 (2009) 4790–4796.

[65] C.J. Chang, C.Y. Lin, M.H. Hsu, Enhanced photocatalytic activity of Ce-doped ZnO nanorods under UV and visible light, J. Taiwan Inst. Chem. Eng. 45 (2014) 1954–1963.

[66] G.N. Dar, A. Umar, S.A. Zaidi, A.A. Ibrahim, M. Abaker, S. Baskoutas, M.S. Al-Assiri, Ce-doped ZnO nanorods for the detection of hazardous chemical, Sensors Actuators B Chem. 173 (2012) 72–78.

[67] P.M. Shirage, A.K. Rana, Y. Kumar, S. Sen, S.G. Leonardi, G. Neri, Sr- and Ni-doping in ZnO nanorods synthesized by a simple wet chemical method as excellent materials for CO and CO_2 gas sensing, RSC Adv. 6 (2016) 82733–82742.

[68] D. Li, J.-F. Huang, L.-Y. Cao, J.-Y. LI, H.-B. OuYang, C.-Y. Yao, Microwave hydrothermal synthesis of Sr^{2+} doped ZnO crystallites with enhanced photocatalytic properties, Ceram. Int. 40 (2014) 2647–2653.

[69] N.N. Kumaran, K. Muraleedharan, Photocatalytic activity of ZnO and Sr^{2+} doped ZnO nanoparticles, J. Water Process Eng. 17 (2017) 264–270.

[70] G. Srinet, R. Kumar, V. Sajal, High Tc ferroelectricity in Ba-doped ZnO nanoparticles, Mater. Lett. 126 (2014) 274–277.

[71] S.D. Bukkitgar, N.P. Shetti, R.M. Kulkarni, S.T. Nandibewoor, Electro-sensing base for mefenamic acid on a 5% barium-doped zinc oxide nanoparticle modified electrode and its analytical application, RSC Adv. 5 (2015) 104891–104899.

[72] S.K. Jesudoss, J.J. Vijaya, N.C.S. Selvam, K. Kombaiah, M. Sivachidambaram, T. Adinaveen, L.J. Kennedy, Effects of Ba doping on structural, morphological, optical, and photocatalytic properties of self-assembled ZnO nanospheres, Clean Technol. Environ. Policy. 18 (2016) 729–741.

[73] N. Reuge, R. Bacsa, P. Serp, B. Caussat, Chemical Vapor Synthesis of Zinc Oxide Nanoparticles: Experimental and Preliminary Modeling Studies, J. Phys. Chem. C. 113 (2009) 19845–19852.

[74] R.M. Alwan, Q.A. Kadhim, K.M. Sahan, R.A. Ali, R.J. Mahdi, N.A. Kassim, A.N. Jassim, Synthesis of Zinc Oxide Nanoparticles via Sol – Gel Route and Their Characterization, 5 (2015) 1–6.

[75] R.K. Sharma, R. Ghose, Synthesis of zinc oxide nanoparticles by homogeneous precipitation method and its application in antifungal activity against Candida albicans, Ceram. Int. 41 (2015) 967–975.

[76] A.K. Ganguli, S. Vaidya, T. Ahmad, Synthesis of nanocrystalline materials through reverse micelles: A versatile methodology for synthesis of complex metal oxides, Bull. Mater. Sci. 31 (2008) 415–419.

[77] S. Hingorani, V. Pillai, P. Kumar, M.S. Multani, D.O. Shah, Microemulsion mediated synthesis of zinc-oxide nanoparticles for varistor studies, Mater. Res. Bull. 28 (1993) 1303–1310.

[78] N. Audebrand, J.-P. Auffrédic, D. Louër, X-ray Diffraction Study of the Early Stages of the Growth of Nanoscale Zinc Oxide Crystallites Obtained from Thermal Decomposition of Four

Precursors. General Concepts on Precursor-Dependent Microstructural Properties, Chem. Mater. 10 (1998) 2450–2461.

[79] S. Musić, Đ. Dragčević, M. Maljković, S. Popović, Influence of chemical synthesis on the crystallization and properties of zinc oxide, Mater. Chem. Phys. 77 (2003) 521–530.

[80] Ü. Özgür, Y.I. Alivov, C. Liu, A. Teke, M.A. Reshchikov, S. Doğan, V. Avrutin, S.-J. Cho, H. Morkoç, A comprehensive review of ZnO materials and devices, J. Appl. Phys. 98 (2005) 41301. doi.10.1063/1.1992666.

[81] A.B. Djurišić, X. Chen, Y.H. Leung, A. Man Ching Ng, ZnO nanostructures: growth, properties and applications, J. Mater. Chem. 22 (2012) 6526–6535.

[82] Z.L. Wang, Nanostructures of zinc oxide, Mater. Today 7 (2004) 26-33,

[83] K. V krishnamurty, The chemistry of the metal oxalato complexes, Chem. Rev. 61 (1961) 213–246.

[84] D. Dollimore, D. Griffiths, Differential thermal analysis study of various oxalates in oxygen and nitrogen, J. Therm. Anal. Calorim. 2 (1970) 229–250.

[85] D. Dollimore, D. Nicholson, 179. The thermal decomposition of oxalates. Part I. The variation of surface area with the temperature of treatment in air, J. Chem. Soc. (1962) 960–965. doi.10.1039/JR9620000960.

[86] D. Dollimore, D.L. Griffiths, D. Nicholson, 488. The thermal decomposition of oxalates. Part II. Thermogravimetric analysis of various oxalates in air and in nitrogen, J. Chem. Soc. (1963) 2617–2623. https://doi.org/10.1039/JR9630002617.

[87] D. Dollimore, The thermal decomposition of oxalates. A review, Thermochim. Acta. 117 (1987) 331–363.

[88] A.M.M. Gadalla, Kinetics of the decomposition of hydrated oxalates of calcium and magnesium in air, Thermochim. Acta. 74 (1984) 255–272.

[89] K. Krishnan, K.N. Ninan, P.M. Madhusudanan, A comprehensive study of the influence of sample mass on the kinetic parameters in isothermal dehydration reactions, Thermochim. Acta. 90 (1985) 229–250.

[90] B. V L'vov, V.L. Boris, The physical approach to the interpretation of the kinetics and mechanisms of thermal decomposition of solids: the state of the art, Thermochim. Acta. 373 (2001) 97–124.

[91] M.V.V.S. Reddy, K. V Lingam, T.K.G. Rao, Radical studies in oxalate systems: E.S.R. of CO_2^- in irradiated potassium oxalate monohydrate, Mol. Phys. 42 (1981) 1267–1269.

[92] N.Z. Lyakhov, V. V Boldyrev, Kinetics and Mechanism of the Dehydration of Crystal Hydrates, Russ. Chem. Rev. 41 (1972) 919–928.

[93] N.S. Fatemi, D. Dollimore, G.R. Heal, Thermal decomposition of oxalates. Part 16. Thermal decomposition studies on cadmium oxalate, Thermochim. Acta. 54 (1982) 167–180.

[94] M. Rossberg, E.F. Khairetdinov, E. Linke, V. V Boldyrev, Effect of mechanical pretreatment on thermal decomposition of silver oxalate under nonisothermal conditions, J. Solid State Chem. 41 (1982) 266–271.

[95] V. V Boldyrev, Topochemical reactions: Particularities of their mechanism and outlook on their research, part II, J. Therm. Anal. Calorim. 8 (1975) 175–194.

[96] V. V Boldyrev, Topochemistry of the Thermal Decomposition of Solid Substances, Russ. Chem. Rev. 42 (1973) 515–528.

[97] P.E. Yankwich, P.D. Zavitsanos, Pyrolysis of zinc oxalate: kinetics and stoichiometry, J. Phys. Chem. 68 (1964) 457–463.

[98] T. Palanisamy, J. Gopalakrishnan, B. Viswanathan, V. Srinivasan, M.V.C. Sastri, Kinetics of thermal decomposition of some metal oxalates, Thermochim. Acta. 2 (1971) 265–273.

[99] R. Majumdar, P. Sarkar, U. Ray, M. Roy Mukhopadhyay, Secondary catalytic reactions during thermal decomposition of oxalates of zinc, nickel and iron(II), Thermochim. Acta. 335 (1999) 43–53.

[100] D. Dollimore, D.L. Griffiths, differential thermal analysis study of various oxalates in oxygen and nitrogen, J. Therm. Anal. 2 (1970) 229–250.

[101] B. Małecka, E. Drożdż-Cieśla, A. Małecki, Mechanism and kinetics of thermal decomposition of zinc oxalate, Thermochim. Acta. 423 (2004) 13–18.

[102] M.A. Mohamed, A.K. Galwey, S.A. Halawy, A comparative study of the thermal reactivities of some transition metal oxalates in selected atmospheres, Thermochim. Acta. 429 (2005) 57–72.

[103] J.D. Danforth, J. Dix, Chemistry and kinetics of the thermal decomposition of zinc and magnesium oxalates, J. Am. Chem. Soc. 93 (1971) 6843–6846.

[104] N.D. Cooper, Complete kinetic and mechanistic decomposition of zinc oxalate with characterization of intermediates and final oxide, Proceedings of the National Conference of Undergraduate Research 2015.

[105] V. V Boldyrev, Thermal decomposition of silver oxalate, Thermochim. Acta. 388 (2002) 63–90.

[106] P. Aggarwal, D. Dollimore, The use of Zinc Oxalate Dihydrate in Establishing The Working Reproducibility of A Simultaneous Tg–Dta Unit, Instrum. Sci. Technol. 24 (1996) 95–102.

[107] C. Hu, J. Mi, S. Shang, J. Shangguan, The study of thermal decomposition kinetics of zinc oxide formation from zinc oxalate dihydrate, J. Therm. Anal. Calorim. 115 (2014) 1119–1125.

[108] A. Koleżyński, A. Małecki, First principles studies of thermal decomposition of anhydrous zinc oxalate, J. Therm. Anal. Calorim. 96 (2009) 645–651.

[109] P.A.N.Y. Xiang, G.X. Ying, F.Z. Yuan, L.I.X. Yu, W.U.Y. Son, A new method determining mechanism function of solid state reaction-the non isothermal kinetic of dehydration of nickel (II) oxalate dihydrate in solid state, Chinese J. Inorg. Chem. 2 (1999).

[110] T. Ahmad, A. Ganguly, J. Ahmed, A.K. Ganguli, O.A.A. Alhartomy, Nanorods of transition metal oxalates: A versatile route to the oxide nanoparticles, Arab. J. Chem. 4 (2011) 125–134.

[111] Z. Wei, N.Y. Yu, H.L. Li, Q.C. Dong, Hua, A Description of Thermal Decomposition Kinetics of Dehydration of Zinc Oxalate Dihydrate, Acta Physico-Chimica Sin. 20 (2004) 33-37.

[112] A. Koleżyński, A. Małecki, Theoretical approach to thermal decomposition process of chosen anhydrous oxalates, J. Therm. Anal. Calorim. 97 (2009) 77–83.

EXPLORATION OF THE THERMAL DECOMPOSITION OF ZINC OXALATE BY EXPERIMENTAL AND COMPUTATIONAL METHODS

2.1. Introduction

Thermal decomposition of metal oxalates has been investigated by many researchers for more than a century [1-12]. Metal oxalates act as good precursors for the synthesis of metal oxide nanoparticles since their thermal decomposition affords homogenous oxide nanoparticles with low cost and can be easily transformed to metal oxides at low temperatures. The resultant metal oxide nanoparticles are receiving growing attention because of their important optical, mechanical, electrical, magnetic, and catalytic behavior [13]. The possibility of obtaining nano-crystalline transition metal oxides by the thermal decomposition of the parent oxalates and the kinetics of their thermal decomposition are not investigated in depth.

ZnO is an n-type semiconductor of band gap 3.37 eV and exciton binding energy of 60 M eV [14]. Owing to its high quantum efficiency several researchers confirmed that it is a better photocatalyst for the degradation of organic pollutants over TiO_2 [15–17]. Few scientific reports are concerned with the thermal decomposition of ZnC_2O_4 [18–24]. There is significant discrepancies between kinetic data of decomposition of ZnC_2O_4, confusion still remains in the mechanism of decomposition and kinetics for each possible step in the mechanism. This study focused on the elucidation of the kinetics and mechanism of

thermal dehydration of $ZnC_2O_4.2H_2O$ and the thermal decomposition of ZnC_2O_4 by non- isothermal DSC technique in flowing N_2 atmosphere.

The absence of a steady portrayal and clarification of the origin and thermal decomposition way of oxalates from the experimental outcomes made us to think for the theoretical clarification of the same. The experimental discoveries can be rationalized through density functional theory (DFT) based on computational investigation [25]. It appears to be sensible to expect that the theoretical investigation of the fundamental features of electron density (topological analysis) and chemical bond (bond order, bond length, *etc.*) should in principle lead to the forecast of the decomposition pathways for metal oxalates [26]. Kolezyn'ıski *et al.* [27–32] recently did the theoretical examination of electronic structure and bonding properties of many transition metal oxalates (including zinc oxalate) which is extremely encouraging and not just gave us extra understanding into the thermal decomposition process in those oxalates yet, besides, depicted it as a progression of consecutive bond-breaking steps proceeding in the theoretically anticipated order. Their whole investigation depends on the topological examination of electron density (Bader's Quantum Theory of Atoms in Molecules formalism) [26] got from first principles FP-LAPW calculations and structural and bonding properties-bond valence, bond strength, and stresses related with a deviation of given structure from perfect one (Brown's Bond Valence Method).

The target of the present work is to examine the dehydration of zinc oxalate dihydrate and the thermal decomposition behavior of

anhydrous zinc oxalate by experimental techniques by non- isothermal DSC technique in flowing N_2 atmosphere and by a theoretical examination of the electronic structure and bonding properties in view of the DFT strategy utilizing Gaussian09W simulation package.

2.2. Experimental

2.2.1. Materials

The reagents used in this study are of analytical grade and employed without any further purification. The chemicals used in the study are $ZnCl_2.4H_2O$ (Himedia, India), $H_2C_2O_4$ (Merck, India), and KBr (Sigma).

2.2.2. Preparation of zinc oxalate dihydrate

An equimolar ratio of $ZnCl_2.4H_2O$, $H_2C_2O_4$ were separately mixed in distilled water to form a homogenous solution. These were mixed thoroughly under vigorous stirring condition up to the formation of a white precipitate of $ZnC_2O_4.2H_2O$

$$ZnCl_2.4H_2O + H_2C_2O_4 \longrightarrow ZnC_2O_4.2H_2O + 2HCl + 2H_2O$$

The precipitate washed several times with distilled water and dried in an air oven, kept at a constant temperature (70 ^{0}C) for 8 hrs. The sample prepared was sieved through the mesh and fixed the particle size in the range of 95–105 µm. The prepared zinc oxalate dihydrate samples then calcined at 473, 683, and 773 K by placing it in a muffle furnace in air. The product of the thermal decomposition of zinc oxalate is zinc

oxide. Similarly, when zinc oxalate is calcined, the product is found to be zinc oxide and not zinc metal. If the product of decomposition/calcination is zinc metal, then there is a possibility of zinc oxide formation when it is placed in the air atmosphere by the reaction with oxygen present in the air. In this case, such a possibility will not arise.

2.2.3. Preparation of pelletized samples

The samples were well-grounded and the powdered samples were pressed using the hydraulic pellet press (KP, SR. No. 1718) under a pressure of 50 kg cm^{-2}. Zinc oxalate dihydrate and thermally heated samples (473, 683, and 773 K) were also pelletized using hydraulic press under the same pressure.

2.2.4. Characterization of the sample

Fourier transform infrared (FT-IR) spectra of the samples was recorded by the transmittance method using a spectrometer (Model: Jasco FT-IR-4100) after diluting the samples with KBr powder. The optical band gap (E_g) of the decomposed product was calculated from UV–Visible reflectance which was measured using UV–Visible diffuse reflectance spectrum (Model: Jasco V-550 spectrophotometer). The powder X-ray diffraction (XRD) patterns of the samples were recorded using a diffractometer (Miniflex 600, Model: RigakuD/Max) with Cu-Kα (λ=1.5418 Å) radiation (40 kV, 15 mA) with a scan rate of 2θ min^{-1} in the region of 20–90^o. The Scanning Electron Microscopic (SEM) analyses of all the samples studied were performed with SEM-EDAX

combination using Carl-Zeiss Gemini SEM 300. The transmission electron microscopic (TEM) analysis of the particles was achieved by using a JEOL Model JEM 2100 field emission transmission electron microscope operated at 200 kV with a 0.18 nm resolution.

2.2.5. Measurement of thermal behavior

TG measurements were made on a Perkin Elmer Pyris Thermal Analyser STA8000 at two heating rates 6 and 8 K min^{-1}. The operational characteristics of the thermal analysis system are as follows: atmosphere: flowing N_2, at a flow rate of 20 mL min^{-1}, sample mass: ~5 mg; and sample pan: aluminium. Duplicate runs were made under similar conditions and found that the data overlap with each other, indicating satisfactory reproducibility. The differential scanning calorimetric (DSC) measurements of the samples were done in the temperature range 303–773 K at four different heating rates, *viz*. 4, 6, 8, and 10 K min^{-1} on a Mettler Toledo DSC822e. The operational characteristics of the DSC system are as follows: atmosphere: flowing N_2 at a flow rate of 50 mL min^{-1}; sample mass~ 5 mg; and sample pan: aluminium.

2.2.6. Computational methodology

The theoretical analysis of the molecule has been done based on the DFT method. The structure is optimized using DFT with 6-31+g (d, p) as a basis set. The level of theory adopted was B3LYP, which consists of Becke's exchange functional [33] in conjunction with the Lee-Yang-Parr correlation functional [34]. All the computational works were

carried out through Gaussian 09 software package. Global reactive descriptors like ionization potential, electron affinity, electronegativity, electrophilicity, softness, hardness, etc., are calculated in order to analyze the extent of reactivity of the molecule.

2.2.6.1. Global reactive descriptors

Global reactive descriptors can be calculated by energy vertical and orbital vertical methods. In the latter, Global reactive descriptors can be written as follows which make use of approximation suggested by Koopman's theorem.

Ionisation Potential $(IP) \approx -E_{HOMO}$ (1)

Electron Affinity $(EA) \approx -E_{LUMO}$ (2)

where E_{HOMO} is the energy of HOMO and E_{LUMO} is the energy of LUMO

Hardness $(\eta) \approx (IP - EA)/2$ (3)

Electronegativity $(\chi) \approx (IP + EA)/2$ (4)

Softness $(S) \approx 1/2\eta$ (5)

Chemical potential $(\mu) \approx -\chi$ (6)

Electrophilicity index $(\omega) \approx \mu^2/2\eta$ (7)

2.3. Results and discussion

2.3.1. Sample characterization

Fig. 1 represents the FT-IR spectra of $ZnC_2O_4.2H_2O$, ZnC_2O_4 calcined at 473, ZnO calcined at 683 and 773 K. The strong broad band centered at about 3,396 cm^{-1} is assigned to stretching modes of hydrated water, υ(O–H); this band arises due to the presence of water present in the sample. The strong band at 1,621 cm^{-1} is characteristic of C=O antisymmetric stretching modes υ_{as}(C=O). The small peaks at 1356 and 1318 cm^{-1} is due to the O–C–O stretching modes; the small bands at 827 and 461 cm^{-1} are due to the O-C=O bending modes υ(O–C=O) and Zn-O stretching modes υ (Zn–O).

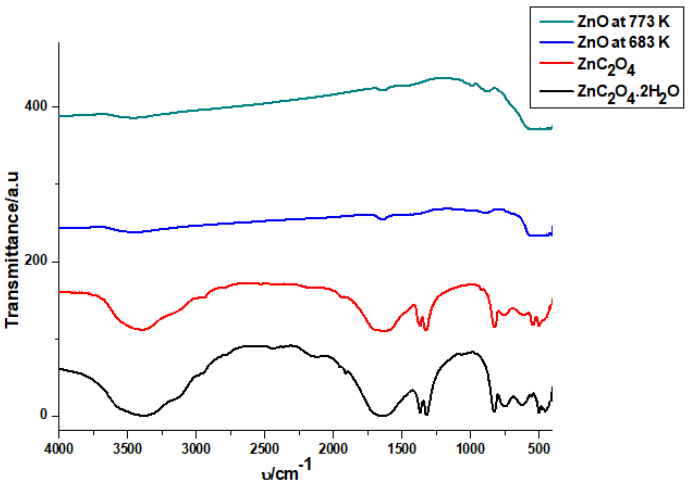

Fig. 1 FT-IR spectra of $ZnC_2O_4.2H_2O$, ZnC_2O_4 calcined at 473, ZnO calcined at 683 and 773 K

FT-IR spectra of ZnO calcined at 683 and 773 K shows only the stretching mode of Zn-O at 461 cm^{-1} indicating that ZnO is the final

product [24]. The FTIR spectra obtained for $ZnC_2O_4.2H_2O$ and ZnO were also compared with the FTIR spectra reported by Chengcheng Hu *et al.* [24] and found that the bands obtained was perfectly matched with the reported values. Chengcheng Hu *et al.* [24] were got the bands at 3394, 1634, a double band at 1364 and 1319, a small band at 822 and one at 496 cm^{-1} and they ascribed these bands to stretching modes of hydrated water, C=O antisymmetric stretching modes, O–C–O stretching modes, O-C=O bending modes and Zn-O stretching modes respectively.

Powder XRD patterns of the sample and thermally heated samples at 473, 683, and 773 K are shown in **Fig. 2** The average crystallite size was calculated using the Debye–Scherrer equation [35].

$$D = K\lambda / \beta Cos\theta \tag{8}$$

where β is the full width at half maximum intensity of the peak (in Rad), K is the crystallite shape factor, a good approximation is 0.9, λ is the wavelength of the incident X-ray (λ = 0.1540 nm for Cu-Kα), D is the crystallite size, and θ is the Bragg angle in degree. The XRD patterns obtained for the sample calcined at 683 and 773 K shows the peaks corresponding to ZnO only. The XRD peaks obtained are well-matched with the previously reported one which was synthesized through oxalate precipitation route [24]. XRD peaks can be indexed on zinc oxide of hexagonal wurtzite phase (JCPDS card no.36–1451, a, b = 3.256 nm, c = 5.22 nm).

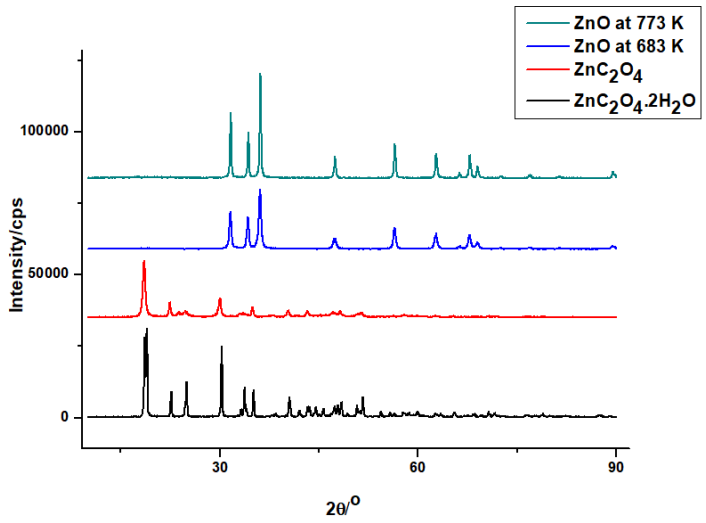

Fig. 2 Powder XRD patterns of $ZnC_2O_4.2H_2O$, ZnC_2O_4 calcined at 473, 683 and 773 K

The peaks at 2θ values 31.59, 34.18, 36.12, 47.41, 56.43, 62.56, 66.43, 67.89 and 68.86^0 represents (100), (022), (101), (102), (110), (103), 200), (112) and (201) planes of wurtzite ZnO. As the calcination temperature increases from 683 to 773 K, ZnO does not decompose but the crystallinity of ZnO increases. This is evident from the XRD patterns of ZnO calcined at 683 and 773 K. The obtained average crystallite size using Debye–Scherrer equation was 22.36 and 44.00 nm for the synthesized ZnO nanoparticles at 683 and 773 K respectively.

TEM images of the ZnO calcined at 773 K are shown in **Figs. 3(a)** and **(b)** and its SAED pattern in **(c)**. **Fig. 3(d)** represents the lattice fringes of the synthesized nanoparticles. TEM images indicate that ZnO nanospheres are formed and their size distribution is not homogeneous. The smallest particle has an average size of 36 nm. TEM images and SAED patterns revealed the high crystallinity of the sample. HR-TEM

images reveal that a chain-like structure is formed by the spherical ZnO nanoparticles. The clear lattice fringes also demonstrated that the nanoparticles are highly crystalline and obtained a lattice spacing of 0.22 nm.

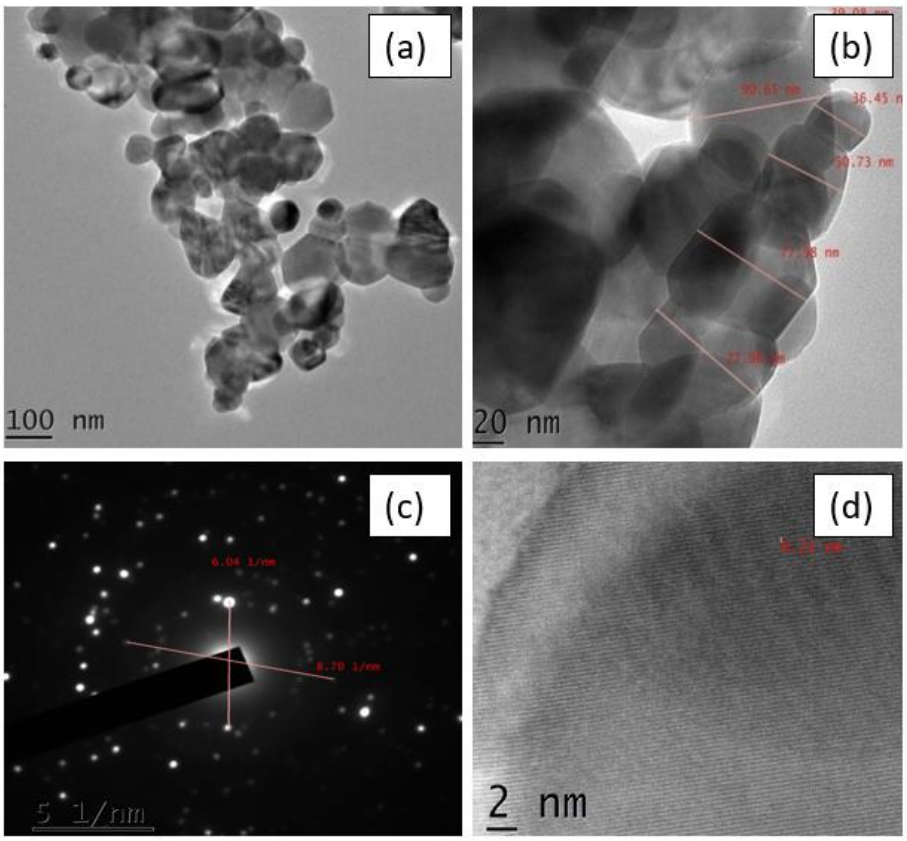

Fig. 3 TEM images of ZnO nanospheres calcined at 773 K (a) and (b), SAED pattern (c) and lattice fringes of the synthesized nanoparticles (d)

Figs. 4(a)-(d) show the SEM images of the sample and thermally heated sample at 473, 683, and 773 K. The morphology of the precursor, $ZnC_2O_4.2H_2O$ is timber like. SEM images of the formed ZnO nanoparticles at 683 K shows small rod-like morphology, further

heating the sample alters the morphology of ZnO nanoparticles and forms spherical ZnO nanoparticles at 773 K. The SEM images obtained for $ZnC_2O_4.2H_2O$ and ZnO calcined at 773 K were compared with the previously reported ones [36,37], it is found that the particle size ranges of ZnO nanoparticles and their morphology were well agreed with the literature. The SEM image of ZnO nanoparticles formed by calcining $ZnC_2O_4.2H_2O$ at 773 K shows that at some locations the spherical nanoparticles formed make chain-like structures that accord well with TEM images.

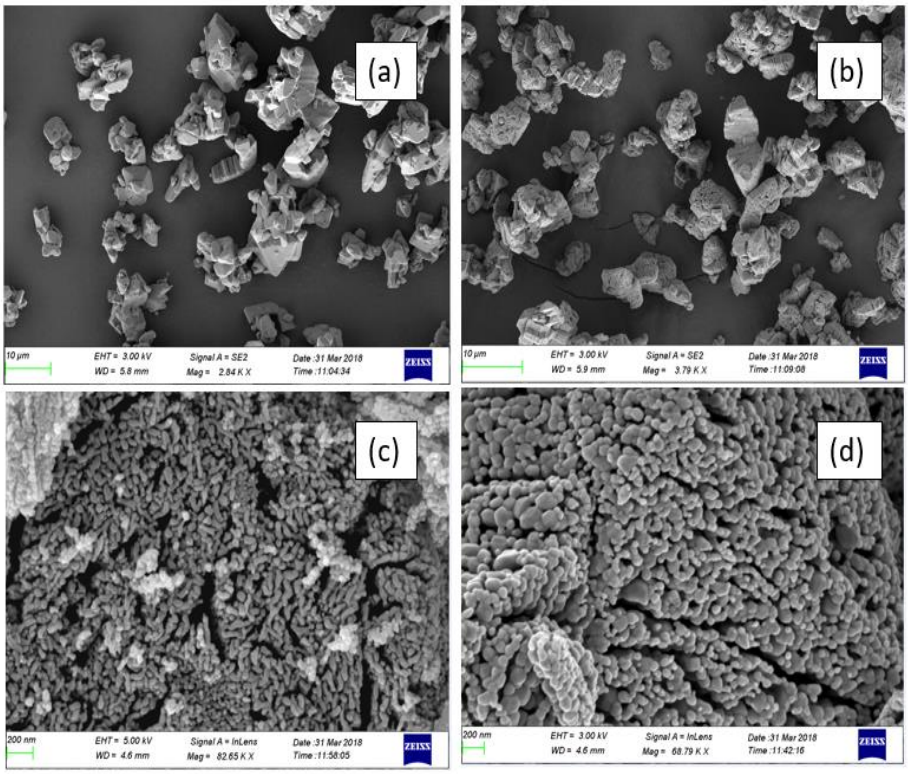

Fig. 4 SEM images of $ZnC_2O_4.2H_2O$ (a), ZnC_2O_4 calcined at 473 (b), 683 (c) and 773 K (d)

A combination of SEM-EDS (Energy-dispersive X-ray spectroscopy EDS, EDAX, EDXS, or XEDS) is used for the elemental analysis of the sample and thermally heated samples at 473, 683 and 773 K. Weight percentages of different elements are given in **Table 1**. The result is consistent with their molecular formula. $ZnC_2O_4.2H_2O$ and ZnC_2O_4 show weight percentages corresponding to Zn, C, and O but the percentage weight of oxygen is lower in ZnC_2O_4 compared to $ZnC_2O_4.2H_2O$ because of the absence of two water molecules in ZnC_2O_4.

Table 1 Weight percentages of different elements from SEM-EDS

Sample	Elements	Weight%	Atomic%
$ZnC_2O_4.2H_2O$	C	14.89	28.90
	O	37.01	53.94
	Zn	48.10	17.16
ZnC_2O_4	C	16.60	32.93
	O	32.61	48.56
	Zn	50.79	18.51
ZnO at 683 K	O	14.57	41.07
	Zn	85.43	58.93
ZnO at 773 K	O	15.99	43.74
	Zn	84.01	56.26

The optical band gap (E_g) of the decomposed product was calculated from UV–Vis reflectance which was measured using the UV–

Vis diffuse reflectance spectrum. The optical band gap is determined by using the Tauc equation

$$(\alpha h\upsilon)^n = B(h\upsilon - Eg) \quad (9)$$

where $h\upsilon$ is the photon energy, α is the absorption coefficient, B is a constant relative to the material and n is either 2 for direct transition or 1/2 for an indirect transition. The $(\alpha h\upsilon)^2$ versus $h\upsilon$ curve (Tauc-plot) of ZnO calcined at 773 K is shown in **Fig. 5** and the band gap obtained was 3.12 eV. The obtained band gap value was compared with the band gap value reported by Nelsa Abraham *et.al* who synthesized ZnO through oxalate precipitation route, and found that the values are well agreed with each other [38].

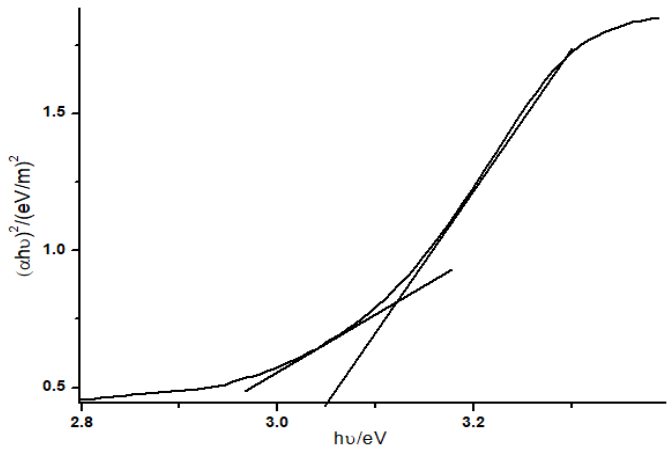

Fig. 5 Tauc plot of ZnO calcined at 773 K

2.3.2. Characterization of thermal decomposition behavior

Fig. 6 shows the result of the thermogravimetric analysis of $ZnC_2O_4.2H_2O$ at two heating rates 6 and 8 K min^{-1}. The figure shows

two different mass loss stages corresponding to dehydration and decomposition. There is a small increase in the temperature of dehydration and decomposition with an increase in heating rate. The first mass loss of 18.60% in the temperature range, 402.36-449.00 K, is consistent with the elimination of 1.96 mol of water molecules. The second mass loss of 37.52% (theoretical mass loss 38.03%) in the temperature range, 626.92-694.92 K indicates the decomposition of ZnC_2O_4. The total mass loss is 56.12%, which is in good agreement with the calculated value of 57.10% (calculated assuming that $ZnC_2O_4.2H_2O$ is completely transformed into ZnO) [24].

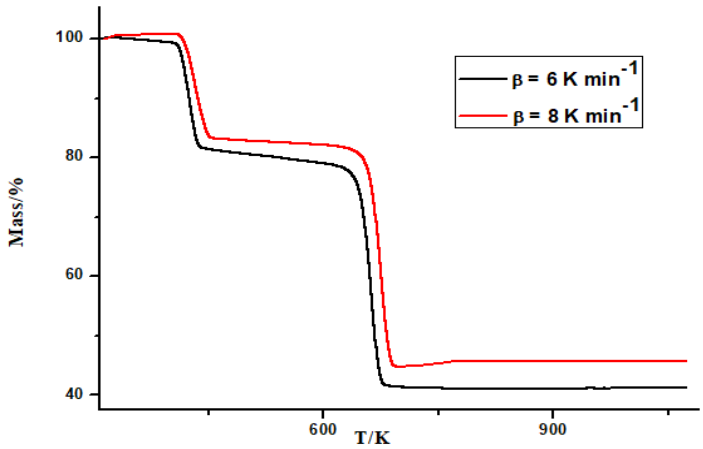

Fig. 6 TG curve of $ZnC_2O_4.2H_2O$ at the heating rates 6 and 8 K min^{-1}

The obtained TG was juxtaposed with the TG reported by Barbara M. *et al.* [23] and Chengcheng Hu *et al.* [24] and it was found that the results agreed with these ones. Barbara M. *et al*. [23] reported that the elimination of 1.88 mol of water molecule in the dehydration stage and decomposition stage starts above 600 K. Chengcheng Hu *et al*. [24]

found that dehydration stage occurred in the temperature range 363-444 K with the removal of 2 mol of water and the decomposition stage took place in the temperature range 573-673 K with a mass loss of 37.2%.

Fig. 7 shows the DSC curves of $ZnC_2O_4.2H_2O$ at different heating rates 4, 6, 8, and 10 K min^{-1}. DSC curves show two endothermic peaks corresponding to dehydration (in the temperature range 423.7-441.9 K) of two molecules of water from $ZnC_2O_4.2H_2O$ and the decomposition (in the temperature range 656.6-676.7 K) of ZnC_2O_4. The two stages were well separated from each other and there is a slight shift in the temperatures of the dehydration and decomposition reaction with an increase in heating rates as observed in TG. The peaks for dehydration and decomposition reactions have become sharper with an increase in heating rate which indicated that reactions are kinetically controlled.

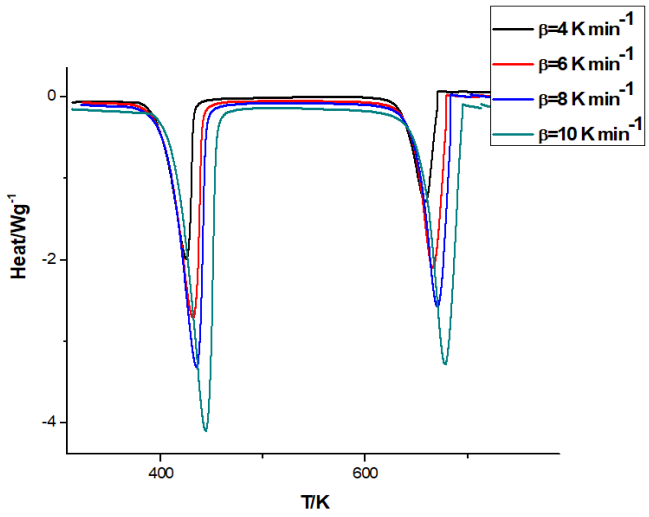

Fig. 7 DSC curves of $ZnC_2O_4.2H_2O$ at different heating rates 4, 6, 8 and 10 K min^{-1}

2.3.3. Kinetic behaviour

The kinetic parameters of solid-state decomposition reaction proceeding in non-isothermal conditions can be studied using the differential form of the kinetic equation;

$$d\alpha / dt = k(T) f(\alpha) \tag{10}$$

where $f(\alpha)$ is a function of α depending on reaction model and

$$k(T) = Ae^{-E_a/RT} \tag{11}$$

where E_a is the activation energy and A is the pre-exponential factor. Arrhenius parameters can be determined only if k (T) and f (α) are separated. Out of model fitting which is based on the single heating curve and model-free method of kinetic analysis, model-free isoconversional methods at multiple heating curves are the most dependable for calculating activation energy of thermal decomposition reaction in non-isothermal conditions [39,40]. Isoconversional methods assume that the reaction rate at a fixed α depends only on temperature and the reaction model is independent on heating rates. The reaction rate alters with the heating rate. The reaction rate is fast at a higher heating rate. The variation in the rate of reaction at different heating rates can be used to determine the activation energy of the reaction. Activation energy is constant throughout the conversion for a single-stage reaction while it varies for complex reactions. The mechanism of the reaction can be explained by studying the variation of activation energy with α. M.J. Starink compared the accuracy of different isoconversional methods in

the determination of activation energy from linear heating rate experiments [41].

Combining equation (11) and (10)

$$d\alpha / dt = Ae^{-E_a/RT} f(\alpha) \tag{12}$$

At non-isothermal conditions, the temperature is increasing with time at the constant heating rate. Integration of Eq. (12) involves solving the temperature integral, I (E, T)

$$g\ (\alpha) = A/\beta \int_0^{Tx} e^{-E_a/RT} dt = A/\beta I\left(E,T\right) \tag{13}$$

this equation has an ineffectual analytical solution. Some approximations or numerical integration is used to solve the equation. All of the approximations lead to a direct isoconversional method in the form:

$$ln\ \left(\beta / T^K\right)\ =\ C - E_a / RT \tag{14}$$

for a selected degree of conversion function, α, a corresponding $T_{\alpha i}$ and heating rate β are used to plot ln (β/T^K) against $1/T_{\alpha i}$, where K is a constant. The activation energy is then determined from the regression slope [42].

2.3.3.1. Isoconversional methods for the calculation of E_a

1. Flynn–Wall–Ozawa (FWO) method [43,44]

$$ln\beta = ln\left(AE / g(\alpha)R\right) - 5.331 - 1.052E_\alpha / RT_{\alpha i} \quad (15)$$

where α is the conversion function. From the slope of the graph lnβ against $1/T_{\alpha i,}$ E_a can be calculated.

2. Kissinger–Akahira–Sunose (KAS) method [45]

KAS is also an integer isoconversional method similar to FWO.

$$ln\beta / T^2 = ln\left(AR / E_a g(\alpha)\right) - E_a / RT \quad (16)$$

E_a can be obtained from the slope of the straight-line graph lnβ /T^2 against 1/T.

3. Tang method [46]

$$ln\left(\beta / T^{1.894661}\right) = ln\left(AE_a / Rg(\alpha)\right) + 3.635041 - 1.894661 ln\, E_a - 1.00145033E_a / RT \quad (17)$$

E_a can be obtained from the slope of the straight-line graph ln (β/$T^{1.894661}$) against 1/T.

4. Starink method [41]

$$ln\beta / T^{1.95} = C^{1.95}(\alpha) - E_a / RT \quad (18)$$

$$ln\beta / T^{1.92} = C^{1.92}(\alpha) - 1.0008E_a / RT \quad (19)$$

5. Boswell method

$$ln\beta / T = C(\alpha) - E_a / RT_{\alpha i} \quad (20)$$

Thermal decomposition of $ZnC_2O_4.2H_2O$ proceeds through dehydration of two molecules of water. DFT WIEN2k FP LAPW *ab initio* package calculations for zinc oxalate by Kolezynski and Malecki suggest that the thermal decomposition of ZnC_2O_4 starts with the breakage of Zn-O bond, forming a partially anchored oxalate ion. The C-C bond then breaks to produce CO_2 and the CO_2^{2-} then decompose to ZnO and CO. This is evident from their topological analysis that in all cases, the C_1–O_1 bond is strongest, then much weaker are C_1 –O_2^i and C_1–C_2 bonds (the latter one is little stronger) and the weakest are Zn–O bonds [27].

The conversion function, α in the range 0.05-0.95 with an interval of 0.05, and their corresponding temperatures are calculated from the experimental heat change data procured from DSC for the dehydration and decomposition reactions. This α-T data were subjected to linear least squares analysis using various model-free isoconversional methods like FWO, KAS, Tang, Starink$^{1.95}$, Starink$^{1.92}$, and Boswell method. The α-T plots for dehydration and decomposition reactions at different heating rates 4, 6, 8, and 10 K min^{-1} are shown in **Fig. 8**. The activation energy values were evaluated from the slope of the linear least squares plots. The linear least squares plot for the two reaction stages, dehydration, and thermal decomposition for the isoconversional methods used for the calculation of activation energy is shown in the

Figs. 9 and **10**. Activation energy obtained for the conversion function α = 0.05-0.95 for dehydration and decomposition reactions using different isoconversional methods are given in **Tables 2** and **3**. **Figs. 11** and **12** show the E_a vs α curves for dehydration and decomposition reactions for different isoconversional methods. The fluctuations in E_a with α for dehydration and decomposition reactions showed that they follow complex reaction pathways. All E_a vs α curves for each reaction show similar trends of variation of activation energy with α. The dependence of E_a on conversion function reveals that the value of E_a is independent on α above 40%, however below 40%, the value dependent on α. This implies that nucleation and growth in solid requires high E_a, once the decay commences, *i.e.*, after the completion of nucleation and its growth, decomposition reaction continues with an almost constant value of E_a till the end of the process [47].

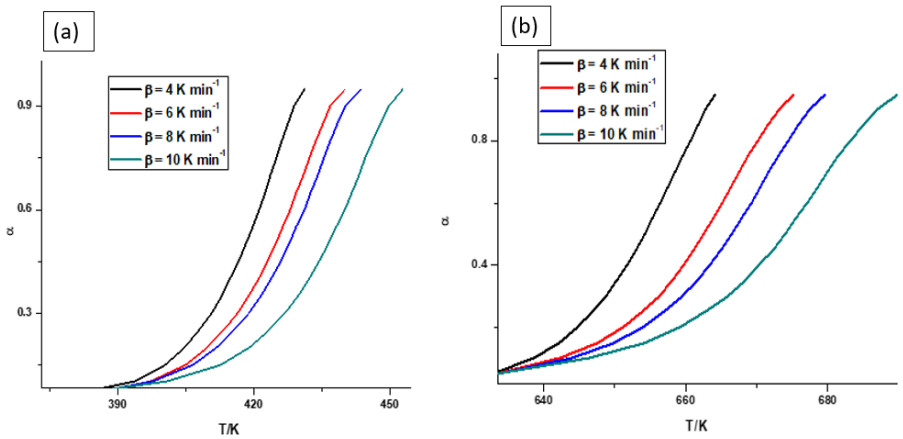

Fig. 8 α-T plots for dehydration of $ZnC_2O_4.2H_2O$ (a) and decomposition of ZnC_2O_4 (b) at different heating rates 4, 6, 8 and 10 K min^{-1}

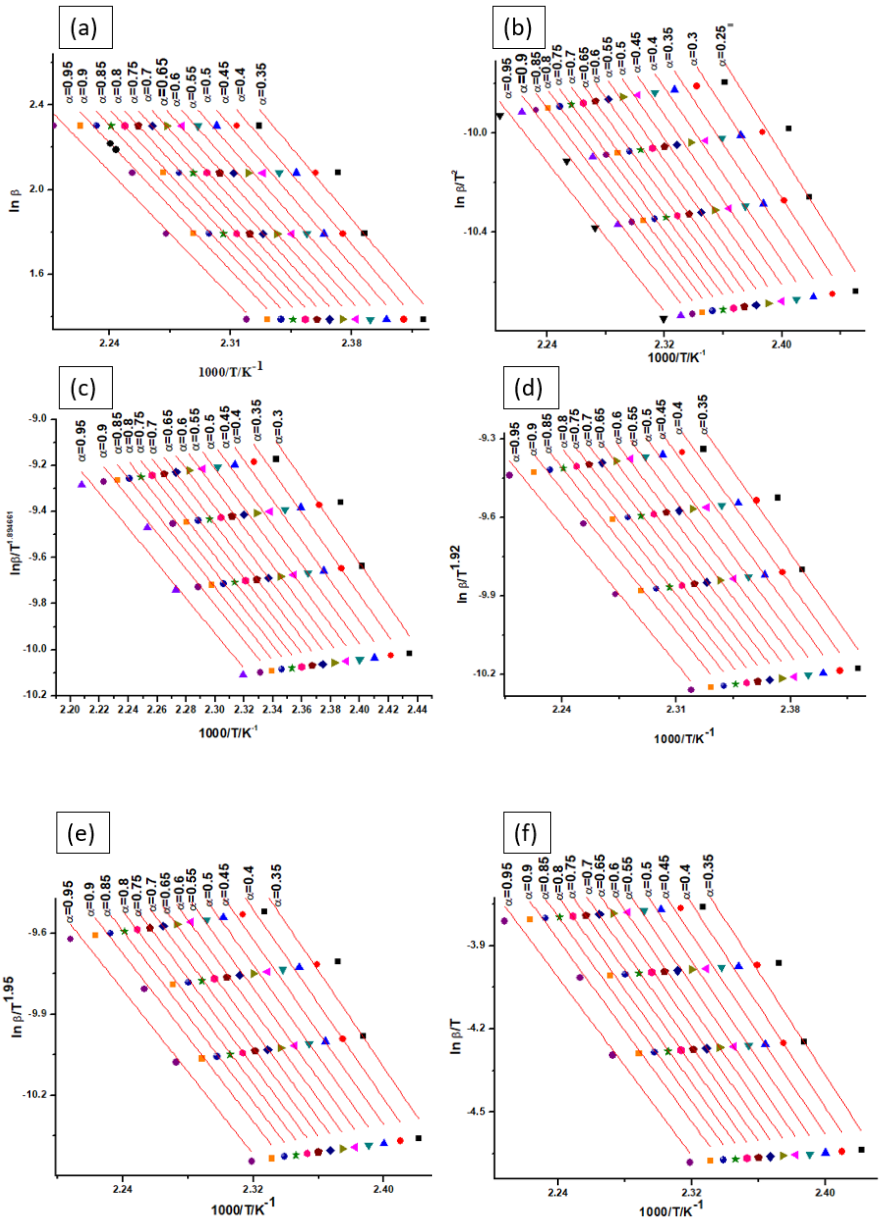

Fig. 9 linear least squares plots for the dehydration reaction for the isoconversional methods of FWO (a), KAS (b), Tang (c), Starink$^{1.92}$ (d), Starink$^{1.95}$ (e) and Boswell (f)

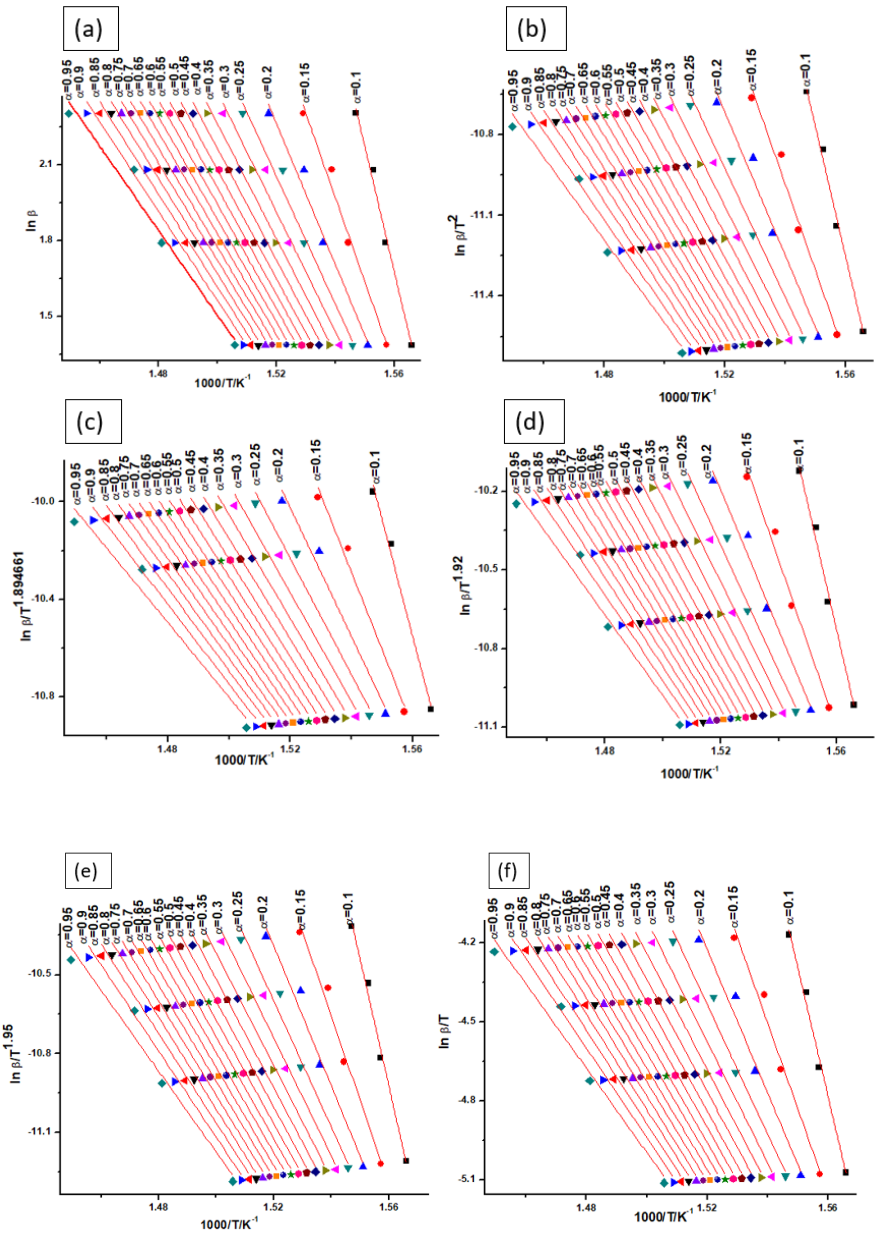

Fig. 10 linear least squares plots for the decomposition reaction for the isoconversional methods of FWO (a), KAS (b), Tang (c), Starink$^{1.92}$ (d), Starink$^{1.95}$ (e) and Boswell (f)

Table 2 Values of E_a in kJ mol^{-1} for the dehydration reaction

α	E_a in kJ mol^{-1}					
	FWO	KAS	Tang	Starink$^{1.92}$	Starink$^{1.95}$	Boswell
0.10	165.40	167.39	167.49	167.52	167.56	170.69
0.15	98.62	96.99	97.20	97.18	97.16	100.37
0.20	86.44	84.08	84.32	84.29	84.25	87.51
0.25	81.37	78.69	78.94	78.90	78.86	82.15
0.30	78.70	75.82	76.08	76.04	76.00	79.31
0.35	76.80	73.79	74.05	74.01	73.97	77.29
0.40	75.54	72.43	72.69	72.65	72.60	75.95
0.45	74.29	71.07	71.34	71.30	71.25	74.61
0.50	73.46	70.17	70.44	70.40	70.35	73.72
0.55	72.82	69.48	69.75	69.71	69.66	73.04
0.60	72.16	68.75	69.03	68.98	68.93	72.33
0.65	71.54	68.08	68.36	68.31	68.26	71.67
0.70	70.96	67.44	67.72	67.68	67.62	71.05
0.75	70.47	66.91	67.19	67.14	67.09	70.52
0.80	69.83	66.21	66.50	66.45	66.39	69.84
0.85	69.09	65.41	65.69	65.64	65.59	69.04
0.90	68.13	64.37	64.66	64.61	64.55	68.02
0.95	66.68	62.80	63.09	63.04	62.98	66.47

Table 3 Values of E_a in kJ mol^{-1} for the decomposition reaction

α	E_a in kJ mol^{-1}					
	FWO	KAS	Tang	Starink$^{1.92}$	Starink$^{1.95}$	Boswell
0.10	390.95	400.59	397.89	400.70	400.86	405.93
0.15	262.61	265.49	263.97	265.71	265.76	270.88
0.20	220.44	221.07	219.93	221.32	221.34	226.48
0.25	199.69	199.19	198.29	199.47	199.46	204.64
0.30	187.17	185.98	185.23	186.27	186.25	191.44
0.35	179.28	177.64	177.01	177.94	177.92	183.12
0.40	173.64	171.68	171.12	171.98	171.96	177.18
0.45	169.62	167.43	166.94	167.74	167.70	172.94
0.50	166.10	163.69	163.27	164.01	163.97	169.21
0.55	163.03	160.45	160.06	160.76	160.73	165.98
0.60	160.24	157.49	157.13	157.81	157.77	163.03
0.65	157.74	154.84	154.46	155.16	155.12	160.39
0.70	154.89	151.82	151.43	152.14	152.10	157.38
0.75	152.01	148.77	148.41	149.09	149.05	154.34
0.80	148.67	145.24	144.84	145.57	145.52	150.82
0.85	144.80	141.14	140.72	141.47	141.42	146.74
0.90	139.78	135.83	135.40	136.17	136.12	141.44
0.95	132.00	127.61	127.18	127.96	127.89	133.24

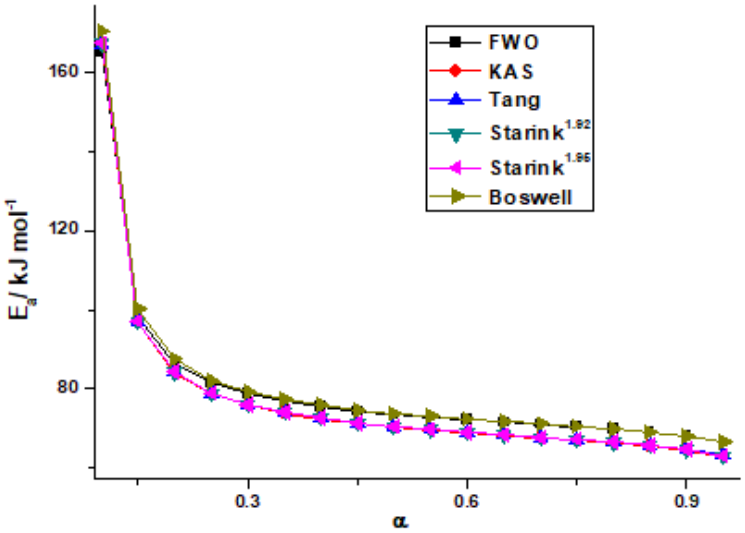

Fig. 11 *E_a vs α* curves for dehydration reaction for different isoconversional methods

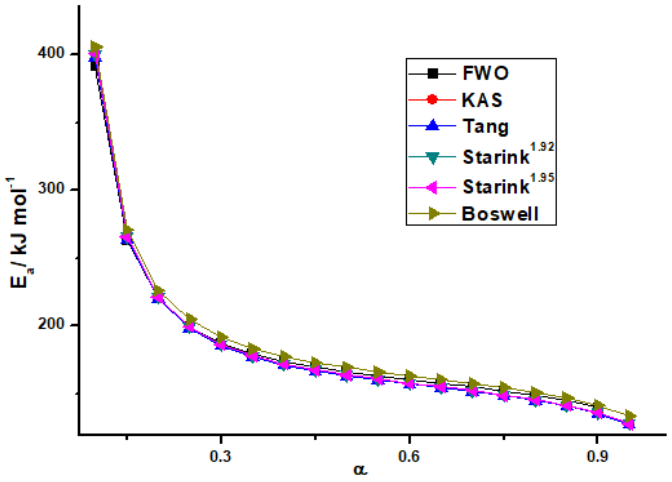

Fig. 12 *E_a vs α* curves for decomposition reaction for different isoconversional methods

Model fitting methods were used to suggest the most probable mechanism. For this, the value of $ln\ (g\ (\alpha)/T^2)$ *vs* $1/T$ of the non-isothermal DSC data at 4 K min^{-1} is plotted. The different reaction models, $f(\alpha)$ used to describe the reaction kinetics and their integrated forms, $g(\alpha)$ are given in **Table 4**. **Figs. 13** and **14** show model fitting least squares plots for dehydration and decomposition reaction. The plot will be a straight line (linear) for a correct mechanism and non-linear for the inaccurate mechanism. The most probable mechanism for dehydration was found to be with $g\ (\alpha) = (1-\alpha)\ *ln\ (1-\alpha) + \alpha$ (i.e., Two-dimensional diffusion, D2) whose $f(\alpha) = -[ln(1-\alpha)]^{-1}$ and for decomposition $g\ (\alpha) = -ln(1-\alpha)^{1/2}$ i.e., Avrami-Erofeev equation A2) whose $f(\alpha) = 2*(1-\alpha)[-ln(1-\alpha)]^{1/2}$.

Table 4 Different reaction models used to describe the reaction kinetics

No.	Code	Reaction model	$f(\alpha)$	$g(\alpha)$
1	P4	Power law	$4\alpha^{3/4}$	$\alpha^{1/4}$
2	P3	Power law	$3\alpha^{2/3}$	$\alpha^{1/3}$
3	P2	Power law	$2\alpha^{1/2}$	$\alpha^{1/2}$
4	P2/3	Power law	$2/3\alpha^{-1/2}$	$\alpha^{3/2}$
5	D1	One-dimensional diffusion	$1/2\alpha^{-1}$	α^2
6	F1	Mampel (first-order)	$1-\alpha$	$-\ln(1-\alpha)$
7	A4	Avrami–Erofeev	$4(1-\alpha)[-\ln(1-\alpha)]^{3/4}$	$(-\ln(1-\alpha))^{1/4}$
8	A3	Avrami–Erofeev	$3(1-\alpha)[-\ln(1-\alpha)]^{2/3}$	$(-\ln(1-\alpha))^{1/3}$
9	A2	Avrami–Erofeev	$2(1-\alpha)[-\ln(1-\alpha)]^{1/2}$	$(-\ln(1-\alpha))^{1/2}$
10	D3	Three-dimensional diffusion	$3/2(1-\alpha)^{2/3}[1-(1-\alpha)^{1/3}]^{-1}$	$(1-(1-\alpha)^{1/3})^2$
11	R3	Contracting sphere	$3(1-\alpha)^{2/3}$	$1-(1-\alpha)^{1/3}$
12	R2	Contracting cylinder	$2(1-\alpha)^{1/2}$	$1-(1-\alpha)^{1/2}$
13	F2	Second-order	$(1-\alpha)^2$	$(1-\alpha)^{-1}-1$
14	D2	Two-dimensional diffusion	$-[\ln(1-\alpha)]^{-1}$	$(1-\alpha)\ *\ln(1-\alpha) + \alpha$

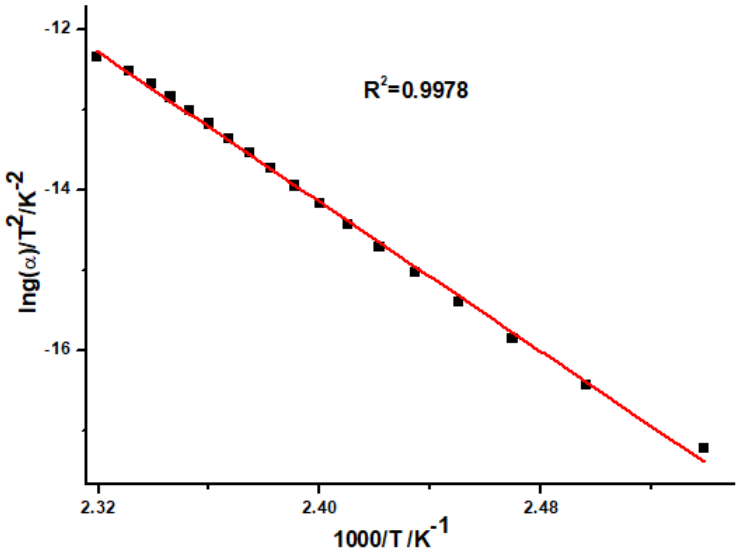

Fig. 13 model fitting least squares plot (Two-dimensional diffusion, D2) for dehydration reaction at a heating rate of 4 K min^{-1}

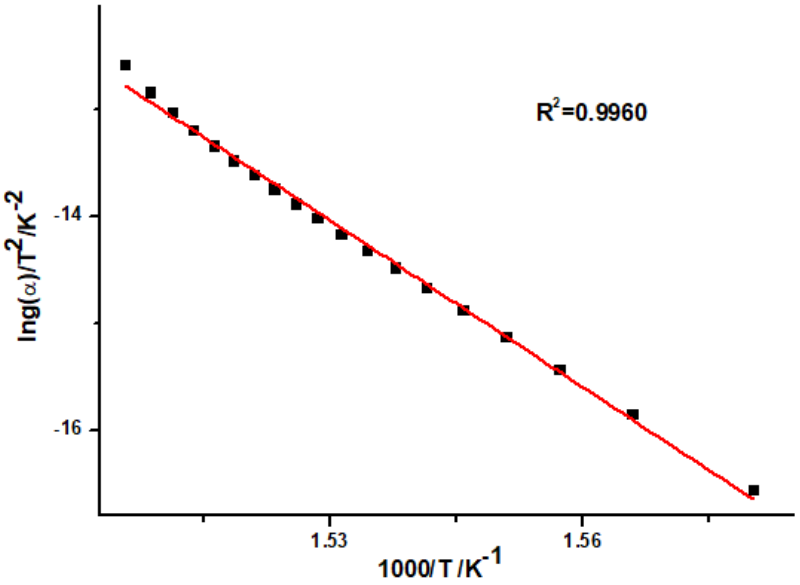

Fig. 14 model fitting least squares plot (Avrami - Erofeev equation, A2) for decomposition reaction at a heating rate of 4 K min^{-1}

2.3.4. Frontier molecular orbital analysis

The ability of a molecule to donate or accept electron can be comprehended from the energy of their frontier molecular orbital HOMO and LUMO. The HOMO and LUMO images of zinc oxalate and ZnO are shown in the **Figs. 15 and 16**. HOMO and LUMO energies represent the electron-donating and accepting ability of the molecule respectively. The HOMO, LUMO energies, and band gaps of zinc oxalate and ZnO are given in **Table 5.**

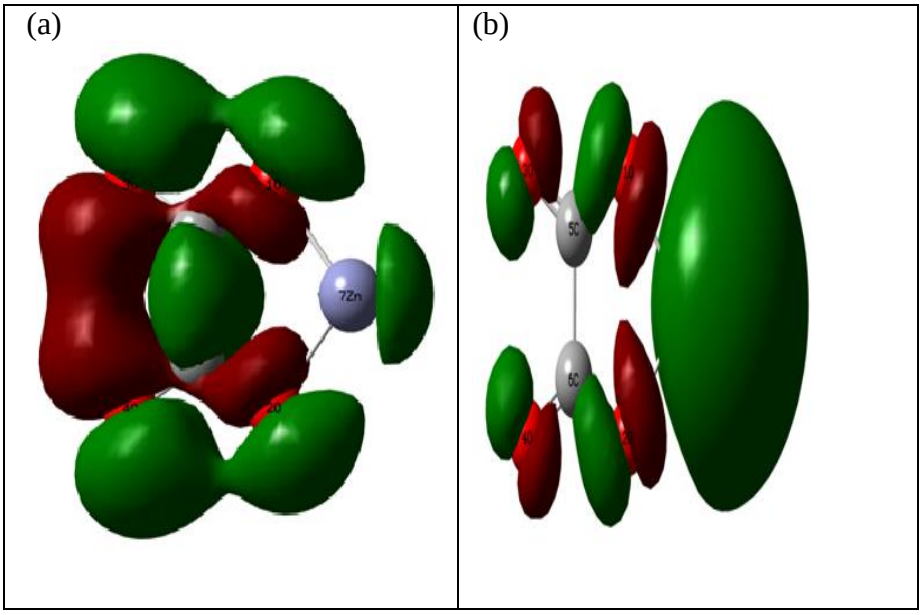

Fig. 15 HOMO (a) and LUMO (b) of zinc oxalate

The band gap obtained for ZnO is 2.54 eV which is comparable with those obtained from the experimental one (3.12 eV). From the values, it is clear that zinc oxalate has a smaller energy gap than silver oxalate but larger value than copper oxalate, and hence its reactivity and

stability are in between these two [26]. From HOMO and LUMO contours, it is clear that electron density in HOMO is concentrated on the carboxylate group and in LUMO it is concentrated on Zn. So, in zinc oxalate, there is a possibility of ligand to metal charge transfer.

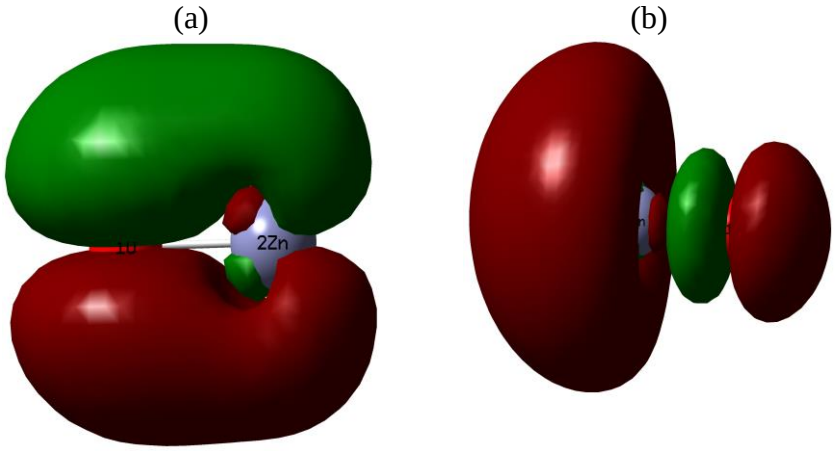

Fig. 16 HOMO (a) and LUMO (b) of ZnO

Table 5 HOMO, LUMO energy and the band gap of zinc oxalate and ZnO

Sample	HOMO (eV)	LUMO (eV)	Eg (eV)
Zinc oxalate	-7.6409	-5.2273	2.4136
ZnO	-6.6342	-4.0953	2.5389

2.3.4.1. Global reactivity descriptors

The calculated Global reactivity descriptors are tabulated in **Table 6**. The molecule having high HOMO energy shows a better reaction with electrophiles and low LUMO energy prefers reaction with

nucleophiles. Since hardness is reflected from the gap between HOMO and LUMO, the hardness of zinc oxalate and hence reactivity is in between copper and silver oxalate [26].

Table 6 Global reactivity descriptors calculated for anhydrous zinc oxalate through the orbital vertical method by B3LYP/6-31+g (d, p)

Global reactivity descriptors	Values in eV
IP	7.6409
EA	5.2273
η	1.2068
χ	6.4341
S	0.4143
μ	-6.4341
ω	17.1518

The molecular structure of anhydrous zinc oxalate has been optimized through the DFT/B3LYP level of theory and 6-31+g (d, p) basis set, and the lowest energy structure is confirmed. Frequency calculation was also performed to detect structure having any negative frequency and the result indicates all frequencies are positive i.e., there is no imaginary frequency, which confirms the optimized structure is at a global minimum. The optimized structure is shown in **Fig. 17**. The color blue, red, and grey indicate the atom of zinc, oxygen, and carbon respectively. The numbering system of the molecule followed the Gauss View numbering format. The computed bond length values obtained for different bonds in anhydrous zinc oxalate are tabulated in **Table 7** and

it has been observed that the bond length values decrease in the order Zn-O, C-C, C-O, and C=O and hence their bond strength increases in the same order. This indicates that the thermal decomposition begins with the breakage of one of the Zn-O bonds leaving a partially anchored zinc oxalate, followed by the breakage of the C-C bond with the elimination of CO_2. Finally, C-O bond breaks with the evolution of CO, and, ZnO exists as the final decomposition product.

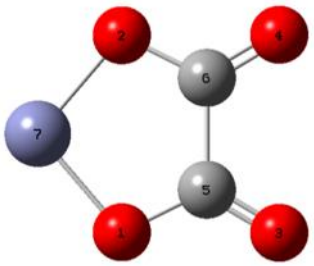

Fig. 17 Optimized structure of zinc oxalate using B3LYP/6-31+g (d, p) as the basis set

Table 7 The bond length values obtained for different bonds in anhydrous zinc oxalate through DFT studies using B3LYP/6-31+g (d, p) as the basis set

Bond	Bond length (Å)
Zn-O_1	1.85
Zn-O_2	1.85
C-O_1	1.36
C-O_2	1.36
C-C	1.60
C=O_1	1.20
C=O_2	1.20

2.4. Conclusion

Zinc oxalate dihydrate was synthesized and characterized. The kinetics of dehydration and decomposition was studied by non-isothermal DSC technique in the N_2 atmosphere at four different heating rates. The product of thermal decomposition, ZnO has been characterized by UV, TEM, SEM-EDAX, and XRD and found that the particles are of nanometer range. The average value of activation energy needed for the different reaction stages is 80.13, 77.22, 77.48, 77.44, 77.39, 80.78, 61.69 (for dehydration reaction), 183.48, 182.00, 181.29, 182.29, 182.27, 187.51, 109.07 (for decomposition reaction) kJ mol^{-1} obtained using the isoconversional methods of FWO, KAS, Tang, Starink$^{1.92}$, Starink$^{1.95}$, and Boswell respectively. All the isoconversional methods studied give similar trends in the variation of activation energy with the conversion function. Changes in the activation energy with the conversion function for all the isoconversional methods studied reflect the complexity of the reaction and changing mechanism during the reaction. Structure and reactivity of zinc oxalate have been investigated using the B3LYP /631+g (dp) level of theory using the Gaussian 09W software. From the theoretical investigation and the bond length values, it is concluded that during the thermal decomposition process, first, one of the Zn-O bond breaks then C-C bond breaks with the elimination of CO_2 and finally C-O bond breaks by evolving CO and ZnO exist as the final decomposition product. Global reactive descriptors were calculated in order to analyze the extent of reactivity of the molecule.

2.5. References

[1] C. Arora, S. Chejara, G. Ramarao, Y.P. Naik, Application of thermogravimetric analysis in study of solid-state reaction between barium oxalate and uranyl oxalate, J. Therm. Anal. Calorim. 124 (2016) 51–56.

[2] C. Arora, A. Sharma, S. Soni, Y. Naik, G. Ramarao, Solid-state reaction of strontium oxalate with uranium oxalate, J. Therm. Anal. Calorim. 124 (2016) 43–49.

[3] L. Guo, H. Arafune, N. Teramae, Synthesis of Mesoporous Metal Oxide by the Thermal Decomposition of Oxalate Precursor, Langmuir. 29 (2013) 4404–4412.

[4] A.M. Donia, Synthesis, identification and thermal analysis of coprecipitates of silver-(cobalt, nickel, copper and zinc) oxalate, Polyhedron. 16 (1997) 3013–3031.

[5] K. Muraleedharan, S. Kripa, DSC kinetics of the thermal decomposition of copper(II) oxalate by isoconversional and maximum rate (peak) methods, J. Therm. Anal. Calorim. 115 (2014) 1969–1978.

[6] N. Deb, An investigation on the solid-state thermal decomposition of bimetallic oxalate and tartrate coordination precursors of lanthanum(III) and palladium(II) ions, J. Anal. Appl. Pyrolysis. 82 (2008) 223–228.

[7] M.A. Mohamed, S.A. Halawy, M.A. Salem, Non-isothermal decomposition of potassium ferrioxalate trihydrate, J. Anal. Appl. Pyrolysis. 55 (2000) 55–67.

[8] A.K. Galwey, M.E. Brown, Thermal decomposition of ionic solids: chemical properties and reactivities of ionic crystalline phases, Elsevier, 1999.

[9] N.S. Fatemi, D. Dollimore, G.R. Heal, Thermal decomposition of oxalates. Part 16. Thermal decomposition studies on cadmium oxalate, Thermochim. Acta. 54 (1982) 167–180.

[10] K. Sabira, K. Muraleedharan, Exploration of the thermal decomposition of zinc oxalate by experimental and computational methods, J. Therm. Anal. Calorim. (2020). https://doi.org/10.1007/s10973-019-09169-6.

[11] V. V Boldyrev, Thermal decomposition of silver oxalate, Thermochim. Acta. 388 (2002) 63–90.

[12] B. V L'vov, V.L. Boris, The physical approach to the interpretation of the kinetics and mechanisms of thermal decomposition of solids: the state of the art, Thermochim. Acta. 373 (2001) 97–124.

[13] T. Ahmad, A.K. Ganguli, A. Ganguly, J. Ahmed, I.A. Wani, S. Khatoon, Chemistry of reverse micelles: a versatile route to the synthesis of nanorods and nanoparticles, Mater. Res. Soc. Symp. Proc. 1142 (2009) 75–88.

[14] S.K. Kansal, M. Singh, D. Sud, Studies on photodegradation of two commercial dyes in aqueous phase using different photocatalysts, J. Hazard. Mater. 141 (2007) 581–590.

[15] C.A.K. Gouvêa, F. Wypych, S.G. Moraes, N. Durán, N. Nagata, P. Peralta-Zamora, Semiconductor-assisted photocatalytic degradation of reactive dyes in aqueous solution, Chemosphere. 40 (2000) 433–440.

[16] M. Muruganandham, I.S. Chen, J.J. Wu, Effect of temperature on the formation of macroporous ZnO bundles and its application in photocatalysis, J. Hazard. Mater. 172 (2009) 700–706.

[17] S. Sakthivel, B. Neppolian, M. V Shankar, B. Arabindoo, M. Palanichamy, V. Murugesan, Solar photocatalytic degradation of

azo dye: comparison of photocatalytic efficiency of ZnO and TiO_2, Sol. Energy Mater. Sol. Cells. 77 (2003) 65–82.

[18] J. Fujita, K. Nakamoto, M. Kobayashi, Infrared spectra of metallic complexes. III. The infrared spectra of metallic oxalates, J. Phys. Chem. 61 (1957) 1014–1015.

[19] J. Mu, D.D. Perlmutter, Thermal decomposition of carbonates, carboxylates, oxalates, acetates, formates, and hydroxides, Thermochim. Acta. 49 (1981) 207–218.

[20] D. Dollimore, The influence of the environment on the thermal decomposition of oxysalts, J. Therm. Anal. Calorim. 11 (2005) 185–200.

[21] A.K. Nikumbh, A.E. Athare, S.K. Pardeshi, Thermal and electrical properties of manganese (II) oxalate dihydrate and cadmium (II) oxalate monohydrate, Thermochim. Acta. 326 (1999) 187–192.

[22] R. Majumdar, P. Sarkar, U. Ray, M.R. Mukhopadhyay, Secondary catalytic reactions during thermal decomposition of oxalates of zinc , nickel and iron (II), Thermochim. Acta. 335 (1999) 43-53.

[23] B. Małecka, E. Drozdz-Cieśla, A. Małecki, Mechanism and kinetics of thermal decomposition of zinc oxalate, Thermochim. Acta. 423 (2004) 13–18.

[24] C. Hu, J. Mi, S. Shang, The study of thermal decomposition kinetics of zinc oxide formation from zinc oxalate dihydrate, J. Therm. Anal. Calorim. 115 (2014) 1119–1125.

[25] S. Reshmi, K.P. Vijayalakshmi, D. Thomas, B.K. George, C.P.R. Nair, Thermal decomposition of a diazido ester: Pyrolysis GC–MS and DFT study, J. Anal. Appl. Pyrolysis. 104 (2013) 603–608.

[26] K. Sarada, K.R. Vijisha, K. Muraleedharan, Exploration of the thermal decomposition of oxalates of copper and silver by experimental and computational methods, J. Anal. Appl. Pyrolysis. 120 (2016) 207–214.

[27] A. Koleżyński, A. Małecki, First principles studies of thermal decomposition of anhydrous zinc oxalate, J. Therm. Anal. Calorim. 96 (2009) 645–651.

[28] A. Koleżyński, A. Małecki, Theoretical approach to thermal decomposition process of chosen anhydrous oxalates, J. Therm. Anal. Calorim. 97 (2009) 77–83.

[29] A. Koleżyński, B. Handke, E. Drożdż-Cieśla, Crystal structure, electronic structure, and bonding properties of anhydrous nickel oxalate, J. Therm. Anal. Calorim. 113 (2013) 319–328.

[30] A. Koleżyński, A. Małecki, Theoretical studies of electronic and crystal structure properties of anhydrous mercury oxalate, J. Therm. Anal. Calorim. 101 (2010) 499–504.

[31] A. Koleżyński, A. Małecki, Theoretical analysis of electronic and structural properties of anhydrous calcium oxalate, J. Therm. Anal. Calorim. 99 (2009) 947–955.

[32] A. Koleżyński, A. Małecki, Theoretical studies of thermal decomposition of anhydrous cadmium and silver oxalates, J. Therm. Anal. Calorim. 96 (2009) 167–173.

[33] A.D. Becke, Density-functional thermochemistry. III. The role of exact exchange, J. Chem. Phys. 98 (1993) 5648–5652.

[34] C. Lee, W. Yang, R.G. Parr, Development of the Colle-Salvetti correlation-energy formula into a functional of the electron density, Phys. Rev. B. 37 (1988) 785–789.

[35] A. Patterson, The Scherrer Formula for X-Ray Paeticle Size Determination, Phys. Rev. 56 (1939) 978-982.

[36] Z. Jia, D. Ren, L. Xu, R. Zhu, Preparation, characterization and photocatalytic activity of porous zinc oxide superstructure, Mater. Sci. Semicond. Process. 15 (2012) 270–276.

[37] R. Velmurugan, M. Swaminathan, An efficient nanostructured ZnO for dye sensitized degradation of Reactive Red 120 dye under solar light, Sol. Energy Mater. Sol. Cells. 95 (2011) 942–950.

[38] N. Abraham, A. Rufus, C. Unni, D. Philip, Nanostructured ZnO with bio-capping for nanofluid and natural dye based solar cell applications, J. Mater. Sci. Mater. Electron. 28 (2017) 16527–16539.

[39] A. Khawam, D.R. Flanagan, Role of isoconversional methods in varying activation energies of solid-state kinetics: II. Nonisothermal kinetic studies, Thermochim. Acta. 436 (2005) 101–112.

[40] S. Vyazovkin, Computational aspects of kinetic analysis.: Part C. The ICTAC Kinetics Project — the light at the end of the tunnel?, Thermochim. Acta. 355 (2000) 155–163.

[41] M.J. Starink, The determination of activation energy from linear heating rate experiments: a comparison of the accuracy of isoconversion methods, Thermochim. Acta. 404 (2003) 163–176.

[42] K. Sarada, K. Muraleedharan, Effect of addition of silver on the thermal decomposition kinetics of copper oxalate, J. Therm. Anal. Calorim. 123 (2016) 643–651.

[43] T. Ozawa, A New Method of Analyzing Thermogravimetric Data, Bull. Chem. Soc. Jpn. 38 (1965) 1881–1886.

[44] J.H. Flynn, L.A. Wall, A quick, direct method for the determination of activation energy from thermogravimetric data, J. Polym. Sci. Part B Polym. Lett. 4 (1966) 323–328.

[45] H.E. Kissinger, Reaction Kinetics in Differential Thermal Analysis, Anal. Chem. 29 (1957) 1702–1706.

[46] T. Wanjun, Æ.C. Donghua, New approximate formula for the generalized temperature integral, J. Therm. Anal. Calorim. 98 (2009) 437–440.

[47] M. Jose John, K. Muraleedharan, M.P. Kannan, T. Ganga Devi, Kinetic studies on the thermal decomposition of phosphate-doped sodium oxalate, J. Therm. Anal. Calorim. 111 (2013) 137–144.

Effect of Ce (III) additives on the kinetics of thermal dehydration and decomposition of zinc oxalate dihydrate

3.1. Introduction

The use of solar energy for a chemical transformation is a significant invention in the field of chemical engineering. Solar energy is abundant natural energy and everybody can access it without anybody's consent and free of charge. In our daily lives, we knowingly or unknowingly use solar power for different purposes. Photocatalysis is a recently booming sector of research that utilizes photoenergy for multiple chemical reactions including photodegradation of organic pollutants using semiconductor catalysts. TiO_2 has been employed as the widely used photocatalyst for the removal of organic pollutants. ZnO can be used as a good alternative to TiO_2 because of its low cost, wide bandgap energy, high oxidative capacity, high chemical stability, low toxicity, and easy method of preparation, also ZnO shows superior qualities than TiO_2 for photodegradation [1–3]. Even though ZnO is a better photocatalyst, there is a problem associated with its rapid recombination of the photoexcited electron-hole pairs, which is the key factor in the process of semiconductor photocatalysis, which limits its commercial use. Therefore, there is a large interest in reducing the recombination rate of electron-hole pairs and to enhance its photocatalytic efficiency [4,5]. Also, as a consequence of its wide bandgap, ZnO can only absorb UV light with the wavelength equal to or

less than 385 nm which constitutes only less than 10% of the total energy of solar radiation. Decreasing the band gap would allow increasing the absorbance from the current UV light to the visible light which constitutes 45% of solar energy and this can be done by metal or non-metal doping [6].

Recent studies showed that the addition of transition and noble metals like platinum, silver, and gold on ZnO accelerate the charge-transfer and thereby enhances the photodegradation process [7–9]. Coupling two semiconductor nanoparticles with different band gap energy and doping with metals have been demonstrated as some of the most effective ways to reduce the recombination rate of electron-hole pairs and to shift the absorption band to the visible region [10–12].

The growing interest of smart materials using metal oxides is due to the possibility of their doping and/ or mixing; which in turn leads to better materials with tunable properties. Doping and mixing can create defects in crystal systems. From the third law of thermodynamics, it is quite clear that a state of perfect order can only be achieved at absolute temperature, above 0 K, entropy increases and depart from the perfect order. Defects can be generated in a crystal in different ways. A defected crystal can cause the alteration of electric, magnetic and other properties of the system. Doping is one of the best and commonly employed methods for producing defects in solids and it creates point defects in the crystal lattice. Several reports are describing the doping of ZnO with metals, but it is still remaining as a hot topic in research to achieve a high quality of crystalline particles with excellent physical and chemical

properties of doped ZnO nanostructures [13]. Lanthanide-doped ZnO nanocrystals are one of the new classes of luminescent materials for advanced display and lighting applications. La, Ce-co-doped ZnO nanoparticles show prominent large red-shift in the ultraviolet region which makes them good prospects for use in visible high-efficiency luminescent flat displays and excellent solar light-activated photocatalysts [14]. Doping with Ce ion enhances the photocatalytic activity against various organic pollutants which can be due to the increased surface oxygen vacancies, higher adsorption capacity, and better separation of electron-hole pairs in nanostructured photocatalyst [15]. Ce-doped ZnO nanorods have been reported as an efficient electron mediator for the fabrication of hydroquinone chemical sensors [16]. Thermal decomposition of Zinc oxalate is studied by several researchers [17-23].

The purpose of the study is because; knowledge of kinetic parameters, such as the reaction rate and activation energy of the thermal decomposition reaction of solids is one of the keys to determine the reaction mechanisms in the solid phase. When changes in the mechanisms are observed, this can lead to a unique characteristic and hence a better knowledge of the materials. Besides this, there are also more practical reasons to know the reaction rates and their temperature dependence. The industry needs measurements of those parameters for the accurate design of installations and treatment conditions because augmentation of temperature or elongation of reaction time means more cost.

In the present study, Ce^{3+} is selected as an additive aliovalent atom for zinc oxalate lattice, whose effective nuclear charge can affect the electroneutrality condition and thereby the defect equilibria. Generally, the amount of foreign atoms up to 1 mol% (or in range of ppm) is considered to give the effect of doping. Above 1 mol%, the atoms are replaced deliberately too many degrees, which give rise to substituent effect. Both the dopants and substituents have various effects on the metal oxides. Thus, the study envisaged knowing the dependence of additive concentration on thermal dehydration and decomposition kinetics of precursor zinc oxalate dihydrate with cerium concentrations 0.1, 1, and 5 mol%. In this regard, the present study focuses on the consequences of Ce^{3+} additives on the kinetics of thermal dehydration and decomposition reactions of zinc oxalate dihydrate in two different atmospheres, nitrogen and air using DSC and TGA techniques.

3.2. Experimental

3.2.1. Materials

The reagents used in this study are of analytical grade and employed without any further purification. The chemicals used in the study are $Zn(NO_3)_2.6H_2O$ (Himedia, India), $Ce(NO_3)_3.6H_2O$ (Himedia, India), $H_2C_2O_4$ (Merck, India) and KBr (Sigma).

3.2.2. Preparation of Ce added zinc oxalate

An equimolar ratio of $Zn(NO_3)_2.6H_2O$, $H_2C_2O_4$ were separately mixed in distilled water to form a homogenous solution. Requisite amount of $Ce(NO_3)_3.6H_2O$ were weighed for preparing cerium doped zinc oxalate of concentrations 0.1, 1, and 5 mol% and added to $Zn(NO_3)_2.6H_2O$ solution and stirred well to get a homogenous solution. To these solutions, the oxalic acid solution was added to precipitate as oxalate and mixed thoroughly under vigorous stirring conditions up to the formation of a white precipitate of Ce containing zinc oxalate. The stirring was continued for 2 hours using a magnetic stirrer. The precipitate washed several times with distilled water and dried in an air oven at 343 K. Pure zinc oxalate is also prepared in the same procedure without adding $Ce(NO_3)_3.6H_2O$. The samples prepared were sieved through a mesh and fixed the particle size in the range of 95-105 µm. The prepared samples are then used for FT-IR, DSC, and TG analyses. The samples were calcined at 773 K for FT-IR, UV-DRS, XRD, FESEM, and HR-TEM analyses.

3.2.3. Characterization of the sample

Fourier transform-infrared (FT-IR) spectra of the samples were recorded by the transmittance method using a spectrometer (Model: Jasco FT-IR-41) after diluting the samples with KBr powder using hydraulic pellet press (KP, SR. No. 1718) under a pressure of 50 kg cm^{-2}. The optical band gap (E_g) of the decomposed products was calculated from ultraviolet-visible reflectance which was measured using

ultraviolet-visible diffuse reflectance spectrum (Model: Jasco V-550 spectrophotometer). The powder X-ray diffraction (XRD) patterns of the samples were recorded using a diffractometer (Miniflex 600, Model: Rigaku D/Max) with Cu-Kα (λ=1.5418 Å) radiation (40 kV, 15 mA) with a scan rate of 2θ min^{-1} in the region of 20-90^o. The FE SEM analysis of the synthesized nanoparticles was studied with CARL ZEISS (USA), model: SIGMA with GEMINI column with a resolution of 1.5 nm. The EDAX spectra were taken with a BRUKER (German) Model: Nano XFlash Detector. The high resolution transmission electron microscopic (HR-TEM) analysis of the particles was achieved by using a JEOL Model: JEM 2100 of LaB6 electron gun operated at 200 kV with 0.18 nm point resolution and 0.14 nm lattice resolution.

3.2.4. Measurement of thermal behavior

TG measurements were made on a Perkin Elmer Pyris Thermal Analyser STA8000 at different heating rates 2, 4, 6, 8, and 10 K min^{-1}. The operational characteristics of the thermal analysis system are as follows: atmosphere: air, sample mass: ~5 mg; and sample pan: silica. Duplicate runs were made under similar conditions and found that the data overlap with each other, indicating satisfactory reproducibility. The differential scanning calorimetric (DSC) measurements of the samples were done in the temperature range 303-773 K at five different heating rates 2, 4, 6, 8, and 10 K min^{-1} on a Mettler Toledo DSC822e. The operational characteristics of the DSC system are as follows: atmosphere: flowing N_2 at a flow rate of 50 mL min^{-1}; sample mass~ 5.1 mg; and sample holder: silica.

3.3. Results and Discussions

3.3.1. Sample characterization

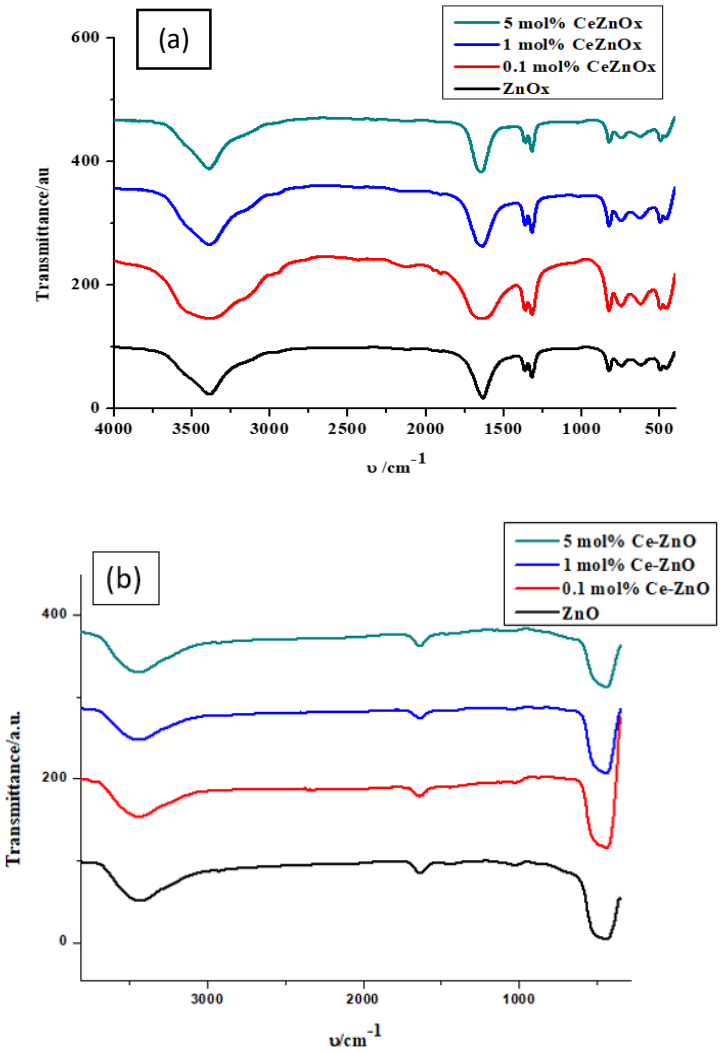

Fig. 1 FT-IR spectra of ZnOx and Ce-ZnOx (a), ZnO and Ce-ZnO (b)

Fig. 1(a) represents FT-IR spectra of ZnOx and Ce-ZnOx of cerium concentrations 0.1, 1, and 5 mol%. There is a broad band at 3385

cm^{-1} which proves the presence of surface hydroxyl water molecule. The strong band above 1600 cm^{-1} is due to the stretching vibration of the carbonyl group. The two small peaks at around 1300 cm^{-1} are due to the stretching vibration of the C-O-C bond. The presence of the Zn-O bond is cleared from the presence of a peak at 458 cm^{-1}. **Fig. 1(b)** shows FT-IR spectra of ZnO and Ce-ZnO of concentrations 0.1, 1, and 5 mol%. The peak at 443 cm^{-1} is responsible for the metal-oxygen (Zn-O) bond. There is a small peak around 1600 cm^{-1} and a broad peak at 3400 cm^{-1} which are responsible for the bending vibration and O-H stretching mode of surface adsorbed water molecule. The FT-IR spectra obtained for zinc oxalate dihydrate and zinc oxide were compared with the FT-IR spectra described by Hu *et al*. and B. Krishnakumar *et al.* and observed that the bands obtained are matched perfectly with the reported ones [4,23,24].

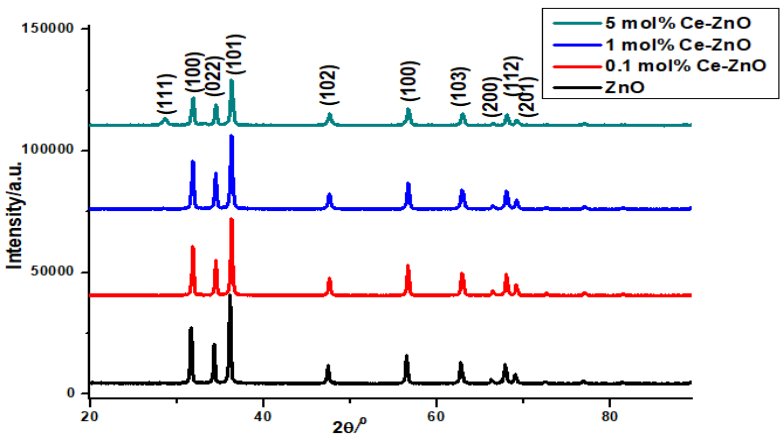

Fig. 2 XRD of ZnO and Ce-ZnO samples calcined at 773 K

Fig. 2 shows XRD of ZnO and Ce-ZnO samples of different cerium concentrations which are calcined at 773 K. As the cerium concentration increases from zero to 5 mol%, a well-defined peak

appears at 2θ value 28.86 nm corresponding to the (111) plane of Ce^{4+} (JCPDS 898436) [25]. This indicates the presence of cerium loading on the ZnO lattice. At lower Ce concentration, there is no peak at 2θ value of 28.86 nm because Ce^{3+} concentration could be too low to be detected by XRD [24]. The peaks at different 2θ values can be indexed to different planes of wurtzite ZnO (JCPDS N 00-036-1451). By doping Ce^{3+} in ZnO, only the ZnO peaks were still detected and no diffraction peaks of other phases were detected, indicating that the Ce^{3+} ions completely substituted for Zn^{2+} ions in ZnO lattice. The intensity of peaks at different planes is decreasing with the addition of cerium. The XRD peaks obtained for ZnO are well-matched with the previously reported one which was synthesized through oxalate precipitation route [23]. The XRD patterns show that there is a slight shift in 2θ values of Ce-ZnO nanoparticles of different Ce concentrations when compared to ZnO nanoparticles. The ionic radius of the dopant Ce^{4+} (97 pm) is higher than that of Zn^{2+} (74 pm). So, doping with Ce^{4+} caused a slight shift in the XRD peaks towards higher diffraction angles. This provides indirect evidence that Ce^{4+} is incorporated into the crystal structure of ZnO causing the crystal to expand. The average crystallite size was calculated using the Debye–Scherrer equation [26].

$$D = K\lambda / \beta cos\theta \tag{1}$$

where β is the full width at half maximum intensity of the peak (in Rad), K is the crystallite shape factor, a good approximation is 0.9, λ is the wavelength of the incident X-ray (λ = 0.1540 nm for Cu-Kα), D is the crystallite size, and θ is the Bragg's angle in degree. The crystallite sizes of the prepared ZnO nanoparticles vary in different planes. The

crystallite sizes obtained for different planes of ZnO vary from 34.1 to 64.8 nm. The crystallite sizes obtained for different planes of 0.1, 1, and 5 mol% Ce-ZnO were found to vary from 35.1 to 65.1 nm, 29.1 to 37.8 nm, and 12.0 to 32.3 nm respectively. It is found that the crystallite sizes obtained for different planes of 0.1, 1, and 5 mol% Ce-ZnO was decreased with cerium addition. The average crystallite size obtained using the Debye-Scherrer equation is 44.06 nm for pure ZnO which is calcined at 773 K. It is very interesting to note that the average crystallite size is decreasing with increasing cerium ion concentration. The size of all cerium loaded samples is in the nanometer range. The average crystallite size obtained using the Debye-Scherrer equation for 0.1, 1 and 5 mol% Ce-ZnO samples which are calcined at 773 K are 43.25, 33.84, and 24.58 nm respectively. It is found that the loading of metal into the semiconductor surface will reduce the crystallite size of the semiconductor when compared to the unloaded semiconductors [7,25]. ZnO crystal structure is more open, the metal ions with a smaller radius cannot only become substitution ions but also easily become interstitial ions, while the ions with larger radius Ce^{4+} (0.97Å) than Zn^{2+} (0.74Å) ions are easier to become substitution ions. Hence the crystallite size of Ce-ZnO is lower than bare ZnO [4]. The lattice constants a, b and c were calculated. The (100) and (002) planes were used to calculate the lattice parameters of the prepared ZnO and Ce-ZnO nanoparticles. The lattice constants a and b are 0.3256 nm and c 0.5220 nm for pure ZnO. The lattice constants a and b are 0.3243 nm and c 0.5199 nm for 0.1 mol% Ce-ZnO. The lattice constants a and b are 0.3244 nm and c 0.5200 nm for 1 mol% Ce-ZnO and the lattice constants a and b are 0.3241 nm and c 0.5197 nm for 5 mol% Ce-ZnO. Thus, doping does not affect the

crystal structure of ZnO but causes minor lattice deformations which leads to a decrease in crystallite size.

Fig. 3 shows the ultraviolet-visible diffuse reflectance spectrum of ZnO and Ce-ZnO samples calcined at 773 K. All the samples show an absorption maximum at 360 nm and it is very clear that there is a noticeable change in absorption maximum with Ce addition.

The optical band gap (E_g) of the decomposed products was calculated from ultraviolet-visible reflectance which was measured using ultraviolet-visible diffuse reflectance spectrum. The optical band gap is determined by using the Tauc equation

$$(\alpha h\upsilon)^n = B(h\upsilon - Eg) \qquad (2)$$

where $h\nu$ is the photon energy, α is the absorption coefficient, B is a constant relative to the material and n is either 2 for direct transition or 1/2 for an indirect transition.

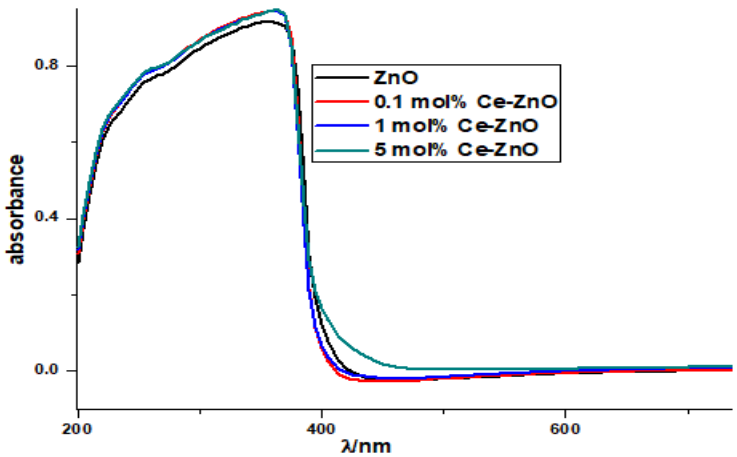

Fig. 3 ultraviolet-visible diffuse reflectance spectra of ZnO and Ce- ZnO samples calcined at 773 K

The $(\alpha h\upsilon)^2$ versus $h\upsilon$ curve (Tauc-plot) of ZnO and Ce-ZnO calcined at 773 K is shown in **Fig. 4.** The band gap obtained for zinc oxalate is 3.14 eV and it is almost the same for 0.1 mol% Ce-ZnO and 1 mol% Ce-ZnO samples. But it is very interesting to note that the band gap is reduced to 3.10 eV for 5 mol% Ce-ZnO sample. The obtained band gap values for ZnO and Ce-ZnO are well agreed with the literature values [3]. This decrease in band gap can be explained due to the charge transfer between the ZnO valence bands or conduction band and 4f level of cerium and now the system got a trapping level. The decrease in the band gap surely enhances its photocatalytic activity by increasing the visible light absorption ability of ZnO [25].

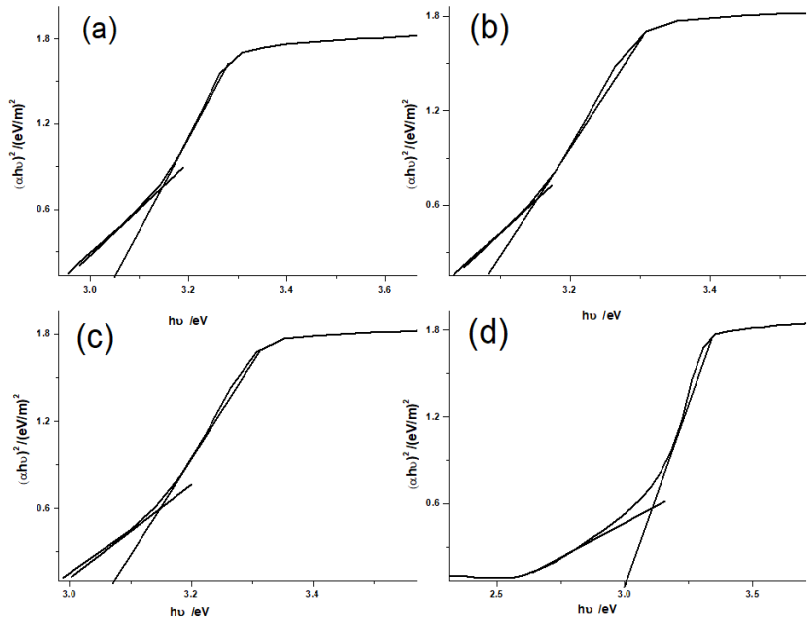

Fig. 4 Tauc-plot of ZnO (a), 0.1 mol% Ce-ZnO (b), 1 mol% Ce-ZnO (c) and 5 mol% Ce-ZnO (d) calcined at 773 K

Fig. 5 shows the HR-TEM images of ZnO calcined at 773 K at different magnification. The figure clearly shows the high crystallinity of the sample. The images at higher magnification prove the spherical shape of the ZnO nanoparticles. The HR-TEM images at different magnifications, lattice fringes, and SAED pattern of 5 mol% Ce-ZnO sample which was calcined at 773 K is shown in **Fig. 6.** The HR-TEM images of Ce-ZnO nanoparticles are very similar to that of ZnO. It is observed from **Fig 6(c)** that spherical nanoparticles of cerium are dispersed on the surface of ZnO as dark spots.

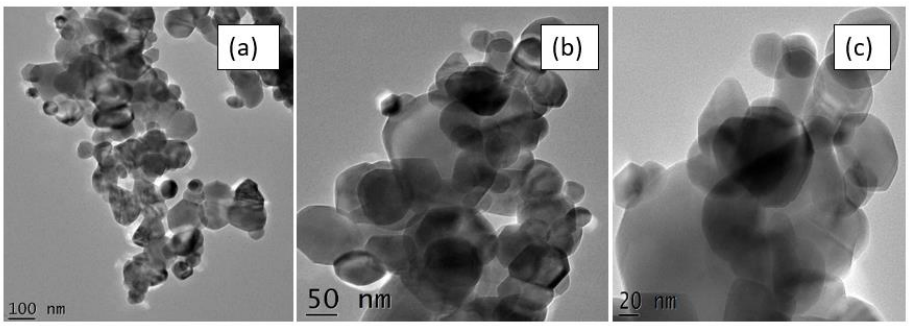

Fig. 5 HR-TEM images of ZnO of 100 nm (a), 50 nm (b) and 20 nm (c)

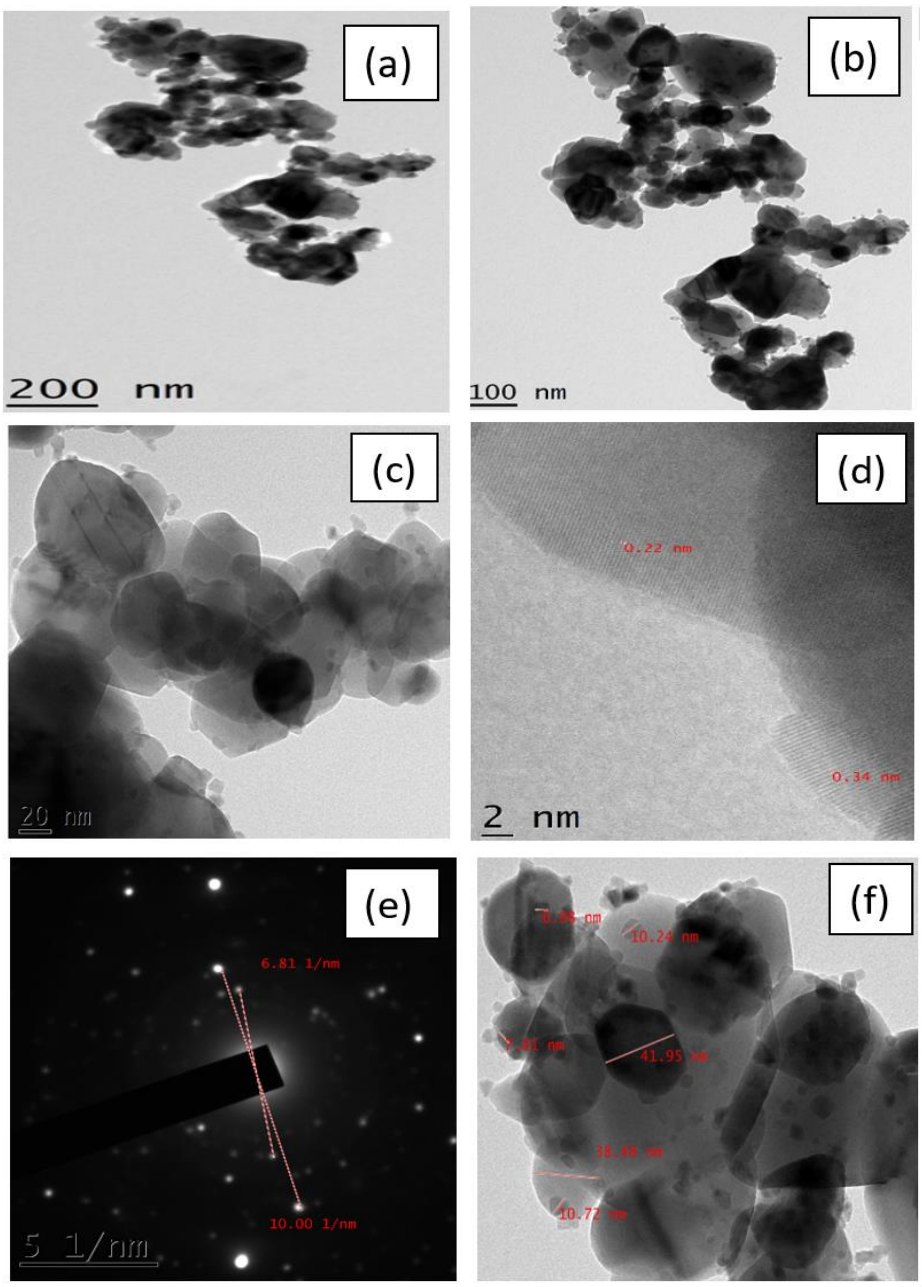

Fig. 6 HR-TEM images of 5 mol% Ce-ZnO sample at 200 nm (a), 100 nm (b), 20 nm (c), lattice fringes (d), SAED (e) pattern and magnified image (f) showing particle size

It is also observed that in addition to spherical nanoparticles of ZnO, some hexagonally structured ZnO nanoparticles are also seen in the HR-TEM image of the 5 mol% Ce-ZnO sample. The SAED pattern of 5 mol% Ce-ZnO sample illustrated bright spotty ring pattern and the clear lattice fringes indicate the good crystallinity of the sample which is in good agreement with the XRD results. The nanoparticles formed are non-homogenous in size and the average diameter of cerium crystallites deposited on the ZnO surface has to size below 11 nm.

Figs. 7 shows FE-SEM images of ZnO and Ce-ZnO samples calcined at 773 K at the magnification 200 nm. The SEM results are well consistent with the results obtained from the HR-TEM results. From the SEM images, it is very clear that the ZnO and Ce-ZnO nanoparticles formed are spherical in shape and some hexagonal shaped nanoparticles are also formed which can also see in the HR-TEM image. The morphology of the ZnO nanoparticles does not change with the addition of cerium ions but the particle size reduced considerably. At a higher concentration of cerium ions, it was observed that cerium ions were dispersed on the surface of ZnO nanoparticles and their number increases with an increase in cerium ion as observed in the HR-TEM images. The FE-SEM images were taken along with their EDAX spectra and the EDAX spectra of ZnO and Ce-ZnO nanoparticles are shown in **Fig. 8.** The EDAX spectrum of ZnO and 0.1 and 1 mol% Ce-ZnO nanoparticles show the peaks corresponding to zinc and oxygen only but in 5 mol% Ce-ZnO there is an additional peak of Ce at 4.8 keV which proves the successful addition of cerium ions in 5 mol% Ce-ZnO. The

FE-SEM and HR-TEM results are correlated with the earlier reported results and found similar observations [3].

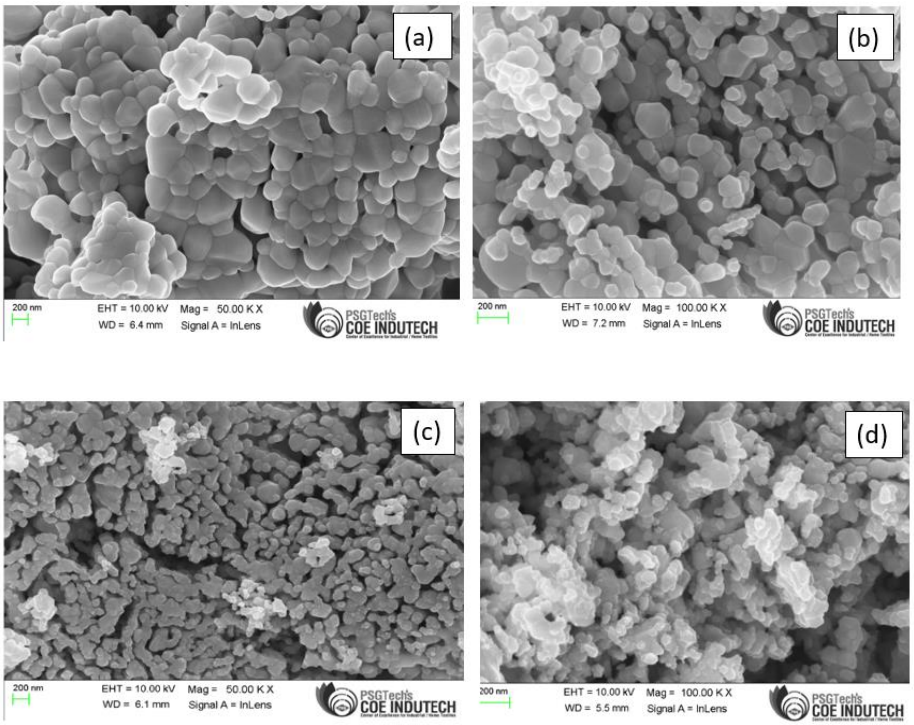

Fig. 7 FE-SEM images of ZnO (a), 0.1 mol% Ce-ZnO (b), 1 mol% Ce-ZnO (c), 5 mol% Ce-ZnO (d) (200 nm) calcined at 773 K

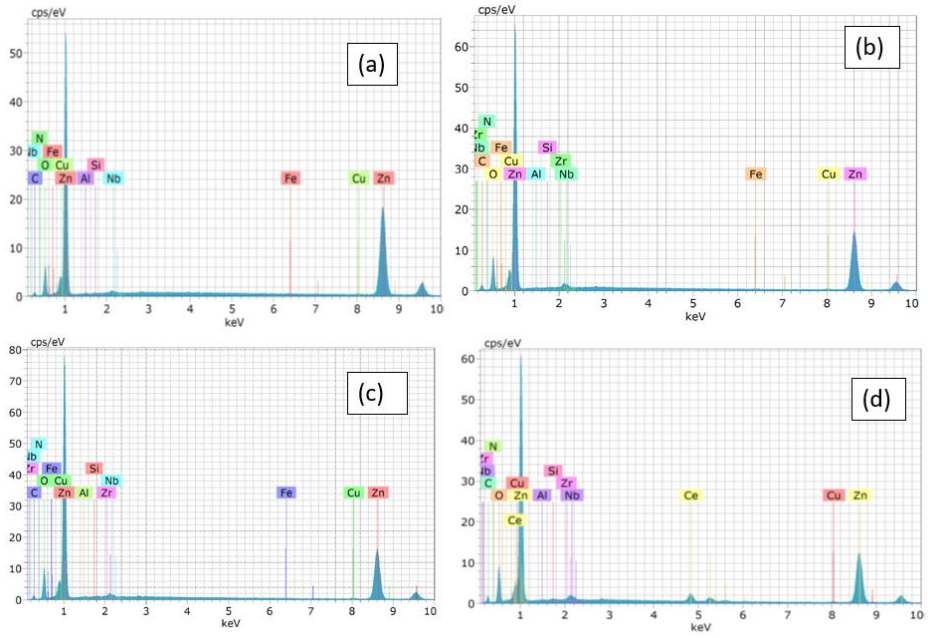

Fig. 8 EDAX spectra of ZnO (a), 0.1 mol % Ce-ZnO (b), 1 mol % Ce-ZnO (c) and 5 mol % Ce-ZnO (d) nanoparticles calcined at 773 K

3.3.2. Characterization of thermal events

Fig. 9 shows DSC curves of zinc oxalate dihydrate and Ce added zinc oxalate dihydrate of different cerium concentrations. From the figures, it is very clear that there are two endothermic peaks that are well separated and the first peak represents the dehydration and the second peak corresponding to the decomposition of oxalate into its oxide. Dehydration reaction taking place in the temperature range 350-450 K and decomposition reaction starts at 600 K and the oxalate is completely transformed into its oxide before 700 K. From these figures, it is clear that as the heating rate increased, the peaks were shifted to a higher

temperature and the peaks become sharper which indicates that the reactions are kinetically controlled.

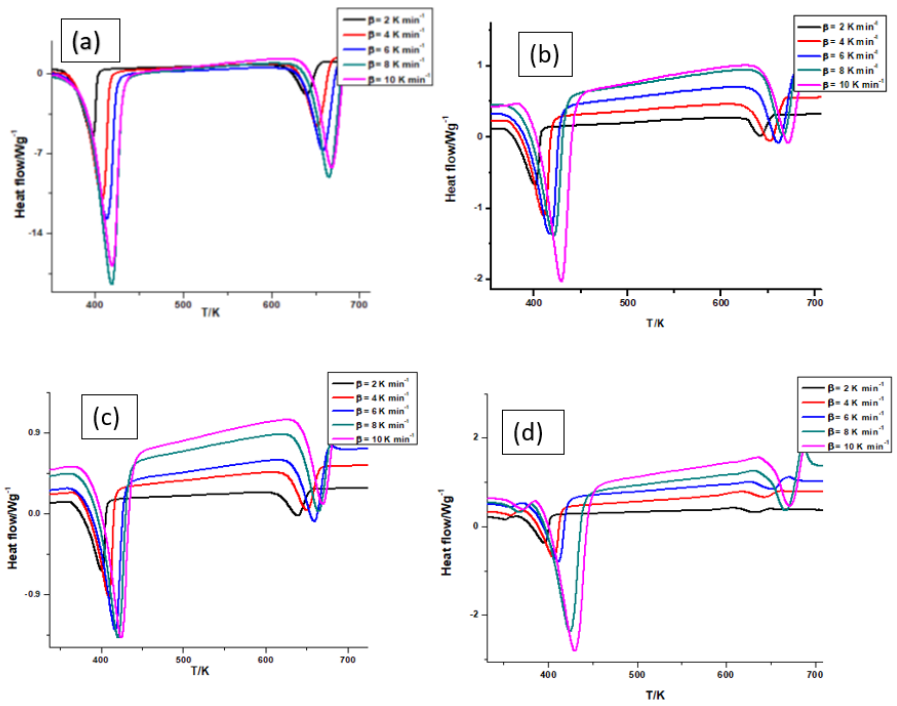

Fig. 9 DSC curve of ZnOx (a), 0.1 mol% Ce-ZnOx (b), 1 mol% Ce-ZnOx (c), 5 mol% Ce-ZnOx (d) at different heating rates

Fig. 10 shows the TG curve of ZnOx and Ce-ZnOx of different Ce concentrations at the heating rate of 2 K min^{-1}. TG was taken for all the samples at 2, 4, 6, 8, 10 K min^{-1} and it is shown in **Fig. 11** and found that all of them show two mass loss stages, one in the temperature range 385-425 K (dehydration) and the second one in 580-660 K (decomposition).

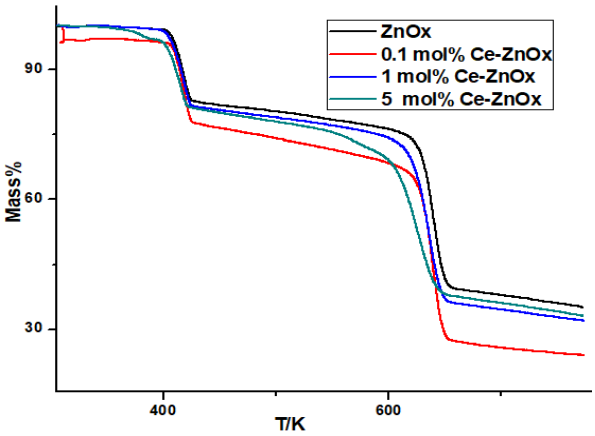

Fig. 10 TG curve of ZnOx and Ce-ZnOx of different Ce concentrations at the heating rate 2 K min^{-1}

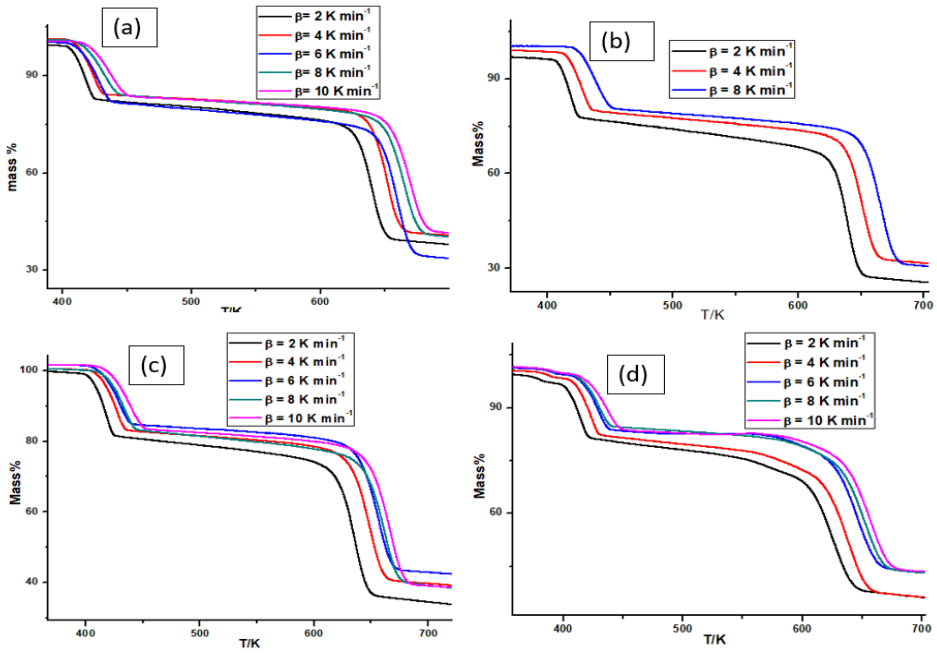

Fig. 11 TG curve of ZnO (a), 0.1 mol % Ce-ZnO (b), 1 mol % Ce-ZnO (c), 5 mol % Ce-ZnO (d) at different heating rates

As the heating rate changes, there is no change in the TG curve but there is a slight increase in temperature as observed in DSC which establishes that the reactions are kinetically controlled. It is found that as the Ce concentration increases from zero to 5 mol%, the dehydration, as well as the decomposition reactions, occurs at a lower temperature. In the temperature range 385-425 K, 17% mass loss occurs, this is attributed to the loss of 1.8 mol of water per mole of oxalate. Since the sample exists in its dihydrate form, the mass loss obtained suggests that dehydration reaction was not completed and some water retained in occlusions in the oxalate structure [23]. The second mass loss of 38.6% (theoretical mass loss 38.03%) indicates the decomposition of ZnC_2O_4 into ZnO. The small increase in mass loss than the theoretical value may be due to the evolution of water that is not dehydrated in the lower temperature and retained in the lattice.

3.3.3. Kinetic behavior

The kinetic parameters of solid state decomposition reaction proceeding in non-isothermal conditions can be studied using the differential form of the kinetic equation;

$$d\alpha / dt = k(T)\, f(\alpha) \tag{3}$$

where $f(\alpha)$ is a function of α depending on reaction model and

$$k(T) = Ae^{-E_a/RT} \tag{4}$$

where E_a is the activation energy and A is the pre-exponential factor. Arrhenius parameters can be determined only if k (T) and $f(\alpha)$ are separated. Out of model fitting which is based on the single heating curve and model-free method of kinetic analysis, model-free isoconversional methods at multiple heating curves are the most dependable for calculating the activation energy of thermal decomposition reaction in non-isothermal conditions [27,28]. Isoconversional methods assume that the reaction rate at a fixed α depends only on temperature and the reaction model is independent on heating rates [28]. The reaction rate alters with the heating rate. The reaction rate is fast at a higher heating rate. The variation in the rate of reaction at different heating rates can be used to determine the activation energy of the reaction. Activation energy is constant throughout the conversion for a single-stage reaction while it varies for complex reactions. The mechanism of the reaction can be explained by studying the variation of activation energy with α. M.J. Starink compared the accuracy of different isoconversional methods in the determination of activation energy from linear heating rate experiments [29].

Combining equation (3) and (4)

$$d\alpha / dt = Ae^{-E_a/RT} f(\alpha) \qquad (5)$$

At non-isothermal conditions, the temperature is increasing with time at the constant heating rate. Integration of Eq. (5) involves solving the temperature integral, I (E, T)

$$g\ (\alpha) = A/\beta \int_0^{Tx} e^{-E_a/RT} dt = A/\beta I(E,T) \qquad (6)$$

this equation has an ineffectual analytical solution. Some approximations or numerical integration is used to solve the equation. All of the approximations lead to a direct isoconversional method in the form: $ln\left(\beta/T^K\right) = C - E_a/RT$ (7)

for a selected degree of conversion function, α, a corresponding $T_{\alpha i}$ and heating rate β are used to plot ln (β/T^K) against $1/T_{\alpha i}$, where K is a constant. The activation energy is then determined from the regression slope [30].

3.3.3.1. Isoconversional methods used for the calculation of E_a:

1. Flynn–Wall–Ozawa (FWO) method [31,32].

$$ln\beta = ln\left(AE/g(\alpha)R\right) - 5.331 - 1.052E_\alpha/RT_{\alpha i} \qquad (8)$$

where α is the conversion function. From the slope of the graph lnβ against $1/T_{\alpha i}$, E_a can be calculated.

2. Kissinger–Akahira–Sunose (KAS) method [33].

KAS is also an integer isoconversional method similar to FWO.

$$ln\beta/T^2{}_{\alpha i} = ln\left(AR/E_a g(\alpha)\right) - E_a/RT_{\alpha i} \qquad (9)$$

E_a can be obtained from the slope of the straight-line graph lnβ $/T^2{}_{\alpha i}$ against $1/T_{\alpha i}$.

3. Tang method [34].

$$ln\left(\beta / T^{1.894661}{}_{\alpha i}\right) = ln\left(AE_a / Rg(\alpha)\right) + 3.635041 - 1.894661 ln\, E_a - 1.00145033 E_a / RT_{\alpha i} \quad (10)$$

E_a can be obtained from the slope of the straight-line graph ln (β/T$^{1.894661}{}_{\alpha i}$) against $1/T_{\alpha i}$.

4. Starink method [29].

$$ln\beta / T^{1.95}{}_{\alpha i} = C^{1.95}(\alpha) - E_a / RT_{\alpha i} \quad (11)$$

$$ln\beta / T^{1.92}{}_{\alpha i} = C^{1.92}(\alpha) - 1.0008 E_a / RT_{\alpha i} \quad (12)$$

5. Boswell method

$$ln\beta / T_{\alpha i} = C(\alpha) - E_a / RT_{\alpha i} \quad (13)$$

3.3.3.1.1. Kinetic analysis of DSC data

The conversion function, α in the range 0.05-1.0 with an interval of 0.05, and their corresponding temperatures are calculated from the experimental heat flow data obtained from DSC. The α-T plots for the dehydration and decomposition reactions of zinc oxalate and cerium added zinc oxalates are shown in **Figs. 12** and **13** respectively. The α-T plots for dehydration reactions for all the samples are almost similar, but for the decomposition reaction, a shift in pattern is observed and this change in the pattern becomes more apparent with a rise in cerium loading.

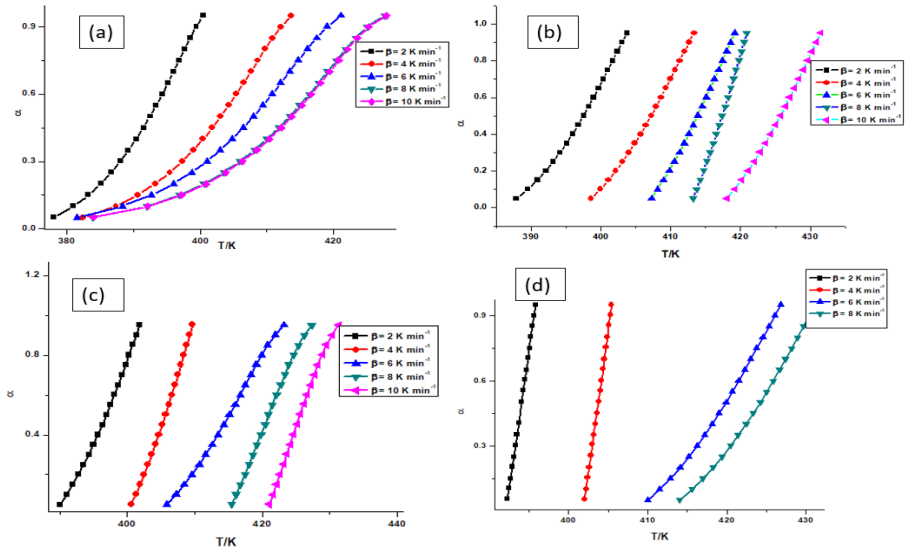

Fig. 12 *α-T* plots for the dehydration stage of ZnOx (a), 0.1 mol% Ce-ZnOx (b), 1 mol% Ce-ZnOx (c) and 5 mol% Ce-ZnOx (d)

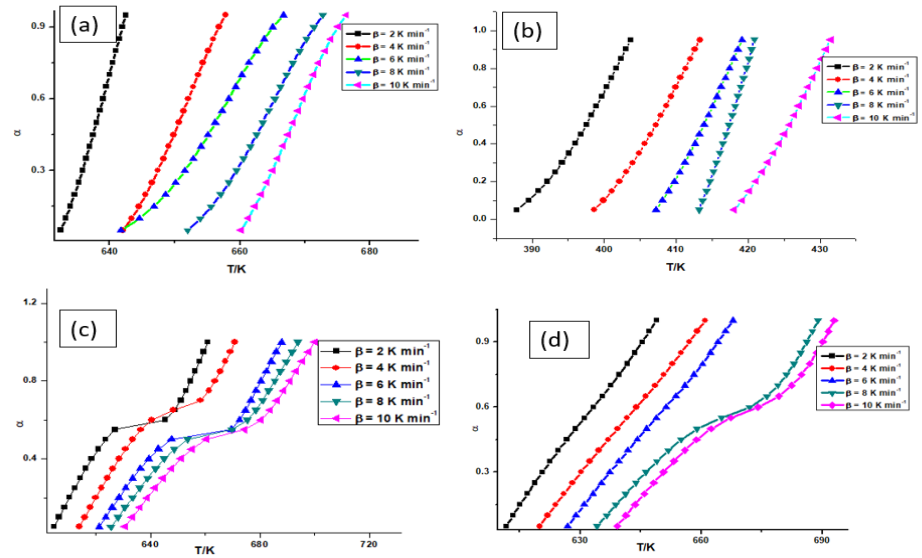

Fig. 13. *α-T* plots for the decomposition stage of ZnOx (a), 0.1 mol% Ce-ZnOx (b), 1 mol% Ce-ZnOx (c) and 5 mol% Ce-ZnOx (d)

This α-T data were subjected to linear least squares analysis using various model-free isoconversional methods like FWO, KAS, Tang, Starink[1.92], Starink[1.95,] and Boswell. The linear least squares analysis plots for the dehydration and decomposition reactions of ZnOx and Ce-ZnOx are shown in the **Figs. 14-21**. All the linear least squares plots give good linearity with R^2 greater than 0.95. The activation energy values were evaluated from the slope of the linear least squares plots. The fluctuations in activation energy with α for dehydration and decomposition reactions showed that they follow complex reaction pathways.

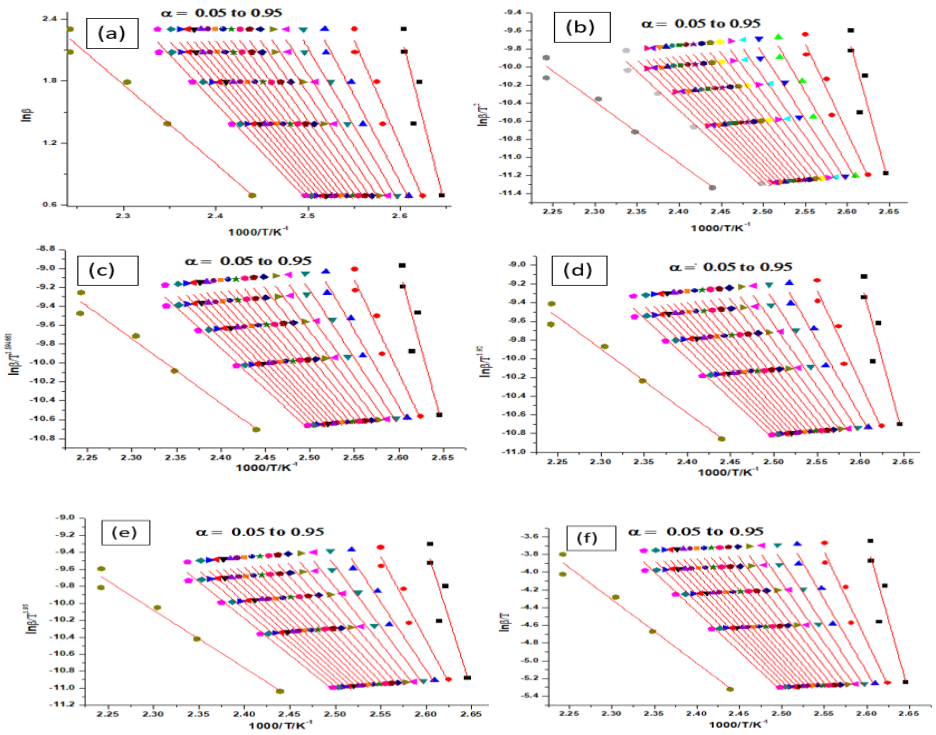

Fig. 14 Linear least squares plot for the dehydration stage of ZnOx for the isoconversional methods of FWO (a), KAS (b), Tang (c), Starink[1.92] (d), Starink[1.95] (e) and Boswell (f) from DSC data

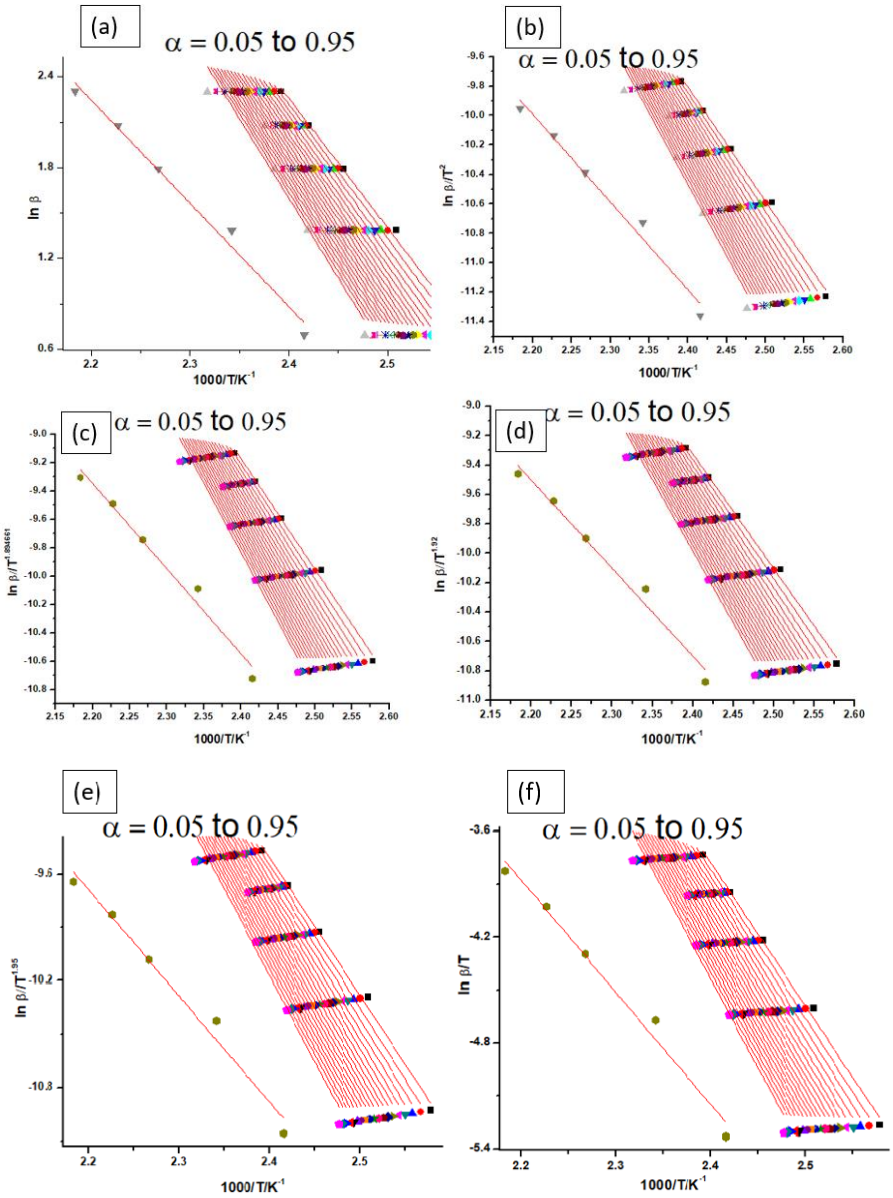

Fig. 15 Linear least squares plot for the dehydration stage of 0.1 mol% Ce-ZnOx for the isoconversional methods of FWO (a), KAS (b), Tang (c), Starink$^{1.92}$ (d), Starink$^{1.95}$ (e) and Boswell (f) from DSC data

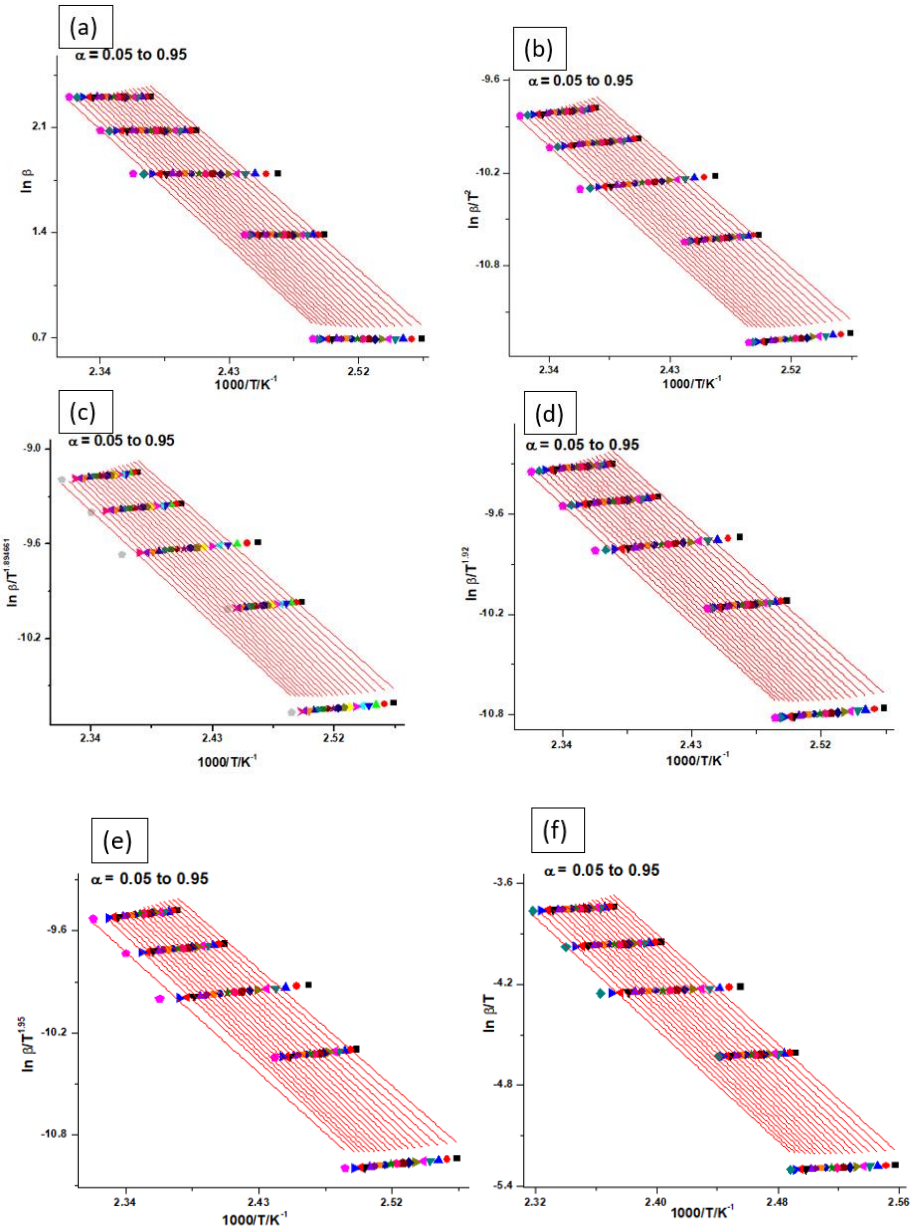

Fig. 16 Linear least squares plot for the dehydration stage of 1 mol% Ce-ZnOx for the isoconversional methods of FWO (a), KAS (b), Tang (c), Starink$^{1.92}$ (d), Starink$^{1.95}$ (e) and Boswell (f) from DSC data

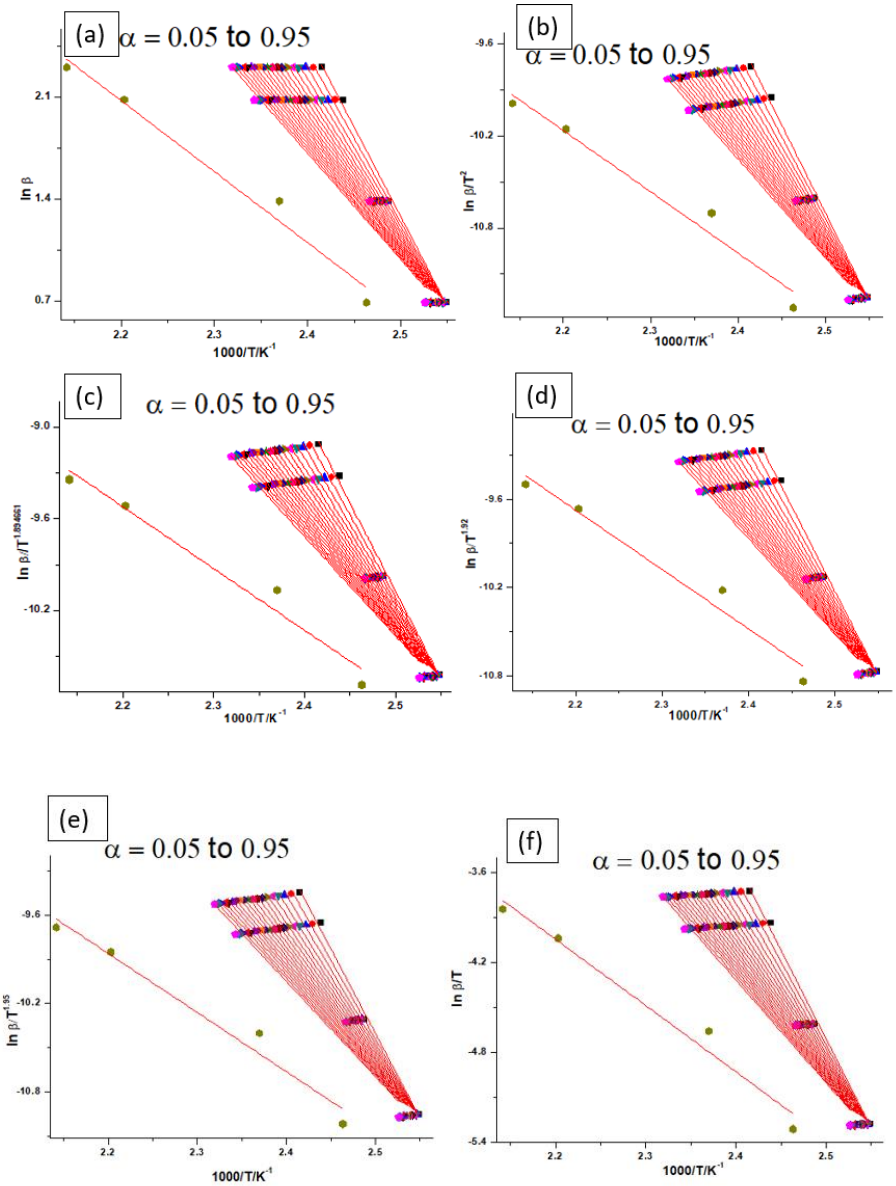

Fig. 17 Linear least squares plot for the dehydration stage of 5 mol% Ce-ZnOx for the isoconversional methods of FWO (a), KAS (b), Tang (c), Starink$^{1.92}$ (d), Starink$^{1.95}$ (e) and Boswell (f) from DSC data

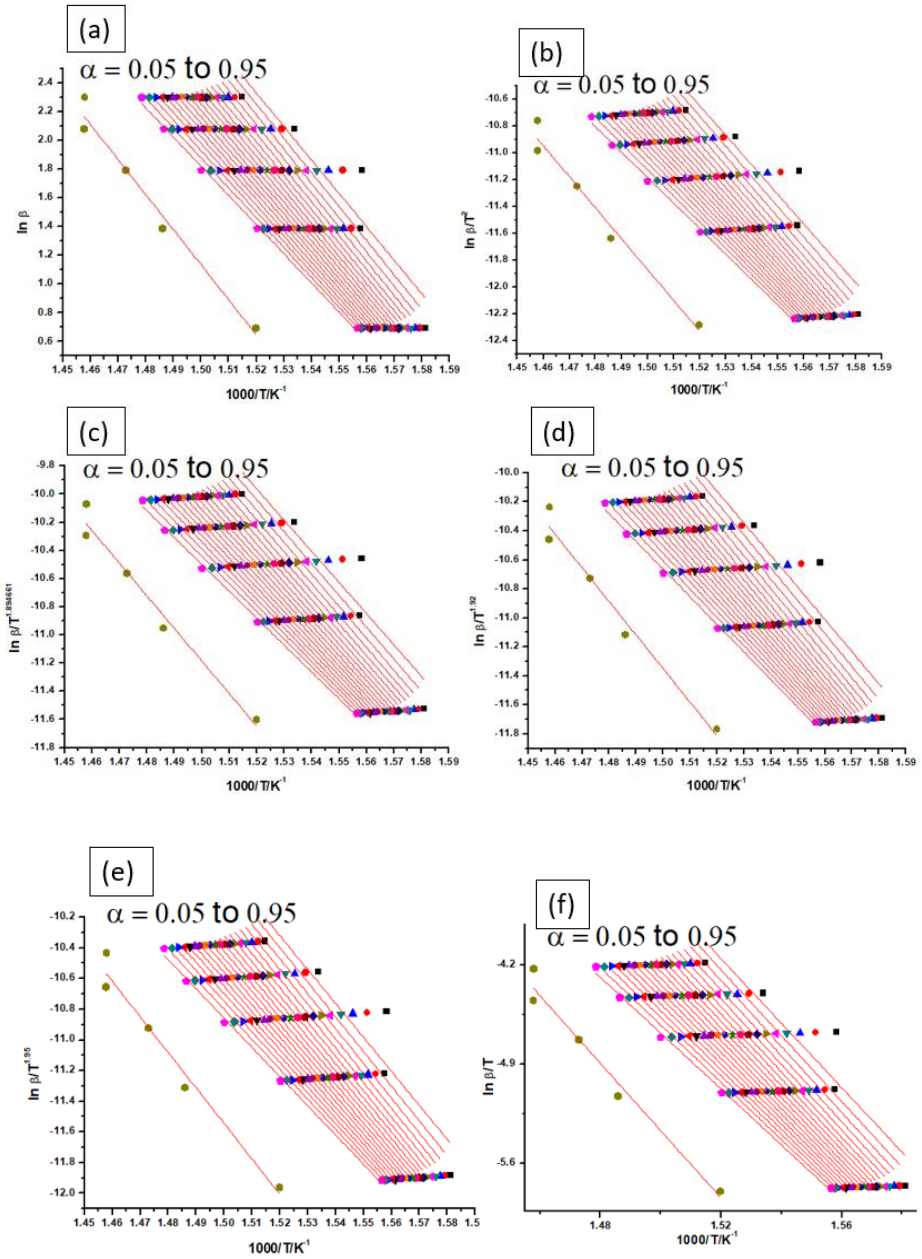

Fig. 18 Linear least squares plot for the decomposition stage of ZnOx for the isoconversional methods of FWO (a), KAS (b), Tang (c), Starink$^{1.92}$ (d), Starink$^{1.95}$ (e) and Boswell (f) from DSC data

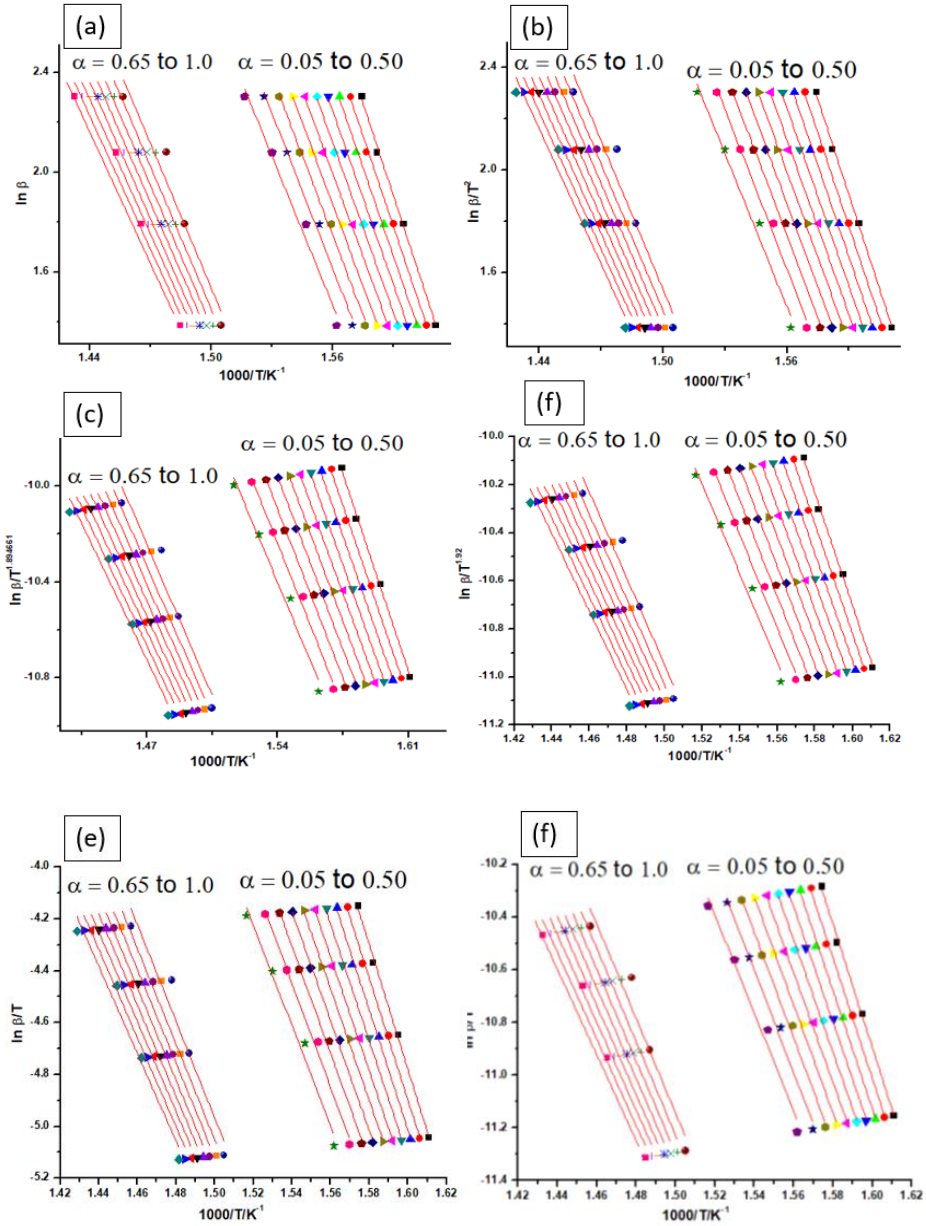

Fig. 19 Linear least squares plot for the decomposition stage of 0.1 mol% Ce-ZnOx for the isoconversional methods of FWO (a), KAS (b), Tang (c), Starink$^{1.92}$ (d), Starink$^{1.95}$ (e) and Boswell (f) from DSC data

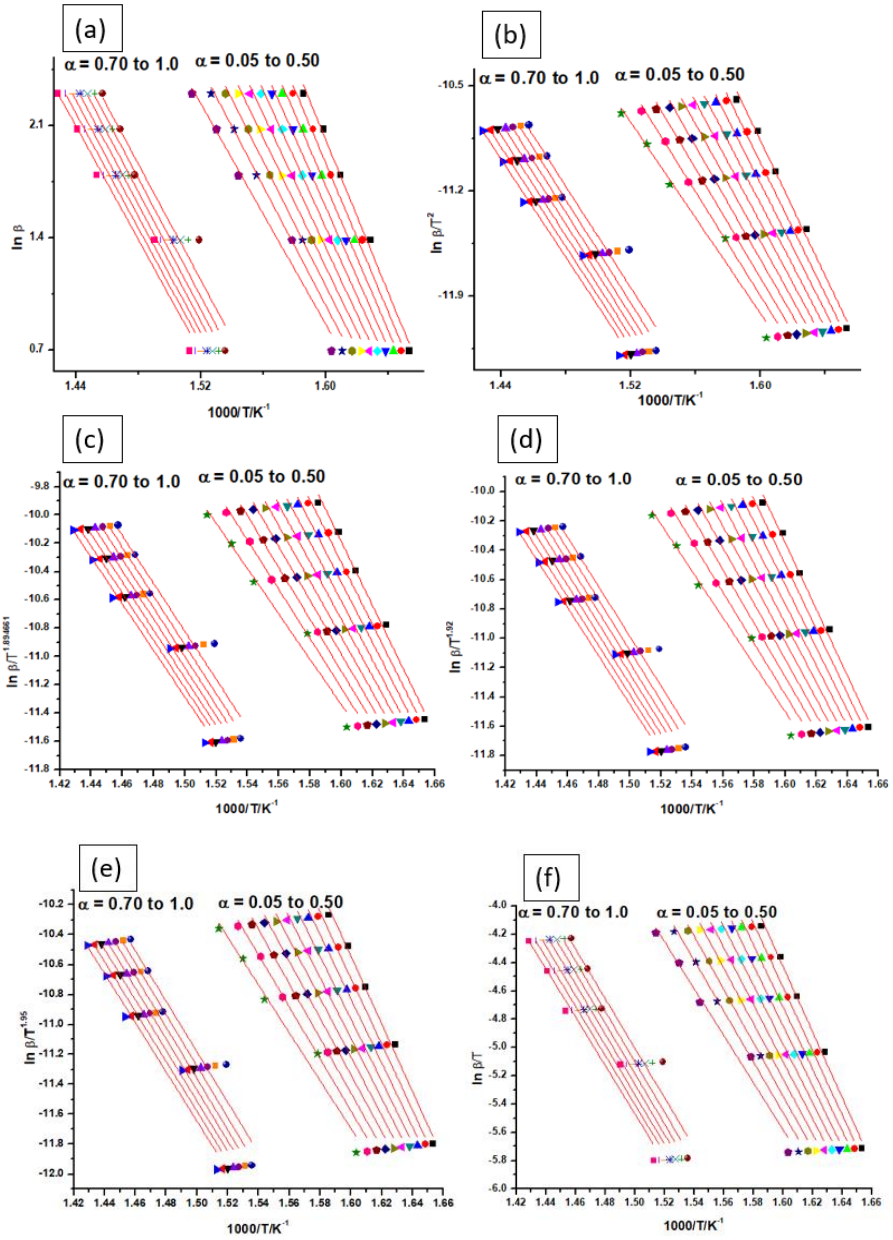

Fig. 20 Linear least squares plot for the decomposition stage of 1 mol% Ce-ZnOx for the isoconversional methods of FWO (a), KAS (b), Tang (c), Starink$^{1.92}$ (d), Starink$^{1.95}$ (e) and Boswell (f) from DSC data

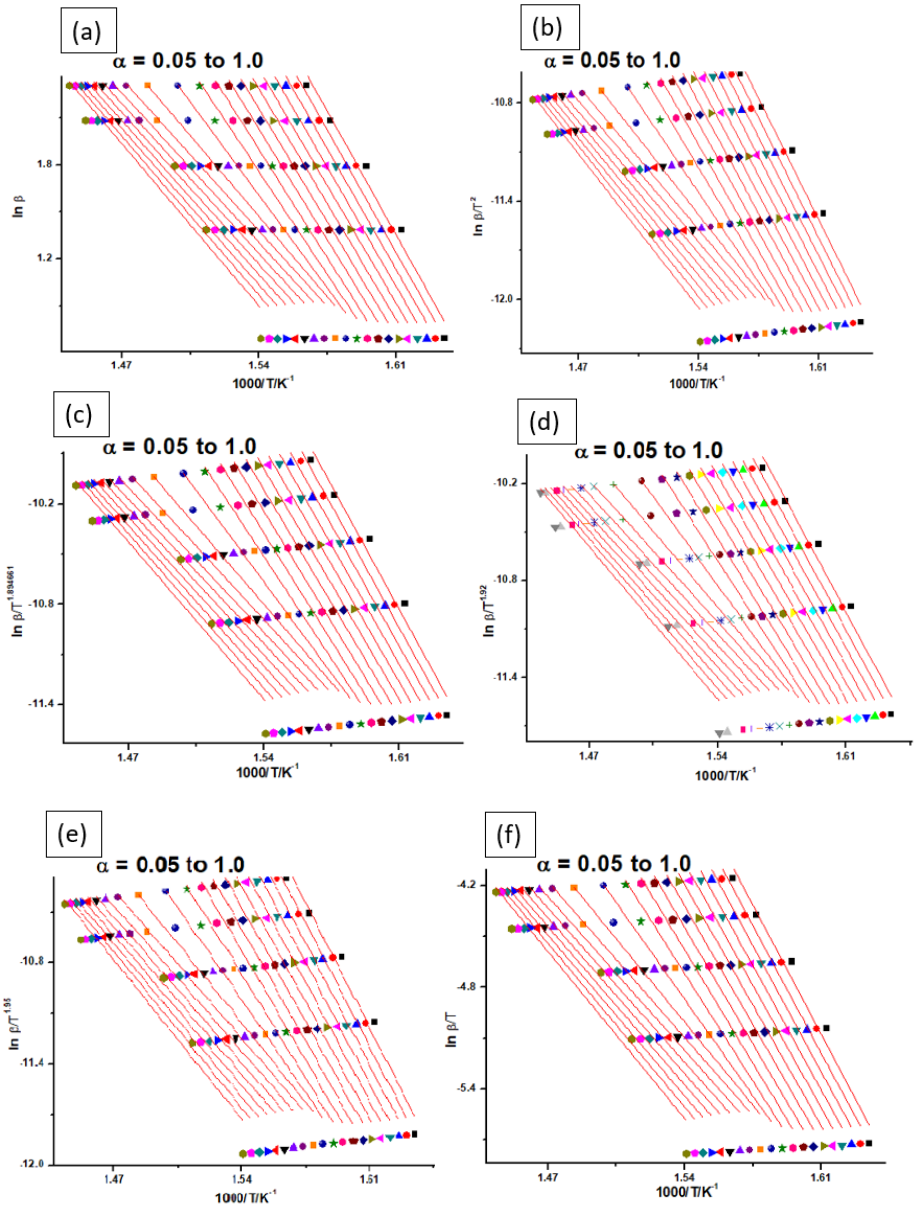

Fig. 21 Linear least squares plot for the decomposition stage of 5 mol% Ce-ZnOx for the isoconversional methods of FWO (a), KAS (b), Tang (c), Starink$^{1.92}$ (d), Starink$^{1.95}$ (e) and Boswell (f) from DSC data

The activation energy needed for the dehydration and decomposition reaction of ZnOx and Ce-ZnOx obtained through the isoconversional methods FWO, KAS, Tang, Starink$^{1.95}$, Starink$^{1.92,}$ and Boswell are given in **Tables 1-8**.

Table 1 Activation energy in kJ mol^{-1} for the dehydration reaction of $ZnOx.2H_2O$ from DSC data

α	FWO	KAS	Tang	Starink$^{1.92}$	Starink$^{1.95}$	Boswell
0.10	162.18	164.19	164.29	164.32	164.35	167.40
0.15	132.79	133.21	133.36	133.36	133.37	136.45
0.20	118.87	118.51	118.69	118.68	118.68	121.78
0.25	110.31	109.47	109.66	109.65	109.64	112.76
0.30	104.52	103.35	103.55	103.53	103.51	106.65
0.35	100.16	98.73	98.94	98.92	98.90	102.05
0.40	96.99	95.38	95.59	95.57	95.55	98.71
0.45	94.35	92.57	92.79	92.77	92.74	95.91
0.50	92.11	90.20	90.42	90.39	90.37	93.55
0.55	90.18	88.15	88.38	88.35	88.32	91.51
0.60	88.47	86.33	86.56	86.53	86.50	89.70
0.65	86.93	84.69	84.92	84.89	84.86	88.07
0.70	85.32	82.98	83.21	83.18	83.15	86.37
0.75	83.83	81.39	81.63	81.60	81.56	84.79
0.80	82.42	79.89	80.13	80.10	80.06	83.30
0.85	80.58	77.93	78.18	78.15	78.11	81.35
0.90	78.40	75.62	75.87	75.83	75.79	79.05
0.95	74.42	71.40	71.66	71.62	71.57	74.84
1.00	60.36	56.38	56.67	56.62	56.56	59.94
Av	**95.96**	**94.23**	**94.45**	**94.42**	**94.40**	**97.59**

Av is the average value

Table 2 Activation energy in kJ mol^{-1} for the dehydration reaction of 0.1 mol% Ce-ZnOx.$2H_2O$ from DSC data

α	FWO	KAS	Tang	Starink$^{1.92}$	Starink$^{1.95}$	Boswell
0.05	67.67	64.50	64.76	64.71	64.66	67.84
0.10	70.06	66.99	67.25	67.21	67.16	70.35
0.15	71.91	68.92	69.17	69.13	69.09	72.29
0.20	73.37	70.44	70.69	70.65	70.60	73.81
0.25	74.65	71.76	72.01	71.98	71.93	75.15
0.30	75.73	72.88	73.13	73.10	73.05	76.27
0.35	76.66	73.85	74.10	74.06	74.02	77.25
0.40	77.49	74.71	74.96	74.92	74.88	78.11
0.45	78.12	75.36	75.61	75.58	75.53	78.77
0.50	78.90	76.16	76.41	76.38	76.33	79.58
0.55	79.42	76.70	76.95	76.91	76.87	80.12
0.60	80.00	77.30	77.55	77.51	77.47	80.73
0.65	80.49	77.81	78.05	78.02	77.98	81.24
0.70	81.03	78.37	78.62	78.58	78.54	81.81
0.75	81.47	78.82	79.06	79.03	78.99	82.26
0.80	81.91	79.26	79.51	79.48	79.44	82.71
0.85	82.43	79.81	80.05	80.02	79.98	83.26
0.90	82.87	80.25	80.50	80.47	80.43	83.72
0.95	83.34	80.74	80.99	80.95	80.91	84.21
1.00	53.94	49.51	49.82	49.76	49.69	53.13
Av	**76.57**	**73.71**	**73.96**	**73.92**	**73.88**	**77.13**

Av is the average value

Table 3 Activation energy in kJ mol^{-1} for the dehydration reaction of 1 mol% Ce-ZnOx.$2H_2O$ from DSC data

α	FWO	KAS	Tang	Starink$^{1.92}$	Starink$^{1.95}$	Boswell
0.05	66.65	63.37	63.64	63.59	63.54	66.74
0.10	67.88	64.66	64.92	64.88	64.83	68.04
0.15	69.00	65.82	66.08	66.04	65.99	69.20
0.20	69.86	66.72	66.98	66.94	66.89	70.11
0.25	70.56	67.45	67.70	67.66	67.61	70.84
0.30	71.17	68.08	68.34	68.30	68.25	71.48
0.35	71.66	68.59	68.84	68.80	68.76	71.99
0.40	72.04	68.97	69.23	69.19	69.14	72.38
0.45	72.40	69.34	69.60	69.56	69.51	72.75
0.50	72.64	69.59	69.85	69.80	69.76	73.00
0.55	72.78	69.73	69.99	69.95	69.91	73.15
0.60	72.92	69.86	70.12	70.08	70.02	73.28
0.65	72.87	69.80	70.06	70.02	69.96	73.23
0.70	72.78	69.70	69.96	69.92	69.85	73.13
0.75	72.55	69.44	69.70	69.66	69.57	72.88
0.80	72.09	68.96	69.22	69.18	69.08	72.40
0.85	71.61	68.44	68.70	68.66	68.51	71.89
0.90	70.59	67.35	67.62	67.57	74.26	70.80
0.95	68.91	65.57	65.84	65.79	65.74	69.03
Av	**71.10**	**67.97**	**68.23**	**71.30**	**68.48**	**71.39**

Av is the average value

Table 4 Activation energy in kJ mol^{-1} for the dehydration reaction of 5 mol% Ce-ZnOx.$2H_2O$ from DSC data

α	FWO	KAS	Tang	Starink$^{1.92}$	Starink$^{1.95}$	Boswell
0.05	96.99	95.34	95.55	95.53	95.51	98.69
0.10	91.00	89.01	89.24	89.21	89.18	92.37
0.15	86.23	83.99	84.22	84.19	84.15	87.35
0.20	82.43	79.97	80.21	80.18	80.14	83.34
0.25	79.20	76.56	76.81	76.77	76.73	79.94
0.30	76.53	73.75	73.99	73.96	73.91	77.13
0.35	74.08	71.16	71.41	71.37	71.33	74.54
0.40	72.01	68.97	69.23	69.19	69.14	72.36
0.45	70.15	67.01	67.27	67.23	67.18	70.41
0.50	68.46	65.22	65.48	65.44	65.39	68.62
0.55	66.95	63.62	63.88	63.84	63.79	67.02
0.60	65.52	62.11	62.38	62.33	62.28	65.52
0.65	64.14	60.65	60.92	60.87	60.82	64.06
0.70	62.94	59.38	59.65	59.60	59.55	62.79
0.75	61.79	58.16	58.44	58.39	58.33	61.58
0.80	60.65	56.95	57.23	57.18	57.13	60.38
0.85	59.58	55.82	56.10	56.05	55.99	59.25
0.90	58.53	54.71	54.99	54.94	54.88	58.15
0.95	57.53	53.65	53.93	53.88	53.82	57.08
1.00	38.43	33.19	33.53	33.46	33.37	36.81
Av	**69.66**	**66.46**	**66.72**	**66.68**	**66.63**	**69.87**

Av is the average value

Table 5 Activation energy in kJ mol^{-1} for the decomposition reaction of $ZnOx.2H_2O$ from DSC data

α	FWO	KAS	Tang	Starink$^{1.92}$	Starink$^{1.95}$	Boswell
0.15	189.18	188.24	188.54	188.52	188.51	193.63
0.20	188.66	187.69	187.98	187.97	187.96	193.08
0.25	187.93	186.90	187.20	187.18	187.17	192.30
0.30	186.72	185.62	185.92	185.90	185.89	191.02
0.35	185.53	184.35	184.65	184.64	184.62	189.76
0.40	184.05	182.79	183.09	183.07	183.06	188.20
0.45	182.56	181.22	181.52	181.50	181.49	186.64
0.50	181.18	179.75	180.06	180.04	180.02	185.17
0.55	179.64	178.12	178.43	178.41	178.39	183.55
0.60	178.07	176.46	176.77	176.75	176.73	181.89
0.65	176.28	174.57	174.89	174.86	174.84	180.01
0.70	174.50	172.68	173.00	172.97	172.95	178.12
0.75	172.65	170.72	171.05	171.02	170.99	176.17
0.80	170.35	168.29	168.63	168.60	168.57	173.75
0.85	167.79	165.58	165.92	165.89	165.86	171.05
0.90	164.67	162.30	162.64	162.60	162.57	167.77
0.95	160.74	158.14	158.49	158.46	158.42	163.62
1.00	192.88	191.74	192.05	192.03	192.02	197.33
Av	**179.08**	**177.51**	**177.82**	**177.80**	**177.78**	**182.95**

Av is the average value

Table 6 Activation energy in kJ mol^{-1} for the decomposition reaction of 0.1 mol% Ce-ZnOx.$2H_2O$ from DSC data

α	FWO	KAS	Tang	Starink$^{1.92}$	Starink$^{1.95}$	Boswell
0.05	195.05	205.19	195.02	195.01	195.01	199.97
0.10	190.87	200.79	190.59	190.58	190.58	195.55
0.15	186.98	196.70	186.48	186.47	186.46	191.45
0.20	182.90	192.42	182.17	182.15	182.14	187.14
0.25	179.16	188.48	178.20	178.18	178.17	183.19
0.30	175.21	184.32	174.02	174.00	173.98	179.02
0.35	172.10	181.04	170.71	170.68	170.66	175.72
0.40	168.40	177.16	166.78	166.76	166.73	171.81
0.45	164.09	172.63	162.22	162.18	162.15	167.26
0.50	157.19	165.37	154.91	154.87	154.83	159.96
0.65	152.35	160.27	149.41	149.37	149.32	154.65
0.70	150.54	158.37	147.49	147.44	147.39	152.74
0.75	148.24	155.94	145.04	144.99	144.93	150.30
0.80	146.40	154.02	143.08	143.03	142.98	148.36
0.85	144.35	151.86	140.90	140.85	140.79	146.18
0.90	142.39	149.79	138.81	138.76	138.70	144.10
0.95	140.63	147.94	136.94	136.89	136.83	142.24
1.00	138.92	146.15	135.13	135.07	135.01	140.43
Av	**163.10**	**171.58**	**160.99**	**160.96**	**160.93**	**166.12**

Av is the average value

Table 7 Activation energy in kJ mol^{-1} for the decomposition reaction of 1 mol% Ce-ZnOx.$2H_2O$ from DSC data

α	FWO	KAS	Tang	Starink$^{1.92}$	Starink$^{1.95}$	Boswell
0.05	188.49	188.02	188.29	188.28	188.28	193.16
0.10	183.47	182.70	182.98	182.97	182.96	187.85
0.15	178.62	177.57	177.86	177.84	177.83	182.74
0.20	173.97	172.64	172.93	172.91	172.90	177.83
0.25	169.21	167.59	167.89	167.87	167.85	172.80
0.30	164.60	162.70	163.02	162.99	162.97	167.93
0.35	159.53	157.33	157.65	157.62	157.59	162.58
0.40	153.94	151.40	151.73	151.70	151.66	156.67
0.45	147.07	144.11	144.46	144.42	144.38	149.41
0.50	136.20	132.61	132.98	132.93	132.88	137.95
0.70	143.61	139.97	140.35	140.31	140.25	145.53
0.75	146.17	142.63	143.01	142.96	142.91	148.20
0.80	146.13	142.55	142.93	142.89	142.83	148.14
0.85	145.13	141.46	141.85	141.80	141.74	147.07
0.90	143.82	140.06	140.44	140.39	140.34	145.68
0.95	142.10	138.22	138.61	138.56	138.50	143.86
1.00	140.31	136.30	136.70	136.64	136.58	141.95
Av	**156.61**	**153.99**	**154.34**	**154.30**	**154.26**	**159.37**

Av is the average value

Table 8 Activation energy in kJ mol^{-1} for the decomposition reaction of 5 mol% Ce-ZnOx.$2H_2O$ from DSC data

α	FWO	KAS	Tang	Starink$^{1.92}$	Starink$^{1.95}$	Boswell
0.05	176.79	175.58	175.25	103.91	175.84	180.78
0.10	174.83	173.49	173.17	105.50	173.75	178.71
0.15	172.61	171.12	170.81	107.40	171.38	176.35
0.20	170.53	168.91	168.61	109.49	169.17	174.15
0.25	168.12	166.33	166.05	111.70	166.59	171.60
0.30	165.68	163.73	163.46	175.86	163.99	169.01
0.35	163.07	160.95	160.69	173.77	161.21	166.25
0.40	160.04	157.71	157.48	171.40	157.98	163.04
0.45	155.93	153.35	153.14	169.19	153.61	158.69
0.50	148.44	145.42	145.25	166.62	145.69	150.79
0.55	133.55	129.69	129.61	164.02	129.96	135.09
0.60	115.89	111.02	111.04	161.24	111.30	116.47
0.65	109.07	103.80	103.85	158.01	104.07	109.27
0.70	107.53	102.13	102.20	153.65	102.41	107.63
0.75	107.78	102.36	102.42	145.73	102.64	107.87
0.80	108.94	103.55	103.61	130.02	103.82	109.08
0.85	110.48	105.14	105.20	111.37	105.42	110.69
0.90	112.32	107.04	107.09	104.15	107.32	112.60
0.95	114.33	109.13	109.16	102.49	109.41	114.70
1.00	116.45	111.34	111.37	102.72	111.62	116.92
Av	**139.62**	**136.09**	**135.97**	**136.41**	**137.66**	**141.48**

Av is the average value

The E_a *vs* α curves for the dehydration reaction of ZnOx and Ce-ZnOx of various Ce concentrations from the DSC data are shown in **Fig. 22**. From the E_a *vs* α curves, it is very clear that the activation energy is continuously changing with α, which reflects the complexity of the reaction. The pattern in which E_a varies with α is different for each sample which implies that different mechanism operates in each sample. The activation energy is continuously decreasing with α for ZnOx. This

implies that the nucleation and growth in solid requires high activation energy, once the reaction starts, which means after the completion of nucleation and its growth, the reaction continues with low activation energy.

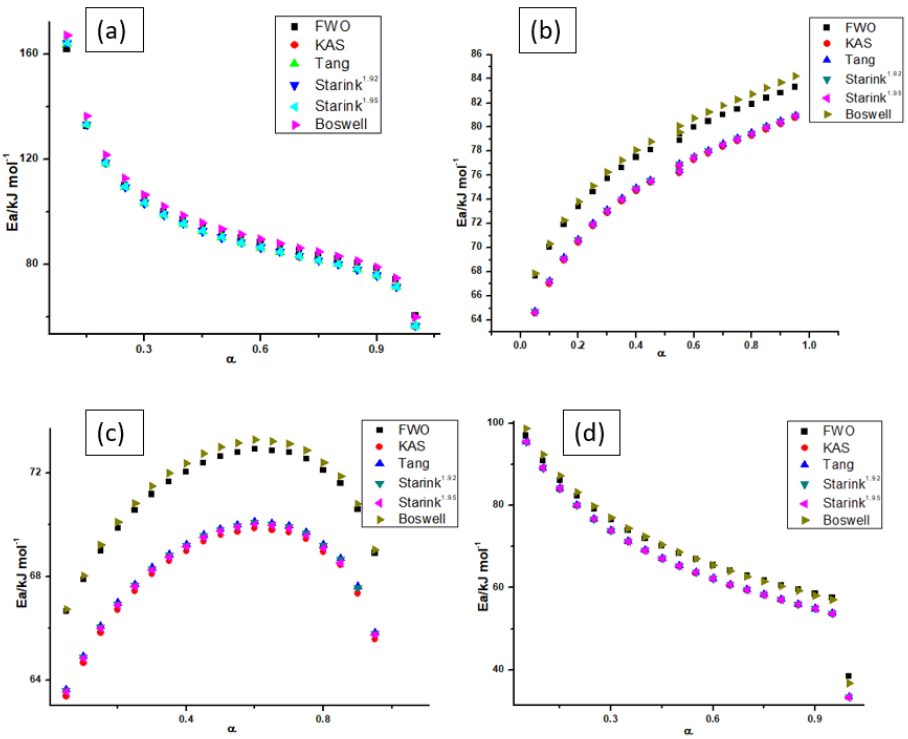

Fig. 22 *E_a vs α* curves for the dehydration stage of ZnOx (a), 0.1 mol% Ce-ZnOx (b), 1 mol% Ce-ZnOx (c) and 5 mol% Ce-ZnOx (d) from DSC data

A similar trend is observed for 5 mol% Ce-ZnOx sample. For 0.1 mol% Ce-ZnOx sample, the activation energy value keeps on increasing with α, and in 1 mol% Ce-ZnOx sample the values of E_a continuously increasing up to 50% conversion, after that it is decreasing.

Fig. 23 shows the variation of activation energy with α for the decomposition reaction of ZnOx and Ce-ZnOx samples. The values of E_a decreasing continuously as the conversion function increases.

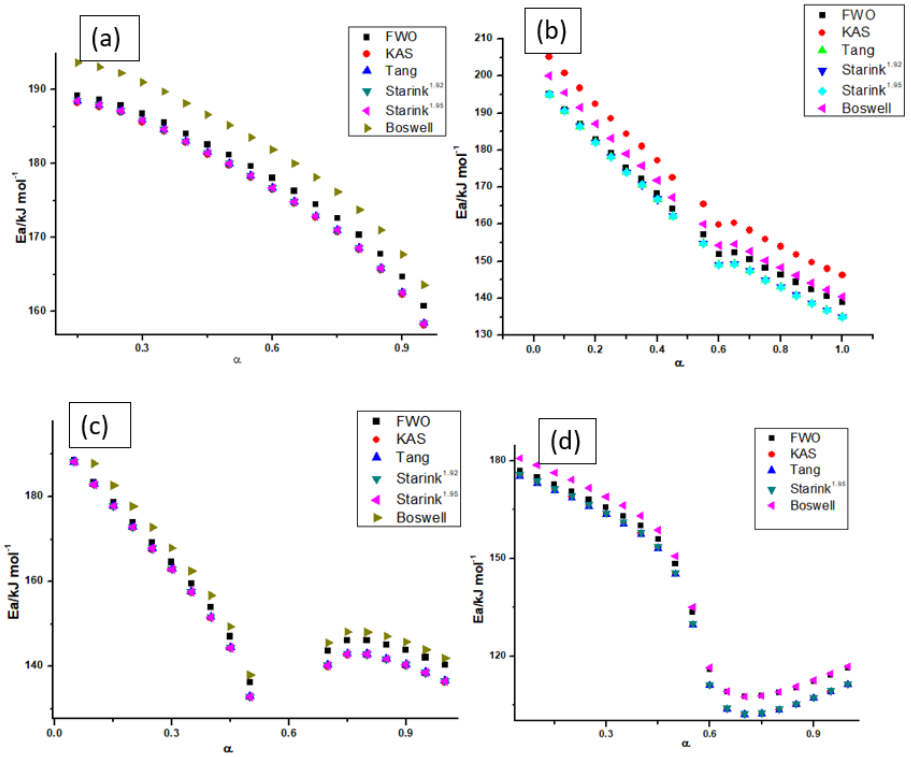

Fig. 23 E_a *vs* alpha curves for the decomposition stage of ZnOx (a), 0.1 mol% Ce-ZnOx (b), 1 mol% Ce-ZnOx (c) and 5 mol% Ce-ZnOx (d) from DSC data

Although all of them show similar trend *i.e.*, a decrease in E_a, the Ce-ZnOx samples show a small increase at around 60% conversion and then decreases. This fluctuation is more visible with an increase in Ce ion concentration which indicates that it is an aftereffect of Ce doping. All the studied samples require a higher value of E_a at the

commencement of decomposition, this may be due to the necessity of higher activation energy for the nucleation and the subsequent growth of the nuclei. Once the decay starts, the reaction requires lesser E_a until the end.

The average values for dehydration and decomposition reactions from the DSC data are given in **Tables 9 and 10** respectively.

Table 9 Summary of E_a values in kJ mol^{-1} for the dehydration reaction from DSC data

Isoconversional method	Pure ZnOx	0.1 mol% Ce-ZnOx	1 mol% Ce-ZnOx	5 mol% Ce-ZnOx
FWO	95.96	76.57	71.10	69.66
KAS	94.23	73.71	67.97	66.46
Tang	94.45	73.96	68.23	66.72
Starink$^{1.92}$	94.42	73.92	71.30	66.68
Starink$^{1.95}$	94.40	73.88	68.48	66.63
Boswell	97.59	77.13	71.39	69.87

From **Table 9**, it is observed that the value of activation energy for the dehydration reaction is regularly decreasing with an increase in Ce ion concentration. The value of E_a needed for the dehydration of pure ZnOx is maximum, then for 0.1 mol% Ce-ZnOx, then 1 mol% Ce-ZnOx and least for 5 mol% Ce-ZnOx. The E_a value for pure ZnOx is 95.96 kJ mol^{-1} and it reduces to 69.66 kJ mol^{-1} for 5 mol% Ce-ZnOx (FWO). There is a decrease of 26.3 kJ mol^{-1} in activation energy is observed for the dehydration reaction of ZnOx when 5 mol% Ce is added to it. From all isoconversional methods used for the calculation, the KAS method gives the least value for activation energy and Boswell gives the higher value.

Table 10 Summary of E_a values in kJ $mol^{-1}$for the decomposition reaction from DSC data

Isoconversional method	Pure ZnOx	0.1 mol% Ce-ZnOx	1 mol% Ce-ZnOx	5 mol% Ce-ZnOx
FWO	179.08	163.10	156.61	139.62
KAS	177.51	171.58	153.99	136.09
Tang	177.82	160.99	154.34	135.97
Starink$^{1.92}$	177.80	160.96	154.30	136.41
Starink$^{1.95}$	177.78	160.93	154.26	137.66
Boswell	182.95	166.12	159.37	141.48

Table 10 shows the values of activation energy needed for the decomposition of ZnOx to ZnO in the nitrogen atmosphere. It is interesting to note that the E_a values are markedly decreasing with an increase in Ce ion concentration. As the Ce ion concentration in the lattice of ZnOx increases from 0 to 5 mol%, there is a drop of 39.46 kJ mol^{-1} in the value of E_a for the decomposition reaction (FWO method). The activation energy required for the decomposition of oxalate into its oxide is highest for pure ZnOx, then 0.1 mol% Ce-ZnOx, then 1 mol% Ce-ZnOx and least for 5 mol% Ce-ZnOx. From all the isoconversional methods used for the determination of E_a, Boswell gives the higher values of activation energy for all the samples except 0.1 mol% Ce-ZnOx and the KAS method gives the least value of activation energy for all the samples except 0.1 mol% Ce-ZnOx. For 0.1 mol% Ce-ZnOx sample, the highest value for E_a is obtained for the KAS method, and least for the Starink$^{1.95}$ method.

It can be explained that, while increasing the concentration of

cerium ion to 5 mol%, the excess of cerium ion (*i.e.*, the cerium ion present in an amount larger than the solubility limit required for doping) may also present at the grain boundaries/ surfaces of the parent oxalate, other than creating point defects. At a suitably high temperature, decomposition is initiated by the appropriate bond redistribution process within the imperfect regions. The total energy required for the transition to a new configuration is lowered by the strain energy at the site of imperfection. The reduction in E_a observed while increasing the cerium ion concentration to 5 mol% is due to the imperfections created by the cerium ion at the grain boundaries other than point defects, which together can act as preferred nucleation centers.

3.3.3.1.2. Kinetic analysis of TG data

The conversion function, α in the range 0.05-1.0 with an interval of 0.05, and their respective temperatures are also determined from the mass loss data obtained from TG. The conversion function during thermal decomposition reaction using TG is measured directly from the mass loss data at that time relative to the overall mass loss data when decomposition is complete. The α-T plots for the dehydration and decomposition reactions of zinc oxalate and cerium added zinc oxalates can be seen in **Figs. 24 and 25** respectively.

The α-T plots for the dehydration and decomposition reactions of all the samples are sigmoidal in shape, however, a minor shift in pattern is observed with the loading of cerium. This α-T data were subjected to linear least squares analysis using different model-free

isoconversional methods such as FWO, KAS, Tang, Starink[1.95], Starink[1.92], and Boswell. The linear least squares analysis plots for the dehydration and decomposition reactions of ZnOx and Ce-ZnOx are shown in the **Figs. 26-33**. All the linear least squares plots give good linearity with R^2 greater than 0.95. The activation energy values were evaluated from the slope of the linear least squares plots and it is given in **Tables 11-18**. The fluctuations in E_a with α for dehydration and decomposition reactions showed that they follow complex reaction pathways.

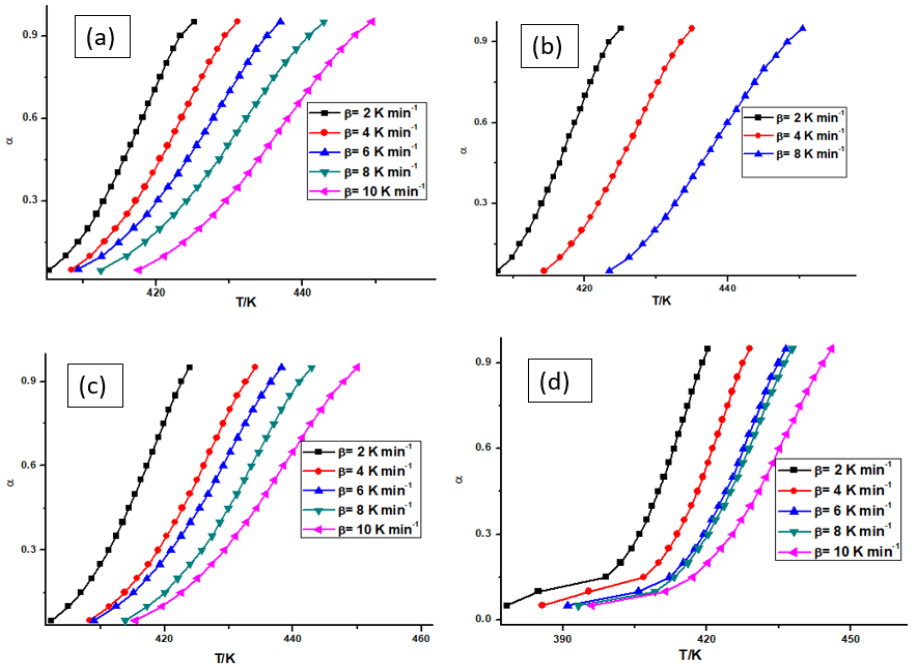

Fig. 24 α-T plots for the dehydration stage of ZnOx (a), 0.1 mol% Ce-ZnOx (b), 1 mol% Ce-ZnOx (c) and 5 mol% Ce-ZnOx (d) from TG data

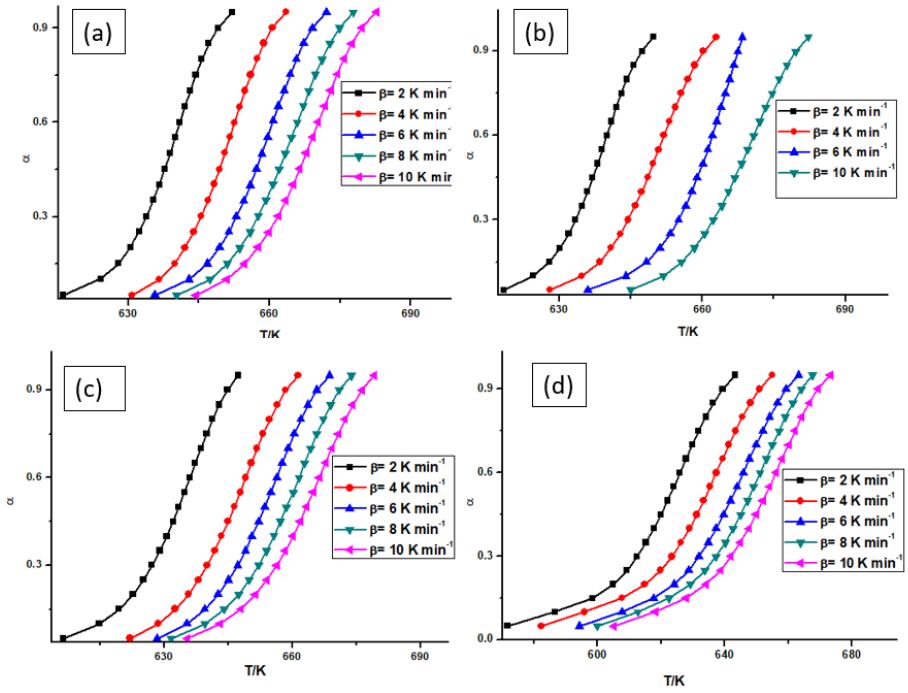

Fig. 25 α-T plots for the decomposition stage of ZnOx (a), 0.1 mol% Ce-ZnOx (b), 1 mol% Ce-ZnOx (c) and 5 mol% Ce-ZnOx (d) from TG data

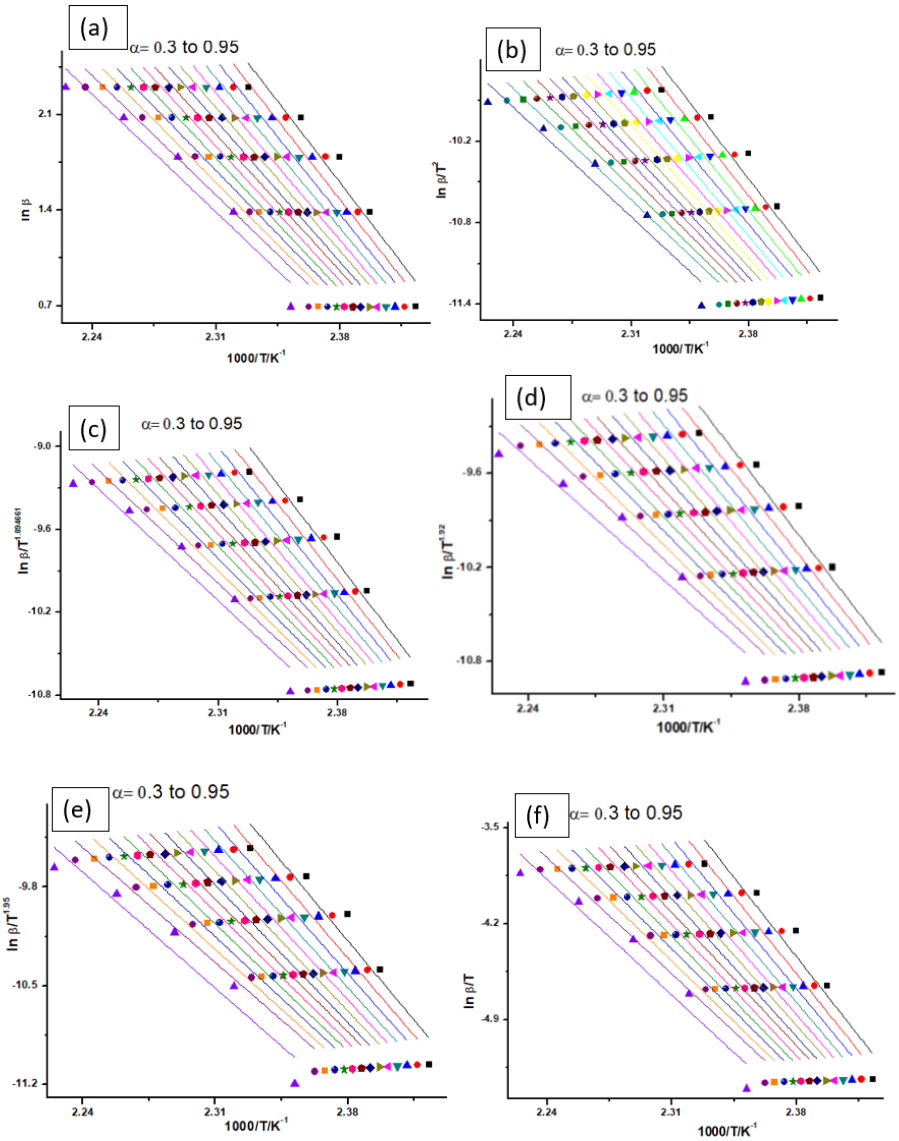

Fig. 26 Linear least squares plot for the dehydration stage of ZnOx for the isoconversional methods of FWO (a), KAS (b), Tang (c), Starink$^{1.92}$ (d), Starink$^{1.95}$ (e) and Boswell (f) from TG data

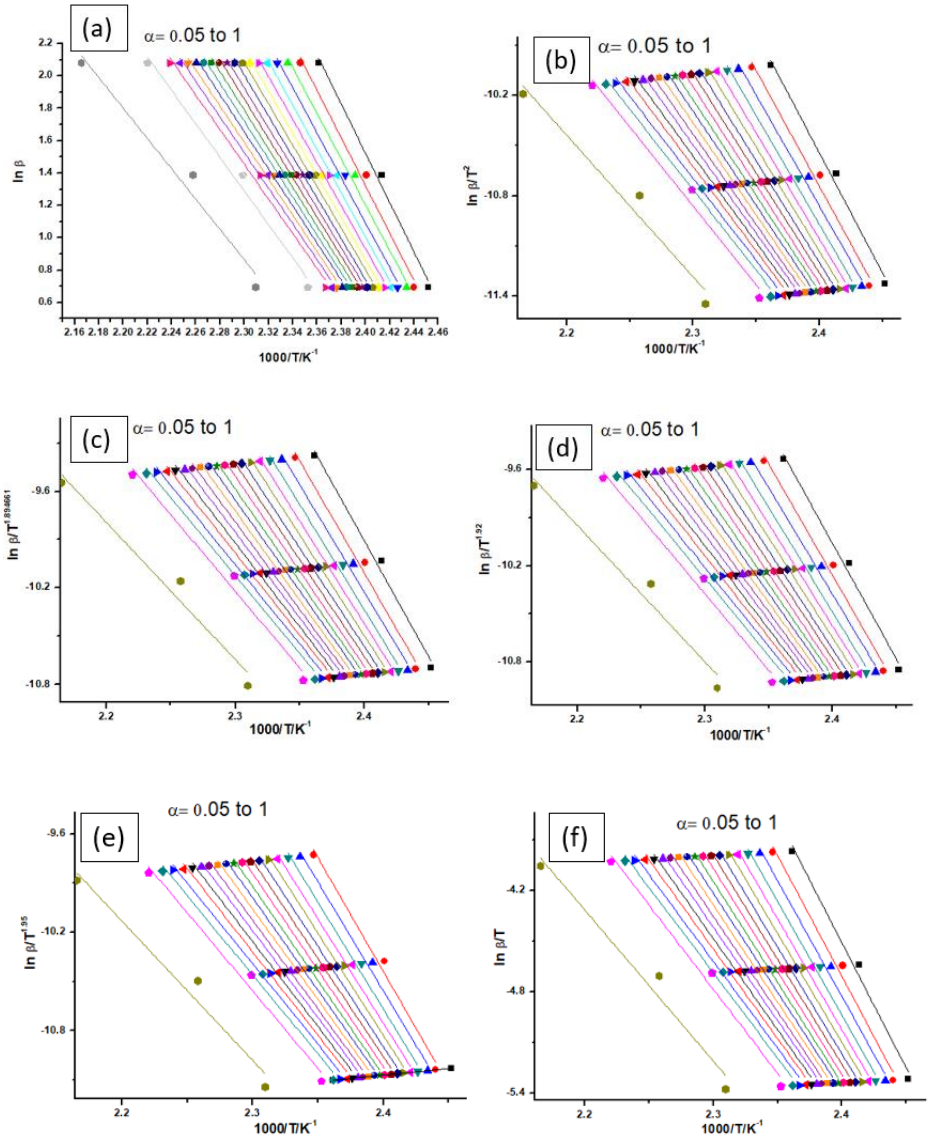

Fig. 27 Linear least squares plot for the dehydration stage of 0.1 mol% Ce-ZnOx for the isoconversional methods of FWO (a), KAS (b), Tang (c), Starink$^{1.92}$ (d), Starink$^{1.95}$ (e) and Boswell (f) from TG data

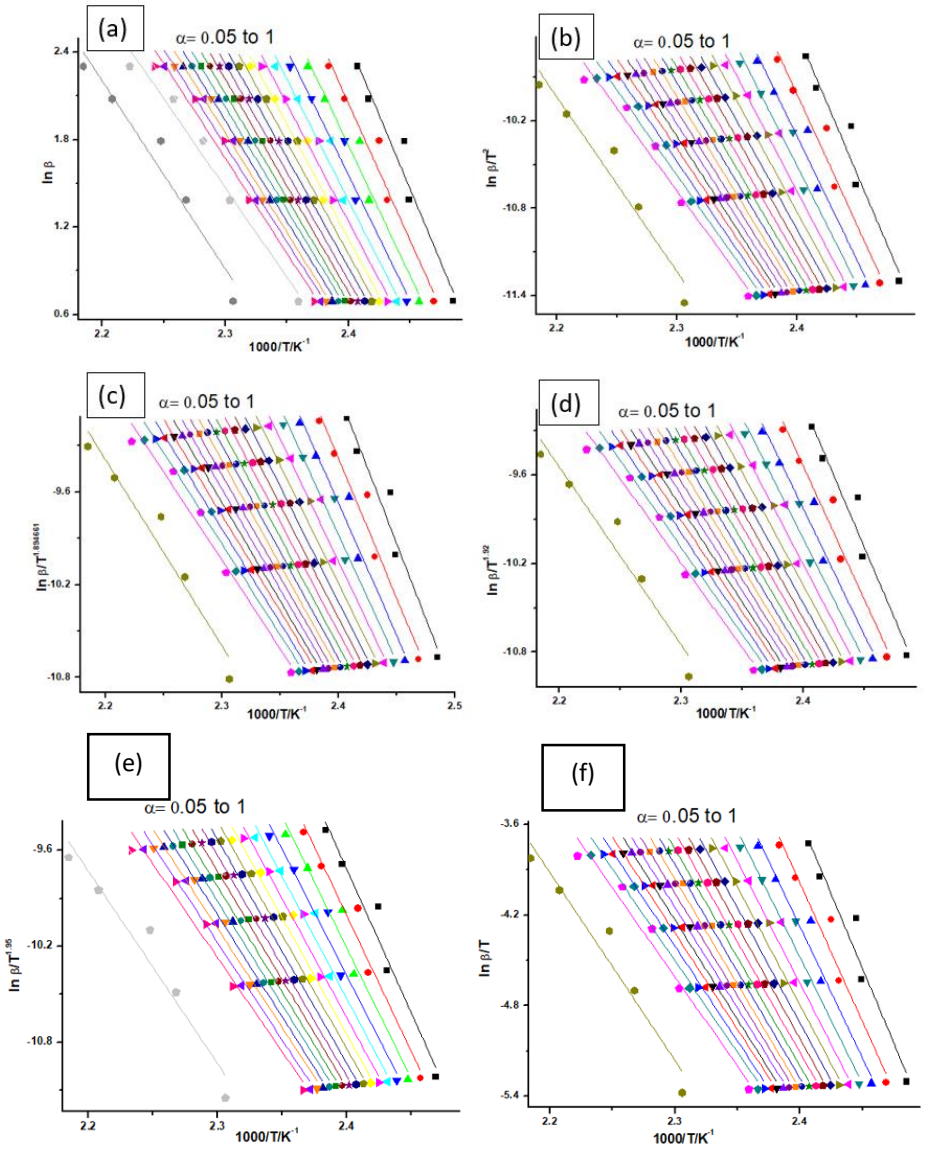

Fig. 28 Linear least squares plot for the dehydration stage of 1 mol% Ce-ZnOx for the isoconversional methods of FWO (a), KAS (b), Tang (c), Starink$^{1.92}$ (d), Starink$^{1.95}$ (e) and Boswell (f) from TG data

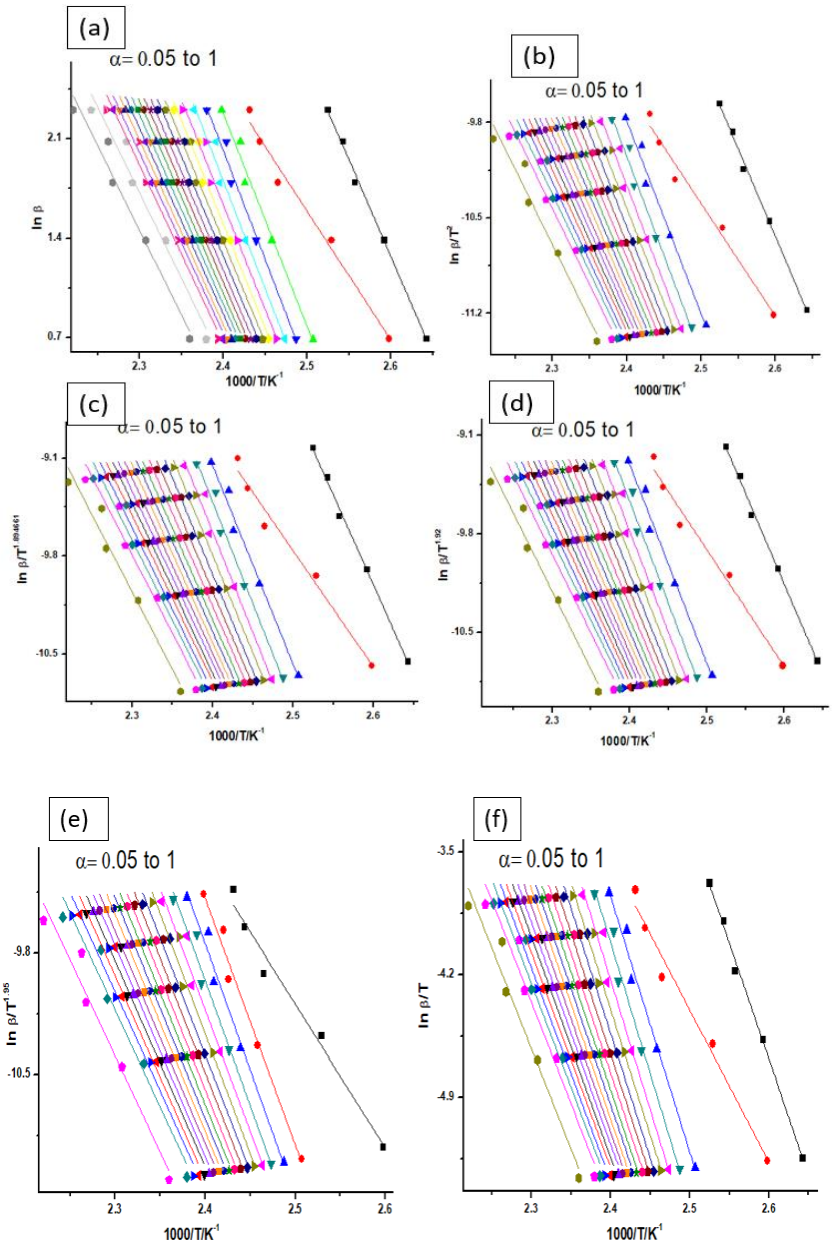

Fig. 29 Linear least squares plot for the dehydration stage of 5 mol% Ce-ZnOx for the isoconversional methods of FWO (a), KAS (b), Tang (c), Starink$^{1.92}$ (d), Starink$^{1.95}$ (e) and Boswell (f) from TG data

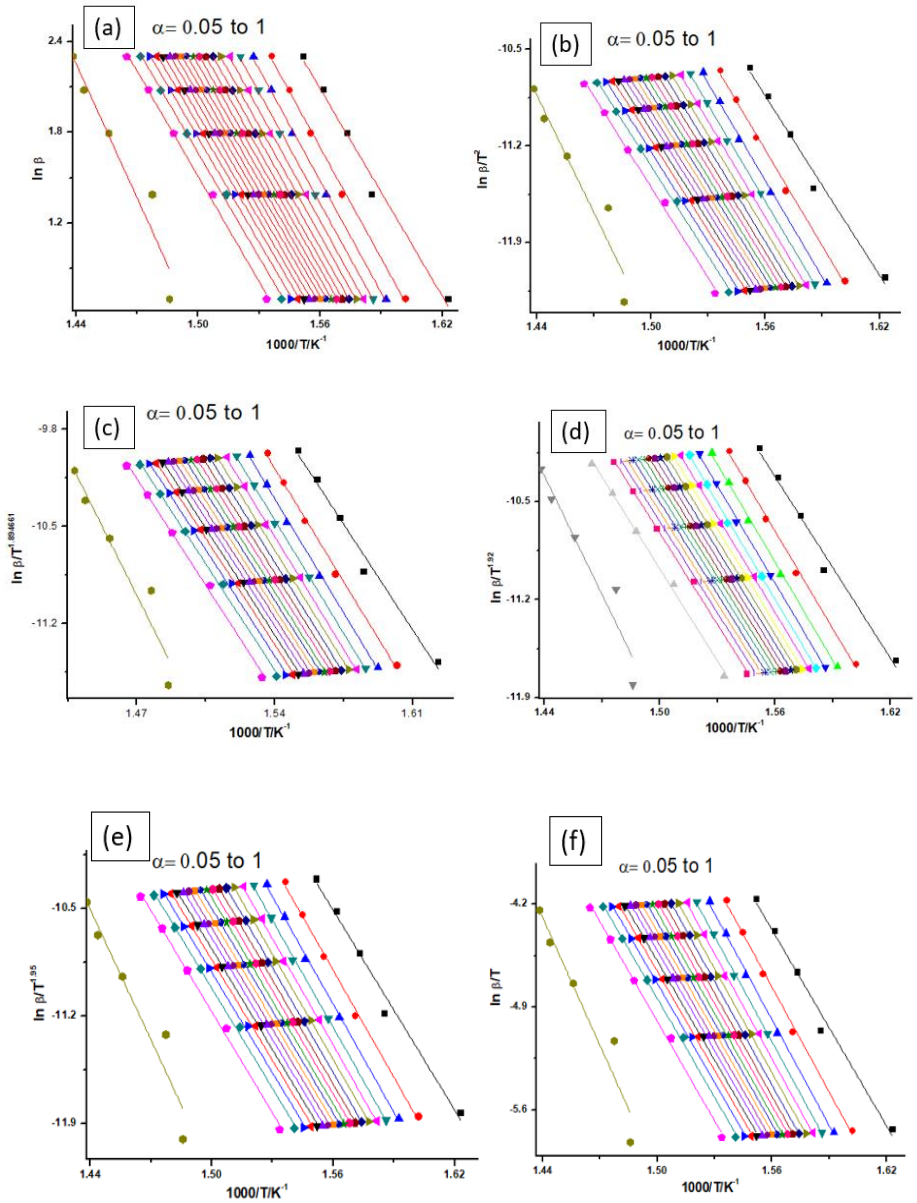

Fig. 30 Linear least squares plot for the decomposition stage of ZnOx for the isoconversional methods of FWO (a), KAS (b), Tang (c), Starink$^{1.92}$ (d), Starink$^{1.95}$ (e) and Boswell (f) from TG data

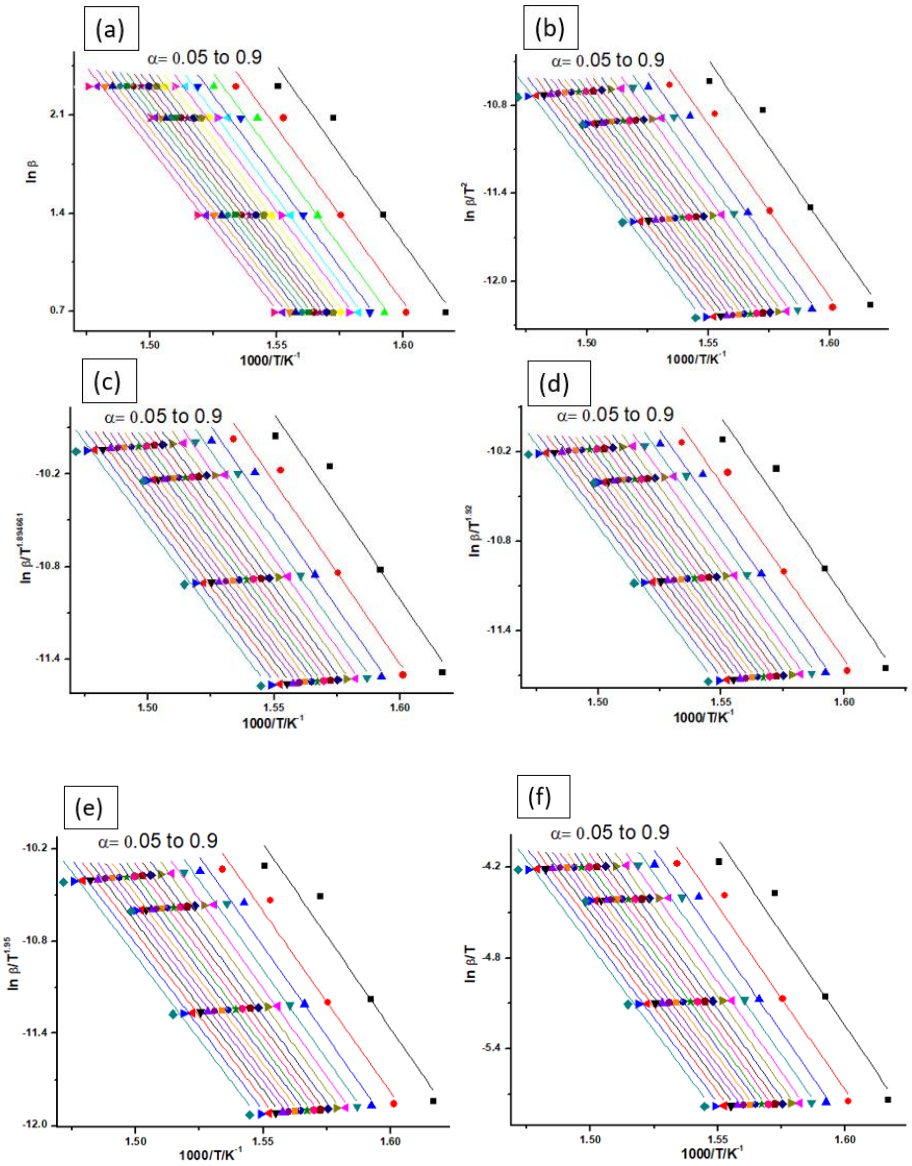

Fig. 31 Linear least squares plot for the decomposition stage of 0.1 mol% Ce-ZnOx for the isoconversional methods of FWO (a), KAS (b), Tang (c), Starink$^{1.92}$ (d), Starink$^{1.95}$ (e) and Boswell (f) from TG data

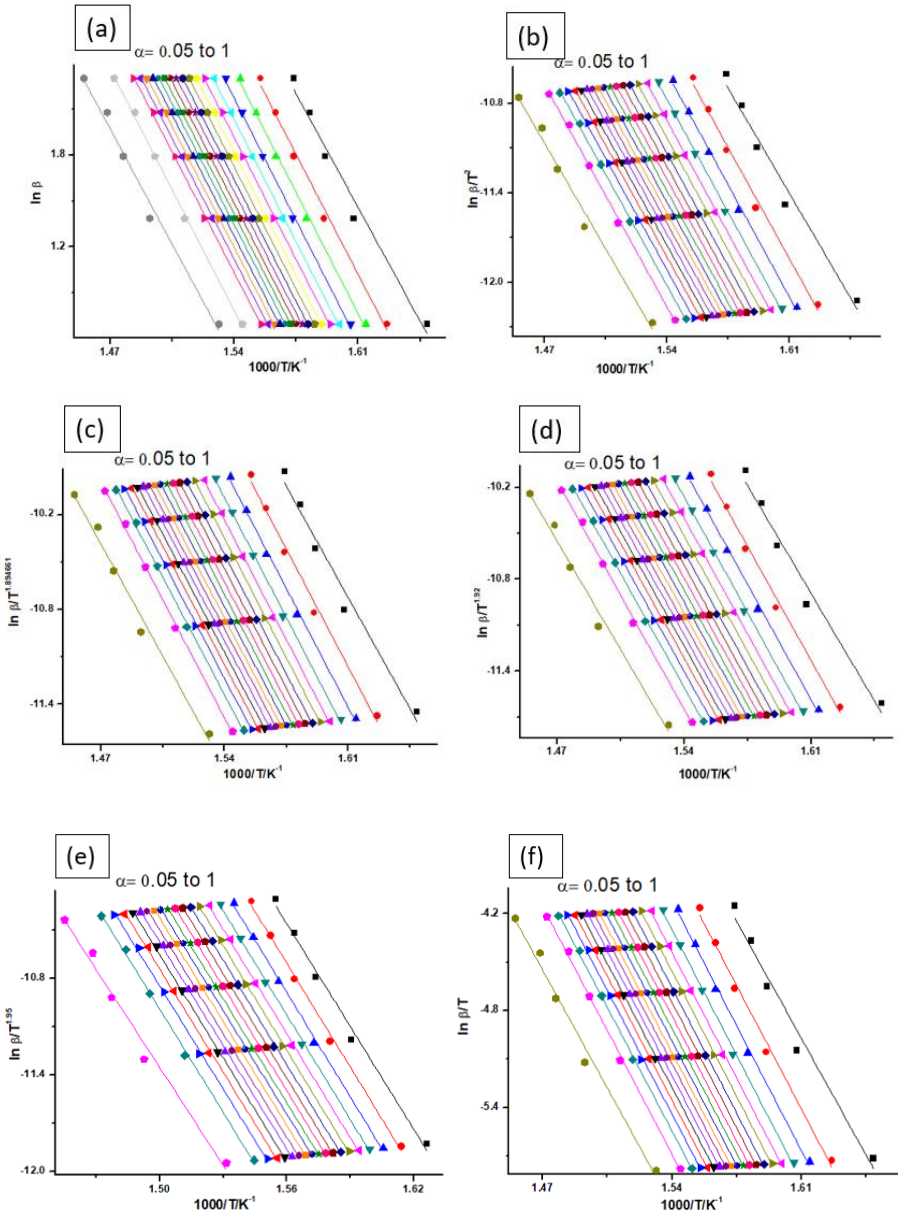

Fig. 32 Linear least squares plot for the decomposition stage of 1 mol% Ce-ZnOx for the isoconversional methods of FWO (a), KAS (b), Tang (c), Starink$^{1.92}$ (d), Starink$^{1.95}$ (e) and Boswell (f) from TG data

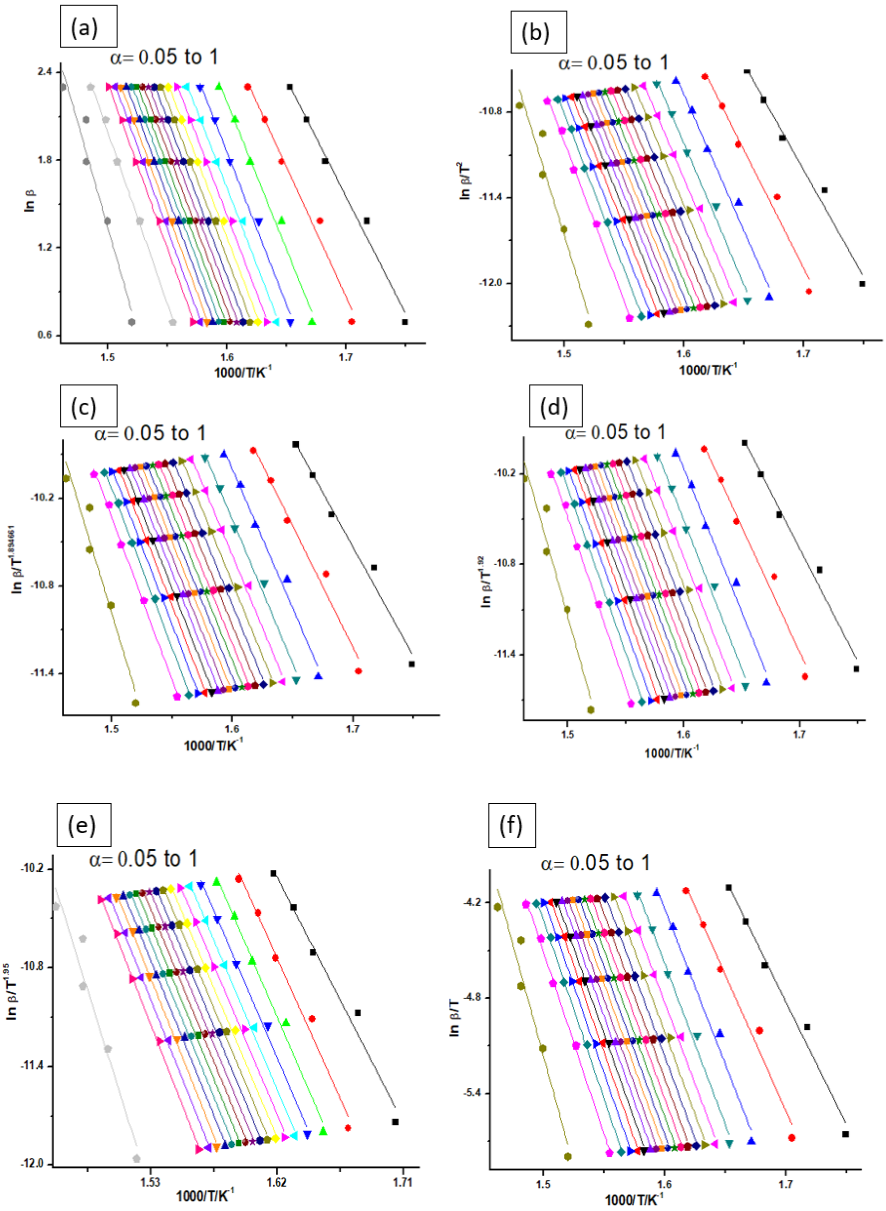

Fig. 33 Linear least squares plot for the decomposition stage of 5 mol% Ce-ZnOx for the isoconversional methods of FWO (a), KAS (b), Tang (c), Starink$^{1.92}$ (d), Starink$^{1.95}$ (e) and Boswell (f) from TG data

Table 11 Activation energy in kJ mol^{-1} for the dehydration reaction of $ZnOx.2H_2O$ from TG data

α	FWO	KAS	Tang	Starink$^{1.92}$	Starink$^{1.95}$	Boswell
0.3	133.63	133.58	133.75	132.99	133.54	136.97
0.35	130.34	130.10	130.28	129.59	130.07	133.50
0.4	127.18	126.75	126.94	126.29	126.72	130.17
0.45	124.20	123.60	123.79	123.19	123.60	127.04
0.5	121.57	120.81	121.00	120.42	120.78	124.24
0.55	118.51	117.57	117.78	117.26	117.62	121.06
0.6	116.89	115.86	116.06	115.46	115.78	119.28
0.65	113.03	111.77	111.99	111.47	111.82	115.27
0.7	111.25	109.88	110.10	109.57	109.87	113.36
0.75	108.71	107.19	107.41	106.82	107.15	110.66
0.8	105.65	103.96	104.19	103.59	103.94	107.45
0.85	103.08	101.23	101.46	100.77	101.09	104.67
0.9	98.93	96.84	97.08	96.31	96.92	100.41
0.95	97.71	95.52	95.77	91.76	97.63	100.14
Av	**115.05**	**113.90**	**112.60**	**114.11**	**114.04**	**117.45**

Av is the average value

Table 12 Activation energy in kJ mol^{-1} for the dehydration reaction of 0.1 mol% Ce-ZnOx.$2H_2O$ from TG data

α	FWO	KAS	Tang	Starink$^{1.92}$	Starink$^{1.95}$	Boswell
0.05	120.30	119.65	119.84	119.83		123.10
0.1	116.26	115.35	115.55	115.54	115.53	118.83
0.15	111.53	110.35	110.56	110.55	110.53	113.84
0.2	109.65	108.35	108.56	108.54	108.52	111.85
0.25	107.01	105.55	105.77	105.75	105.73	109.06
0.3	105.01	103.43	103.65	103.63	103.61	106.95
0.35	103.04	101.34	101.56	101.54	101.52	104.87
0.4	101.26	99.45	99.68	99.65	99.63	102.99
0.45	99.81	97.91	98.14	98.12	98.09	101.46
0.5	97.65	95.62	95.85	95.82	95.79	99.17
0.55	95.94	93.81	94.05	94.02	93.99	97.37
0.6	94.17	91.93	92.18	92.15	92.11	95.50
0.65	92.53	90.19	90.43	90.40	90.37	93.76
0.7	90.63	88.18	88.42	88.39	88.35	91.76
0.75	88.78	86.21	86.46	86.43	86.39	89.80
0.8	86.98	84.30	84.56	84.52	84.48	87.90
0.85	84.62	81.80	82.06	82.02	81.98	85.41
0.9	83.07	80.14	80.41	80.37	80.32	83.76
0.95	81.86	78.83	79.10	79.06	79.01	82.47
1	74.14	70.56	70.85	70.80	70.74	74.28
Av	**97.21**	**95.15**	**95.38**	**95.36**	**94.04**	**98.71**

Av is the average value

Table 13 Activation energy in kJ mol^{-1} for the dehydration reaction of 1 mol% Ce-ZnOx.$2H_2O$ from TG data

α	FWO	KAS	Tang	Starink$^{1.92}$	Starink$^{1.95}$	Boswell
0.05	159.42	160.91	161.04	161.06		164.31
0.1	148.51	149.38	149.52	149.53	149.55	152.81
0.15	141.09	141.54	141.69	141.70	141.71	144.98
0.2	135.97	136.11	136.28	136.28	136.28	139.57
0.25	131.43	131.31	131.48	131.48	131.48	134.79
0.3	127.17	126.80	126.98	126.97	126.97	130.29
0.35	124.24	123.70	123.88	123.88	123.87	127.20
0.4	121.76	121.06	121.26	121.25	121.24	124.58
0.45	118.82	117.95	118.15	118.14	118.12	121.47
0.5	117.07	116.09	116.29	116.28	116.27	119.63
0.55	115.40	114.31	114.51	114.50	114.48	117.85
0.6	113.36	112.15	112.36	112.34	112.32	115.70
0.65	110.90	109.54	109.75	109.73	109.71	113.10
0.7	109.06	107.59	107.81	107.79	107.77	111.16
0.75	107.48	105.90	106.13	106.11	106.08	109.49
0.8	104.45	102.69	102.92	102.90	102.87	106.29
0.85	102.78	100.92	101.15	101.13	101.10	104.52
0.9	99.55	97.49	97.73	97.70	97.67	101.11
0.95	96.78	94.56	94.80	94.77	94.74	98.19
1	101.96	99.85	100.09	100.06	100.03	103.55
Av	**119.36**	**118.20**	**118.69**	**118.68**	**116.44**	**122.03**

Av is the average value

Table 14 Activation energy in kJ mol^{-1} for the dehydration reaction of 5 mol% Ce-ZnOx.$2H_2O$ from TG data

α	FWO	KAS	Tang	Starink$^{1.92}$	Starink$^{1.95}$	Boswell
0.05	107.67	106.83	107.02	107.00		110.05
0.1	71.70	68.81	69.06	69.02	68.98	72.12
0.15	118.16	117.53	117.71	117.71	117.70	120.92
0.2	121.20	120.67	120.86	120.85	120.85	124.09
0.25	119.94	119.31	119.49	119.48	119.48	122.74
0.3	116.70	115.87	116.06	116.05	116.04	119.32
0.35	115.35	114.42	114.62	114.60	114.59	117.88
0.4	112.47	111.36	111.57	111.55	111.54	114.84
0.45	110.82	109.60	109.81	109.79	109.77	113.09
0.5	109.48	108.17	108.38	108.37	108.35	111.67
0.55	108.10	106.70	106.92	106.90	106.88	110.21
0.6	106.98	105.50	105.72	105.70	105.68	109.02
0.65	105.22	103.63	103.85	103.83	103.81	107.16
0.7	103.27	101.55	101.78	101.75	101.73	105.09
0.75	102.46	100.69	100.92	100.89	100.87	104.24
0.8	100.04	98.12	98.35	98.33	98.30	101.68
0.85	98.99	97.00	97.23	97.21	97.18	100.57
0.9	96.95	94.83	95.07	95.04	95.01	98.41
0.95	94.96	92.71	92.95	92.92	92.89	96.30
1	94.10	91.74	91.98	91.95	91.92	95.36
Av	**105.73**	**104.25**	**104.47**	**104.45**	**104.29**	**107.74**

Av is the average value

Table 15 Activation energy in kJ mol^{-1} for the decomposition reaction of $ZnOx.2H_2O$ from TG data

α	FWO	KAS	Tang	Starink$^{1.92}$	Starink$^{1.95}$	Boswell
0.05	181.06	180.01	180.30	180.28	180.27	185.24
0.1	193.53	193.00	193.27	193.27	193.26	198.29
0.15	195.17	194.66	194.94	194.93	194.93	199.99
0.2	193.86	193.24	193.52	193.51	193.51	198.59
0.25	192.84	192.13	192.42	192.41	192.40	197.50
0.3	191.06	190.23	190.52	190.50	190.49	195.61
0.35	190.45	189.56	189.86	189.84	189.83	194.96
0.4	189.17	188.20	188.49	188.48	188.47	193.60
0.45	187.88	186.81	187.11	187.09	187.08	192.23
0.5	187.32	186.21	186.51	186.49	186.48	191.63
0.55	185.91	184.71	185.01	184.99	184.98	190.14
0.6	185.17	183.90	184.21	184.19	184.17	189.35
0.65	184.23	182.89	183.20	183.18	183.17	188.35
0.7	184.31	182.96	183.27	183.25	183.23	188.42
0.75	183.31	181.89	182.20	182.18	182.16	187.37
0.8	182.70	181.22	181.53	181.51	181.49	186.71
0.85	182.64	181.14	181.45	181.43	181.41	186.64
0.9	182.35	180.79	181.11	181.08	181.06	186.31
0.95	183.85	182.32	182.64	182.62	182.60	187.86
1	234.41	235.23	235.49	235.50	235.51	240.92
Av	**189.56**	**188.55**	**188.85**	**188.84**	**188.83**	**193.99**

Av is the average value

Table 16 Activation energy in kJ mol^{-1} for the decomposition reaction of 0.1 mol% Ce-ZnOx.$2H_2O$ from TG data

α	FWO	KAS	Tang	Starink$^{1.92}$	Starink$^{1.95}$	Boswell
0.05	199.86	199.75	200.01	200.01	200.01	205.00
0.1	196.31	195.91	196.18	196.18	196.18	201.21
0.15	195.31	194.80	195.08	195.07	195.07	200.14
0.2	193.15	192.49	192.77	192.76	192.75	197.84
0.25	192.21	191.46	191.75	191.74	191.73	196.83
0.3	190.29	189.42	189.71	189.70	189.69	194.80
0.35	189.26	188.30	188.60	188.59	188.57	193.70
0.4	188.20	187.17	187.47	187.45	187.44	192.58
0.45	187.45	186.36	186.66	186.65	186.64	191.78
0.5	186.17	185.00	185.30	185.29	185.27	190.43
0.55	185.30	184.06	184.37	184.35	184.34	189.50
0.6	184.41	183.11	183.42	183.40	183.38	188.55
0.65	184.24	182.91	183.22	183.20	183.18	188.36
0.7	183.28	181.89	182.20	182.18	182.16	187.35
0.75	182.65	181.20	181.52	181.50	181.48	186.68
0.8	182.14	180.64	180.96	180.94	180.92	186.13
0.85	181.98	180.45	180.77	180.74	180.72	185.95
0.9	182.45	180.91	181.23	181.20	181.18	186.42
0.95	181.16	179.51	179.83	179.81	179.78	185.04
Av	**187.67**	**186.60**	**186.90**	**186.88**	**186.87**	**192.02**

Av is the average value

Table 17 Activation energy in kJ mol^{-1} for the decomposition reaction of 1 mol% Ce-ZnOx.$2H_2O$ from TG data

α	FWO	KAS	Tang	Starink$^{1.92}$	Starink$^{1.95}$	Boswell
0.05	168.26	166.70	167.00	166.98		171.86
0.1	177.69	176.48	176.77	176.76	176.74	181.70
0.15	179.56	178.37	178.67	178.65	178.63	183.63
0.2	180.55	179.35	179.65	179.63	179.62	184.64
0.25	180.63	179.40	179.70	179.68	179.66	184.71
0.3	180.27	178.98	179.28	179.26	179.25	184.31
0.35	180.61	179.30	179.61	179.59	179.57	184.65
0.4	180.70	179.37	179.68	179.66	179.64	184.74
0.45	180.47	179.10	179.41	179.39	179.37	184.48
0.5	180.11	178.71	179.01	178.99	178.97	184.09
0.55	179.82	178.37	178.68	178.66	178.64	183.77
0.6	179.27	177.78	178.09	178.07	178.05	183.19
0.65	179.10	177.58	177.89	177.87	177.85	183.00
0.7	179.45	177.92	178.23	178.21	178.19	183.35
0.75	178.98	177.40	177.72	177.70	177.68	182.85
0.8	178.96	177.35	177.67	177.65	177.62	182.81
0.85	178.57	176.91	177.23	177.21	177.19	182.38
0.9	178.38	176.68	177.00	176.98	176.95	182.17
0.95	178.70	176.97	177.30	177.27	177.25	182.48
1	170.42	168.15	168.49	168.46	168.43	173.72
Av	**178.52**	**177.04**	**177.35**	**177.33**	**177.86**	**182.43**

Av is the average value

Table 18 Activation energy in kJ mol^{-1} for the decomposition reaction of 5 mol% Ce-ZnOx.$2H_2O$ from TG data

α	FWO	KAS	Tang	Starink$^{1.92}$	Starink$^{1.95}$	Boswell
0.05	127.04	123.87	124.21	124.16		128.76
0.1	140.63	137.93	138.26	138.22	176.74	142.94
0.15	159.71	157.83	158.14	158.11	178.63	162.92
0.2	165.23	163.53	163.83	163.81	179.62	168.68
0.25	166.31	164.59	164.89	164.87	179.66	169.77
0.3	168.55	166.89	167.20	167.18	179.25	172.10
0.35	168.44	166.73	167.04	167.01	179.57	171.96
0.4	169.31	167.60	167.91	167.89	179.64	172.86
0.45	170.31	168.62	168.93	168.90	179.37	173.89
0.5	171.04	169.35	169.66	169.64	178.97	174.64
0.55	172.03	170.36	170.67	170.65	178.64	175.67
0.6	172.62	170.94	171.25	171.23	178.05	176.27
0.65	173.79	172.14	172.45	172.43	177.85	177.48
0.7	174.67	173.04	173.35	173.33	178.19	178.40
0.75	175.39	173.76	174.07	174.05	177.68	179.13
0.8	178.23	176.71	177.02	177.00	177.62	182.10
0.85	179.13	177.62	177.94	177.91	177.19	183.04
0.9	182.75	181.38	181.69	181.67	176.95	186.82
0.95	186.30	185.05	185.36	185.34	177.25	190.52
Av	**168.50**	**169.72**	**167.05**	**167.02**	**178.38**	**172.00**

Av is the average value

The E_a *vs* α curves for the dehydration reaction of ZnOx and Ce-ZnOx of various Ce concentrations are shown in **Fig. 34.** From the E_a *vs* α curves, it is very clear that for all the samples, the activation energy is continuously changing with α, which reflects the complexity of the reaction.

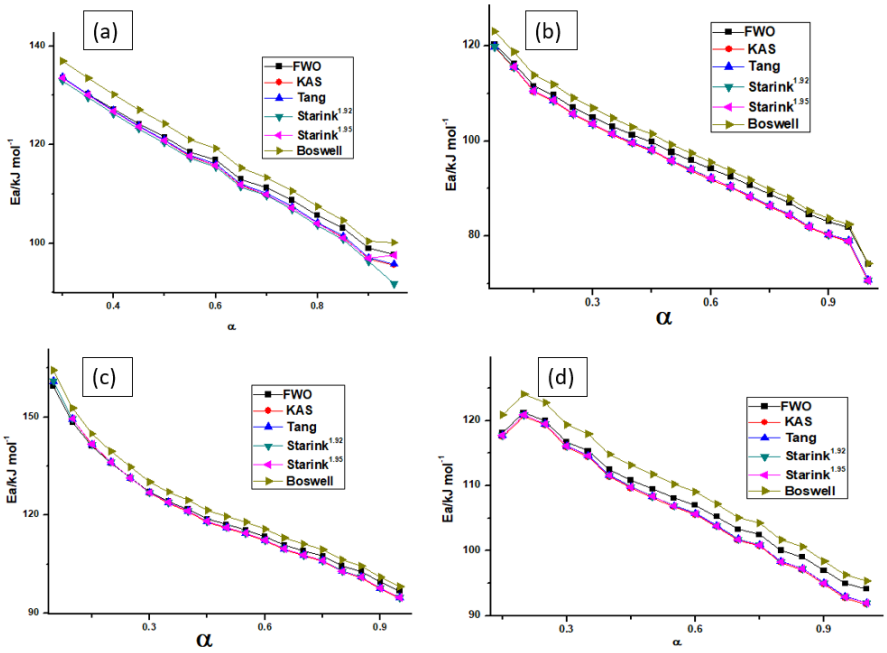

Fig. 34 E_a vs α curves for the dehydration stage of ZnOx (a), 0.1 mol% Ce-ZnOx (b), 1 mol% Ce-ZnOx (c), and 5 mol% Ce-ZnOx (d) from TG data

The variation of E_a with α is different for each sample in nitrogen atmosphere as obtained from the DSC data which implies that different mechanism operates in each sample but the pattern in which E_a varies with α is similar in all cases revealing that same mechanism is operating in all the samples in air. The activation energy is continuously decreasing with α for ZnOx and cerium added samples. This implies that the nucleation and growth in solid requires high activation energy, once the reaction starts, which means after the completion of nucleation and its growth, the reaction continues with low activation energy.

Fig. 35 shows the variation of activation energy with α for the decomposition reaction of ZnOx and Ce-ZnOx samples. The values of E_a decreasing continuously as the conversion function increases in pure and 0.1 mol% Ce-ZnOx. Pure ZnOx and 0.1 mol% Ce-ZnOx samples require a higher value of E_a at the commencement of decomposition, this may be due to the necessity of higher activation energy for the nucleation and the subsequent growth of the nuclei. Once the decay starts, the reaction requires lesser E_a until the end.

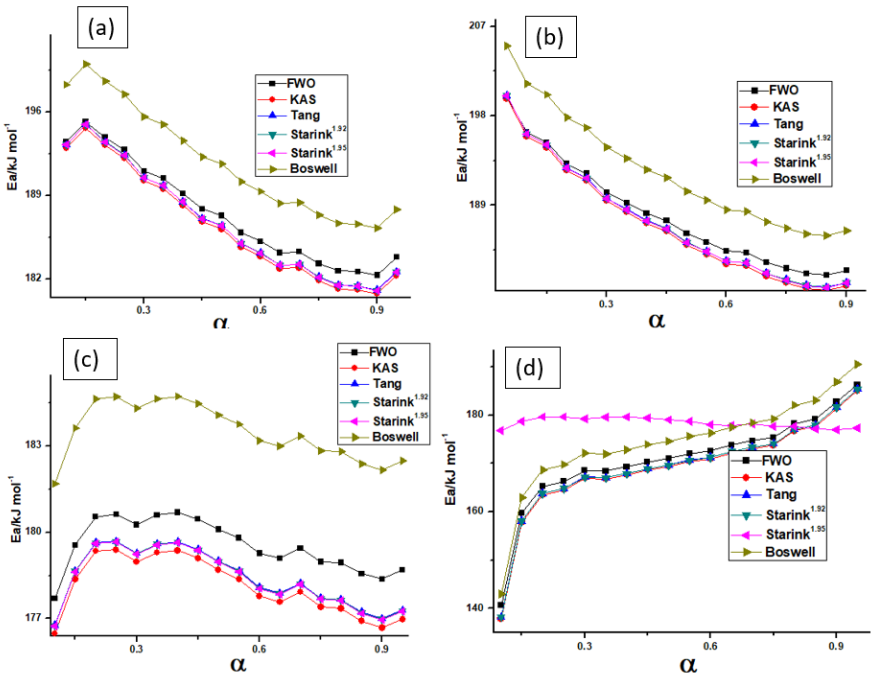

Fig. 35 E_a vs α curves for the decomposition stage of ZnOx (a), 0.1 mol% Ce-ZnOx (b), 1 mol% Ce-ZnOx (c), and 5 mol% Ce-ZnOx (d) from TG data

In 1 mol% Ce-ZnOx activation energy is decreasing but at some points of conversion, there is a slight increase is also observed. In 5 mol% Ce-ZnOx, the pattern in which E_a varies with α is completely different from all other samples reflecting that the cerium loading has a positive role in changing the mechanism of thermal decomposition of zinc oxalate into its oxide.

The average values for dehydration and decomposition reactions in the air using TG are given in **Tables 19** and **20** respectively.

Table 19 Summary of E_a values in kJ mol^{-1} for the dehydration reaction from TG data

Isoconversional method	Pure ZnOx	0.1 mol% Ce-ZnOx	1 mol% Ce-ZnOx	5 mol% Ce-ZnOx
FWO	115.05	97.21	119.36	105.73
KAS	113.90	95.15	118.20	104.25
Tang	112.60	95.38	118.69	104.47
Starink$^{1.92}$	114.11	95.36	118.68	104.45
Starink$^{1.95}$	114.04	94.04	116.44	104.29
Boswell	117.45	98.71	122.03	107.74

From **Table 9**, it is observed that in the nitrogen atmosphere, the value of activation energy for the dehydration reaction is regularly decreasing with an increase in Ce ion concentration, but it has been observed that there is no such regular decrease is present in air. The value of activation energy for pure ZnOx is 115.05 kJ mol^{-1} and this value is dropped into 97.21 kJ mol^{-1} by the addition of 0.1 mol% cerium. The value of activation energy is increased to 119.35 kJ mol^{-1} by loading 1 mol% cerium and it is then decreased to 105.72 kJ mol^{-1}. From these values, it is very clear that the sample atmosphere has a positive role in the determination of activation energy of thermal decomposition

reactions. It is also clear from the DSC data in nitrogen atmosphere and TG data in air, that the activation energy for the dehydration reaction is higher in air than in nitrogen atmosphere for all the samples studied. This may be due to the presence of constituents in the air.

Table 20 shows the values of activation energy needed for the decomposition of ZnOx to ZnO. It is interesting to note that the E_a values are decreasing with an increase in Ce ion concentration in air which is also noted in nitrogen atmosphere too. The activation energy required for the decomposition of oxalate into its oxide is highest for Pure ZnOx and least for 5 mol% Ce-ZnOx in air atmosphere. From all the isoconversional methods used for the determination of E_a, Boswell gives the higher values of activation energy for all the samples studied.

Table 20 Summary of E_a values in kJ mol^{-1} for the decomposition reaction from TG data

Isoconversional method	Pure ZnOx	0.1 mol% Ce-ZnOx	1 mol% Ce-ZnOx	5 mol% Ce-ZnOx
FWO	189.56	187.67	178.52	168.50
KAS	188.55	186.60	177.04	169.72
Tang	188.85	186.90	177.35	167.05
Starink$^{1.92}$	188.84	186.88	177.33	167.02
Starink$^{1.95}$	188.83	186.87	177.86	178.38
Boswell	193.99	192.02	182.43	172.00

The activation energy needed for the decomposition of zinc oxalate into zinc oxide is decreased by the addition of cerium into the zinc oxalate lattice in air and nitrogen atmosphere but the decrease in value is more pronounced in the nitrogen atmosphere. As the Ce ion concentration in the lattice of ZnOx increases from 0 to 5 mol%, there is a drop of 39.46 kJ mol^{-1} in the value of E_a for the decomposition

reaction (FWO method) in nitrogen atmosphere but in air, there is only a lowering of 21.06 kJ mol^{-1}. So the effect of the addition of cerium on the lowering of activation energy is more effect in nitrogen atmosphere. Also, the value of activation energy for the decomposition reaction is higher in air than nitrogen atmosphere.

3.4. Conclusion

We have succeeded in the synthesis of ZnOx and Ce-ZnOx of different Ce ion concentrations 0.1, 1, and 5 mol% by precipitation and co-precipitation method. These samples were characterized by FT-IR and thermal events were studied by using the DSC technique in flowing nitrogen atmosphere at the rate of 50 mL min^{-1} and TG-DTA in flowing air at five different heating rates 2, 4, 6, 8 and 10 K min^{-1}. The decomposed products were also characterized by using UV-DRS, FT-IR, XRD, FE-SEM, EDAX, and HR-TEM. From the powder XRD of all the samples, it is observed that all the oxides synthesized are nanoparticles and the particle size is reduced with increasing cerium loading. From UV-DRS and Tauc plot, it is found that the band gap is reduced to 3.10 eV from 3.14 eV by the addition of 5 mol% cerium. Kinetics of thermal dehydration and decomposition reactions were then studied by utilizing model free isoconversional methods. From the study, it is found that the value of activation energy for the dehydration reaction is regularly decreasing with an increase in Ce ion concentration in N_2. The value of E_a needed for the dehydration of pure ZnOx is maximum and least for 5 mol% Ce-ZnOx. The E_a value for pure ZnOx is 95.96 kJ mol^{-1} and it reduces to 69.66 kJ mol^{-1} for 5 mol% Ce-ZnOx in nitrogen atmosphere (FWO). There is a decrease of 26.3 kJ mol^{-1} in

activation energy value is observed in nitrogen atmosphere for the dehydration reaction of ZnOx when 5 mol% Ce is added to it. Also, it was very interesting to note that the E_a values are markedly decreasing with an increase in Ce ion concentration for the decomposition reaction of ZnOx to ZnO in nitrogen. As the Ce ion concentration in the lattice of ZnOx increases from 0 to 5 mol%, there is a drop of 39.46 kJ mol^{-1} in the value of E_a for the decomposition reaction (FWO method) in nitrogen atmosphere. The activation energy required for the decomposition of oxalate into its oxide is highest for Pure ZnOx and least for 5 mol% Ce-ZnOx in N_2 atmosphere. It is found that there is no regular decrease in the activation energy for the dehydration reaction in air. It is also noticed that the E_a values are decreasing for the decomposition reaction with an increase in Ce ion concentration in air which is also noted in the nitrogen atmosphere too. As the Ce ion concentration in the lattice of ZnOx increases from 0 to 5 mol%, there is a lowering of 21.06 kJ mol^{-1} in the value of E_a for the decomposition reaction (FWO method) in air. From these observations, it is clear that the decomposition atmosphere has a positive role in determining the activation energy of thermal reactions. It is also observed that the effect of the addition of cerium on the lowering of activation energy is more in nitrogen atmosphere. Also, the value of activation energy for the dehydration as well as decomposition reaction is higher in air than nitrogen atmosphere. In conclusion, it can be said that, to bring out the high concentration of ionic defect, aliovalent cations in large quantities may be employed in zinc oxalate precursors; which can help the formation of energetically favorable modified zinc oxide nanostructures.

3.5. References

[1] A.I. Mitsionis, T.C. Vaimakis, The effect of thermal treatment in TiO_2 photocatalytic activity, J. Therm. Anal. Calorim. 112 (2013) 621–628.

[2] R. Saravanan, S. Karthikeyan, V.K. Gupta, G. Sekaran, V. Narayanan, A. Stephen, Enhanced photocatalytic activity of ZnO/CuO nanocomposite for the degradation of textile dye on visible light illumination, Mater. Sci. Eng. C. 33 (2013) 91–98.

[3] V. Kuzhalosai, B. Subash, M. Shanthi, A novel sunshine active cerium loaded zinc oxide photocatalyst for the effective degradation of AR 27 dye, Mater. Sci. Semicond. Process. 27 (2014) 924–933.

[4] B. Krishnakumar, B. Subash, M. Swaminathan, AgBr – ZnO – An efficient nano-photocatalyst for the mineralization of Acid Black 1 with UV light, Sep. Purif. Technol. 85 (2012) 35–44.

[5] J. Liqiang, W. Dejun, W. Baiqi, L. Shudan, X. Baifu, F. Honggang, S. Jiazhong, Effects of noble metal modification on surface oxygen composition, charge separation and photocatalytic activity of ZnO nanoparticles, J. Mol. Catal. A Chem. 244 (2006) 193–200.

[6] F. Barka-Bouaifel, B. Sieber, N. Bezzi, J. Benner, P. Roussel, L. Boussekey, S. Szunerits, R. Boukherroub, Synthesis and photocatalytic activity of iodine-doped ZnO nanoflowers, J. Mater. Chem. 21 (2011) 10982–10989.

[7] B. Subash, B. Krishnakumar, V. Pandiyan, M. Swaminathan, M. Shanthi, Synthesis and characterization of novel WO_3 loaded Ag–ZnO and its photocatalytic activity, Mater. Res. Bull. 48 (2013) 63–69.

[8] O. Bechambi, M. Chalbi, W. Najjar, S. Sayadi, Photocatalytic activity of ZnO doped with Ag on the degradation of endocrine disrupting under UV irradiation and the investigation of its antibacterial activity, Appl. Surf. Sci. 347 (2015) 414-420.

[9] P. Pawinrat, O. Mekasuwandumrong, J. Panpranot, Synthesis of Au–ZnO and Pt–ZnO nanocomposites by one-step flame spray pyrolysis and its application for photocatalytic degradation of dyes, Catal. Commun. 10 (2009) 1380–1385.

[10] D. Li, H. Haneda, N. Ohashi, S. Hishita, Y. Yoshikawa, Synthesis of nanosized nitrogen-containing MOx–ZnO (M = W, V, Fe) composite powders by spray pyrolysis and their visible-light-driven photocatalysis in gas-phase acetaldehyde decomposition, Catal. Today 93–95 (2004) 895–901.

[11] D. Li, H. Haneda, Photocatalysis of sprayed nitrogen-containing Fe_2O_3–ZnO and WO_3–ZnO composite powders in gas-phase acetaldehyde decomposition, J. Photochem. Photobiol. A Chem. 160 (2003) 203–212.

[12] K.K. Akurati, A. Vital, J.-P. Dellemann, K. Michalow, T. Graule, D. Ferri, A. Baiker, Flame-made WO_3/TiO_2 nanoparticles: Relation between surface acidity, structure and photocatalytic activity, Appl. Catal. B Environ. 79 (2008) 53–62.

[13] L.F. Koao, F.B. Dejene, M. Tsega, H.C. Swart, Annealed Ce^{3+}-doped ZnO flower-like morphology synthesized by chemical bath deposition method, Phys. B Condens. Matter. 480 (2016) 53–57.

[14] J. Iqbal, X. Liu, H. Zhu, Z.B. Wu, Y. Zhang, D. Yu, R. Yu, Raman and highly ultraviolet red-shifted near band-edge properties of LaCe-co-doped ZnO nanoparticles, Acta Mater. 57 (2009) 4790–4796.

[15] C.-J. Chang, C.-Y. Lin, M.-H. Hsu, Enhanced photocatalytic activity of Ce-doped ZnO nanorods under UV and visible light, J. Taiwan Inst. Chem. Eng. 45 (2014) 1954–1963.

[16] G.N. Dar, A. Umar, S.A. Zaidi, A.A. Ibrahim, M. Abaker, S. Baskoutas, M.S. Al-Assiri, Ce-doped ZnO nanorods for the detection of hazardous chemical, Sensors Actuators B Chem. 173 (2012) 72–78.

[17] C. Artini, I. Nelli, M. Pani, G.A. Costa, V. Caratto, F. Locardi,

Thermal decomposition of Ce-Sm and Ce-Lu mixed oxalates: Influence of the Sm- and Lu-doped ceria structure, Thermochim. Acta. 651 (2017) 100–107.

[18] V. Berbenni, C. Milanese, G. Bruni, A. Girella, A. Marini, Synthesis of calcium metastannate ($CaSnO_3$) by solid state reactions in mechanically activated mixtures calcium citrate tetra hydrate [$Ca_3(C_6H_5O_7)_2 \cdot 4H_2O$] – tin(II) oxalate ($SnC_2O_4$), Thermochim. Acta. 608 (2015) 59–64.

[19] M. Niculescu, V. Sasca, C. Muntean, M.-S. Milea, D. Roşu, M.-C. Pascariu, E. Sisu, I. Ursoiu, V. Pode, P. Budrugeac, Thermal behavior studies of the homopolynuclear coordination compound iron(III) polyoxalate, Thermochim. Acta. 623 (2016) 36–42.

[20] J. Mu, D.D. Perlmutter, Thermal decomposition of carbonates, carboxylates, oxalates, acetates, formates, and hydroxides, Thermochim. Acta. 49 (1981) 207–218..

[21] V. Kornienko, Influence of cation nature on the thermal decomposition of oxalates, Ukr. Chem. J. 23 (1957) 159–167.

[22] B. Małecka, E. Drozdz-Cieśla, A. Małecki, Mechanism and kinetics of thermal decomposition of zinc oxalate, Thermochim. Acta. 423 (2004) 13–18.

[23] C. Hu, J. Mi, S. Shang, The study of thermal decomposition kinetics of zinc oxide formation from zinc oxalate dihydrate, J. Therm. Anal. Calorim. 115 (2014) 1119–1125.

[24] O. Yayapao, S. Thongtem, A. Phuruangrat, T. Thongtem, Sonochemical synthesis, photocatalysis and photonic properties of 3% Ce-doped ZnO nanoneedles, Ceram. Int. 39 (2013) S563–S568.

[25] B. Subash, B. Krishnakumar, R. Velmurugan, M. Swaminathan, M. Shanthi, Catalysis Science & Technology Synthesis of Ce co-doped Ag – ZnO photocatalyst with excellent performance for NBB dye degradation under natural sunlight illumination w, Catal. Sci. Technol. 2 (2012) 2319–2326.

[26] A.L. Patterson, The Scherrer Formula for X-Ray Particle Size Determination, Phys. Rev. 56 (1939) 978–982.

[27] A. Khawam, D.R. Flanagan, Role of isoconversional methods in varying activation energies of solid-state kinetics: II. Nonisothermal kinetic studies, Thermochim. Acta. 436 (2005) 101–112.

[28] S. Vyazovkin, Computational aspects of kinetic analysis.: Part C. The ICTAC Kinetics Project — the light at the end of the tunnel?, Thermochim. Acta. 355 (2000) 155–163.

[29] M.J. Starink, The determination of activation energy from linear heating rate experiments: a comparison of the accuracy of isoconversion methods, Thermochim. Acta. 404 (2003) 163–176.

[30] K. Sarada, K. Muraleedharan, Effect of addition of silver on the thermal decomposition kinetics of copper oxalate, J. Therm. Anal. Calorim. 123 (2016) 643–651.

[31] J.H. Flynn, L.A. Wall, A quick, direct method for the determination of activation energy from thermogravimetric data, J. Polym. Sci. Part B Polym. Lett. 4 (1966) 323–328.

[32] T. Ozawa, A New Method of Analyzing Thermogravimetric Data, Bull. Chem. Soc. Jpn. 38 (1965) 1881–1886.

[33] H.E. Kissinger, Reaction Kinetics in Differential Thermal Analysis, Anal. Chem. 29 (1957) 1702–1706.

[34] T. Wanjun, Æ.C. Donghua, New approximate formula for the generalized temperature integral, J. Therm. Anal. Calorim. 98 (2009) 437–440.

IMPACT ON THE KINETICS OF THERMAL DECOMPOSITION OF ZINC OXALATE BY THE ADDITION OF STRONTIUM ION

4.1. Introduction

ZnO is one of the best metal oxides with exciting properties to be used at the nanoscale level. The strong piezoelectric and pyroelectric properties make ZnO a better candidate in mechanical actuators, piezoelectric sensors, and surface wave acoustic devices [1]. Nanostructured ZnO powders found in many applications such as gas sensors [2], solar cells [3], varistors [4], and photocatalysis with high chemical activity [5]. Although several chemical methods of synthesis have been available for the synthesis of nanostructured ZnO powders [6–9], precipitation and thermal decomposition are common methods that can be used for large scale production. The basic advantage of using zinc oxalate as the precursor for obtaining ZnO nanoparticles is that it is a simple, low-cost, and mass-scale production method and it requires low temperature.

Doping ZnO nanostructures with metal ions is a strategy to modify their electronic and optical performance and improve their applications. There is plenty of reports available on the doping of metals Ce, Ni, Mn, Ga, In, Mg, Al, Sb, Ag, and Co to tailor the desirable properties of ZnO nanostructures [9–18]. There are numerous reports available on the application of Sr doped ZnO [19–22]. Sr doped ZnO show enhancement in gas sensing properties and this nanostructure is a

promising candidate for the fabrication of sensor devices for monitoring indoor air quality [23]. Recent studies have shown that Sr doped ZnO nanostructures exhibit an increase in photocatalytic activity [24–26]. Since the doping of Sr on the ZnO lattice structure greatly influences the electronic, optical, and photocatalytic properties of ZnO, the kinetic study of formation is also an important topic. There is no reports in literature till now, discussing on the kinetics of formation of Sr-ZnO from the oxalate precursors, this work introduces the kinetics of thermal decomposition of strontium added zinc oxalate of different strontium concentration using DSC technique in N_2 atmosphere.

4.2. Experimental

4.2.1. Materials

The reagents used in this study are of analytical grade and employed without any further purification. The chemicals used in the study are $Zn(NO_3)_2.6H_2O$ (Himedia, India), $Sr(NO_3)_2$ (Himedia, India), $H_2C_2O_4$ (Merck, India), and KBr (Sigma).

4.2.2. Preparation of Sr added zinc oxalate

Solution with Sr concentrations (0.1, 1, 2, and 5 mol%) of $ZnNO_3$ are taken to obtain four different concentrations of strontium zinc oxalate. The solutions were co-precipitated by adding 1 M oxalic acid solution with warming and stirring. The resultant solution was stirred for another 2 h. The reacted solution was kept for some time to settle the precipitate, then filtered off and washed several times with

distilled water and air-dried in an oven kept at 333 K for 8 h and was used for characterization and thermal analyses. The precipitates of strontium zinc oxalates were powdered and stored in a vacuum desiccator. The samples, $SZ_{0.1}$, SZ_1, SZ_2, and SZ_5 represent the strontium zinc oxalates synthesized with Sr concentrations 0.1, 1, 2, and 5 mol% respectively. Pure zinc oxalates designated as Z was also prepared as per the aforementioned method as reference samples. The pure and strontium added zinc oxalates were calcined at 773 K for the characterization purposes. The samples, ZO, $SZO_{0.1}$, SZO_1, SZO_2, and SZO_5 represent zinc oxide and strontium zinc oxides synthesized by the calcination of strontium zinc oxalates with Sr concentrations, 0.1, 1, 2 and 5 mol% respectively.

4.2.3. Preparation of pelletized samples

The samples were well-grounded and the powdered samples were diluted with KBr powder. Zinc oxalate dihydrate and the strontium doped/mixed samples and their corresponding oxides were pelletized using hydraulic pellet press (KP, SR. No. 1718) under a pressure of 50 kg cm^{-2}.

4.2.4. Characterization of the sample

Fourier Transform Infrared (FT-IR) spectra of the samples were recorded by the transmittance method using a spectrometer (Model: Jasco FTIR 41) after diluting the samples with KBr powder. The optical bandgap (E_g) of the decomposed products was calculated from UV-Visible reflectance which was measured using the UV-Visible diffuse

reflectance spectrum (Model: Jasco V-550 spectrophotometer). The powder X-ray diffraction (XRD) patterns of the oxide samples were recorded using a diffractometer (Miniflex 600, Model: RigakuD/Max) with Cu-Kα (λ = 1.5418 Å) radiation (40 kV, 15 mA) with a scan rate of 2θ min^{-1} in the region of 20-90^o. The high-resolution transmission electron microscopic (HRTEM) analysis and selected area (electron) diffraction (SAED) patterns of the particles were taken by using Talos 200 system.

4.2.5. Measurement of thermal behavior

Thermogravimetric measurement were carried out on a Perkin Elmer Pyris Thermal Analyser STA8000 at different heating rates 2, 4, 6, 8, and 10 K min^{-1}. The operational characteristics of the thermal analysis system are as follows: atmosphere: air, sample mass: ~5 mg; and sample pan: silica. Duplicate runs were made under similar conditions and found that the data overlap with each other, indicating satisfactory reproducibility. The differential scanning calorimetric (DSC) measurements of the samples were done in the temperature range 303-773 K at five different heating rates 2, 4, 6, 8, and 10 K min^{-1} on a Mettler Toledo DSC822e. The operational characteristics of the DSC system are as follows: atmosphere: flowing N_2 at a flow rate of 50 mL min^{-1}; sample mass~ 5 mg; and sample pan: silica.

4.3. Results and Discussion

4.3.1. Sample characterization

The optical bandgap (E_g) of the decomposed products was calculated from UV-Vis reflectance which was measured using the UV-Vis diffuse reflectance spectrum. The optical bandgap is determined by using the Tauc equation

$$(\alpha h\upsilon)^n = B(h\upsilon - Eg) \quad (1)$$

where $h\upsilon$ is the photon energy, α is the absorption coefficient, B is a constant relative to the material and n is either 2 for direct transition or 1/2 for an indirect transition. The $(\alpha h\upsilon)^2$ versus $h\upsilon$ curve (Tauc-plot) of pure ZnO and Sr added ZnO ($SZO_{0.1}$, SZO_1, SZO_2, and SZO_5) calcined at 773 K are shown in **Fig. 1**. It is found that the value of the bandgap decreased by the addition of strontium ion into the ZnO lattice. The addition of strontium ion into ZnO lattice creates oxygen vacancies and this increases the defect concentration and this is one of the most important factors for the narrowing of bandgap [24].

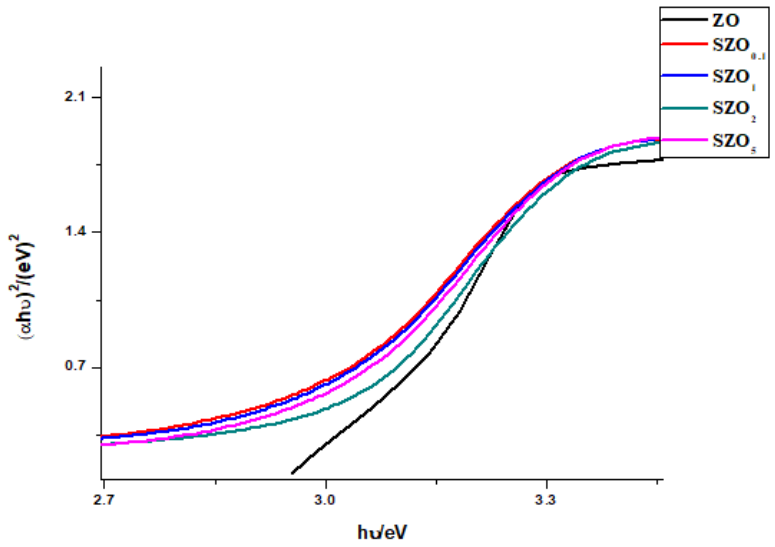

Fig. 1 Tauc-plot of ZnO and Sr-ZnO samples calcined at 773 K

The oxygen vacancies energy forms a band tail below the conduction band of ZnO. The bandgap obtained for ZnO is 3.03 eV and all the strontium added samples have a bandgap of lower than 3.03 eV and this indicates that oxygen vacancies are created by the addition of strontium and this creates an impurity level near the valance band by oxygen vacancy level energies and induced bandgap narrowing.

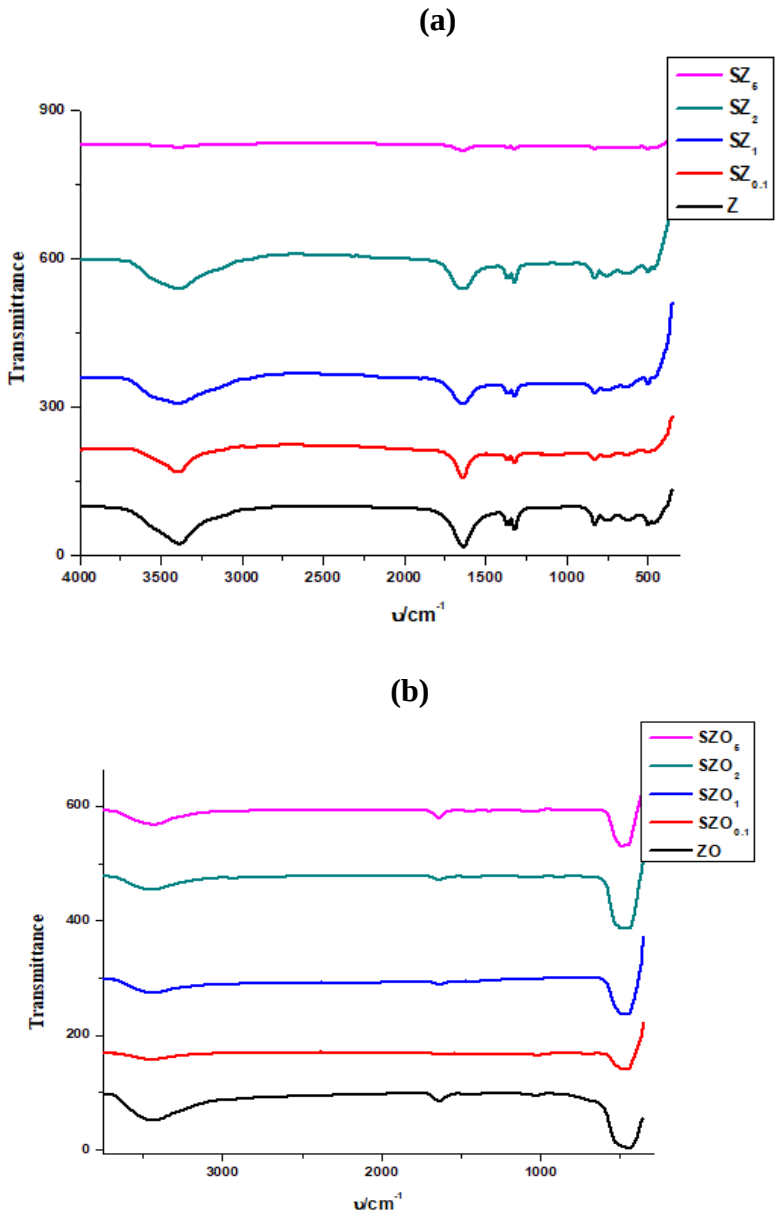

Fig. 2 FTIR spectra of zinc oxalate dihydrate and strontium-zinc oxalate dihydrate (a) and their corresponding oxides (b)

The FTIR spectroscopic analysis reveals the different bond vibrations present in the pure and strontium added zinc oxalates and their corresponding oxide nanoparticles obtained by the calcination of the oxalate precursors at 773 K. **Fig. 2** shows the FTIR spectra of zinc oxalate dihydrate and the strontium added samples and their oxide nanoparticles obtained. The strong broad band centered near 3,400 cm^{-1} is assigned to stretching modes of hydrated water, υ (O–H); this band arises due to the presence of water present in the sample. The strong band at around 1,628 cm^{-1} is characteristic of C=O antisymmetric stretching modes υ_{as} (C=O). The small peaks at 1356 and 1318 cm^{-1} is due to the O–C–O stretching modes.

The small band at 827 cm^{-1} is due to the O–C=O bending modes υ (O–C=O) and Zn-O stretching modes υ (Zn–O) is around 460 cm^{-1}. The oxide samples show a strong band near 460 cm^{-1} and the absence of oxalate bands reflects the formation of oxide particles from the oxalate precursor.

Fig. 3 shows the XRD patterns of zinc oxide and Sr added zinc oxides. The XRD pattern reveals that both the ZnO and the Sr containing oxides are highly crystalline in nature. The crystalline sizes were determined by using the Scherrer equation:

$$d = 0.9\lambda/\beta\cos\theta \quad (2)$$

where d is the crystallite size, λ is the wavelength of the X-ray used (1.5418 Å), θ is the Bragg's angle in degree, β is the full width at half maximum intensity of the peak (in Rad), K is the crystallite shape

factor, a good approximation is 0.9. The peaks at 2θ values 31.65, 34.30, 36.12, 47.40, 56.40, 62.71, 66.24, 67.81, and 68.99^0 can be indexed to (100), (022), (101), (102), (110), (103), (200), (112), and (201) planes of hexagonal wurtzite structure of ZnO (JCPDS N 00-036-1451).The particle sizes of all the samples are in the nanometer range and the average particle size decreases with strontium addition. In general, the amount of foreign atoms up to 1 mol% (or in range of ppm) is considered to give the effect of doping. Above 1 mol%, the atoms are replaced deliberately too many degrees, which give rise to substituent effect. It is known that the loading of metal into the semiconductor surface will reduce the crystalline size of the semiconductor when compared to the unloaded semiconductors [27,28]. ZnO crystal structure is more open, the metal ions with a smaller radius cannot only become substitution ions but also easily become interstitial ions, while the ions with larger radius Sr^{2+} (1.12 Å) than Zn^{2+} (0.74Å) ions are easier to become substitution ions. Hence the crystalline size of Sr-ZnO is lower than pure ZnO [29]. The crystallite size obtained for ZnO, $SZO_{0.1}$, SZO_1, SZO_2, and SZO_5 in (100) plane is 44.1, 42.2, 30.2, 33.1, 29.6 nm respectively. The average crystallite size obtained for ZnO is 44.06 nm and it reduced to 39.7 nm upon the addition of 5 mol% Sr evidencing the substitutional effect of Sr. The particle size obtained in different planes is different reflecting the inhomogeneity of the formation of nanoparticles. The XRD patterns show that there is a gradual shift of 2θ values to higher values upon the addition of strontium ions. The ionic radius mismatch between the Zn^{2+} and Sr^{2+} arose due to the difference in the size of Zn^{2+} and $Sr^{2+}$and causes the crystal system to expand and results in the shift

of Bragg's diffraction angles. The shift in 2θ values provides indirect evidence to the incorporation of Sr^{2+} ion in the ZnO structure [29].

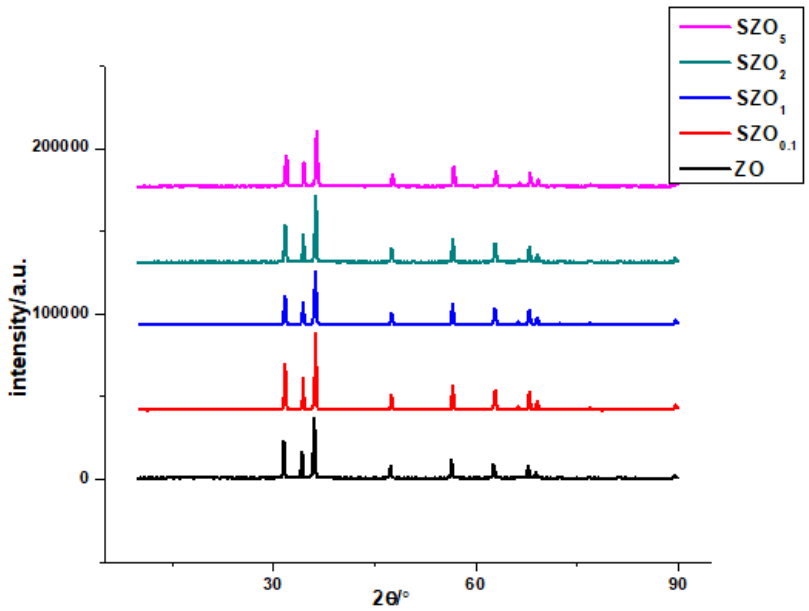

Fig. 3 XRD patterns of ZnO and Sr-ZnO samples calcined at 773 K

Figs. 4 and 5 show the HRTEM images, SAED patterns, and lattice fringes of SZO_1 and SZO_5 respectively. The TEM images of the two samples reflect the formation of spherical nanoparticles of ZnO. The HRTEM images of the Sr-ZnO samples were compared with that of ZnO prepared through the same procedure reported in [30, 31] and found that the morphology of the particles is similar. The HRTEM images of the two Sr added samples show that the spherical nanoparticles are arranged in a chain-like structure. On increasing the concentration of strontium ions from 1 to 5 mol%, the size of the particles gets reduced and the particles get a more ordered hexagonal arrangement. The clear lattice fringes and bright spotty ring pattern in the SAED patterns of the two

samples indicate the good crystallinity of the formed oxides which is in good agreement with the XRD results. It is clear from the SAED patterns that the crystallinity of SZO_5 is higher than that of SZO_1. The addition of strontium ion does not change the morphology of the nanoparticles but there is some increase in crystallinity on increasing the concentration of strontium ions.

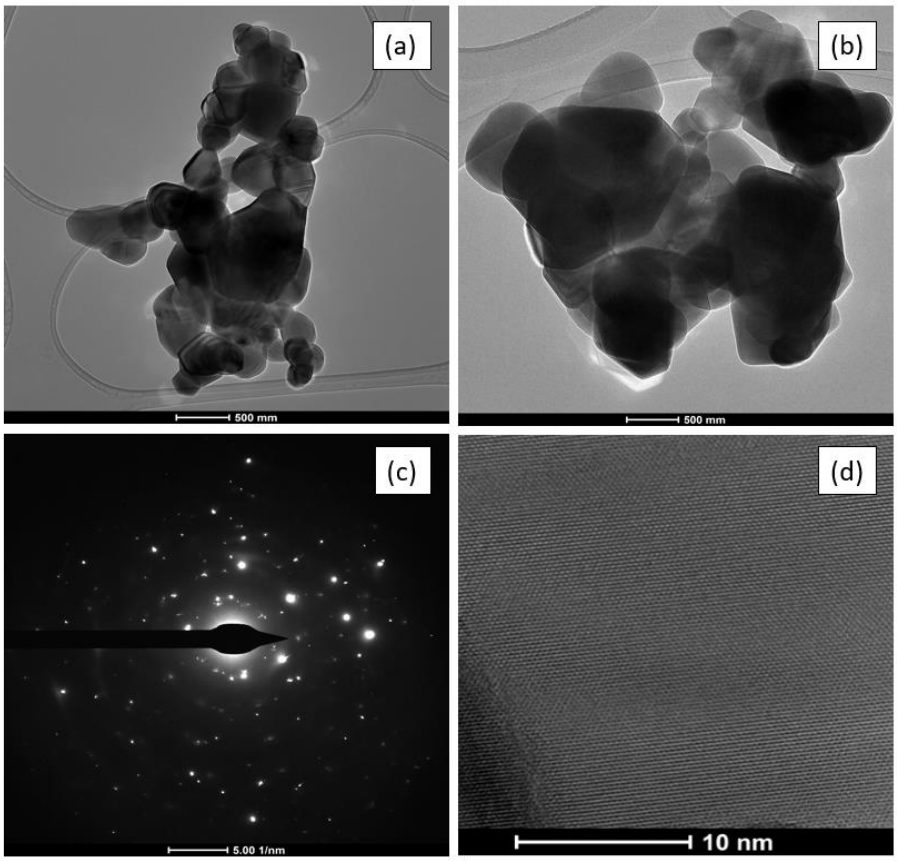

Fig. 4 HRTEM images (a) and (b), SAED pattern (c), lattice fringes (d) of SZO_1

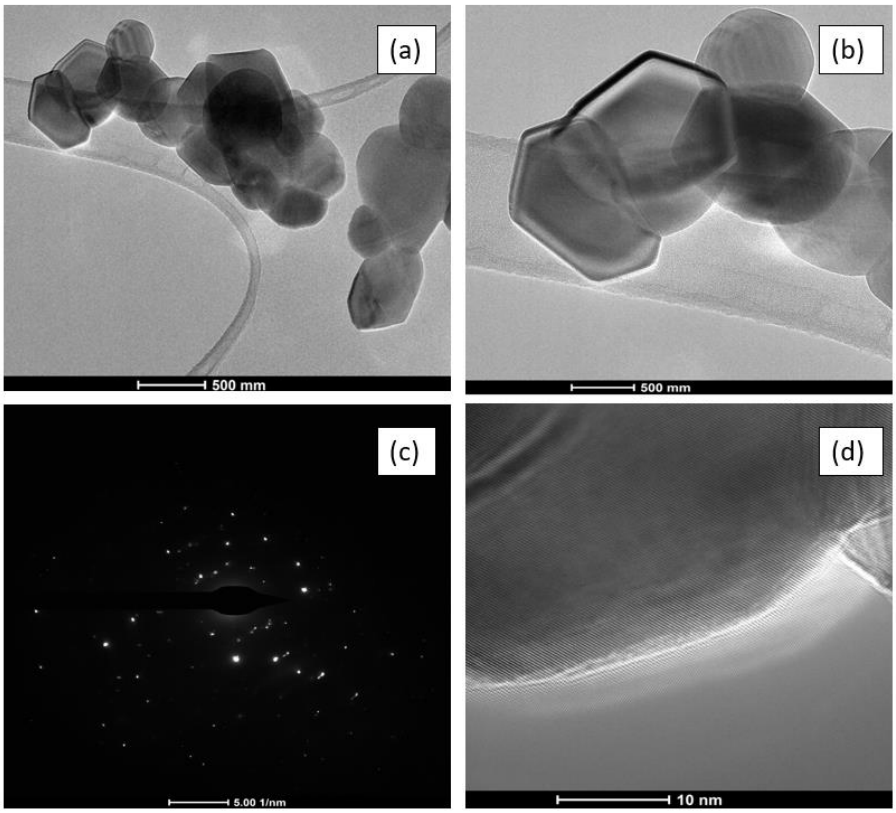

Fig. 5 HRTEM images (a) and (b), SAED pattern(c), lattice fringes (d), of SZO_5

Fig. 6 shows the TG curves obtained for zinc oxalate and the zinc-strontium oxalates of strontium concentration 0.1, 1, 2, and 5 mol% at the heating rate 2 K min^{-1}. Thermogravimetric analysis shows two mass loss stages, the first one corresponding to the dehydration of two molecules of water and the second one corresponding to the decomposition of oxalates into their oxides by the removal of CO_2 and CO. The dehydration reaction occurs in the temperature range 380 - 440 K and the decomposition reaction occurs in the temperature range 600 -

700 K. **Fig. 7** TG curve of zinc oxalate dihydrate (a), SZ0.1 (b), SZ1 (c), SZ2 (d) and SZ5 (e) samples at different heating rates.

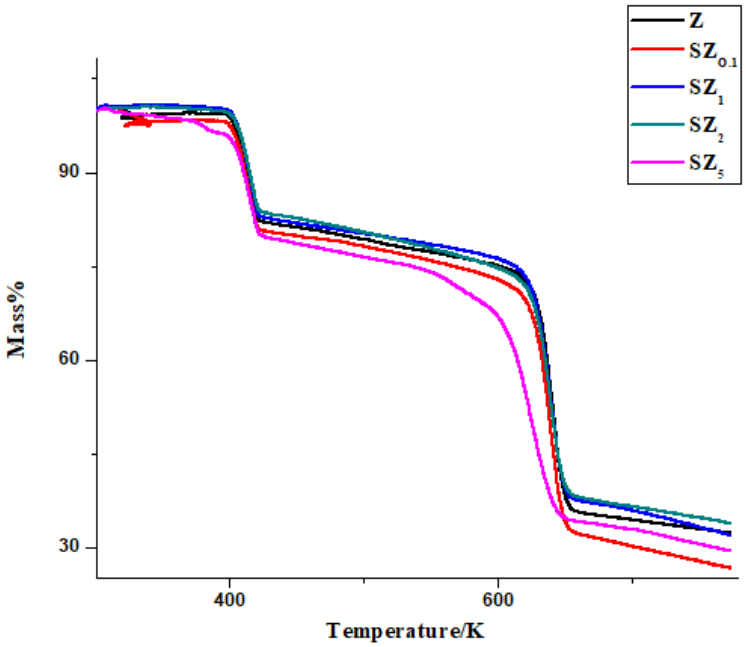

Fig. 6 TG curve of zinc oxalate dihydrate and Sr-zinc oxalate dihydrate samples at the heating rate of 2 K min^{-1}

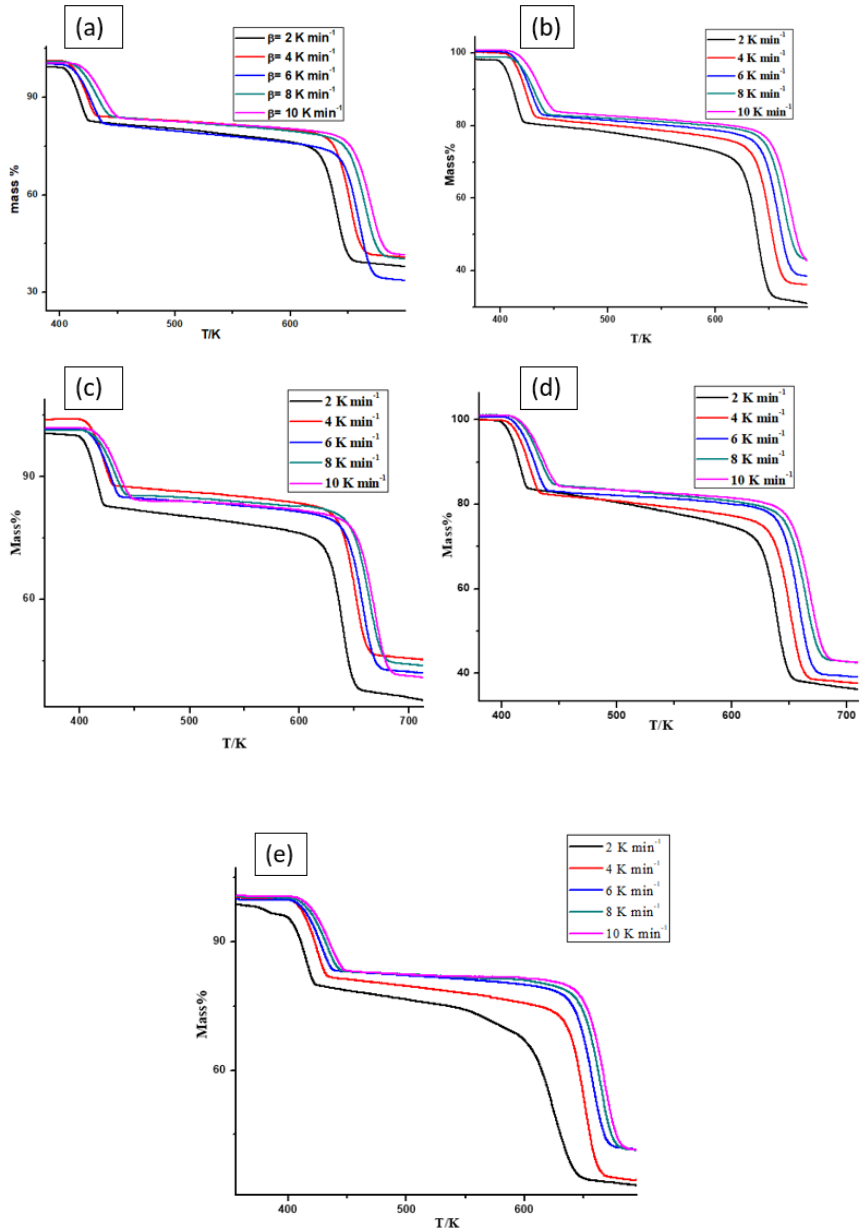

Fig. 7 TG curve of zinc oxalate dihydrate (a), $SZ_{0.1}$ (b), SZ_1 (c), SZ_2 (d) and SZ_5 (e) samples at different heating rates

Both the dehydration and decomposition temperature slightly shifted to higher values as the heating rate increases. The first mass loss of around 17.34% in the temperature range 380-440 K is consistent with the elimination of 2 mol of water molecules. The second mass loss of around 38.98% (theoretical mass loss 38.03%) observed in the temperature range 600-700 K indicates the decomposition of ZnC_2O_4 into ZnO. The total mass loss is 56.32%, which is in good agreement with the calculated value of 57.10% that can be calculated if it is assumed that the $ZnC_2O_4.2H_2O$ is completely transformed into ZnO [31]. The obtained TG was correlated with the previously reported one by Barbara M. *et al.* [32] and Chengcheng Hu *et al.* [31] and it was found that the results agree well with these.

The DSC curves obtained for zinc oxalate dihydrate and the zinc-strontium oxalates dihydrate of strontium concentration 0.1, 1, 2, and 5 mol% at different heating rates 2, 4, 6, 8 and 10 K min^{-1} are shown in **Fig. 8.** The DSC curves of pure and strontium containing samples show two endothermic peaks that are well separated from each other. The first peak corresponding to dehydration of two molecules of water and the second peak represents the decomposition of oxalates into their oxides. For pure zinc oxalate, the dehydration occurs in the temperature of 338-444 K. For pure zinc oxalate, the decomposition reaction occurs in the temperature range 600-690 K. All Sr added zinc oxalate decomposes in the temperature range of 620-700 K. The decomposition of oxalate into its oxide is slightly shifted to higher temperature with the addition of strontium. The peak temperature and enthalpy for the dehydration and decomposition reactions for all the samples increases with an increase in the heating rate. The peak temperature for dehydration and

decomposition reactions of all the Sr added zinc oxalates samples has a slightly lower value than that of the pure zinc oxalate.

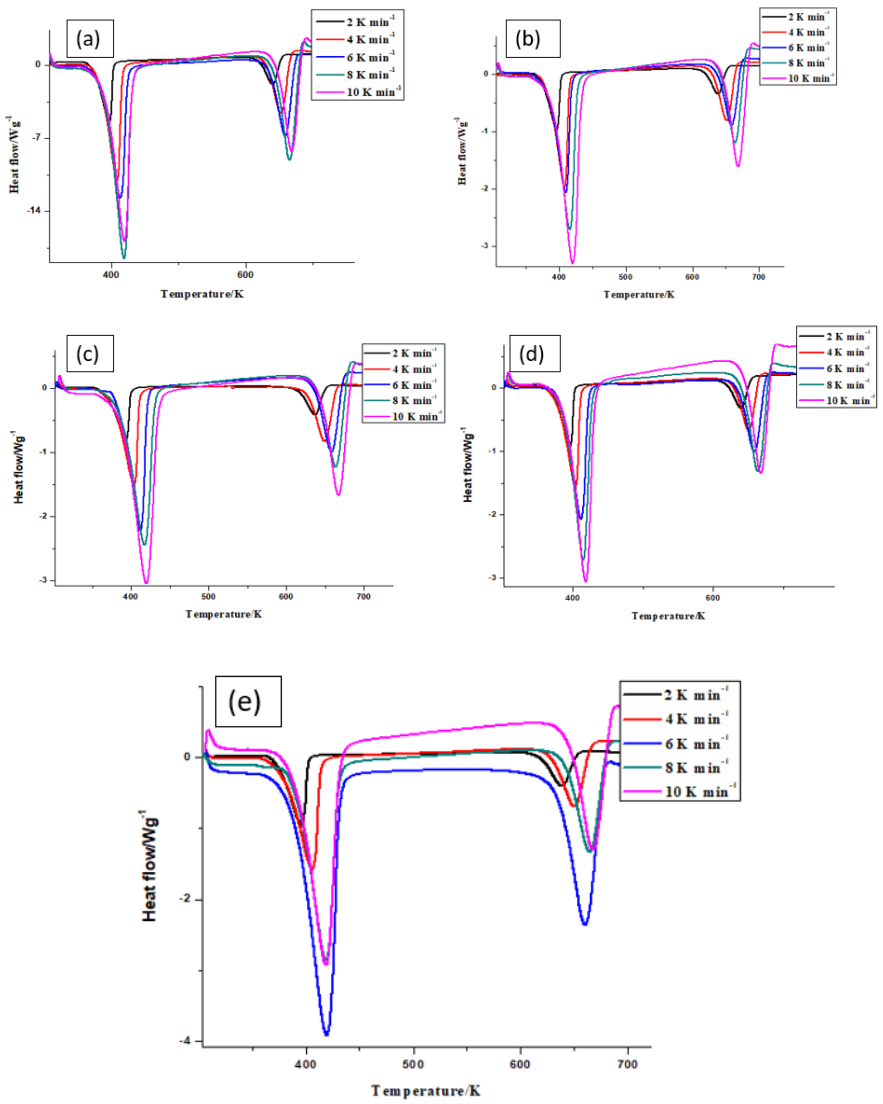

Fig. 8 DSC curve for zinc oxalate dihydrate (a) and $SZ_{0.1}$ (b), SZ_1 (c), SZ_2 (d) and SZ_5 (e) samples at different heating rates

4.3.2. Kinetic analysis

Model-free methods seem to be the most effective methods for computing the activation energy of thermally activated processes [33–38]. The advantage of using model-free approaches to evaluate kinetic data is that they do not presume any model or mechanism for determining E_a, even at different temperature ranges. This method considers that the reaction mechanism does not change with reaction conversion (α), temperature, and heating rate. Isoconversional methods are model-free methods that evaluate activation energy at different values of α [39].

4.3.2.1. Isoconversional methods

The methods take their origin in the single-step kinetic equation

$$d\alpha / dt = Ae^{-E_a/RT} f(\alpha) \tag{3}$$

and make use of the isoconversional principle which states that at a constant extent of α, the reaction rate is a function of temperature only so that:

$$\left[\frac{d\ln(d\alpha / dt)}{dT^{-1}}\right]_{\alpha} = -E\alpha / \mathrm{R} \tag{4}$$

In Eqs. (3) and (4), A and E are Arrhenius parameters (the pre-exponential factor and the activation energy, respectively), $f(\alpha)$ is the reaction model, R is the gas constant, T is the temperature, t is the time and α is the extent of conversion, which can be determined from TG

runs as a fractional mass loss or from DSC runs as a fractional heat release. For nonisothermal conditions when the temperature is raised at a constant heating rate β, integration of Eq. (3) involves solving the temperature integral, *I (E, T)*

$$g\ (\alpha) = A/\beta \int_0^{Tx} e^{-E_a/RT} dt = A/\beta I\left(E,T\right) \qquad (5)$$

This equation does not have an analytical solution. It is solved by using either approximations or numerical integration. All of the approximations lead to a direct isoconversional method in the form:

$$ln\ \left(\beta / T^K\right)\ =\ C - E_a / RT \qquad (6)$$

for a selected degree of conversion function, α, a corresponding $T_{\alpha i}$ and heating rate β are used to plot ln (β/T^K) against $1/T_{\alpha i}$, where K is a constant. The activation energy is then determined from the regression slope.

4.3.2.1.1. Isoconversional methods used for the calculation of E_a

(i) Flynn–Wall–Ozawa (FWO) method [40,41]

$$ln\beta = ln\left(AE / g\left(\alpha\right)R\right) - 5.331 - 1.052E_\alpha / RT_{\alpha i} \qquad (7)$$

where α is the conversion function. From the slope of the graph lnβ against $1/T_{\alpha i,}$ E_a can be calculated.

(ii) Kissinger–Akahira–Sunose (KAS) method [42]

KAS is also an integer isoconversional method similar to FWO.

$$ln\beta / T^2 = ln\left(AR / E_a g(\alpha)\right) - E_a / RT \quad (8)$$

E_a can be obtained from the slope of the straight-line graph lnβ /T^2 against *1/T*.

(iii) Tang method [43]

$$ln\left(\beta / T^{1.894661}\right) = ln\left(AE_a / Rg(\alpha)\right) + 3.635041 - 1.894661 ln\, E_a - 1.00145033 E_a / RT \quad (9)$$

E_a can be obtained from the slope of the straight-line graph ln ($\beta/T^{1.894661}$) against *1/T*.

(iv) Starink method [35]

$$ln\beta / T^{1.95} = C^{1.95}(\alpha) - E_a / RT \quad (10)$$

$$ln\beta / T^{1.92} = C^{1.92}(\alpha) - 1.0008 E_a / RT \quad (11)$$

(v) Boswell method

$$ln\beta / T = C(\alpha) - E_a / RT_{\alpha i} \quad (12)$$

The conversion function, α in the range 0.05-0.95 with an interval of 0.05, and their corresponding temperatures are determined from the experimental heat flow data procured from DSC for the decomposition reaction. The α versus temperature curve for the

decomposition of the pure and Sr containing samples of strontium concentration 0.1, 1, 2, and 5 mol% are shown in **Fig. 9 (a)-(e)**. For all samples, the α-T curve has a sigmoidal shape.

The α-T data obtained from the DSC data for decomposition reaction were subjected to linear least-squares analysis (in the range α = 0.05 to 0.95) using the isoconversional methods of FWO, KAS, Tang, Starink$^{1.92}$, Starink$^{1.95,}$ and Boswell to obtain the values of activation energy (E_a) and the linear least squares plots are given in the **Figs. 10-14.** The activation energy is calculated from the slope of the linear least squares plots and the obtained values of activation energies are presented in **Tables 1-5.** Boswell method has the highest value of E_a for pure and strontium containing samples. Both FWO and Boswell methods give larger value for E_a than KAS, Tang, Starink$^{1.92,}$ and Starink$^{1.95}$ methods. The activation energy obtained from different isoconversional methods for the decomposition of oxalate has almost the same value. The average values of activation energies for the decomposition of pure zinc oxalate and strontium zinc oxalates are summarized in **Table 6.**

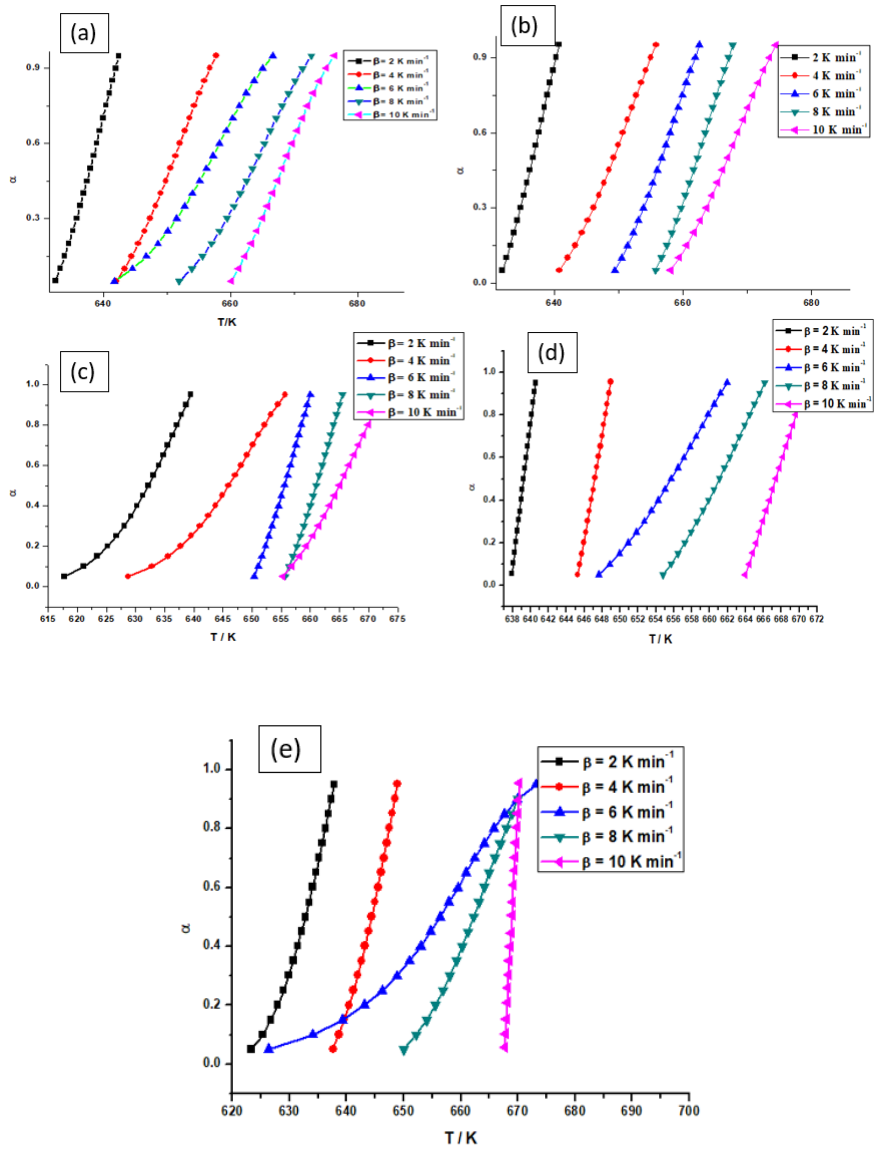

Fig. 9 α -*T* curves for the decomposition of the pure (a) and $SZ_{0.1}$ (b), SZ_1 (c), SZ_2 (d) and SZ_5 (e)

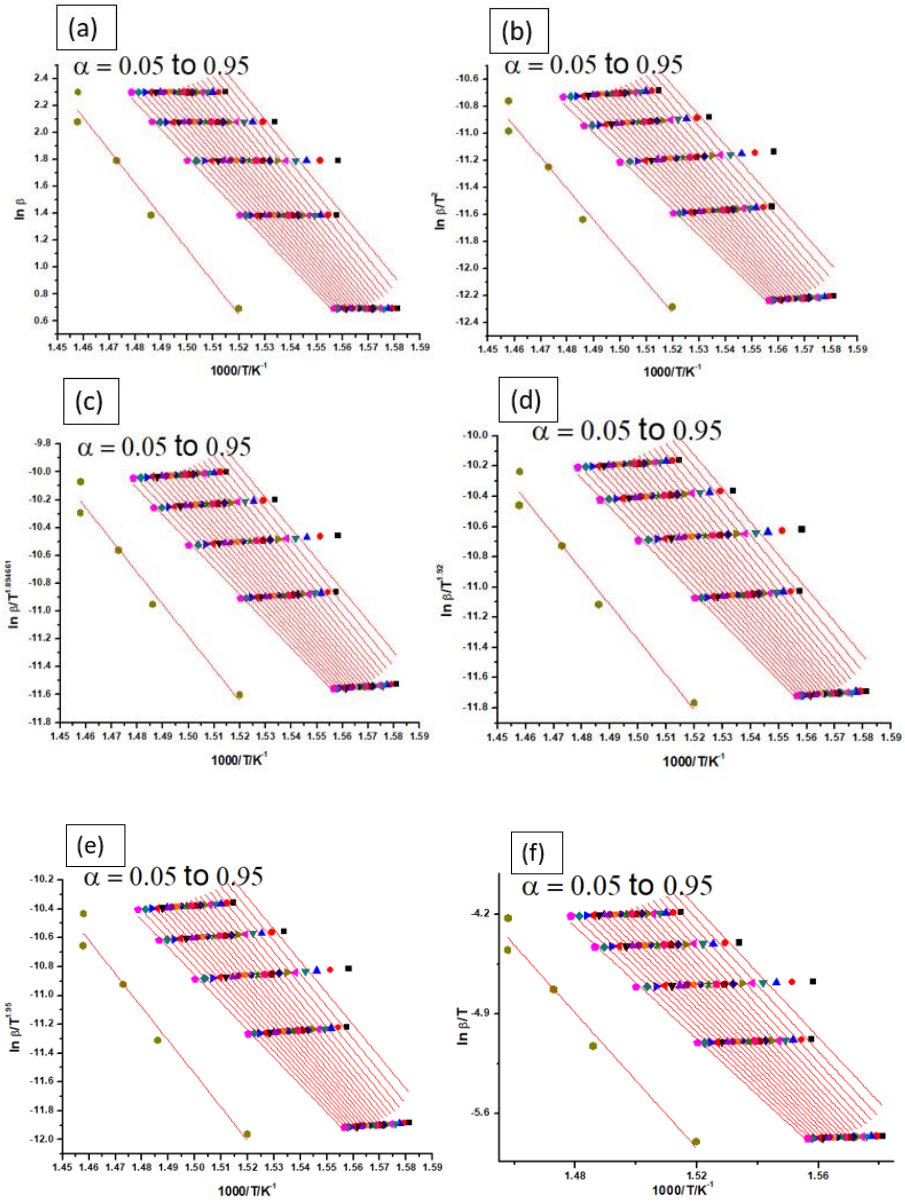

Fig. 10 Linear least squares plot for the decomposition stage of ZnOx for the isoconversional methods of FWO (a), KAS (b), Tang (c), Starink$^{1.92}$ (d), Starink$^{1.95}$ (e) and Boswell (f)

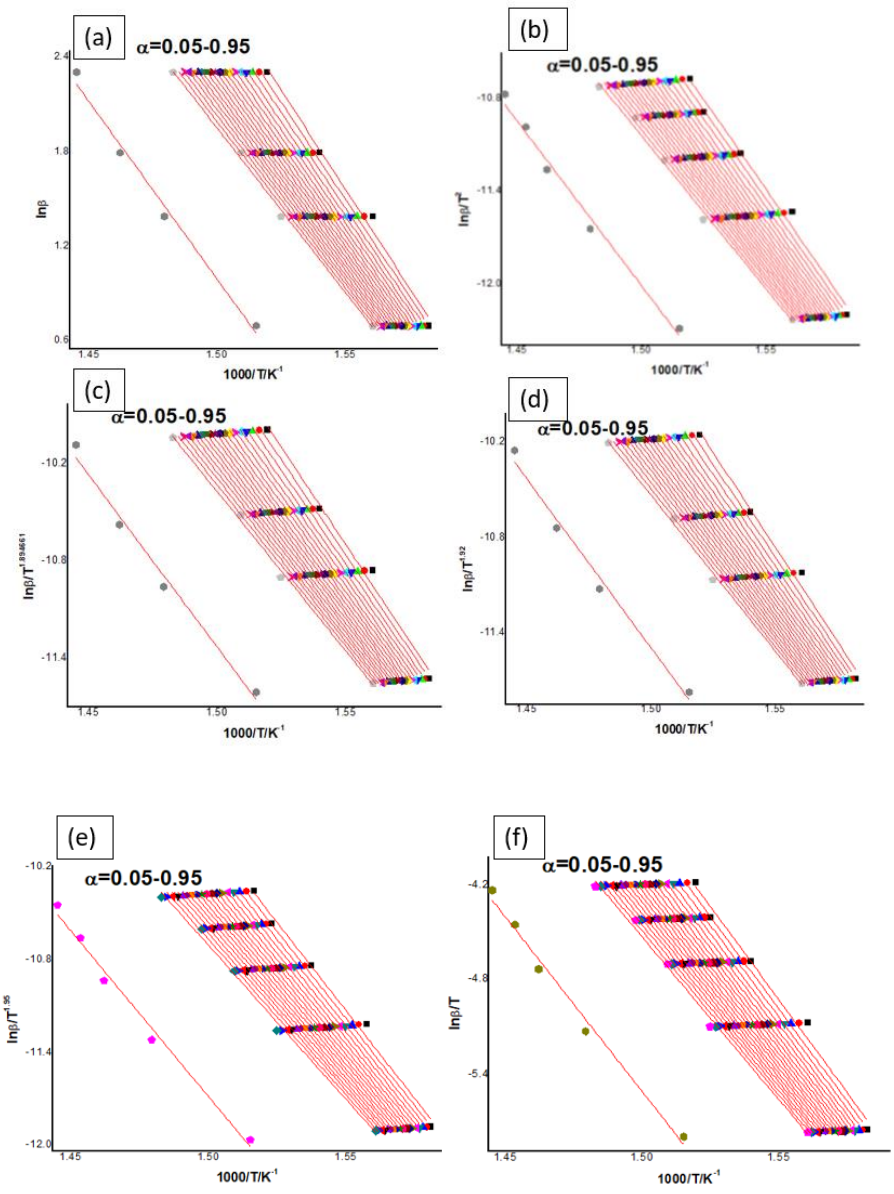

Fig. 11 Linear least squares plot for the decomposition stage of $SZ_{0.1}$ for the isoconversional methods of FWO (a), KAS (b), Tang (c), Starink$^{1.92}$ (d), Starink$^{1.95}$ (e) and Boswell (f)

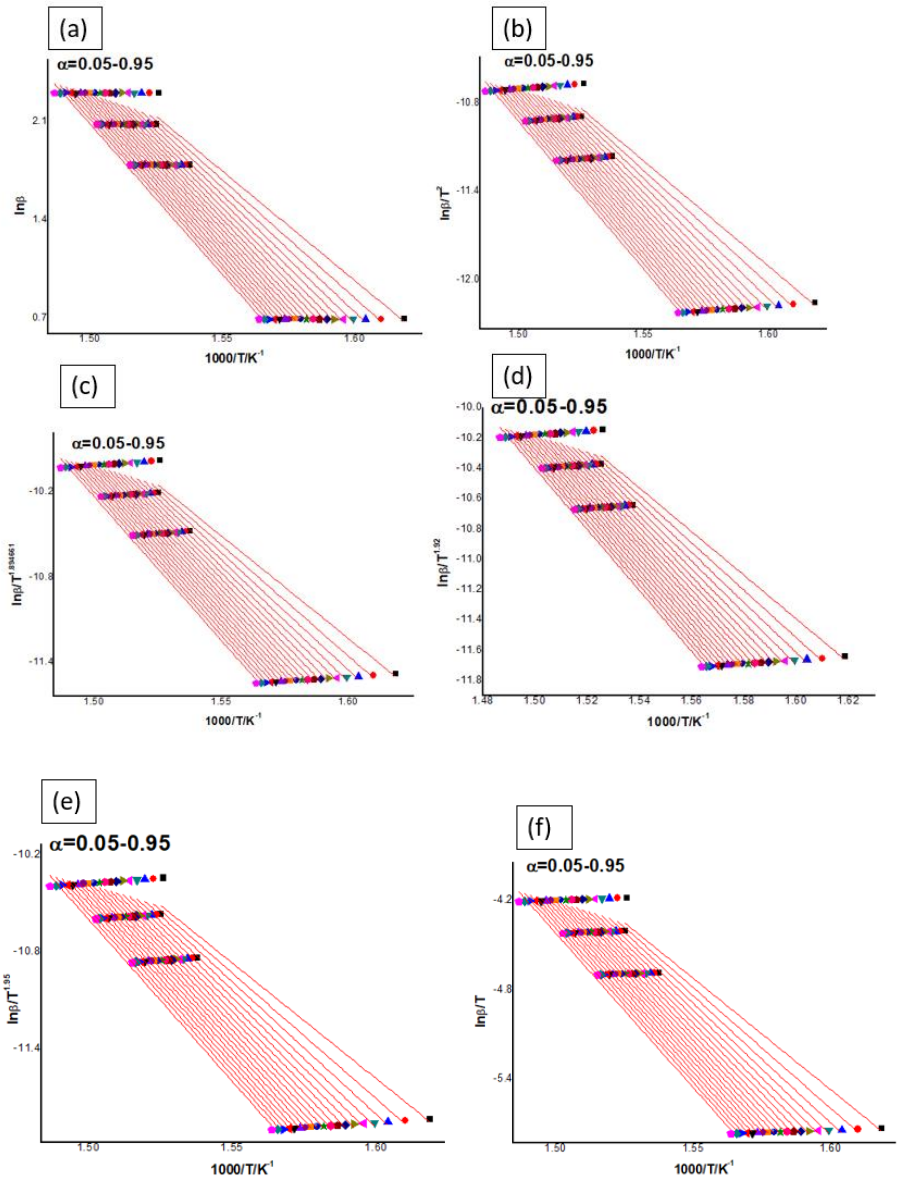

Fig. 12 Linear least squares plot for the decomposition stage of SZ_1 for the isoconversional methods of FWO (a), KAS (b), Tang (c), Starink$^{1.92}$ (d), Starink$^{1.95}$ (e) and Boswell (f)

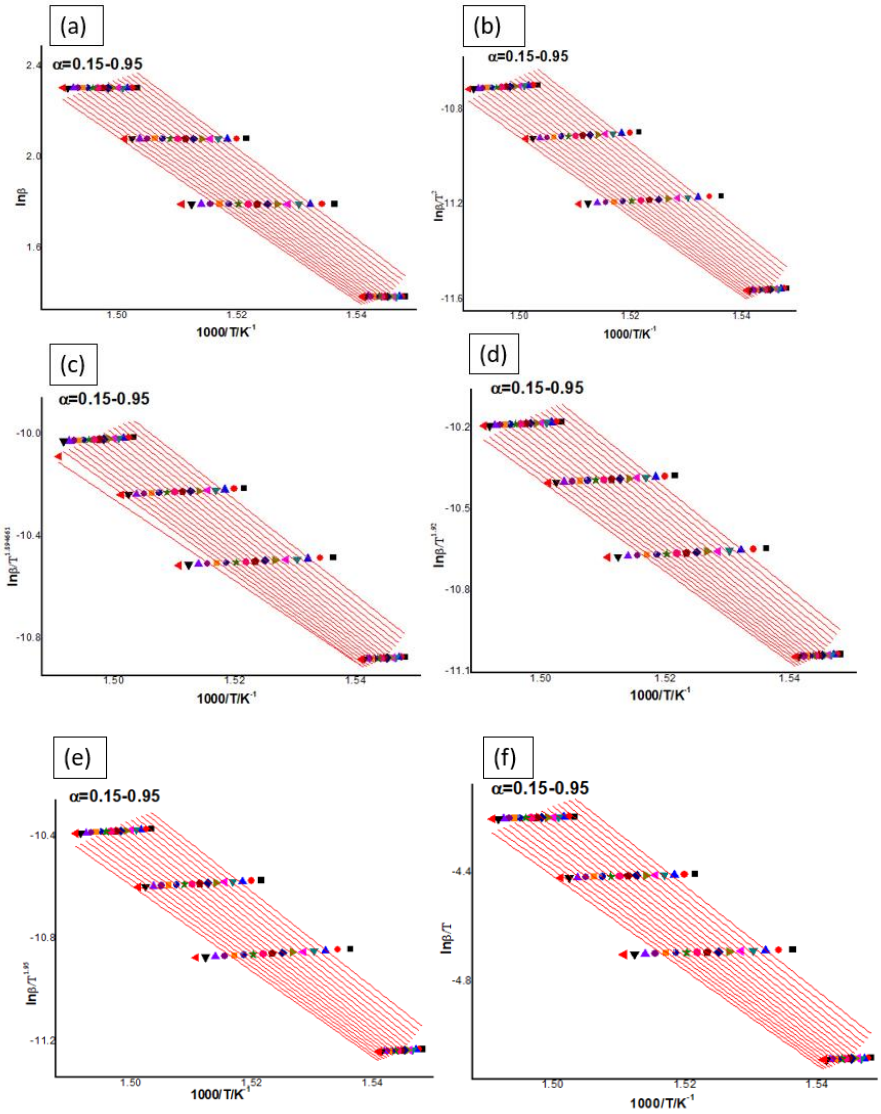

Fig. 13 Linear least squares plot for the decomposition stage of SZ_2 for the isoconversional methods of FWO (a), KAS (b), Tang (c), Starink$^{1.92}$ (d), Starink$^{1.95}$ (e) and Boswell (f)

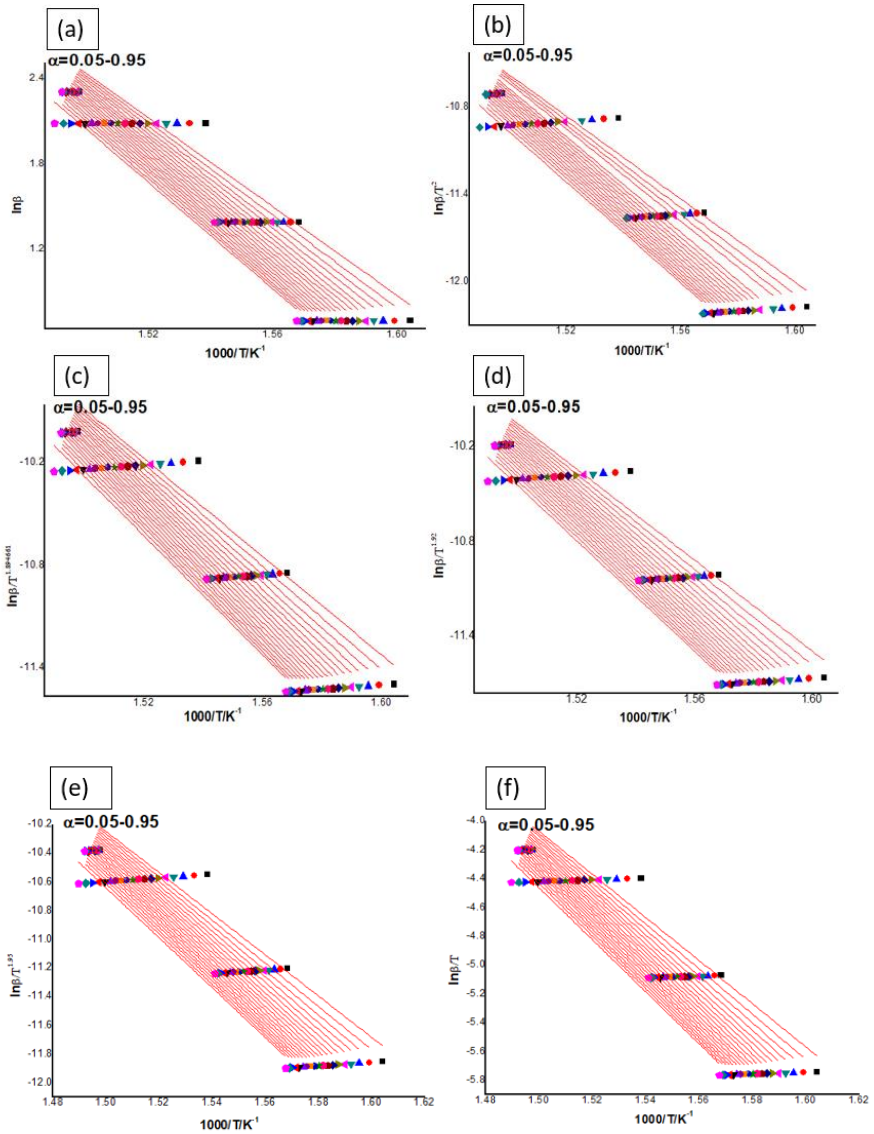

Fig. 14 Linear least squares plot for the decomposition stage of SZ_5 for the isoconversional methods of FWO (a), KAS (b), Tang (c), Starink$^{1.92}$ (d), Starink$^{1.95}$ (e) and Boswell (f)

Table 1 Values of activation energy (E_a) obtained from different integral isoconversional methods for the decomposition of pure zinc oxalate.

	E_a (kJ mol^{-1})					
α	FWO	KAS	Tang	Starink$^{1.92}$	Starink$^{1.95}$	Boswell
0.05	184.45	183.49	183.79	183.78	183.76	188.87
0.10	188.24	187.49	187.78	187.77	187.76	192.87
0.15	189.18	188.24	188.536	188.52	188.51	193.63
0.20	188.66	187.68	187.98	187.96	187.95	193.07
0.25	187.92	186.89	187.19	187.18	187.16	192.29
0.30	186.72	185.61	185.91	185.90	185.88	191.02
0.35	185.52	184.35	184.65	184.63	184.62	189.76
0.40	184.04	182.78	183.09	183.07	183.05	188.20
0.45	182.56	181.21	181.52	181.50	181.48	186.63
0.50	181.17	179.74	180.05	180.03	180.01	185.17
0.55	179.63	178.11	178.43	178.40	178.38	183.54
0.60	178.06	176.45	176.77	176.75	176.72	181.89
0.65	176.28	174.56	174.88	174.86	174.83	180.00
0.70	174.49	172.67	172.99	172.97	172.94	178.12
0.75	172.64	170.72	171.04	171.02	170.99	176.17
0.80	170.35	168.29	168.62	168.59	168.56	173.75
0.85	167.78	165.58	165.91	165.88	165.85	171.04
0.90	164.67	162.29	162.63	162.60	162.56	167.76
0.95	160.74	158.14	158.49	158.45	158.41	163.62
*Av	179.07	177.50	177.82	177.80	177.78	182.94

*Av is the average value of activation energy

Table 2 Values of activation energy (E_a) obtained from different integral isoconversional methods for the decomposition of $SZ_{0.1}$

α	E_a (kJ mol^{-1})					
	FWO	KAS	Tang	Starink$^{1.92}$	Starink$^{1.95}$	Boswell
0.05	182.23	197.61	181.28	181.27	181.00	161.97
0.10	194.74	194.13	194.41	194.41	187.58	177.49
0.15	191.89	191.11	191.40	191.39	185.90	176.04
0.20	189.24	188.32	188.61	188.60	184.28	174.49
0.25	187.04	185.98	186.28	186.27	183.07	173.06
0.30	185.23	184.67	184.38	184.36	181.58	171.35
0.35	183.37	182.10	182.41	182.39	180.37	183.83
0.40	181.72	180.35	180.67	180.65	179.16	196.20
0.45	180.20	178.74	179.06	179.03	178.01	194.41
0.50	178.75	177.21	177.53	177.51	176.85	192.68
0.55	177.34	175.72	176.04	176.02	175.73	191.02
0.60	175.94	174.23	174.55	174.53	174.68	189.40
0.65	174.63	172.85	173.17	173.15	173.44	188.19
0.70	173.24	171.38	171.71	171.68	172.32	186.71
0.75	171.92	169.98	170.31	170.28	170.87	185.51
0.80	170.29	168.26	168.59	168.56	169.31	184.30
0.85	168.53	166.40	166.73	166.70	167.88	183.16
0.90	166.85	164.61	164.95	164.92	166.16	182.00
0.95	164.97	162.63	162.97	162.94	178.49	180.88
*Av	178.85	177.32	177.63	177.61	177.12	182.77

*Av is the average value of activation energy.

Table 3 Values of activation energy (E_a) obtained from different integral isoconversional methods for the decomposition of SZ_1

α	E_a (kJ mol^{-1})					
	FWO	KAS	Tang	Starink$^{1.92}$	Starink$^{1.95}$	Boswell
0.05	123.29	119.13	119.51	119.46	119.39	124.41
0.10	133.07	129.38	129.75	129.70	129.64	134.68
0.15	139.89	136.52	136.88	136.84	136.79	141.84
0.20	144.86	141.73	142.08	142.04	142.00	147.06
0.25	148.84	145.90	146.25	146.21	146.17	151.24
0.30	152.14	149.35	149.69	149.65	149.61	154.70
0.35	154.82	152.15	152.49	152.46	152.42	157.51
0.40	157.17	154.61	154.95	154.91	154.87	159.97
0.45	159.23	156.76	157.10	157.06	157.03	162.13
0.50	160.92	158.52	158.86	158.83	158.79	163.90
0.55	162.50	160.17	160.50	160.47	160.44	165.56
0.6	163.89	161.63	161.96	161.93	161.90	167.02
0.65	164.94	162.71	163.05	163.01	162.98	168.12
0.70	165.98	163.79	164.13	164.10	164.06	169.20
0.75	167.04	164.89	165.22	165.19	165.16	170.31
0.80	167.72	165.60	165.93	165.90	165.87	171.02
0.85	168.35	166.24	166.57	166.55	166.52	171.67
0.90	168.74	166.64	166.97	166.94	166.91	172.08
0.95	169.11	167.01	167.35	167.32	167.29	172.46
*Av	156.45	153.83	154.17	154.14	154.10	159.20

*Av is the average value of activation energy

Table 4 Values of activation energy (E_a) obtained from different integral isoconversional methods for the decomposition of SZ_2

α	E_a (kJ mol^{-1})					
	FWO	KAS	Tang	Starink$^{1.92}$	Starink$^{1.95}$	Boswell
0.15	155.40	152.59	152.75	152.90	152.86	158.03
0.20	157.44	154.73	154.88	155.04	155.00	160.18
0.25	158.44	155.78	155.94	156.09	156.05	161.23
0.30	159.09	156.45	156.62	156.76	156.72	161.90
0.35	159.12	156.48	156.65	156.79	156.75	161.93
0.40	158.91	156.25	156.43	156.56	156.53	161.71
0.45	158.25	155.56	155.74	155.87	155.83	161.02
0.50	157.42	154.68	154.86	154.99	154.95	160.14
0.55	156.30	153.50	153.70	153.81	153.77	158.96
0.60	155.07	152.20	152.40	152.52	152.48	157.67
0.65	153.67	150.73	150.93	151.04	151.00	156.19
0.70	152.06	149.02	149.24	149.34	149.30	154.49
0.75	150.34	147.21	147.43	147.53	147.48	152.68
0.80	148.60	145.38	145.60	145.70	145.65	150.85
0.85	146.63	143.30	143.53	143.62	143.57	148.78
0.90	144.57	141.13	141.38	141.46	141.41	146.61
0.95	142.50	138.95	132.30	139.27	139.22	144.43
*Av	153.75	150.82	150.61	151.13	151.09	156.28

*Av is the average value of the activation energy.

Table 5 Values of activation energy (E_a) obtained from different integral isoconversional methods for the decomposition of SZ_5

α	E_a (kJ mol^{-1})					
	FWO	KAS	Tang	Starink$^{1.92}$	Starink$^{1.95}$	Boswell
0.05	123.29	118.98	119.37	119.31	119.25	124.34
0.10	128.67	124.62	125.00	124.95	124.89	129.99
0.15	132.70	128.85	129.23	129.18	129.12	134.23
0.20	135.82	132.12	132.49	132.44	132.39	137.50
0.25	138.51	134.94	135.31	135.26	135.21	140.33
0.30	140.79	137.34	137.70	137.66	137.60	142.73
0.35	142.72	139.35	139.71	139.67	139.62	144.74
0.40	144.44	141.16	141.52	141.48	141.43	146.56
0.45	145.83	142.61	142.97	142.93	142.88	148.01
0.50	147.00	143.83	144.19	144.15	144.10	149.24
0.55	148.07	144.95	145.31	145.26	145.22	150.36
0.60	148.86	145.77	146.13	146.09	146.05	151.19
0.65	149.60	146.54	146.90	146.85	146.81	151.96
0.70	150.03	146.98	147.34	147.30	147.25	152.41
0.75	150.27	147.23	147.58	147.54	147.50	152.66
0.80	150.17	147.12	147.48	147.44	147.39	152.55
0.85	149.79	146.71	147.07	147.02	146.98	152.14
0.90	149.02	145.88	146.25	146.20	146.16	151.33
0.95	147.66	144.45	144.81	144.77	144.72	149.90
*Av	143.33	139.97	140.08	140.04	139.99	145.38

*Av is the average value of activation energy.

Table 6 The average values of E_a for the decomposition of zinc oxalate and strontium zinc oxalates

Samples	E_a (kJ mol^{-1})					
	FWO	KAS	Tang	Starink$^{1.92}$	Starink$^{1.95}$	Boswell
Pure	179.07	177.50	177.82	177.80	177.78	182.94
$SZ_{0.1}$	178.85	177.32	177.63	177.61	177.12	182.77
SZ_1	156.45	153.83	154.17	154.14	154.10	159.20
SZ_2	153.75	150.82	150.61	151.13	151.09	156.28
SZ_5	143.33	139.97	140.88	140.04	139.99	145.38

The average value of activation energies for the decomposition of pure zinc oxalate in N_2 atmosphere obtained is 179.07, 177.50, 177.82, 177.80, 177.88, and 182.94 kJ mol^{-1} by FWO, KAS, Tang, Starink$^{1.92}$, Starink$^{1.95,}$ and Boswell respectively. The values of activation energy are regularly decreasing with increasing strontium concentration. The average values of activation energy for the decomposition of zinc oxalate and $SZ_{0.1,}$ $SZ_{1,}$ $SZ_{2,}$ and SZ_5 using the FWO method are 179.07, 178.85, 156.45, 153.75, and 143.33 kJ mol^{-1} respectively. From these values of activation energies, it is very clear that the addition of strontium ions into zinc oxalate has a positive role in reducing the activation energies. The addition of 5 mol% strontium ion into zinc oxalate reduces the value of activation energy to a considerable amount of 35.74 kJ mol^{-1}.

The dependence of activation energy with α, obtained from DSC data for the six isoconversional methods for the pure and Sr doped oxalates $SZ_{0.1}$, SZ_1, $SZ_{2,}$ and SZ_5 are shown in **Fig. 15 (a) - (e).** The activation energy values calculated by using the six isoconversional methods are compatible with each other and show similar trends in

variation with α for the decomposition of pure and strontium zinc oxalates. The E_a values obtained for pure zinc oxalate shows a maximum at α = 0.15 and then decreases continuously with the increase in the value of the fraction of conversion. In the doped sample $SZ_{0.1}$, the activation energy increased initially and show a maximum at α = 0.10 and then decreases continuously except in Boswell (in Boswell method, the activation energy first increases then decreases, again increases and then decreases continuously). In the case of SZ_1, the activation energy values increase gradually and reach a maximum value at α = 0.95. In the case of SZ_2, the E_a value shows a sharp increase with α and has a maximum value at α = 0.35 and then decreases gradually. In the case of SZ_5, the E_a value gradually increases, reaches a maximum value at α = 0.75, and then decreases. The variation of E_a with α in SZ_1, SZ_2, and SZ_5 samples is first increasing, reaches a maximum value, and then decreases. The results show that there is no general trend in the variation of activation energy with the conversion fraction in pure and strontium zinc oxalates, but it is observed that the average E_a value decreased with an increase in the strontium content from 0.1 to 5 mol%. The variation in the value of activation energy, E_a with the extent of conversion indicates the complexity of the reaction. The variation of activation energy during thermal decomposition reflects the changing mechanism during the course of the reaction.

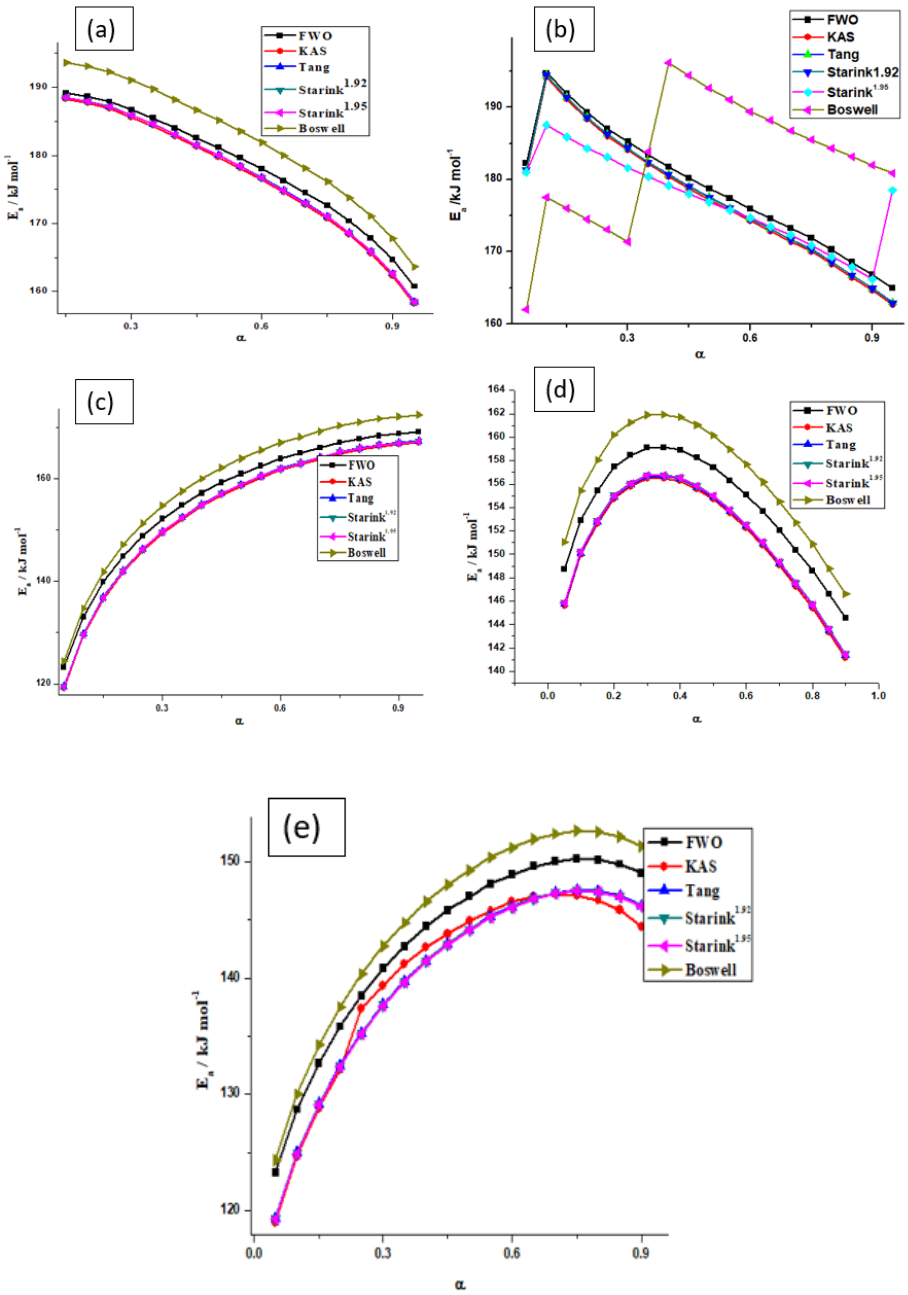

Fig. 15. *E_a vs α* curves for the decomposition of the pure (a), $SZ_{0.1}$ (b), SZ_1 (c), SZ_2 (d) and SZ_5 (e)

Model fitting methods were used to suggest the most probable mechanism. For this, the value of *ln (g (α)/T²) vs 1/T* of the non-isothermal DSC data at 2 K min^{-1} is plotted. The different reaction models *f(α)* used to describe the reaction kinetics and their integrated forms *g(α)* are given in **Table 7**.

Table 7. Different reaction models used to describe the reaction kinetics

No.	Code	Reaction model	*f(α)*	Function *g(α)*
1	P4	Power law	$4\alpha^{3/4}$	$\alpha^{1/4}$
2	P3	Power law	$3\alpha^{2/3}$	$\alpha^{1/3}$
3	P2	Power law	$2\alpha^{1/2}$	$\alpha^{1/2}$
4	P2/3	Power law	$2/3\alpha^{-1/2}$	$\alpha^{3/2}$
5	D1	One-dimensional diffusion	$1/2\alpha^{-1}$	α^2
6	F1	Mampel (first-order)	$1-\alpha$	$-\ln(1-\alpha)$
7	A4	Avrami–Erofeev	$4(1-\alpha)[-\ln(1-\alpha)]^{3/4}$	$(-\ln(1-\alpha))^{1/4}$
8	A3	Avrami–Erofeev	$3(1-\alpha)[-\ln(1-\alpha)]^{2/3}$	$(-\ln(1-\alpha))^{1/3}$
9	A2	Avrami–Erofeev	$2(1-\alpha)[-\ln(1-\alpha)]^{1/2}$	$(-\ln(1-\alpha))^{1/2}$
10	D3	Three-dimensional diffusion	$3/2(1-\alpha)^{2/3}[1-(1-\alpha)^{1/3}]^{-1}$	$(1-(1-\alpha)^{1/3})^2$
11	R3	Contracting sphere	$3(1-\alpha)^{2/3}$	$1-(1-\alpha)^{1/3}$
12	R2	Contracting cylinder	$2(1-\alpha)^{1/2}$	$1-(1-\alpha)^{1/2}$
13	F2	Second-order	$(1-\alpha)^2$	$(1-\alpha)^{-1}-1$
14	D2	Two-dimensional diffusion	$-[\ln(1-\alpha)]^{-1}$	$(1-\alpha)*\ln(1-\alpha)+\alpha$

Fig. 16 (a)-(d) show model fitting least squares plots for the decomposition reaction of strontium added zinc oxalates. The plot will be a straight line for a correct mechanism and non-linear for the inaccurate mechanism. The most probable mechanism for

decomposition reaction of pure zinc oxalate was found to be $g(\alpha) = -\ln(1-\alpha)^{1/2}$ *i.e.*, Avrami-Erofeev equation A2) whose $f(\alpha) = 2*(1-\alpha)[-\ln(1-\alpha)]^{1/2}$ [30].

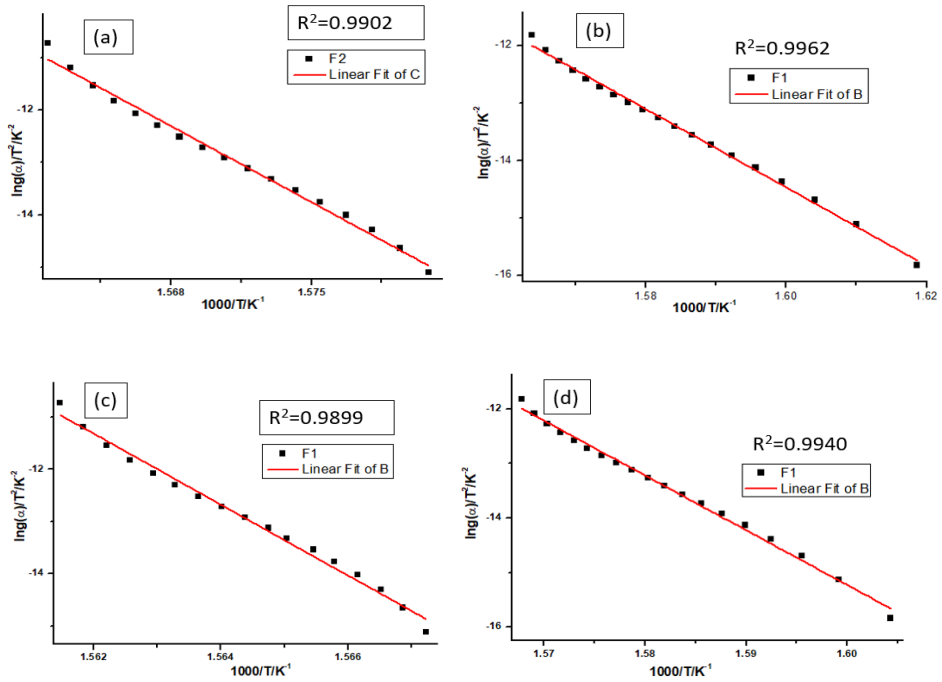

Fig. 16 Model fitting least squares plots for the decomposition reaction of $SZ_{0.1}$ (a), SZ_1 (b), SZ_2 (c), and SZ_5 (d) at a heating rate of 2 K min^{-1}

The most probable mechanism for decomposition reaction of $SZ_{0.1}$ was found to be with $g(\alpha) = (1-\alpha)^{-1}-1$ *i.e.*, Mampel (second-order F2) whose $f(\alpha) = (1-\alpha)^2$ and for SZ_1, SZ_2, and SZ_5, $g(\alpha) = -\ln(1-\alpha)$ *i.e.*, Mampel (First-order F1) whose $f(\alpha) = 1-\alpha$. From the model fitting studies, it is inferred that the mechanism of the thermal decomposition reaction is changed with the addition of strontium. All the strontium containing samples obeys Mampel equations.

4.4. Conclusion

The synthesized zinc oxalate and strontium-zinc oxalates were characterized by using FT-IR and TG in air and confirmed the formation of zinc oxalate dihydrate and the decomposition into their corresponding oxides. The decomposition products ZnO/ Sr-ZnO were analyzed by using UV-DRS, FTIR, XRD, and HRTEM. The bandgap of ZnO decreased from 3.03 eV by the addition of strontium ions into the ZnO lattice due to the creation of oxygen vacancies. The average crystallite size obtained from XRD measurements using Scherrer equation for ZnO is 44.06 nm and it reduced to 39.7 nm upon the addition of 5 mol% Sr evidencing the substitutional effect of Sr. The kinetic analysis of zinc-strontium oxalates prepared to show a decrease in the average value of activation energy with an increase in the concentration of strontium ion. As the extent of conversion varies, the energy of activation also changes, which indicates the complexity of the reaction. The variation of activation energy during the thermal decomposition reflects the changing mechanism during the course of the reaction. It is interesting to note that the activation energy for zinc oxalate decomposition is decreased from 179.07 to 143.33 kJ mol^{-1} by the addition of 5 mol% strontium. The addition of strontium into zinc oxalate also cause to change the mechanism of the thermal decomposition reaction. Pure zinc oxalate obeys Avrami-Erofeev equation and all the strontium containing samples follow the Mampel equation during thermal decomposition reaction.

4.5. References

[1] S. Suwanboon, P. Amornpitoksuk, A. Haidoux, J.C. Tedenac, Structural and optical properties of undoped and aluminium doped zinc oxide nanoparticles via precipitation method at low temperature, J. Alloys Compd. 462 (2008) 335–339.

[2] A.K. Galway, M.E. Brown, Thermal decomposition of ionic solids, Elsevier, 1999.

[3] S. Suwanboon, P. Amornpitoksuk, A. Sukolrat, Dependence of optical properties on doping metal, crystallite size and defect concentration of M-doped ZnO nanopowders (M=Al, Mg, Ti), Ceram. Int. 37 (2011) 1359–1365.

[4] S.M. Gheno, R.H.G.A. Kiminami, M.R. Morelli, P.I. Paulin Filho, Electric force microscopy investigations of barrier formations in ZnO-based varistors, J. Eur. Ceram. Soc. 30 (2010) 549–554.

[5] Y. Wang, X. Li, N. Wang, X. Quan, Y. Chen, Controllable synthesis of ZnO nanoflowers and their morphology-dependent photocatalytic activities, Sep. Purif. Technol. 62 (2008) 727–732.

[6] J. Zheng, Z.-Y. Jiang, Q. Kuang, Z.-X. Xie, R.-B. Huang, L.-S. Zheng, Shape-controlled fabrication of porous ZnO architectures and their photocatalytic properties, J. Solid State Chem. 182 (2009) 115–121.

[7] X. Wei, D. Chen, Synthesis and characterization of nanosized zinc aluminate spinel by sol–gel technique, Mater. Lett. 60 (2006) 823–827.

[8] M. Salavati-Niasari, N. Mir, F. Davar, ZnO nanotriangles: Synthesis, characterization and optical properties, J. Alloys Compd. 476 (2009) 908–912.

[9] C.J. Cong, L. Liao, J.C. Li, L.X. Fan, K.L. Zhang, Synthesis, structure and ferromagnetic properties of Mn-doped ZnO nanoparticles, Nanotechnology. 16 (2005) 981–984.

[10] C.J. Cong, J.H. Hong, Q.Y. Liu, L. Liao, K.L. Zhang, Synthesis, structure and ferromagnetic properties of Ni-doped ZnO nanoparticles, Solid State Commun. 138 (2006) 511–515.

[11] G.N. Dar, A. Umar, S.A. Zaidi, A.A. Ibrahim, M. Abaker, S. Baskoutas, M.S. Al-Assiri, Ce-doped ZnO nanorods for the detection of hazardous chemical, Sensors Actuators B Chem. 173 (2012) 72–78.

[12] J. Zhong, S. Muthukumar, Y. Chen, Y. Lu, H.M. Ng, W. Jiang, E.L. Garfunkel, Ga-doped ZnO single-crystal nanotips grown on fused silica by metalorganic chemical vapor deposition, Appl. Phys. Lett. 83 (2003) 3401–3403.

[13] J. Jie, G. Wang, X. Han, Q. Yu, Y. Liao, G. Li, J.G. Hou, Indium-doped zinc oxide nanobelts, Chem. Phys. Lett. 387 (2004) 466–470.

[14] L. Zhu, M. Zhi, Z. Ye, B. Zhao, Catalyst-free two-step growth of quasialigned ZnMgO nanorods and their properties, Appl. Phys. Lett. 88 (2006) 113106.

[15] R.-C. Wang, C.-P. Liu, J.-L. Huang, S.-J. Chen, Single-crystalline AlZnO nanowires/nanotubes synthesized at low temperature, Appl. Phys. Lett. 88 (2006) 23111.

[16] S.H. Kim, A. Umar, Y.K. Park, J.-H. Kim, E.W. Lee, Y.B. Hahn, Non-catalytic growth of high-aspect-ratio Sb-doped ZnO nanowires by simple thermal evaporation process: Structural and optical properties, J. Alloys Compd. 479 (2009) 290–293.

[17] A.A. Ibrahim, G.N. Dar, S.A. Zaidi, A. Umar, M. Abaker, H. Bouzid, S. Baskoutas, Growth and properties of Ag-doped ZnO nanoflowers for highly sensitive phenyl hydrazine chemical sensor application, Talanta. 93 (2012) 257–263.

[18] W. Liang, B.D. Yuhas, P. Yang, Magnetotransport in Co-Doped ZnO Nanowires, Nano Lett. 9 (2009) 892–896.

[19] T.A. Vijayan, R. Chandramohan, S. Valanarasu, J. Thirumalai, S.P. Subramanian, Comparative investigation on nanocrystal

structure, optical, and electrical properties of ZnO and Sr-doped ZnO thin films using chemical bath deposition method, J. Mater. Sci. 43 (2008) 1776–1782.

[20] W. Water, Y.-S. Yan, Characteristics of strontium-doped ZnO films on love wave filter applications, Thin Solid Films. 515 (2007) 6992–6996.

[21] T. Das, B.K. Das, K. Parashar, R. Kumar, H.K. Choudhary, A. V Anupama, B. Sahoo, P.K. Sahoo, S.K.S. Parashar, Effect of Sr-doping on sinterability, morphology, structure, photocatalytic activity and AC conductivity of ZnO ceramics, J. Mater. Sci. Mater. Electron. 28 (2017) 13587–13595.

[22] S.L. Perumal, P. Hemalatha, M. Alagara, K.N. Pandiyaraj, Investigation of structural, optical and photocatalytic properties of Sr doped ZnO nanoparticles, Int. J. Chem. Phys. Sci. 4 (2015) 1–13.

[23] P.M. Shirage, A.K. Rana, Y. Kumar, S. Sen, S.G. Leonardi, G. Neri, Sr- and Ni-doping in ZnO nanorods synthesized by a simple wet chemical method as excellent materials for CO and CO_2 gas sensing, RSC Adv. 6 (2016) 82733–82742.

[24] R. Yousefi, F. Jamali-Sheini, M. Cheraghizade, S. Khosravi-Gandomani, A. Sáaedi, N.M. Huang, W.J. Basirun, M. Azarang, Enhanced visible-light photocatalytic activity of strontium-doped zinc oxide nanoparticles, Mater. Sci. Semicond. Process. 32 (2015) 152–159.

[25] D. Li, J.-F. Huang, L.-Y. Cao, J.-Y. LI, H.-B. OuYang, C.-Y. Yao, Microwave hydrothermal synthesis of Sr^{2+} doped ZnO crystallites with enhanced photocatalytic properties, Ceram. Int. 40 (2014) 2647–2653.

[26] N.N. Kumaran, K. Muraleedharan, Photocatalytic activity of ZnO and Sr^{2+} doped ZnO nanoparticles, J. Water Process Eng. 17 (2017) 264–270.

[27] B. Subash, B. Krishnakumar, V. Pandiyan, M. Swaminathan, M. Shanthi, Synthesis and characterization of novel WO_3 loaded Ag

– ZnO and its photocatalytic activity, Mater. Res. Bull. 48 (2013) 63–69.

[28] B. Subash, B. Krishnakumar, R. Velmurugan, M. Swaminathan, M. Shanthi, Synthesis of Ce co-doped Ag – ZnO photocatalyst with excellent performance for NBB dye degradation under natural sunlight illumination, Catal. Sci. Technol. 2 (2012) 2319–2326.

[29] V. Kuzhalosai, B. Subash, M. Shanthi, A novel sunshine active cerium loaded zinc oxide photocatalyst for the effective degradation of AR 27 dye, Mater. Sci. Semicond. Process. 27 (2014) 924–933.

[30] K. Sabira, K. Muraleedharan, Exploration of the thermal decomposition of zinc oxalate by experimental and computational methods, J. Therm. Anal. Calorim. https://doi.org/10.1007/s10973-019-09169-6.

[31] C. Hu, J. Mi, S. Shang, J. Shangguan, The study of thermal decomposition kinetics of zinc oxide formation from zinc oxalate dihydrate, J. Therm. Anal. Calorim. 115 (2014) 1119–1125.

[32] B. Małecka, E. Dro, A. Małecki, Mechanism and kinetics of thermal decomposition of zinc oxalate, Thermochim. Acta. 423 (2004) 13–18.

[33] S. Vyazovkin, N. Sbirrazzuoli, Isoconversional Analysis of the Nonisothermal Crystallization of a Polymer Melt, Macromol. Rapid Commun. 23 (2002) 766–770.

[34] A.A. Joraid, A.A. Abu-Sehly, M.A. El-Oyoun, S.N. Alamri, Nonisothermal crystallization kinetics of amorphous $Te_{51.3}As_{45.7}Cu_3$, Thermochim. Acta. 470 (2008) 98–104.

[35] M.J. Starink, The determination of activation energy from linear heating rate experiments: a comparison of the accuracy of isoconversion methods, Thermochim. Acta. 404 (2003) 163–176.

[36] A. Khawam, D.R. Flanagan, Role of isoconversional methods in varying activation energies of solid-state kinetics: II.

Nonisothermal kinetic studies, Thermochim. Acta. 436 (2005) 101–112.

[37] S. Vyazovkin, Model-free kinetics, J. Therm. Anal. Calorim. 83 (2006) 45–51.

[38] M.J. Starink, Activation energy determination for linear heating experiments: deviations due to neglecting the low temperature end of the temperature integral, J. Mater. Sci. 42 (2007) 483–489.

[39] K. Sarada, K. Muraleedharan, Effect of addition of silver on the thermal decomposition kinetics of copper oxalate, J. Therm. Anal. Calorim. 123 (2016) 643–651.

[40] T. Ozawa, A New Method of Analyzing Thermogravimetric Data, Bull. Chem. Soc. Jpn. 38 (1965) 1881–1886.

[41] J.H. Flynn, L.A. Wall, A quick, direct method for the determination of activation energy from thermogravimetric data, J. Polym. Sci. Part B Polym. Lett. 4 (1966) 323–328.

[42] H.E. Kissinger, Reaction Kinetics in Differential Thermal Analysis, Anal. Chem. 29 (1957) 1702–1706.

[43] C.W. Wanjun Tang, Yuwen Liu, Hen Zhang, New approximate formula for Arrhenius temperature integral, Thermochim. Acta. 408 (2003) 39–43.

EFFECT OF BARIUM ADDITION ON THE KINETICS OF THERMAL DEHYDRATION AND DECOMPOSITION OF ZINC OXALATE DIHYDRATE

5.1. Introduction

Nanomaterials are among the most challenging areas of current scientific and technological research because of their tremendous possibilities in generating novel shapes, structures, and the unusual phenomena associated with these materials [1] [2]. Mixed metal oxide (MMO) nanoparticles (also called heterometal oxide nanoparticles) can play an appreciable role in many areas of chemistry and physics. The unique electronic and magnetic properties obtained when combining two metals in an oxide matrix have been well studied. However, the most common use for MMOs has been in the area of catalysis [3].

Among the nanostructured metal oxides, ZnO is considered to be one of the best metal oxides that can be used at a nanoscale level [4]. From this point of view, nanostructured ZnO powders display great power in many applications such as gas sensors, solar cells, ultraviolet (UV) photonic devices, blue-green laser diodes, nonlinear optical devices, varistors and photocatalyst with high chemical activity [5] [6]. ZnO is known to be used as a highly efficient desulfurizer of coal-derived fuel gas and chemically synthesized gases since it can reduce the concentration of H_2S to a few parts per million [7]. Amongst many metal oxides, zinc oxide (ZnO) has remained as a very prominent low-cost wide band-gap semiconducting material.

Doping ZnO nanostructures with metal ions is a strategy to modify their electronic and optical performance and improve their applications [8]. Doping ZnO with transition metal enhances the ferromagnetic and piezoelectric coefficients with predicted Curie temperature above room temperature [9] The literature review revealed that there are plenty of reports showing the optical and magnetic properties of transition and non-transition metals doped ZnO. Gupta *et al.* [10] reported ferroelectric transition around 343 K in K doped ZnO nanorods, Yang *et al.* observed and explained the multiferroic behavior of Cr doped ZnO [11]. Effects of Ba doping on structural, optical, and ferroelectric properties of ZnO nanoparticles prepared by a low-cost thermal decomposition method are presented by Gunjan Srinet *et al*., and they observed that some structural transformation in the morphology of nanostructure has occurred with Ba doping. The doping of Ba also causes a red shift in the UV–visible spectra, a high value of dielectric constant, transition temperature, a high value of remnant polarization, and low value of the coercive field which can be useful for potential applications [12]. S. D. Bukkitgar *et al.*, studied the mefenamic acid-sensing properties of 5% barium doped ZnO nanoparticles using glassy carbon electrodes and the developed method was used in the in-vitro analysis of mefenamic acid in pharmaceutical formulations and spiked human urine samples [13]. Ba-doped ZnO nanospheres show superior photocatalytic efficiency compared to pure ZnO and commercial TiO_2 [3]. The doping of Ba on ZnO nanoparticles causes changes in the optical, mechanical, photocatalytic, and electric

properties of ZnO, so it is very important to study the effect of Ba doping on the kinetics of formation of ZnO nanoparticles.

Transition metal oxalates act as the precursors for the synthesis of oxide nanoparticles. Transition metal oxalates, where oxalate ($C_2O_4^{2-}$) is the simplest dicarboxylate, are representative of transition metal oxide precursors because of the advantages of low cost, various preparation methods, and easy transformation at relatively low temperatures [14]. Ultra-fine transition metal particles are a base for developing technologies such as metal injection moulding, ceramics, and thick/thin-film applications.

There is plenty of reports available on thermal decomposition of zinc oxalate [15–21] but there is no report on the effect of Ba addition on the kinetics of the formation of Ba-ZnO from their oxalate precursors. The present investigation aims to the synthesis and characterization of Ba doped zinc oxide nanoparticles by a simple, low cost, co-precipitation method followed by decomposition and the examination of the kinetics of the thermal decomposition of the formation of ZnO and Ba-ZnO nanoparticles from their oxalates precursors by non-isothermal TG in the air and DSC in N_2 with a view of obtaining the kinetic parameters and also to study the effect of barium doping on the kinetics of dehydration and decomposition of zinc oxalate dihydrate, the knowledge of which helps in the modification of the decomposition products by suitably altering the oxalate precursor.

5.2. Experimental Section

5.2.1. Materials

AnalaR grade zinc nitrate hexahydrate**,** oxalic acid ($H_2C_2O_4.2H_2O$), barium nitrate, all of Merck, India; assay ≥99.9%, and KBr (Sigma) were used.

5.2.2. Preparation of Ba added zinc oxalate

The solutions of zinc nitrate with four different concentrations of barium, 2, 3, 4, and 5 mol % which are designated as $BZOx_2$, $BZOx_3$, $BZOx_4$, and $BZOx_5$ are prepared in deionized water. The solutions were co-precipitated by adding 0.1 M oxalic acid solution with warming and stirring. The resultant solution was stirred for another 2 h. The reacted solution was kept for some time to settle down the precipitate, then filtered off and washed several times with deionized water and air-dried in an oven kept at 343 K and was used for characterization and thermal analysis. The precipitates of Ba-ZnOx were powdered. Pure zinc oxalates (ZnOx) were also prepared as per the above-mentioned method as a reference sample without adding barium. The zinc oxide and barium containing ZnO nanoparticles were designated as ZO, BZO_2, BZO_3, BZO_4, and BZO_5 of barium concentrations 2, 3, 4, and 5 mol% respectively.

5.2.3. Characterization of the sample

Fourier transform infrared (FT-IR) spectra of the samples was recorded by the transmittance method using a spectrometer (Model:

Jasco FT-IR-4100) after diluting the samples with KBr powder. For taking the FT-IR spectra of the samples, the samples were well-grounded and the powdered samples were pressed using the hydraulic pellet press (KP, SR. No. 1718) under a pressure of 50 kg cm^{-2}. The optical band gap (Eg) of the decomposed product was calculated from UV–Visible reflectance which was measured using UV–Visible diffuse reflectance spectrum (Model: Jasco V-550 spectrophotometer). The powder X-ray diffraction (XRD) patterns of the samples were recorded using a diffractometer (Miniflex 600, Model: RigakuD/Max) with Cu-Kα (λ=1.5418 Å) radiation (40 kV, 15 mA) with a scan rate of 2θ min^{-1} in the region of 20–90^o.

5.2.4. Measurement of thermal behavior

TG measurements were made on a Perkin Elmer Pyris Thermal Analyser STA8000 at five different heating rates 2, 4, 6, 8, and 10 K min^{-1}. The operational characteristics of the thermal analysis system are as follows: atmosphere: air, sample mass: ~5 mg; and sample pan: silica. Duplicate runs were made under similar conditions and found that the data overlap with each other, indicating satisfactory reproducibility. The differential scanning calorimetric (DSC) measurements of the samples were done in the temperature range 303–773 K at five different heating rates, 2, 4, 6, 8, and 10 K min^{-1} on a Mettler Toledo DSC822e. The operational characteristics of the DSC system are as follows: atmosphere: flowing N_2 at a flow rate of 50 mL min^{-1}; sample mass ~5 mg; and sample holder: silica.

5.3. Results and discussion

5.3.1. Sample characterization

Fig. 1 shows the FT-IR spectra of zinc oxalate and barium added zinc oxalate of barium concentrations 2, 3, 4, and 5 mol%, and **Fig. 2** shows the FT-IR spectra of ZnO and Ba-ZnO nanoparticles. The strong broad band centered at about 3,410 cm^{-1} is assigned to stretching modes of hydrated water, υ(O–H); this band arises due to the presence of water present in the sample. The strong band at 1,640 cm^{-1} is characteristic of C=O antisymmetric stretching modes υ_{as}(C=O). The small peaks at 1349 and 1323 cm^{-1} is due to the O–C–O stretching modes and the small bands at 821 and 468 cm^{-1} are due to the O-C=O bending modes υ(O–C=O) and Zn-O stretching modes υ (Zn–O). The FT-IR spectra of ZnO and Ba-ZnO nanoparticles show only the stretching mode of Zn-O at 465 cm^{-1} indicating that ZnO only is the final product.

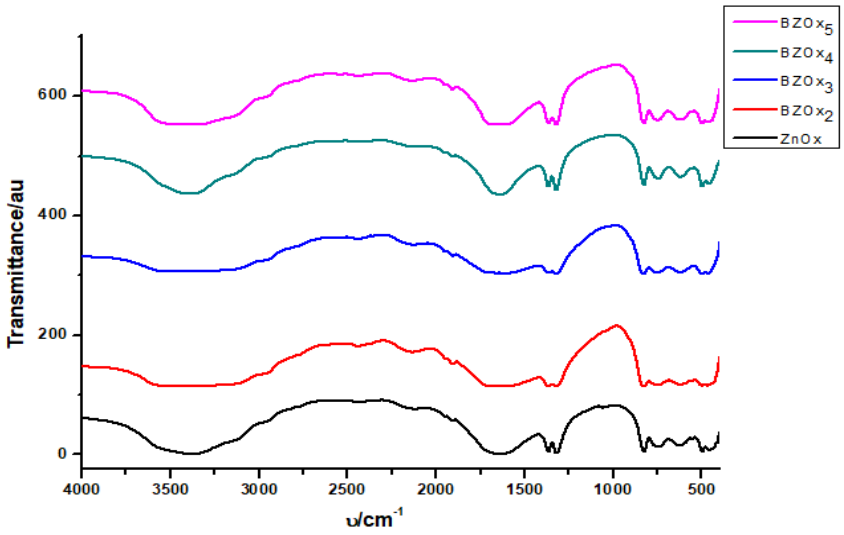

Fig. 1 FT-IR spectra of ZnOx and Ba-ZnOx

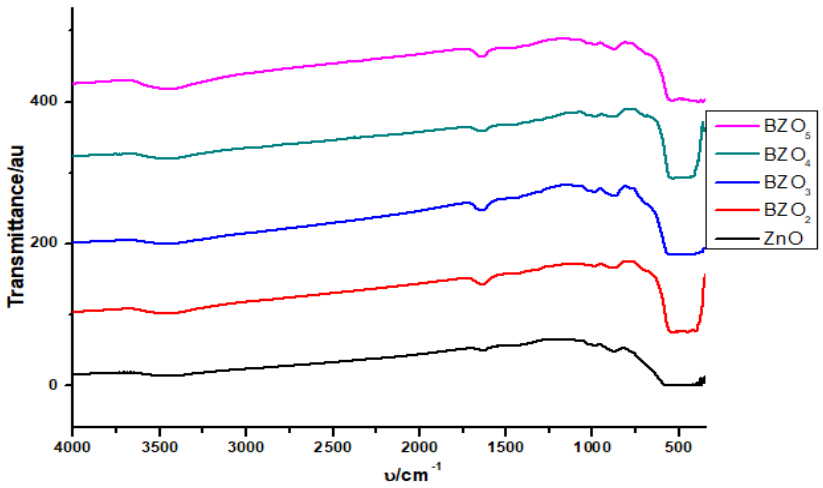

Fig. 2 FT-IR spectra of ZnO and Ba-ZnO nanoparticles

The FTIR spectra obtained for $ZnC_2O_4.2H_2O$ and ZnO were compared with the FTIR spectra reported by Chengcheng Hu *et al.* [18] and found that the bands obtained was perfectly matched with this one.

Fig. 3 shows the structural characteristics of zinc oxide nanoparticles and its mixed oxides with barium in different ratios (2, 3, 4, and 5 mol %) investigated by powder XRD. These XRD patterns reveal that both the zinc oxalate and its mixed oxalates with barium are highly crystalline in nature. The peaks centered at 31.75, 34.69, 36.58, 47.70, 56.74, 63.05, 66.62, 68.31, and 69.36 can be assigned to the (100), (022), (101), (102), (110), (103), (200), (112) and (201) planes of wurtzite ZnO. The absence of an additional peak of barium in the XRD pattern indicates the successful doping of barium in the ZnO lattices.

The position of the peaks and crystallinity did not change by the incorporation of barium in the ZnO lattice. The crystallite size is

determined from the XRD line broadening using the Debye-Scherrer equation [22]:

$$d = 0.9\lambda/\beta\cos\theta \quad (1)$$

where d is the crystallite size, λ is the wavelength used in XRD (0.15418 nm), θ is the Bragg angle in radians, β is the full width at half maximum intensity in radians. The crystallite size of ZnO and Ba-ZnO nanoparticles are different in different planes. The crystallite sizes along (100) planes for ZnO and BZO_2, BZO_3, BZO_4, and BZO_5 are 35.6, 46.9, 47.7, 45.8, and 45.6 nm respectively. The crystallite size first increased with Ba addition up to 3 mol% then it is decreasing on further addition of Ba loading. The decrease in size is not much visible by the addition of barium greater than 4 mol%. The average crystallite size in all the barium added ZnO nanoparticles were higher than that of pure ZnO nanoparticles.

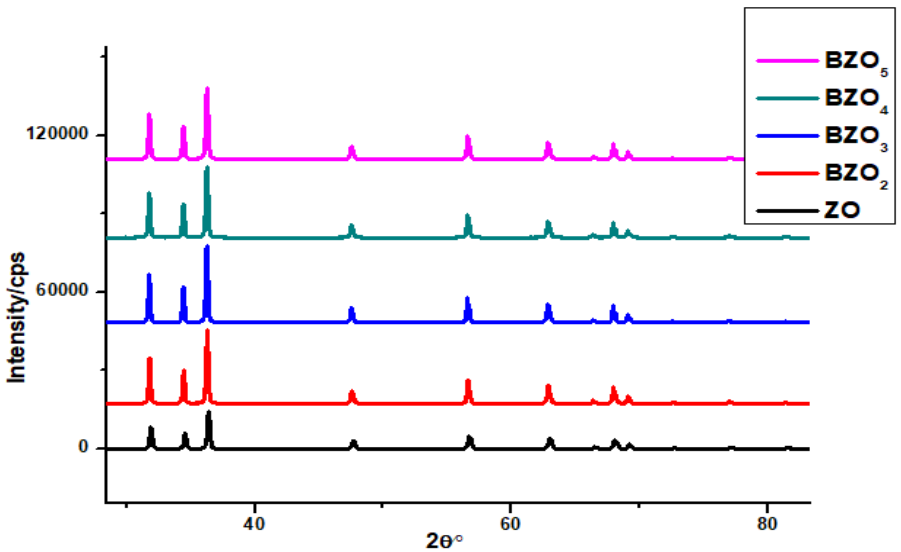

Fig. 3 Powder XRD pattern of ZnO and Ba-ZnO nanoparticles

Fig. 4 shows the Fig. 4 UV-Visible spectra of ZnO and *Ba-ZnO nanoparticles* and from the spectra, it is observed that all oxide nanoparticles have adsorption maximum at about 360 nm. **Fig. 5** shows the Tauc-plot of ZnO and Ba-ZnO nanoparticles. The optical band gap (E_g) of the decomposed product was calculated from UV–Vis reflectance which was measured using the UV–Vis diffuse reflectance spectrum. The optical band gap is determined by using the Tauc equation

$$(\alpha h\upsilon)^n = B(h\upsilon - Eg) \qquad (2)$$

where $h\upsilon$ is the photon energy, α is the absorption coefficient, B is a constant relative to the material and n is either 2 for direct transition or 1/2 for an indirect transition. The band gap obtained for ZnO nanoparticles is 2.95 eV.

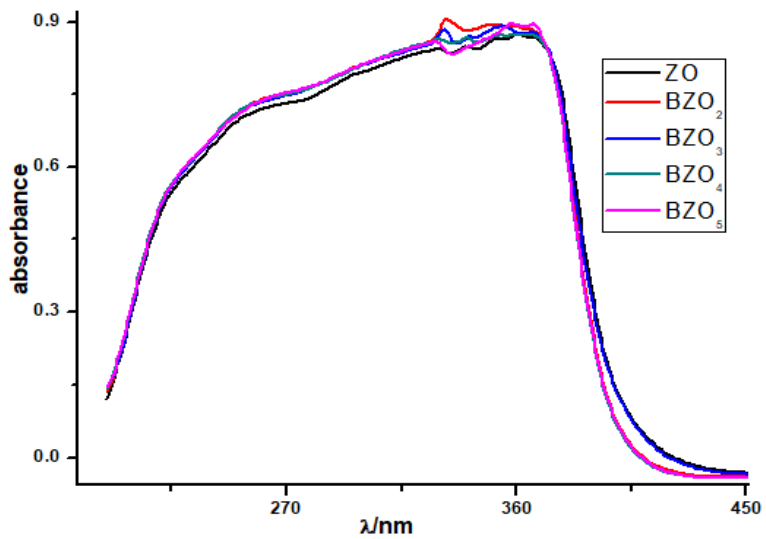

Fig. 4 UV-Visible spectra of ZnO and Ba-ZnO nanoparticles

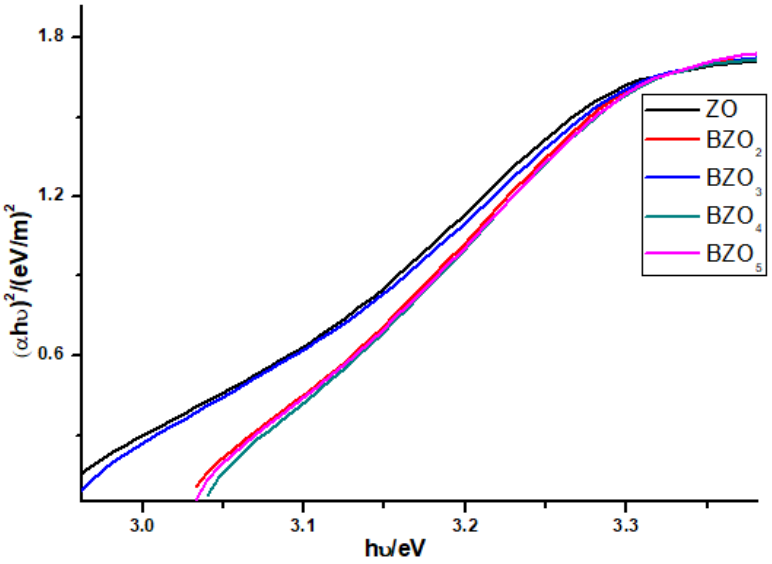

Fig. 5 Tauc-plot of ZnO and Ba-ZnO nanoparticles

The band gap obtained for barium added ZnO nanoparticles are higher than that of pure ZnO. The band gap obtained for BZO_2, BZO_3, BZO_4, and BZO_5 is 3.02, 2.96, 3.02, and 3.01 eV respectively.

5.3.2. Characterization of thermal events

The DSC curves obtained for the thermal decomposition of zinc oxalate and the barium-zinc oxalates are shown in **Fig. 6 (a)-(e)**.

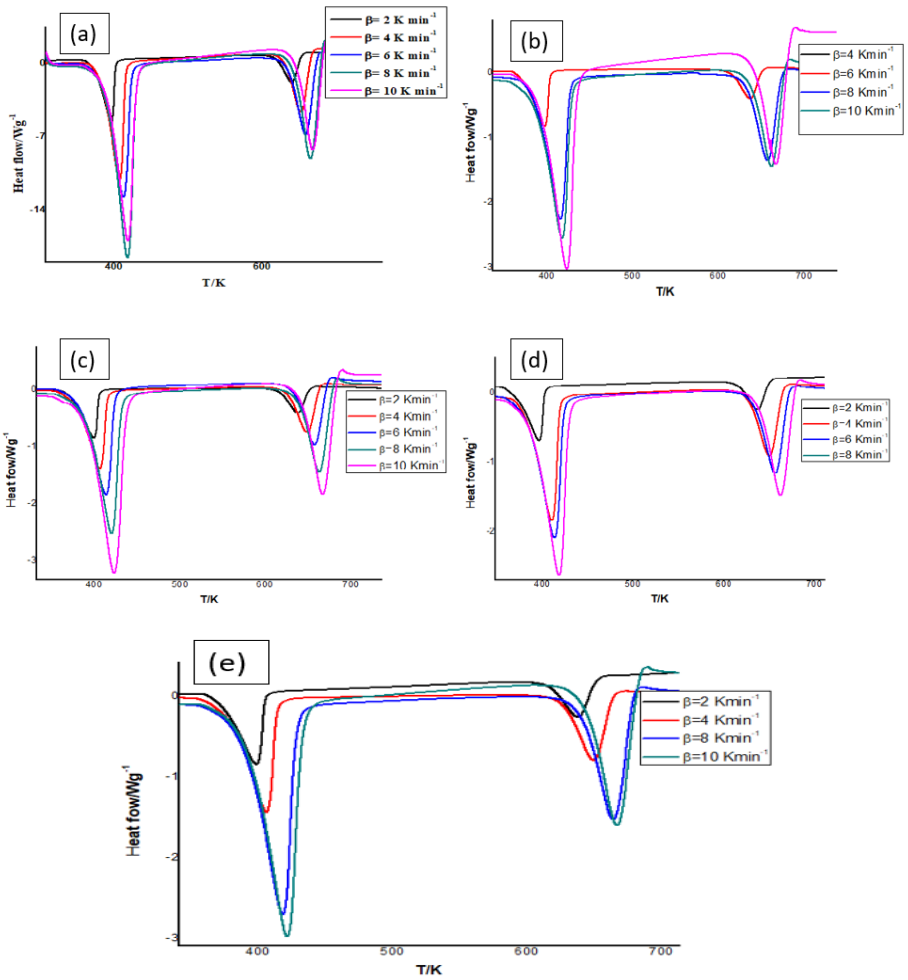

Fig. 6 DSC plots of ZnOX (a), $BZOx_2$ (b), $BZOx_3$ (c), $BZOx_4$ (d), and $BZOx_5$ (e)

The temperature for the dehydration and decomposition reactions are shifted to higher values with the increase of heating rates indicating that the reactions are kinetically controlled. The peak temperature for the dehydration and decomposition reactions is not much affected by the addition of barium. **Fig. 7(a)-(e)** show the TG plot

of ZnOx and Ba-ZnOx samples of different barium concentrations at different heating rates 2, 4, 6, 8, and 10 K min^{-1} and **Fig. 7 (f)** shows the TG curve of ZnOx and Ba-ZnOx samples at a heating rates 2 K min^{-1}. The thermogravimetric analysis shows two mass loss stages, the first one corresponding to the dehydration reaction (380-440 K) and the second stage corresponding to the decomposition of oxalate into oxide (597-684 K).

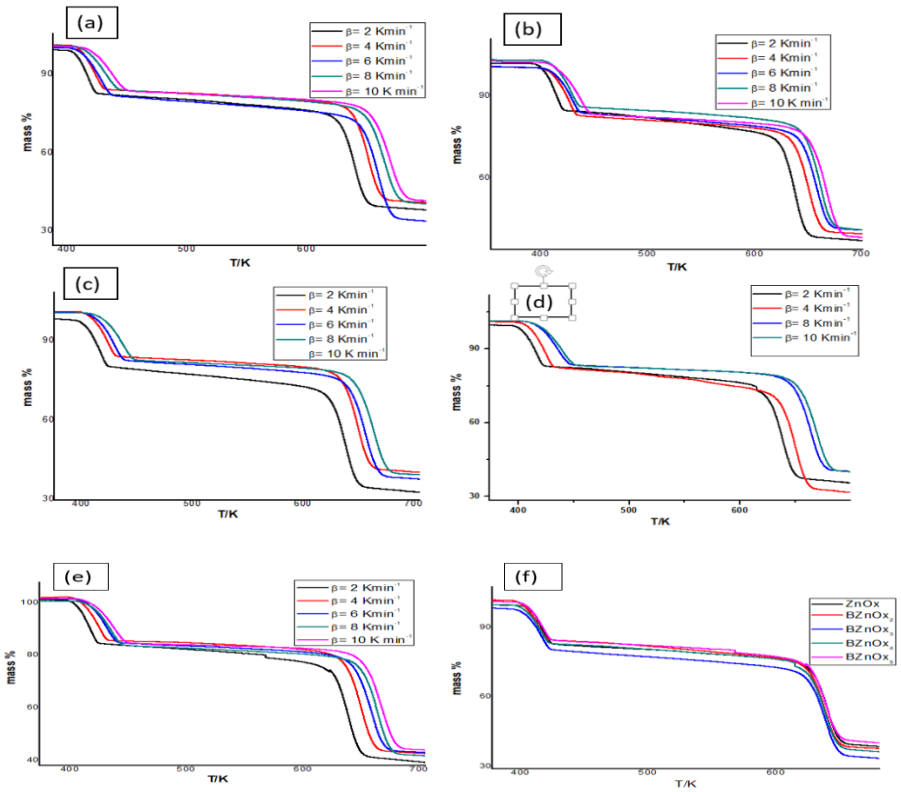

Fig. 7 TG of ZnOx (a), $BZOx_2$ (b), $BZOx_3$ (c), $BZOx_4$ (d) and $BZOx_5$ (e) at different heating rates and pure and Ba-ZnOx samples at a heating rate of 2 K min^{-1} (f)

From **Fig. 7 (a)-(e)**, it is observed that the temperature for the dehydration and decomposition reaction is shifted to higher values with the increase of heating rates as observed in the case of DSC which confirms the reactions are under kinetic control. It is observed from **Fig. 7 (f)** that the temperature for dehydration and decomposition reaction is not much affected by barium addition. Thermogravimetric analysis indicates that the decomposition reaction occurs in a single step in the temperature range 597 to 684 K. The first mass loss of 17% corresponding to dehydration of nearly 2 molecules of water and the second mass loss of 39.25 % corresponding to the decomposition of zinc oxalate into zinc oxide nanoparticles.

5.3.3. Kinetic behavior

The activation energy for the dehydration of Ba-ZnOx is calculated by employing different isoconversional methods like FWO, KAS, Tang, Starink$^{1.92}$, Starink$^{1.95,}$ and Boswell using DSC in nitrogen and TG in the air [23-27]. The value of activation energy for the decomposition of Ba-ZnOx is calculated by using different isoconversional methods like FWO, KAS, Tang, Starink$^{1.92}$, Starink$^{1.95,}$ and Boswell using DSC in nitrogen. Kinetic analysis of pure ZnOx is not described here since it is mentioned in detail in the third chapter.

5.3.3.1. Kinetic analysis of DSC data for the dehydration reaction

The conversion function, α in the range 0.05-1.0 with an interval of 0.05 for the dehydration reaction, and their corresponding temperatures are calculated from the experimental heat flow data

obtained from DSC. The α-T plots for the dehydration reaction of barium added zinc oxalates $BZOx_2$, $BZOx_3$, $BZOx_4$, and $BZOx_5$ are shown in **Fig. 8 (a)-(d).** The α-T plots for dehydration reactions for all the samples are sigmoidal in shape.

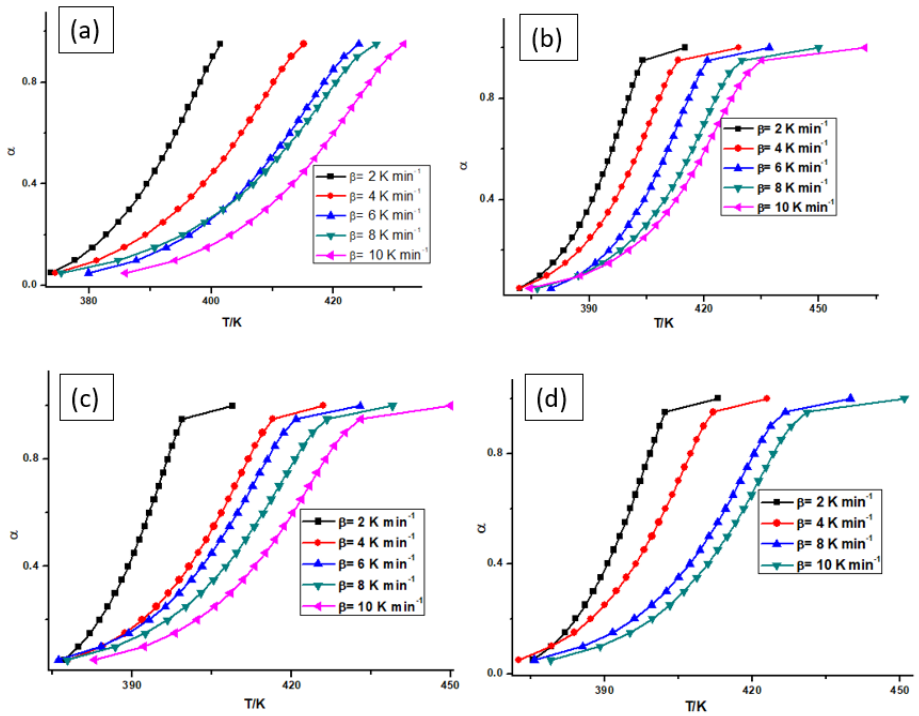

Fig. 8 α-T plots for the dehydration of $BZOx_2$ (a), $BZOx_3$ (b), $BZOx_4$ (c) and $BZOx_5$ (d) from DSC data

This α-T data were subjected to linear least squares analysis using various model-free isoconversional methods like FWO, KAS, Tang, Starink[1.92], Starink[1.95], and Boswell. The linear least squares analysis plots for the dehydration reactions of Ba-ZnOx are shown in the **Figs. 9-12**. All the linear least squares plots give good linearity with R^2 greater than 0.95. The activation energy values were evaluated from the slope

of the linear least square plots using various mathematical equations. The obtained values of activation energies for the dehydration reaction are given in **Tables 1-4.**

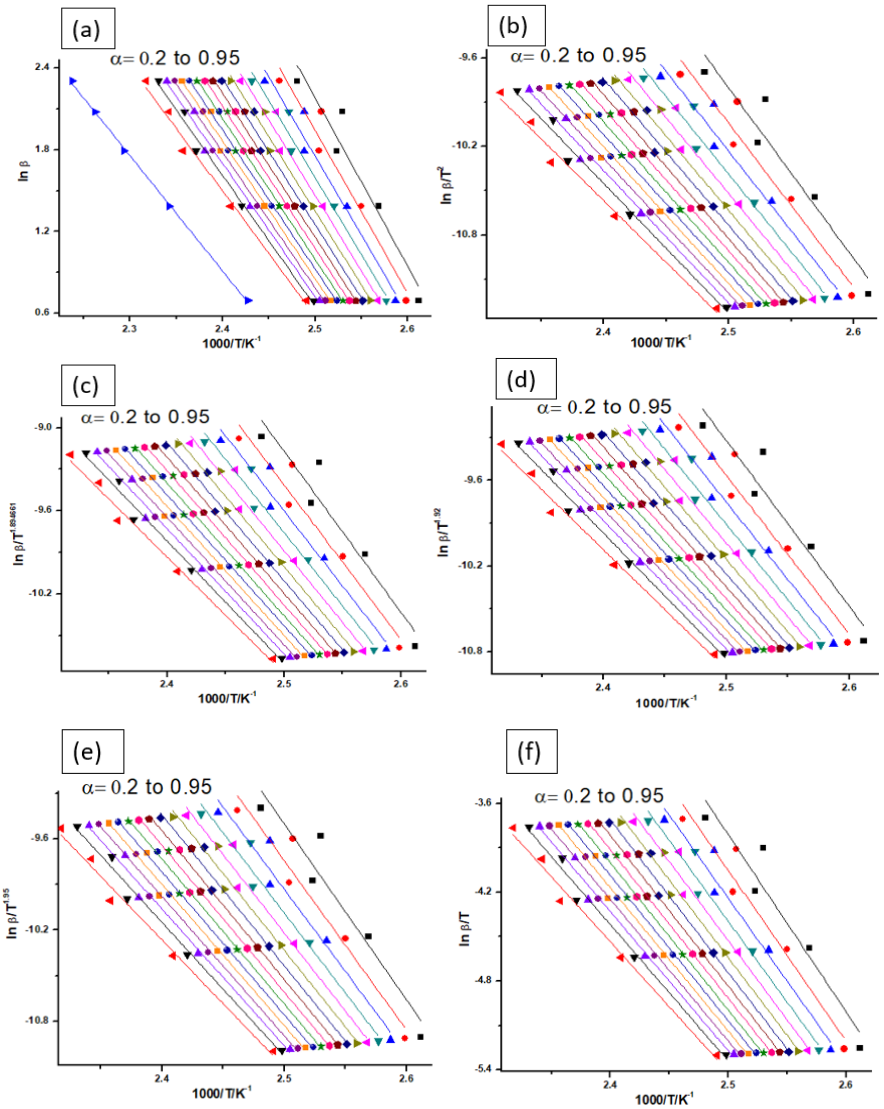

Fig. 9 Linear least squares plot for the dehydration stage of $BZOx_2$ for the isoconversional methods of FWO (a), KAS (b), Tang (c), Starink$^{1.92}$ (d), Starink$^{1.95}$ (e) and Boswell (f) from DSC data

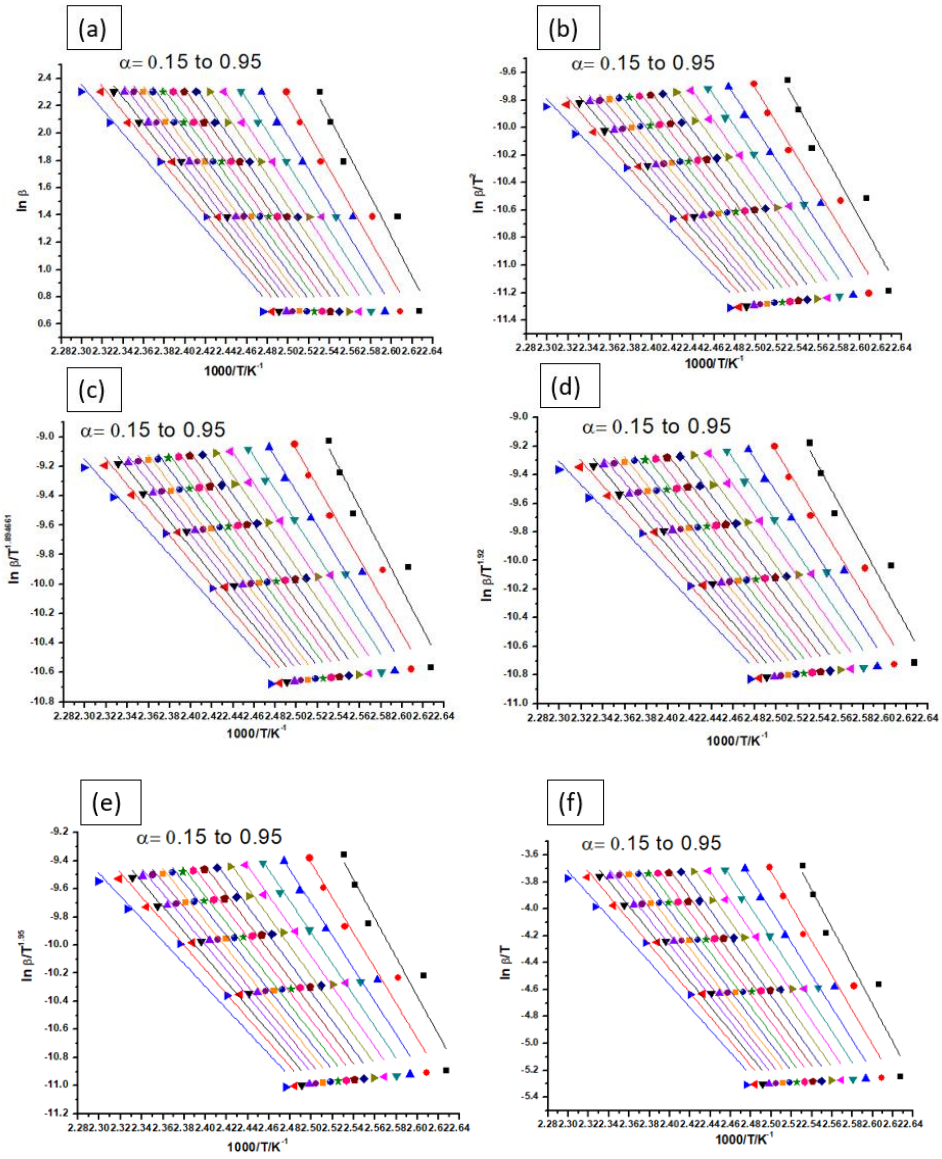

Fig. 10 Linear least squares plot for the dehydration stage of $BZOx_3$ for the isoconversional methods of FWO (a), KAS (b), Tang (c), Starink$^{1.92}$ (d), Starink$^{1.95}$ (e) and Boswell (f) from DSC data

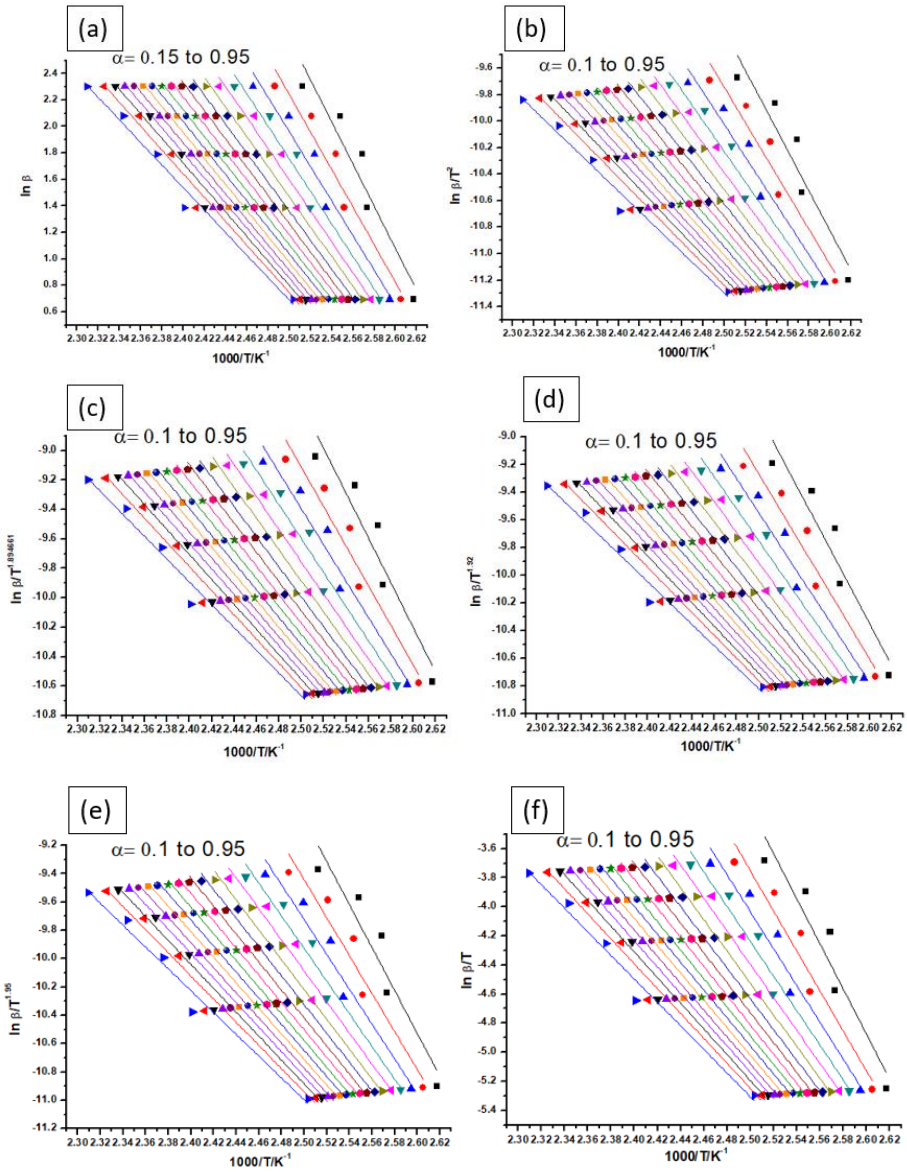

Fig. 11 Linear least squares plot for the dehydration stage of $BZOx_4$ for the isoconversional methods of FWO (a), KAS (b), Tang (c), Starink$^{1.92}$ (d), Starink$^{1.95}$ (e) and Boswell (f) from DSC data

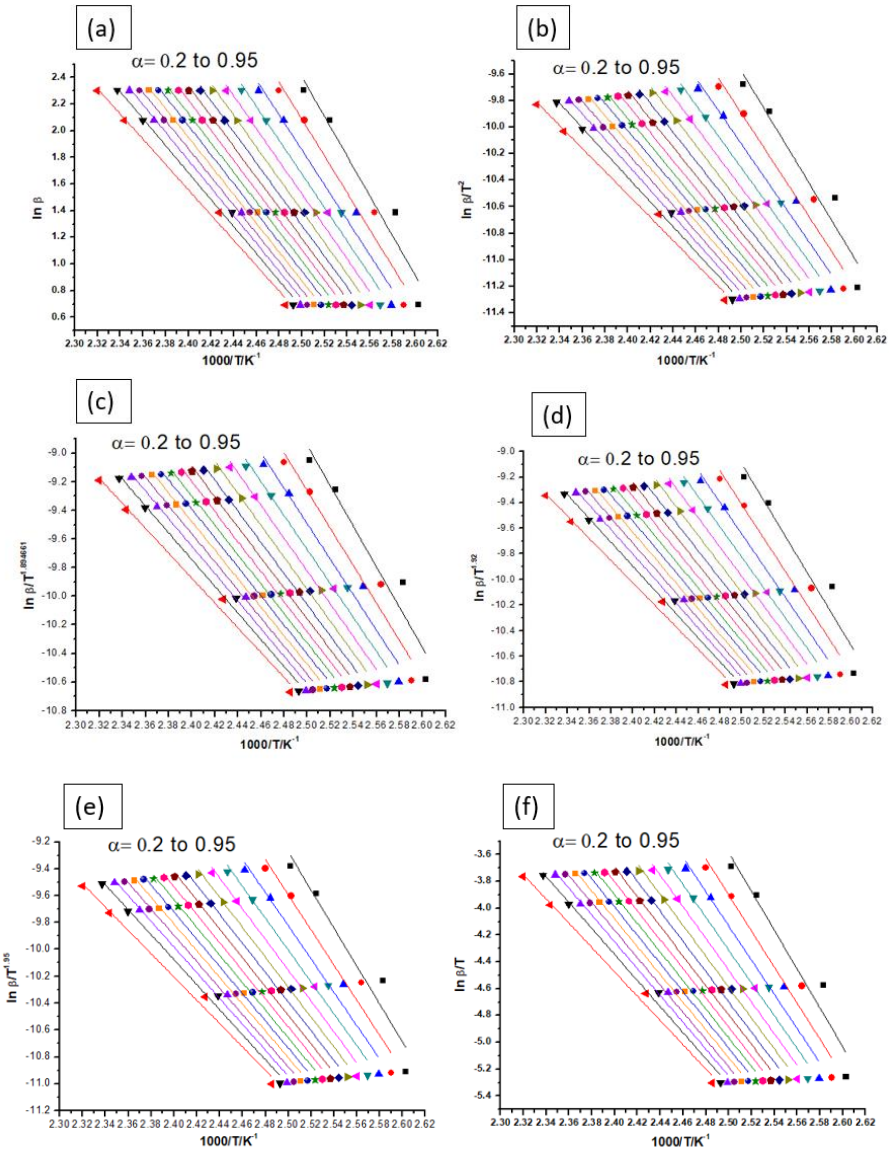

Fig. 12 Linear least squares plot for the dehydration stage of $BZOx_5$ for the isoconversional methods of FWO (a), KAS (b), Tang (c), Starink$^{1.92}$ (d), Starink$^{1.95}$ (e) and Boswell (f) from DSC data

Table 1 Values of E_a for the dehydration of $BZOx_2$ from DSC data

α	E_a (kJ mol^{-1})					
	FWO	KAS	Tang	Starink$^{1.92}$	Starink$^{1.95}$	Boswell
0.20	97.69	96.24	96.45	96.43	96.41	99.51
0.25	94.26	92.59	92.80	92.78	92.75	95.87
0.30	91.67	89.83	90.05	90.02	89.99	93.13
0.35	89.45	87.47	87.69	87.67	87.64	90.79
0.40	87.61	85.50	85.73	85.70	85.67	88.83
0.45	86.04	83.83	84.06	84.03	84.00	87.17
0.50	84.77	82.47	82.70	82.67	82.63	85.82
0.55	83.66	81.27	81.51	81.48	81.44	84.64
0.60	82.57	80.11	80.35	80.31	80.28	83.49
0.65	81.69	79.16	79.40	79.37	79.33	82.55
0.70	80.63	78.03	78.27	78.24	78.20	81.43
0.75	79.76	77.09	77.34	77.30	77.26	80.50
0.80	78.70	75.95	76.20	76.16	76.12	79.37
0.85	77.58	74.76	75.01	74.97	74.93	78.19
0.90	75.99	73.06	73.32	73.28	73.23	76.50
0.95	72.69	69.56	69.82	69.78	69.73	73.01
***Av**	84.05	81.68	81.92	81.89	81.85	85.05

***Av** average value of activation energy

Table 2 Values of E_a for the dehydration of $BZOx_3$ from DSC data

α	E_a (kJ mol^{-1})					
	FWO	KAS	Tang	Starink$^{1.92}$	Starink$^{1.95}$	Boswell
0.15	114.93	114.46	114.63	114.62	114.62	117.68
0.20	104.67	103.60	103.80	103.78	103.77	106.86
0.25	98.40	96.95	97.16	97.14	97.12	100.23
0.30	94.21	92.50	92.72	92.69	92.67	95.81
0.35	91.17	89.27	89.49	89.46	89.43	92.59
0.40	88.89	86.84	87.06	87.04	87.01	90.18
0.45	87.00	84.81	85.04	85.02	84.98	88.17
0.50	85.49	83.20	83.44	83.40	83.37	86.57
0.55	84.05	81.66	81.90	81.87	81.83	85.04
0.60	82.91	80.44	80.68	80.65	80.61	83.83
0.65	81.74	79.19	79.43	79.39	79.36	82.59
0.70	80.62	77.99	78.23	78.20	78.16	81.40
0.75	79.56	76.85	77.10	77.06	77.02	80.27
0.80	78.30	75.49	75.75	75.71	75.66	78.93
0.85	76.78	73.87	74.13	74.09	74.04	77.32
0.90	74.56	71.51	71.77	71.73	71.68	74.97
0.95	69.89	66.56	66.83	66.78	66.73	70.04
***Av**	86.66	84.42	84.66	84.62	84.59	87.79

***Av** average value of activation energy

Table 3 Values of E_a for the dehydration of $BZOx_4$ from DSC data

α	E_a (kJ mol^{-1})					
	FWO	KAS	Tang	Starink$^{1.92}$	Starink$^{1.95}$	Boswell
0.15	125.83	125.89	126.05	126.05	126.05	129.13
0.20	112.05	111.34	111.53	111.52	111.51	114.61
0.25	103.32	102.12	102.32	102.31	102.29	105.41
0.30	97.30	95.76	95.97	95.95	95.92	99.06
0.35	92.92	91.12	91.34	91.31	91.29	94.44
0.40	89.45	87.44	87.66	87.63	87.60	90.77
0.45	86.61	84.43	84.66	84.63	84.60	87.77
0.50	84.34	82.02	82.25	82.22	82.19	85.37
0.55	82.40	79.96	80.19	80.16	80.12	83.32
0.60	80.69	78.14	78.38	78.34	78.30	81.51
0.65	79.11	76.46	76.70	76.66	76.62	79.84
0.70	77.64	74.89	75.14	75.10	75.06	78.28
0.75	76.27	73.43	73.68	73.65	73.60	76.84
0.80	74.79	71.85	72.11	72.07	72.02	75.27
0.85	73.15	70.11	70.37	70.33	70.28	73.53
0.90	71.05	67.88	68.14	68.10	68.05	71.31
0.95	67.30	63.90	64.17	64.12	64.07	67.35
***Av**	86.72	84.51	84.74	84.71	84.68	87.87

***Av** average value of activation energy

Table 4 Values of E_a for the dehydration of $BZOx_5$ from DSC data

α	E_a (kJ mol^{-1})					
	FWO	KAS	Tang	Starink$^{1.92}$	Starink$^{1.95}$	Boswell
0.20	117.78	117.39	117.56	117.56	117.55	120.65
0.25	109.41	108.54	108.73	108.72	108.71	111.82
0.30	103.90	102.70	102.90	102.88	102.86	106.00
0.35	99.77	98.32	98.53	98.51	98.49	101.64
0.40	96.63	94.99	95.20	95.18	95.15	98.32
0.45	94.14	92.34	92.56	92.54	92.51	95.69
0.50	92.13	90.20	90.42	90.40	90.37	93.56
0.55	90.35	88.30	88.53	88.50	88.47	91.67
0.60	88.88	86.74	86.97	86.94	86.90	90.12
0.65	87.44	85.21	85.44	85.41	85.37	88.60
0.70	86.27	83.96	84.19	84.16	84.13	87.36
0.75	84.99	82.58	82.82	82.79	82.75	85.99
0.80	83.79	81.31	81.55	81.51	81.48	84.73
0.85	82.26	79.67	79.91	79.88	79.84	83.10
0.90	80.01	77.28	77.53	77.49	77.45	80.72
0.95	74.91	71.88	72.14	72.10	72.05	75.34
***Av**	92.04	90.09	90.31	90.28	90.26	93.46

***Av** average value of activation energy

The average value of activation energy obtained for pure ZnOx is 95.96 kJ mol^{-1}. The average values of activation energy obtained for $BZOx_2$, $BZOx_3$, $BZOx_4$, and $BZOx_5$ are 84.05, 86.66, 86.72, 92.04 kJ mol^{-1} respectively. The values of activation energy obtained for all Ba added ZnOx samples are less than that of pure ZnOx. There is no regular trend in the decrease of activation energy with Ba addition. **Fig. 13 (a)-(d)** shows the variation of activation energy with conversion function. From the E_a *vs* α curves, it is very clear that the activation energy is continuously changing with α, which reflects the complexity of the reaction. The E_a *vs* α curve for the dehydration reaction of $BZOx_2$,

$BZOx_3$, $BZOx_4$, and $BZOx_5$ are similar and which is also identical with that of pure ZnOx. All the samples require a high value of E_a at the commencement of the reaction and once the reaction starts, it continuous with the lower value of E_a. This implies that the nucleation and growth in solid requires high activation energy, once the reaction starts, which means after the completion of nucleation and its growth, the reaction continues with low activation energy.

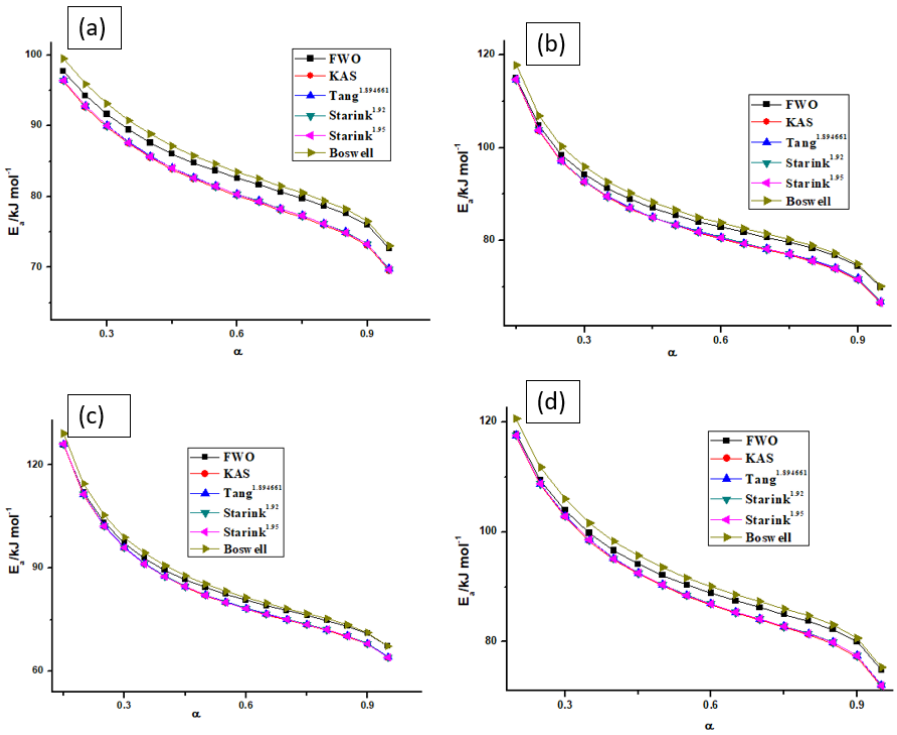

Fig. 13 E_a *vs* α curve for the dehydration reaction of $BZOx_2$ (a), $BZOx_3$ (b), $BZOx_4$ (c) and $BZOx_5$ (d) from DSC data

5.3.3.2. Kinetic analysis of DSC data for the decomposition reaction

The conversion function, α in the range 0.05-1.0 with an interval of 0.05 for the decomposition reaction, and their corresponding temperatures are calculated from the experimental heat flow data obtained from DSC. The α-T plots for the decomposition reaction of barium added zinc oxalates $BZOx_2$, $BZOx_3$, $BZOx_4$, and $BZOx_5$ are shown in **Fig. 14 (a)-(d).** The α-T plots for decomposition reaction for all the samples are sigmoidal in shape. This α-T data were subjected to linear least squares analysis using various model-free isoconversional methods like FWO, KAS, Tang, Starink$^{1.92}$, Starink$^{1.95}$, and Boswell. The linear least squares analysis plots for the decomposition reactions of Ba-ZnOx are shown in the **Figs. 15-18**. All the linear least squares plots give good linearity with R^2 greater than 0.95. The activation energy values were evaluated from the slope of the linear least square plots using various mathematical equations. The obtained values of E_a for the decomposition reaction are given in **Tables 5-8.**

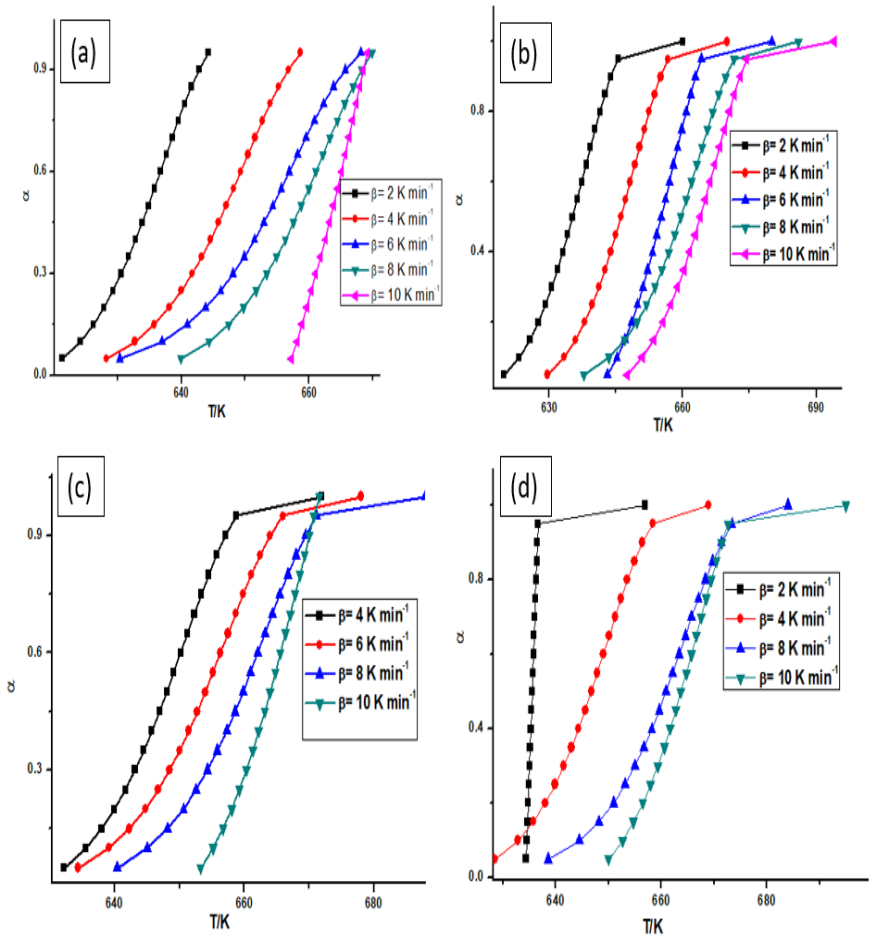

Fig. 14 α-T plots for the decomposition of $BZOx_2$ (a), $BZOx_3$ (b), $BZOx_4$ (c) and $BZOx_5$ (d) from DSC data

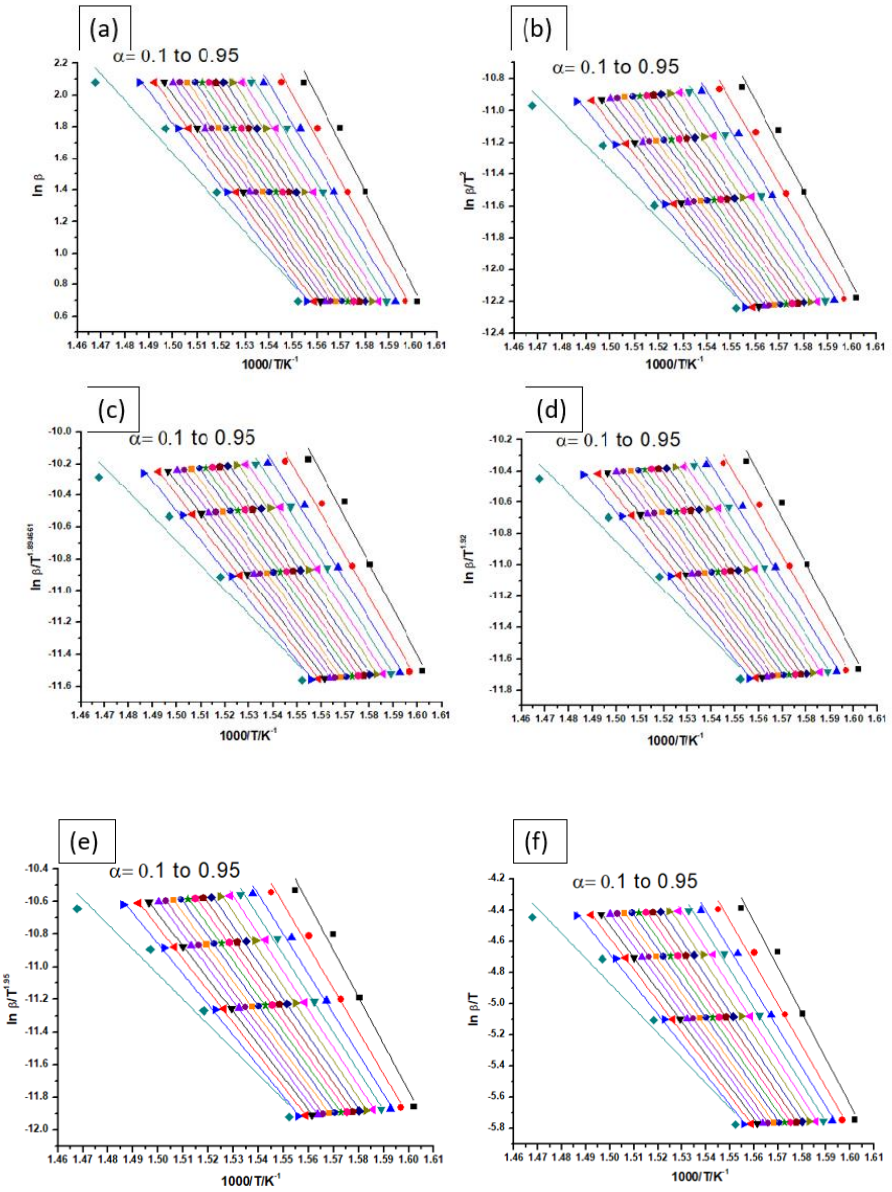

Fig. 15 Linear least squares plot for the decomposition stage of $BZOx_2$ for the isoconversional methods of FWO (a), KAS (b), Tang (c), Starink$^{1.92}$ (d), Starink$^{1.95}$ (e) and Boswell (f) from DSC data

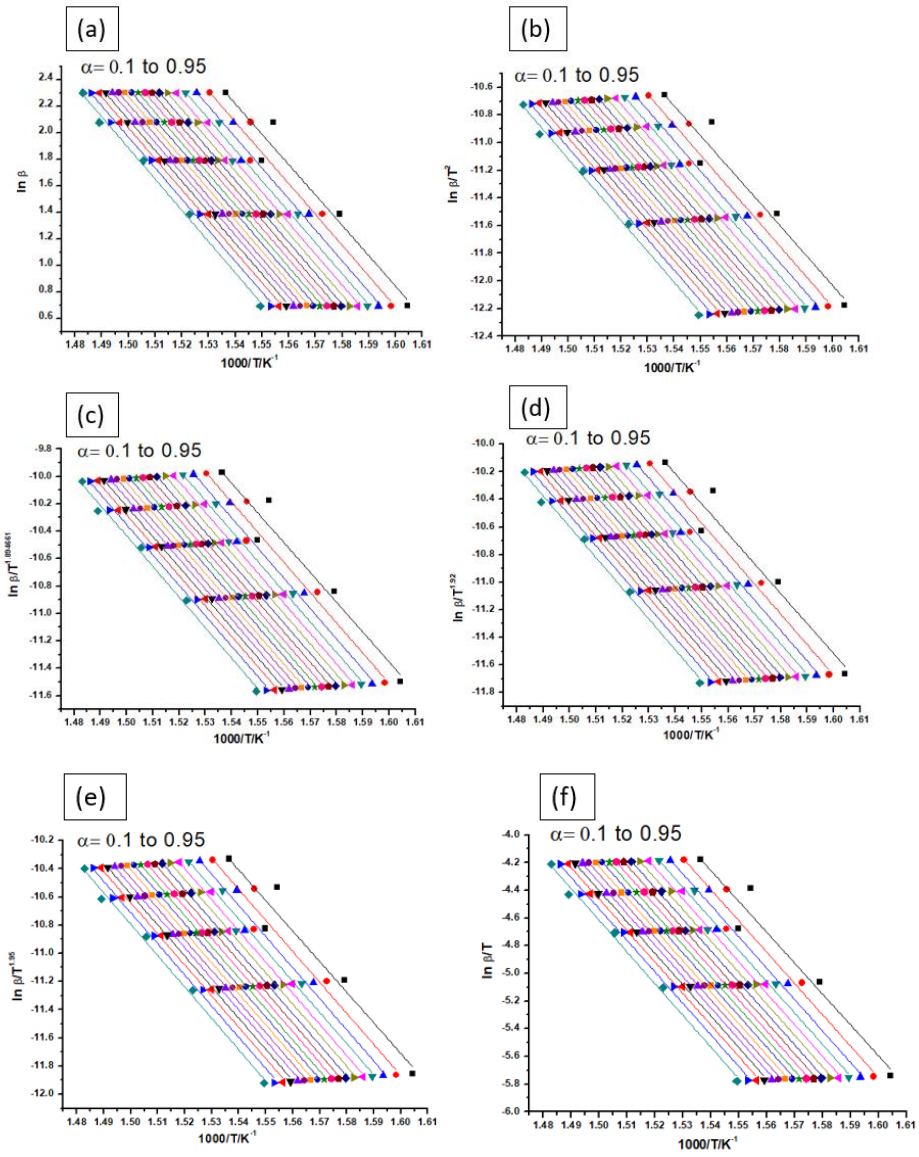

Fig. 16 Linear least squares plot for the decomposition stage of $BZOx_3$ for the isoconversional methods of FWO (a), KAS (b), Tang (c), Starink$^{1.92}$ (d), Starink$^{1.95}$ (e) and Boswell (f) from DSC data

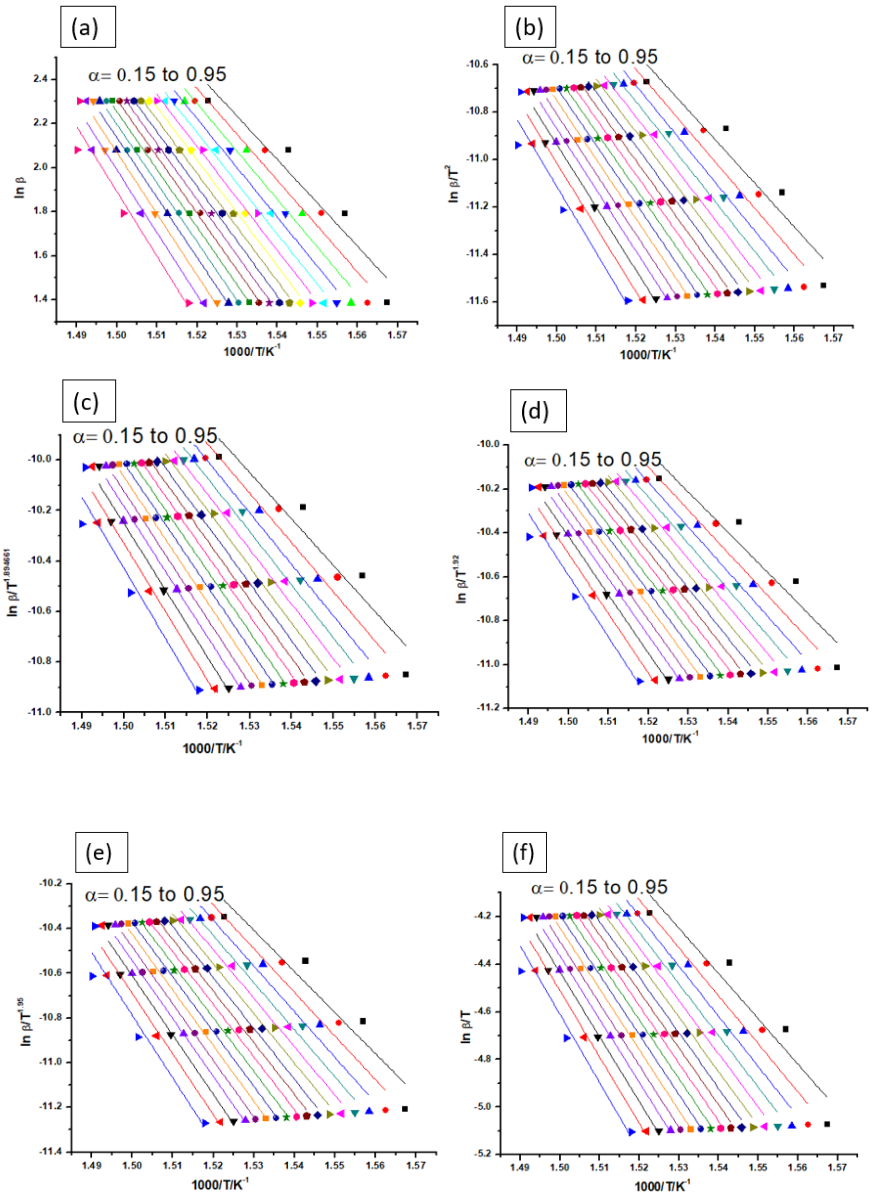

Fig. 17 Linear least squares plot for the decomposition stage of $BZOx_4$ for the isoconversional methods of FWO (a), KAS (b), Tang (c), Starink$^{1.92}$ (d), Starink$^{1.95}$ (e) and Boswell (f) from DSC data

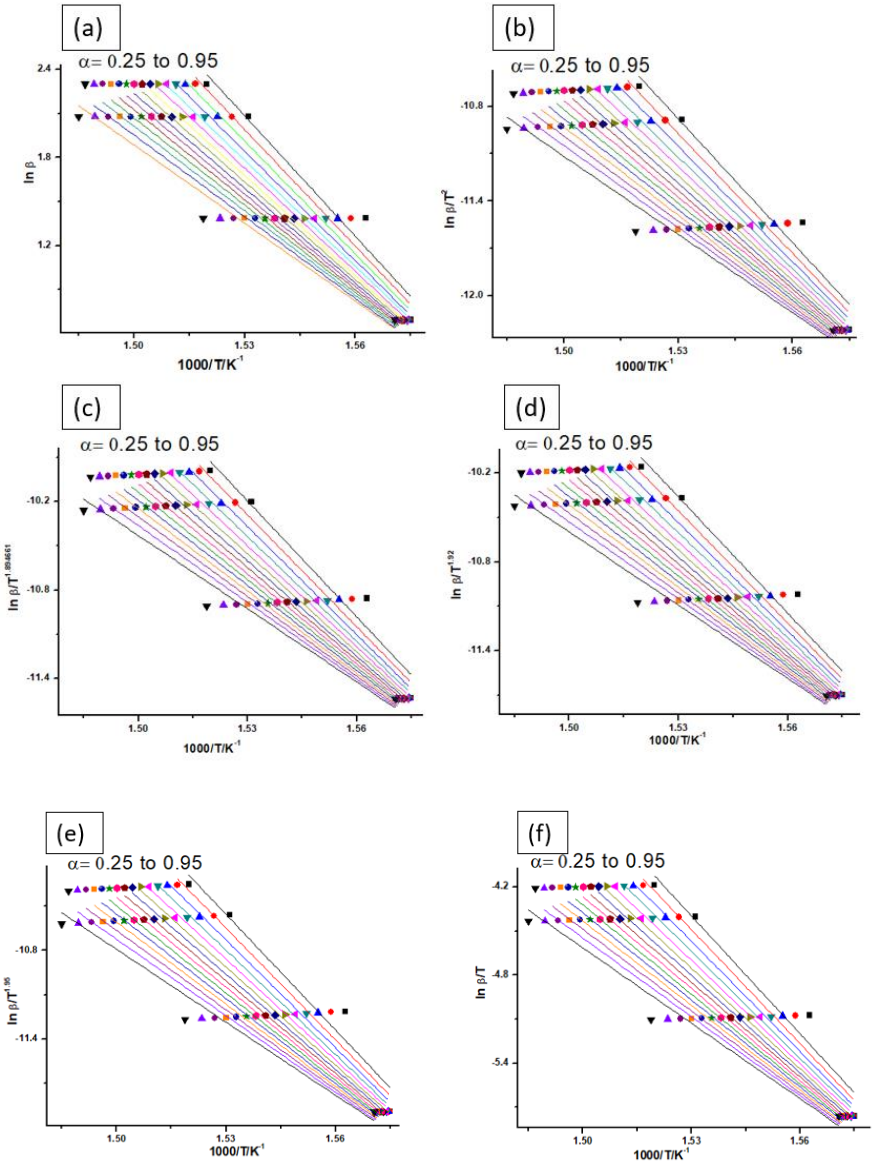

Fig. 18 Linear least squares plot for the decomposition stage of $BZOx_5$ for the isoconversional methods of FWO (a), KAS (b), Tang (c), Starink$^{1.92}$ (d), Starink$^{1.95}$ (e) and Boswell (f) from DSC data

Table 5 Values of E_a for the decomposition of $BZOx_2$ from DSC data

α	E_a (kJ mol^{-1})					
	FWO	KAS	Tang	Starink$^{1.92}$	Starink$^{1.95}$	Boswell
0.1	236.83	238.62	238.82	238.85	238.88	243.88
0.15	215.90	216.55	216.79	216.80	216.81	221.84
0.20	203.57	203.54	203.80	203.80	203.80	208.85
0.25	197.88	197.52	197.80	197.79	197.79	202.85
0.30	193.75	193.16	193.44	193.43	193.42	198.49
0.35	189.93	189.11	189.40	189.39	189.38	194.46
0.40	186.99	185.99	186.29	186.27	186.26	191.35
0.45	184.67	183.53	183.83	183.81	183.80	188.90
0.50	182.72	181.47	181.77	181.75	181.74	186.85
0.55	180.61	179.23	179.53	179.51	179.49	184.61
0.60	179.13	177.65	177.96	177.94	177.92	183.05
0.65	176.69	175.07	175.38	175.36	175.34	180.47
0.70	174.28	172.51	172.83	172.80	172.78	177.92
0.75	172.39	170.50	170.83	170.80	170.77	175.93
0.80	168.78	166.69	167.02	166.99	166.96	172.12
0.85	164.95	162.63	162.97	162.93	162.90	168.08
0.90	158.11	155.40	155.75	155.72	155.68	160.87
0.95	131.62	127.46	127.85	127.79	127.73	132.96
***Av**	180.12	182.03	182.34	182.32	182.30	187.42

***Av** average value of activation energy

Table 6 Values of E_a for the decomposition of $BZOx_3$ from DSC data

α	E_a (kJ mol^{-1})					
	FWO	KAS	Tang	Starink$^{1.92}$	Starink$^{1.95}$	Boswell
0.1	181.34	180.18	180.48	180.46	180.45	185.47
0.15	183.85	182.78	183.08	183.06	183.05	188.09
0.20	184.47	183.41	183.70	183.69	183.67	188.74
0.25	184.68	183.60	183.90	183.88	183.87	188.94
0.30	184.83	183.73	184.02	184.01	184.00	189.08
0.35	184.80	183.68	183.97	183.96	183.94	189.04
0.40	184.58	183.42	183.72	183.71	183.69	188.80
0.45	184.57	183.39	183.70	183.68	183.66	188.78
0.50	184.56	183.36	183.67	183.65	183.63	188.76
0.55	184.64	183.43	183.74	183.72	183.70	188.84
0.60	184.53	183.30	183.60	183.58	183.57	188.71
0.65	184.50	183.25	183.55	183.53	183.52	188.67
0.70	184.42	183.15	183.45	183.44	183.42	188.58
0.75	184.45	183.15	183.46	183.44	183.43	188.60
0.80	184.50	183.19	183.50	183.48	183.46	188.64
0.85	184.88	183.57	183.88	183.86	183.84	189.03
0.90	185.19	183.88	184.19	184.17	184.15	189.35
0.95	186.24	184.96	185.26	185.25	185.23	190.44
***Av**	184.50	183.30	183.60	183.59	183.57	188.70

***Av** average value of activation energy

Table 7 Values of E_a for the decomposition of $BZOx_4$ from DSC data

α	E_a (kJ mol^{-1})					
	FWO	KAS	Tang	Starink$^{1.92}$	Starink$^{1.95}$	Boswell
0.15	155.36	152.68	153.02	152.99	152.95	158.06
0.20	164.44	162.20	162.53	162.50	162.47	167.60
0.25	171.42	169.52	169.84	169.82	169.79	174.93
0.30	176.50	174.84	175.16	175.13	175.11	180.26
0.35	181.39	179.97	180.28	180.26	180.24	185.40
0.40	185.91	184.70	185.01	184.99	184.97	190.14
0.45	189.69	188.66	188.96	188.95	188.93	194.11
0.50	193.00	192.13	192.43	192.42	192.41	197.59
0.55	196.45	195.74	196.04	196.02	196.02	201.20
0.60	200.11	199.57	199.86	199.85	199.85	205.04
0.65	203.88	203.53	203.81	203.80	203.80	209.00
0.70	207.09	206.89	207.17	207.16	207.16	212.37
0.75	210.83	210.81	211.08	211.08	211.08	216.30
0.80	214.83	215.01	215.27	215.27	215.28	220.50
0.85	219.68	220.08	220.35	220.35	220.36	225.59
0.90	224.95	225.61	225.86	225.87	225.89	231.13
0.95	231.85	232.85	233.09	233.11	233.13	238.38
***Av**	195.73	192.62	192.92	192.90	192.89	198.08

***Av** average value of activation energy

Table 8 Values of E_a for the decomposition of $BZOx_5$ from DSC data

α	E_a (kJ mol^{-1})					
	FWO	KAS	Tang	Starink$^{1.92}$	Starink$^{1.95}$	Boswell
0.25	216.63	217.15	217.40	217.41	217.42	222.52
0.30	209.62	209.76	210.02	210.02	210.03	215.14
0.35	202.88	202.66	202.93	202.93	202.93	208.05
0.40	196.65	196.09	196.38	196.37	196.36	201.49
0.45	190.61	189.73	190.02	190.01	190.00	195.12
0.50	185.31	184.14	184.44	184.42	184.41	189.54
0.55	180.20	178.76	179.07	179.05	179.03	184.17
0.60	175.28	173.58	173.89	173.87	173.85	178.99
0.65	170.57	168.61	168.94	168.91	168.88	174.02
0.70	166.00	163.79	164.12	164.09	164.06	169.21
0.75	161.55	159.11	159.45	159.41	159.38	164.53
0.80	156.98	154.28	154.63	154.59	154.55	159.71
0.85	152.10	149.14	149.50	149.46	149.42	154.58
0.90	146.85	143.61	143.97	143.93	143.88	149.05
0.95	140.53	136.95	137.33	137.28	137.23	142.40
***Av**	176.78	175.16	175.47	175.45	175.43	180.57

***Av** average value of activation energy

The activation energy needed for the decomposition of ZnOx to ZnO in the N_2 atmosphere is 179.08 kJ mol^{-1} and this value is in $BZOx_2$, $BZOx_3$, $BZOx_4$, and $BZOx_5$ are 180.12, 184.50, 195.73, and 176.78 kJ mol^{-1} respectively. The value of E_a for the decomposition reaction of all the barium added samples are higher than that of pure ZnOx except $BZOx_5$. From the XRD data, the size of all Ba added samples are found

to be higher than that of pure ZnO and this may be a reason for the increase in the value of activation energy.

Fig. 19 (a)-(d) shows the E_a *vs* α curve for the decomposition reaction of $BZOx_2$, $BZOx_3$, $BZOx_4$, and $BZOx_5$ obtained from the DSC data. From the E_a *vs* α curves, it is understood that the activation energy is continuously varying with α, reflecting the complexity of the reaction. The E_a *vs* α curve for the dehydration reaction of $BZOx_2$, and $BZOx_5$ are similar and which is also identical with that of pure ZnOx. The pure ZnOx and $BZOx_2$, $BZOx_5$ samples require a high value of E_a at the commencement of the reaction, and once the reaction starts, it continues with a lower value of E_a. This implies that the nucleation and growth require high activation energy, once the decomposition reaction starts, which means after the completion of nucleation and its growth, the reaction continues with low activation energy. In $BZOx_3$, the activation energy is initially increasing and almost constant for 85% conversion and then increases. In $BZOx_4$, the activation energy is increasing continuously. The variation of E_a with α shows different mechanisms are operating for the decomposition reaction in Ba-ZnOx of different Ba concentrations.

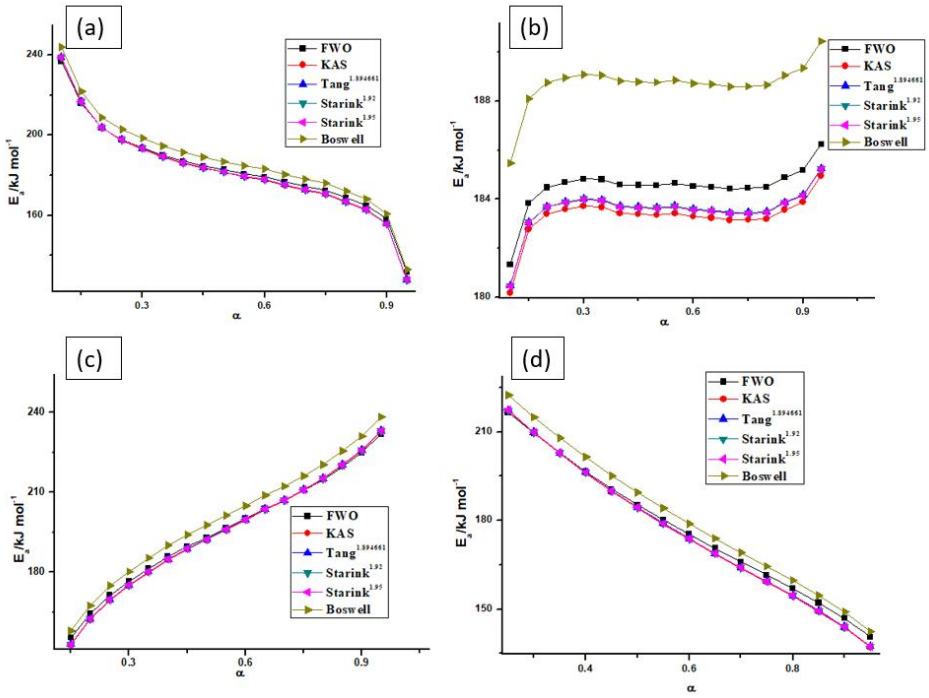

Fig. 19 *E_a vs α* curve for the decomposition reaction of $BZOx_2$ (a), $BZOx_3$ (b), $BZOx_4$ (c) and $BZOx_5$ (d) from DSC data

5.3.3.3. Kinetic analysis of TG data for the dehydration reaction

The reaction conversion function in the range 0.05-1.0 with an interval of 0.05 for the dehydration reaction is also calculated from the mass loss data obtained from the TG. The *α-T* plots for the dehydration reaction of barium added zinc oxalates $BZOx_2$, $BZOx_3$, $BZOx_4$, and $BZOx_5$ are shown in **Fig. 20 (a)-(d).**

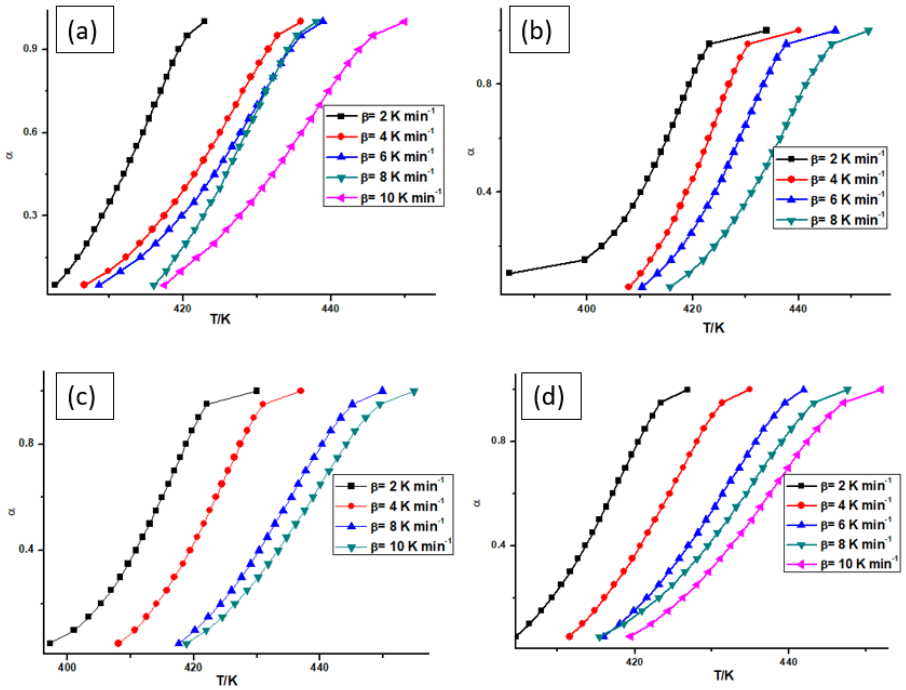

Fig. 20 α-T plots for the dehydration of $BZOx_2$ (a), $BZOx_3$ (b), $BZOx_4$ (c) and $BZOx_5$ (d) from TG data

The α-T plots for dehydration reactions for all the samples are sigmoidal in shape. This α-T data were subjected to linear least squares analysis using various model-free isoconversional methods like FWO, KAS, Tang, Starink$^{1.92}$, Starink$^{1.95}$, and Boswell. The linear least squares analysis plots for the dehydration reactions of Ba-ZnOx are shown in the **Figs. 21-24**. All the linear least squares plots give good linearity with R^2 greater than 0.95. The activation energy values were evaluated from the slope of the linear least square plots using various mathematical equations. The activation energy values obtained are given in **Tables 9-12.**

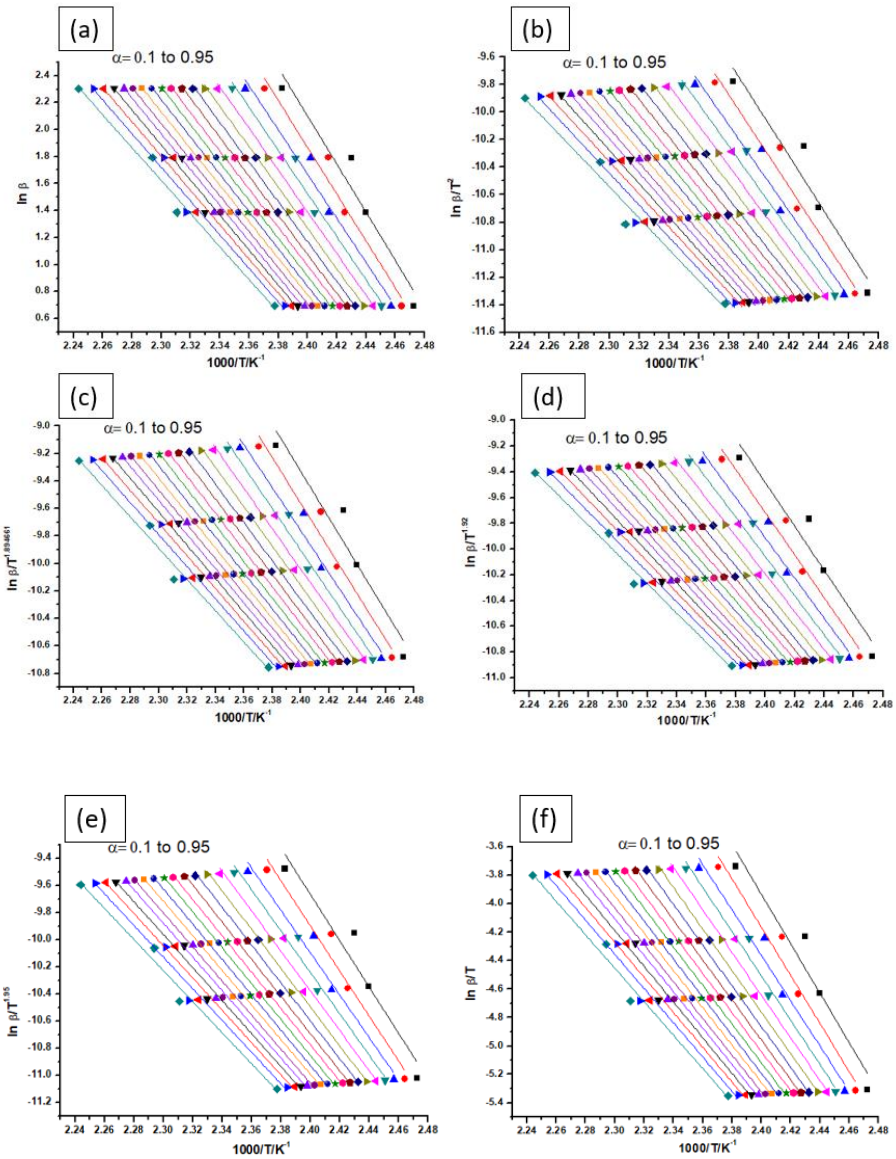

Fig. 21 Linear least squares plot for the dehydration stage of $BZOx_2$ for the isoconversional methods of FWO (a), KAS (b), Tang (c), Starink$^{1.92}$ (d), Starink$^{1.95}$ (e) and Boswell (f) from TG data

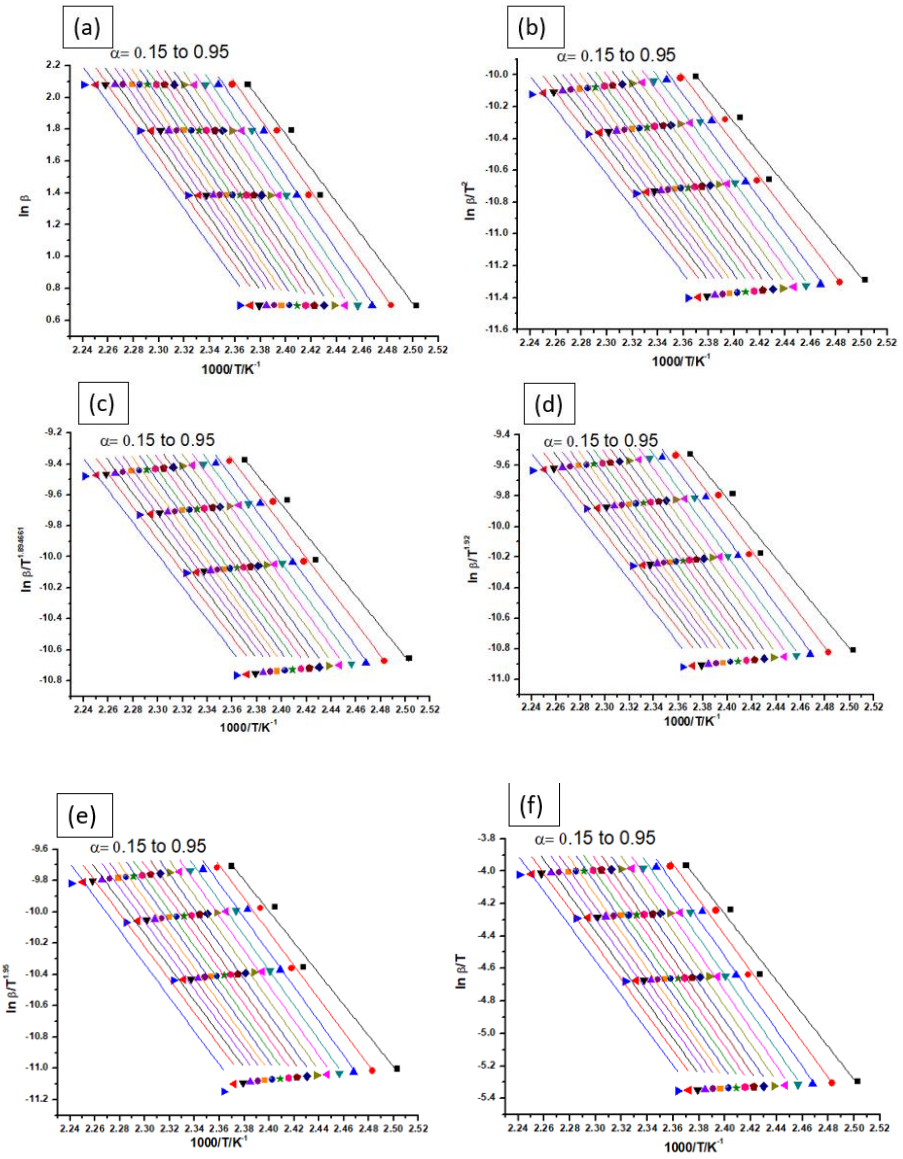

Fig. 22 Linear least squares plot for the dehydration stage of $BZOx_3$ for the isoconversional methods of FWO (a), KAS (b), Tang (c), Starink$^{1.92}$ (d), Starink$^{1.95}$ (e) and Boswell (f) from TG data

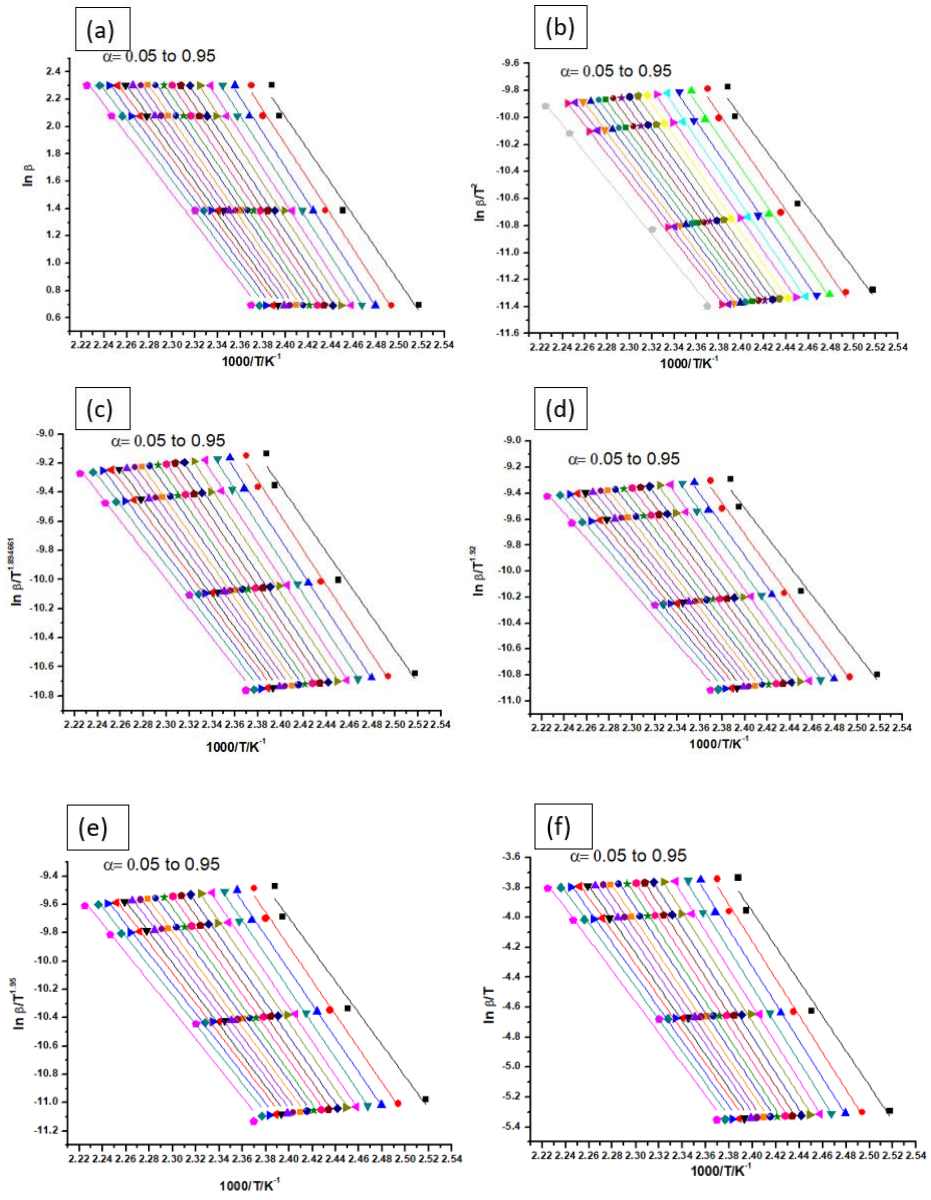

Fig. 23 Linear least squares plot for the dehydration stage of $BZOx_4$ for the isoconversional methods of FWO (a), KAS (b), Tang (c), Starink$^{1.92}$ (d), Starink$^{1.95}$ (e) and Boswell (f) from TG data

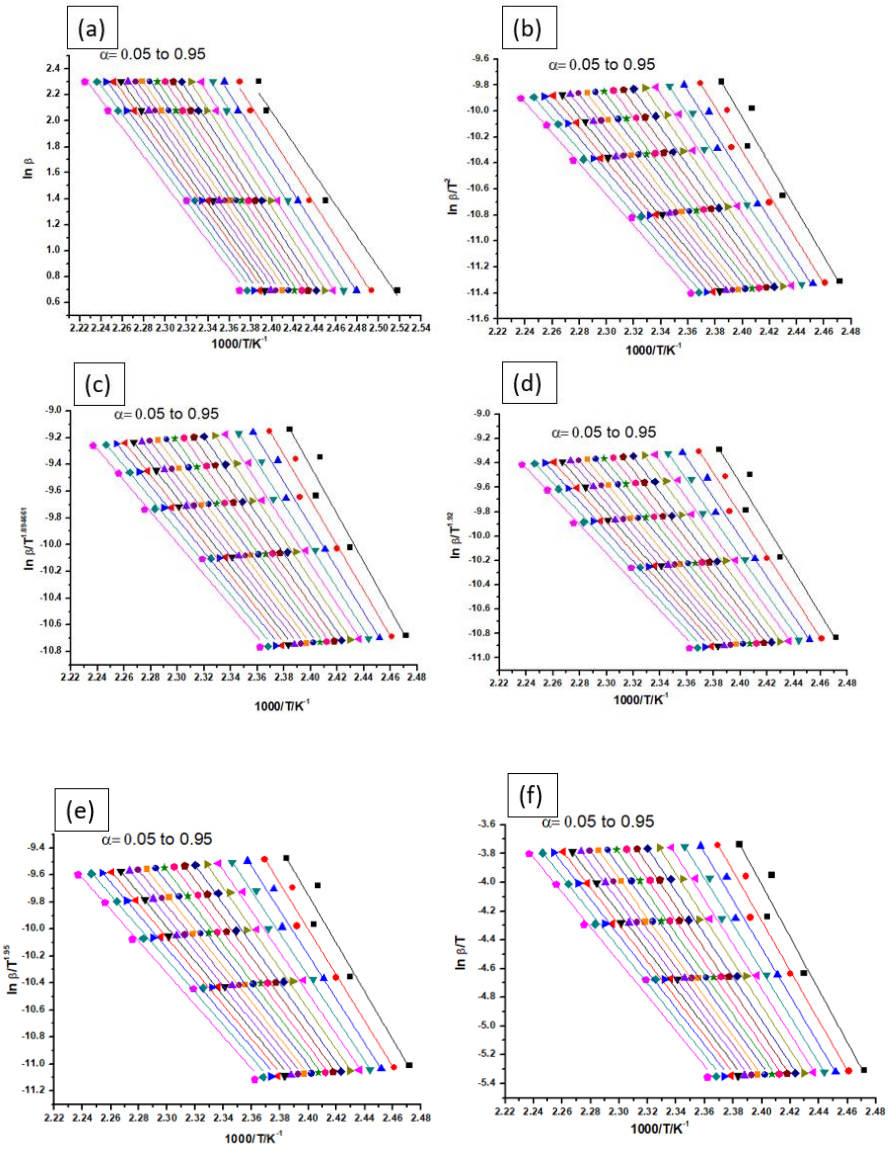

Fig. 24 Linear least squares plot for the dehydration stage of $BZOx_5$ for the isoconversional methods of FWO (a), KAS (b), Tang (c), Starink$^{1.92}$ (d), Starink$^{1.95}$ (e) and Boswell (f) from TG data

Table 9 Values of E_a for the dehydration of $BZOx_2$ from TG data

α	E_a (kJ mol^{-1})					
	FWO	KAS	Tang	Starink$^{1.92}$	Starink$^{1.95}$	Boswell
0.1	140.80	142.07	141.42	141.43	141.97	144.69
0.15	137.12	137.95	137.53	137.54	138.05	140.81
0.20	129.43	129.79	129.43	129.42	129.82	132.70
0.25	126.35	126.42	126.17	126.16	126.56	129.45
0.30	122.03	121.81	121.61	121.60	121.99	124.90
0.35	119.07	118.62	118.49	118.48	118.82	121.78
0.40	116.51	115.89	115.78	115.76	116.09	119.07
0.45	114.46	113.68	113.61	113.59	113.89	116.91
0.50	112.01	111.06	111.02	111.00	111.29	114.32
0.55	110.81	109.77	109.74	109.72	110.00	113.05
0.60	109.15	107.99	107.98	107.96	108.21	111.30
0.65	107.12	105.84	105.83	105.81	106.04	109.15
0.70	105.50	104.07	104.11	104.09	104.36	107.44
0.75	104.55	103.08	103.10	103.07	103.30	106.43
0.80	102.54	100.94	100.97	100.95	101.17	104.31
0.85	100.43	98.68	98.73	98.71	98.95	102.07
0.90	98.67	96.80	96.87	96.84	97.18	100.21
0.95	96.49	94.54	94.55	94.52	95.17	97.91
***Av**	114.06	113.28	113.16	113.15	113.49	116.47

***Av** average value of activation energy

Table 10 Values of E_a for the dehydration of $BZOx_3$ from TG data

α	E_a (kJ mol^{-1})					
	FWO	KAS	Tang	Starink$^{1.92}$	Starink$^{1.95}$	Boswell
0.15	83.81	81.35	81.59	81.56	82.57	84.76
0.20	89.66	87.46	87.69	87.66	88.45	90.89
0.25	92.56	90.47	90.71	90.68	91.29	93.93
0.30	93.69	91.63	91.86	91.83	92.35	95.10
0.35	94.24	92.17	92.41	92.38	92.83	95.65
0.40	94.33	92.25	92.48	92.46	92.86	95.74
0.45	94.41	92.30	92.54	92.51	92.91	95.81
0.50	94.44	92.32	92.55	92.52	92.86	95.83
0.55	94.42	92.28	92.52	92.49	92.83	95.81
0.60	93.90	91.70	91.94	91.91	92.21	95.24
0.65	93.99	91.78	92.02	91.99	92.30	95.33
0.70	93.47	91.22	91.46	91.43	91.69	94.77
0.75	92.19	89.85	90.09	90.06	90.35	93.41
0.80	91.73	89.35	89.59	89.56	89.84	92.92
0.85	90.52	88.06	88.31	88.27	88.60	91.64
0.90	89.55	87.00	87.26	87.22	87.61	90.60
0.95	88.52	85.90	86.15	86.12	89.09	89.51
***Av**	92.08	89.83	90.07	90.04	90.63	93.35

***Av** average value of activation energy

Table 11 Values of E_a for the dehydration of $BZOx_4$ from TG data

α	E_a (kJ mol^{-1})					
	FWO	KAS	Tang	Starink$^{1.92}$	Starink$^{1.95}$	Boswell
0.05	95.00	93.16	93.38	93.36	93.33	96.55
0.1	100.78	99.90	99.40	99.37	100.06	102.60
0.15	101.11	100.34	99.70	99.68	100.24	102.93
0.20	101.80	101.14	100.40	100.38	100.84	103.64
0.25	101.48	100.81	100.03	100.01	100.41	103.28
0.30	100.28	99.64	98.75	98.72	99.05	102.01
0.35	99.65	98.95	98.06	98.04	98.37	101.34
0.40	99.16	98.48	97.53	97.50	97.77	100.81
0.45	98.17	97.44	96.47	96.44	96.72	99.75
0.50	97.65	96.91	95.91	95.88	96.11	99.20
0.55	96.25	95.48	94.42	94.39	94.62	97.72
0.60	95.16	94.34	93.25	93.22	93.46	96.56
0.65	94.92	94.13	92.98	92.95	93.15	96.30
0.70	93.55	92.68	91.53	91.50	91.71	94.85
0.75	92.54	91.63	90.45	90.42	90.60	93.78
0.80	91.00	90.03	88.81	88.78	88.98	92.15
0.85	89.79	88.75	87.52	87.49	87.70	90.86
0.90	88.19	87.08	85.82	85.78	86.04	89.17
0.95	85.73	84.51	83.20	83.16	84.91	86.56
***Av**	95.91	95.02	94.08	94.06	94.43	97.37

***Av** average value of activation energy

Table 12 Values of E_a for the dehydration of $BZOx_5$ from TG data

α	E_a (kJ mol^{-1})					
	FWO	KAS	Tang	Starink$^{1.92}$	Starink$^{1.95}$	Boswell
0.05	147.62	148.45	148.59	148.60	148.62	151.87
0.1	139.99	141.34	140.55	140.55	141.22	143.83
0.15	134.98	136.16	135.25	135.25	135.81	138.54
0.20	130.05	131.07	130.05	130.05	130.53	133.34
0.25	126.37	127.28	126.16	126.15	126.57	129.46
0.30	124.41	125.19	124.07	124.07	124.43	127.38
0.35	121.55	122.20	121.06	121.05	121.38	124.37
0.40	119.01	119.55	118.37	118.35	118.67	121.68
0.45	116.97	117.42	116.20	116.19	116.46	119.52
0.50	114.53	114.89	113.63	113.61	113.88	116.95
0.55	113.04	113.33	112.05	112.03	112.29	115.38
0.60	111.53	111.71	110.45	110.43	110.66	113.78
0.65	109.87	109.98	108.68	108.66	108.91	112.02
0.70	108.45	108.51	107.18	107.16	107.38	110.53
0.75	106.86	106.83	105.49	105.47	105.70	108.84
0.80	105.17	105.07	103.70	103.67	103.90	107.05
0.85	103.52	103.35	101.94	101.92	102.17	105.31
0.90	101.67	101.40	99.98	99.95	100.23	103.35
0.95	98.96	98.57	97.12	97.09	97.99	100.49
***Av**	117.61	118.02	116.87	116.86	117.20	120.19

***Av** average value of activation energy

The activation energy obtained for the dehydration of pure ZnOx dihydrate from the TG in the air is 115.05 kJ mol^{-1}. All the Ba containing samples except $BZOx_5$ have a lower value of activation energy than pure

ZnOx. The values obtained for the dehydration of $BZOx_2$, $BZOx_3$, $BZOx_4$, and $BZOx_5$ are 114.06, 92.08, 95.91, and 117.61 kJ mol^{-1} respectively. It is also observed that the value of activation energy obtained from TG data in the air is higher than that of the value obtained from DSC data in the nitrogen atmosphere indicating that the dehydration reaction is easier in nitrogen than in air. So it can be concluded that the reaction atmosphere also plays an important role in deciding the value of activation energy and also the mechanism of the reaction.

Fig. 25 (a)-(d) shows the variation of activation energy with α for the dehydration reaction of Ba-ZnOx samples obtained from the TG data in the air. The pattern in which E_a changes with α is similar in pure ZnOx and $BZOx_2$ and $BZOx_5$. In these two the E_a is continuously decreasing as the reaction progress. The activation energy is higher at the beginning of the reaction and after that, it is decreasing reflecting that nucleation and growth in solid require high activation energy, once the reaction starts, which means after the completion of nucleation and its growth, the reaction continues with low activation energy. In $BZOx_3$ and $BZOx_4$, there is a small hike at the very beginning of the reaction and then decreased continuously.

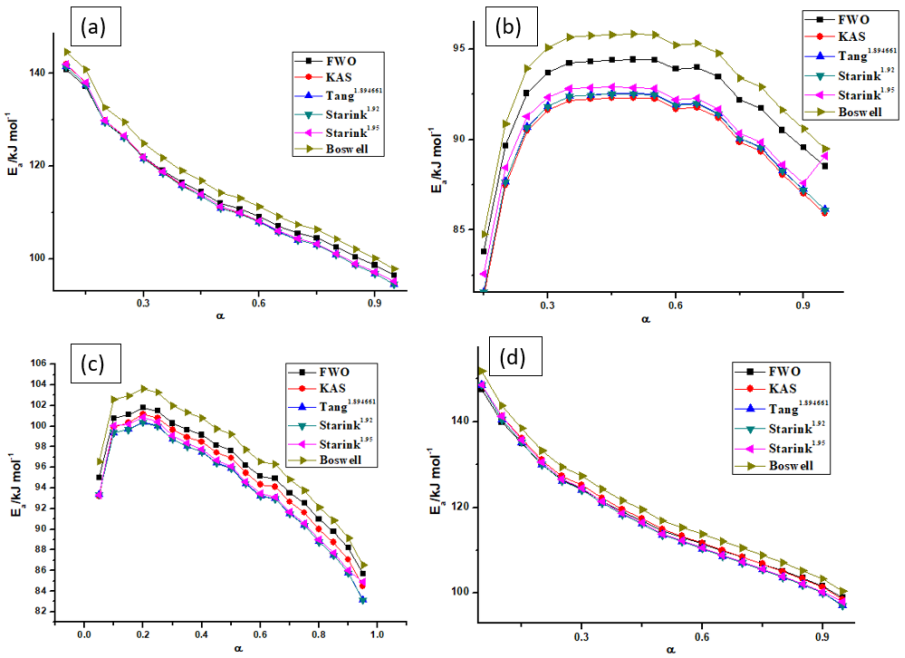

Fig. 25 *E_a vs α* curve for the dehydration reaction of $BZOx_2$ (a), $BZOx_3$ (b), $BZOx_4$ (c) and $BZOx_5$ (d) from TG data

5.3.3.4. Model fitting method

Model fitting methods were used to suggest the most probable mechanism for thermal dehydration and decomposition reactions. For this, the value of *ln (g (α)/T^2) vs 1/T* of the non-isothermal DSC data at 2 K min^{-1} is plotted using different reaction models described in the first chapter. The plot will be a straight line for a correct mechanism and non-linear for the inaccurate mechanism. **Fig. 26** represent the model fitting least squares plots for the dehydration reaction of $BZOx_2$ (a), $BZOx_3$ (b), $BZOx_4$ (c), and $BZOx_5$ (d). All these samples show good linearity with models F1, A3, A4, A2, and A1.34. So it can be concluded that the dehydration reaction in all these samples

follows the same mechanism. In all these samples, the E_a *vs* α curve was also similar.

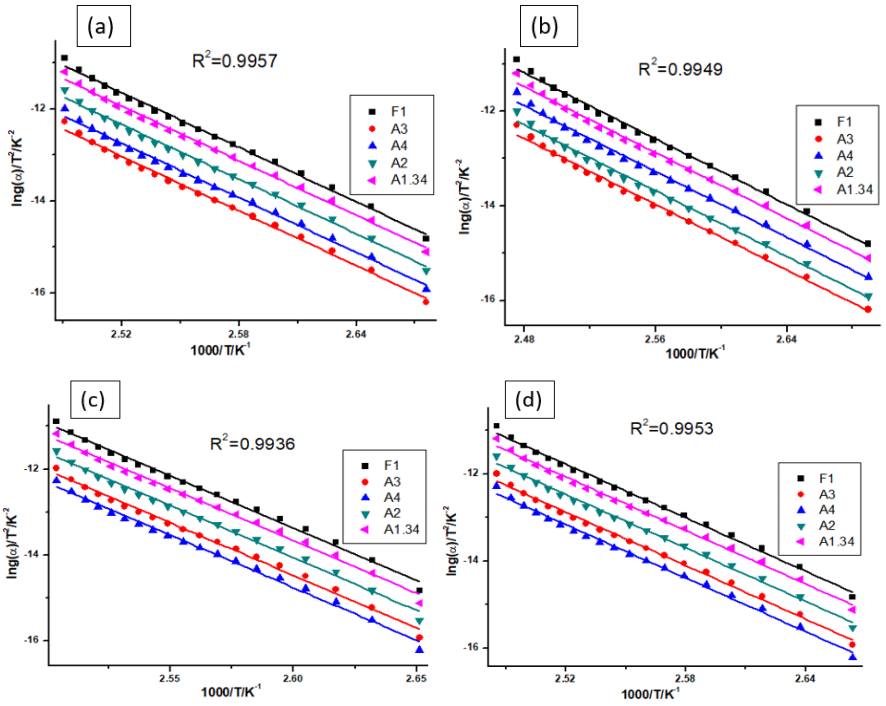

Fig. 26 model fitting least squares plots for the dehydration reaction of $BZOx_2$ (a), $BZOx_3$ (b), $BZOx_4$ (c), and $BZOx_5$ (d)

Fig. 27 represents the model fitting least squares plots for the decomposition reaction of $BZOx_2$ (a), $BZOx_3$ (b), $BZOx_4$ (c), and $BZOx_5$ (d). The samples $BZOx_2$ (a), $BZOx_3$ (b), and $BZOx_4$ show good linearity with models F1, A3, A4, A2, and A1.34 indicating that same mechanism of decomposition is operating. The barium containing sample $BZOx_5$ shows good linearity with model F2. The obtained models for the dehydration and decomposition reaction and their integrated forms are given in **Table 13.**

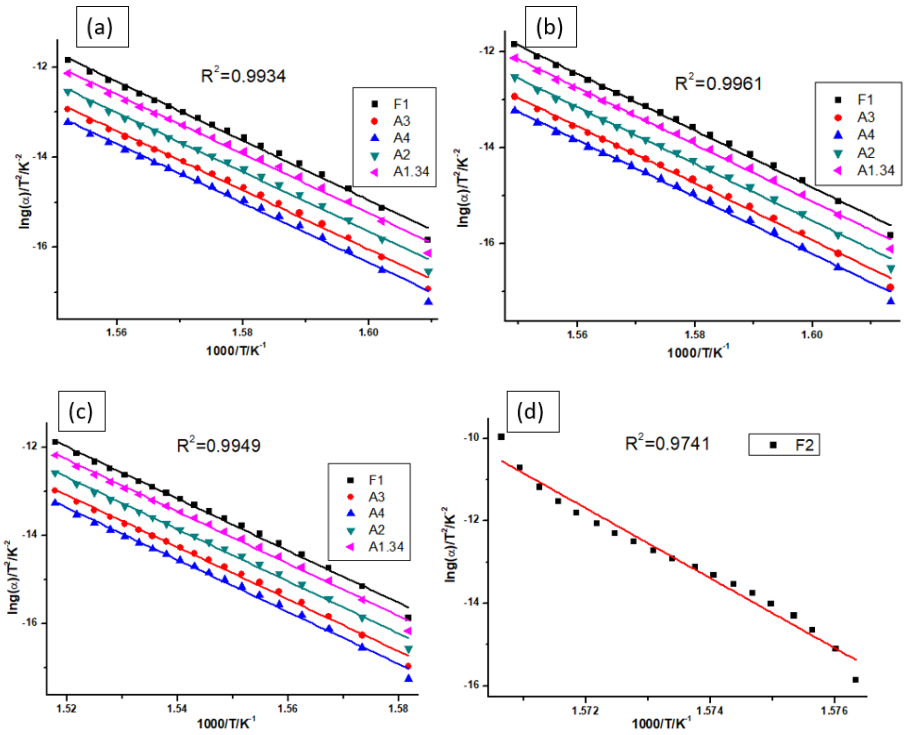

Fig. 27 model fitting least squares plots for the decomposition reaction of $BZOx_2$ (a), $BZOx_3$ (b), $BZOx_4$ (c), and $BZOx_5$ (d)

Table 13 Obtained models for the dehydration and decomposition reaction and their integrated form

Code	Reaction model	*f(α)*	Function *g(α)*
F1	Mampel (first-order)	1- α	–ln (1–α)
A4	Avrami–Erofeev	$4(1- \alpha)[-\ln(1- \alpha)]^{3/4}$	$(-\ln (1-\alpha))^{1/4}$
A3	Avrami–Erofeev	$3(1- \alpha)[-\ln(1- \alpha)]^{2/3}$	$(-\ln (1-\alpha))^{1/3}$
A2	Avrami–Erofeev	$2(1- \alpha)[-\ln(1- \alpha)]^{1/2}$	$(-\ln (1-\alpha))^{1/2}$
A1.34	Avrami–Erofeev	$1.34(1-\alpha)[-\ln(1-\alpha)]^{0.34/1.34}$	$(-\ln (1-\alpha))^{1/1.34}$
F2	Second-order	$(1- \alpha)^2$	$(1-\alpha)^{-1}-1$

5.4. Conclusion

In this study, we have succeeded in the synthesis of barium containing zinc oxide nanoparticles through a simple, low cost, oxalate co-precipitation route followed by the thermal decomposition. The synthesized oxalate samples were characterized by FT-IR. The formed barium zinc oxide particles were characterized by FT-IR, UV-DRS, and XRD and found that the oxide particles are in the nanometer range. The band gap is increased by the addition of barium. The activation energy for the formation of barium containing zinc oxide nanoparticles was calculated by using different isoconversional methods. The activation energy obtained for the dehydration reaction of ZnOx, $BZOx_2$, $BZOx_3$, $BZOx_4$, and $BZOx_5$ in the nitrogen atmosphere is 95.96, 84.05, 86.66, 86.72, and 92.04 kJ mol^{-1} (FWO method) and the corresponding values in the air are 115.05, 114.06, 92.08, 95.91, 117.61 kJ mol^{-1} (FWO method) respectively. All the Ba containing samples have a lower value of E_a than pure ZnOx in nitrogen. In the air, all samples except $BZOx_5$ have a lower value of E_a than pure ZnOx. Since the value of activation energy in the N_2 atmosphere is smaller than that of air, the dehydration reaction is favourable in the nitrogen atmosphere than in air. The activation energy obtained for the decomposition reaction of ZnOx, $BZOx_2$, $BZOx_3$, $BZOx_4$, and $BZOx_5$ in the nitrogen atmosphere is 179.08, 180.12, 184.50, 195.73, and 176.78 kJ mol^{-1} (FWO method). From these values, it can be concluded that the value of E_a for the decomposition reaction of all the barium added samples are higher than that of pure ZnOx except $BZOx_5$.

5.5. References

[1] G.A. Ozin, A. Arsenault, Nanochemistry: a chemical approach to nanomaterials, Royal Society of Chemistry, 89(1992) 3977-3979.

[2] M. Verelst, T.O. Ely, C. Amiens, E. Snoeck, P. Lecante, A. Mosset, M. Respaud, J.M. Broto, B. Chaudret, Synthesis and Characterization of CoO, Co_3O_4, and Mixed Co/CoO Nanoparticles, Chem. Mater. 11 (1999) 2702–2708.

[3] S.K. Jesudoss, J.J. Vijaya, N.C.S. Selvam, K. Kombaiah, M. Sivachidambaram, T. Adinaveen, L.J. Kennedy, Effects of Ba doping on structural, morphological, optical, and photocatalytic properties of self-assembled ZnO nanospheres, Clean Technol. Environ. Policy. 18 (2016) 729–741.

[4] S.K. Kansal, M. Singh, D. Sud, Studies on photodegradation of two commercial dyes in aqueous phase using different photocatalysts, J. Hazard. Mater. 141 (2007) 581–590.

[5] S. Suwanboon, P. Amornpitoksuk, A. Sukolrat, Dependence of optical properties on doping metal, crystallite size, and defect concentration of M-doped ZnO nanopowders (M=Al, Mg, Ti), Ceram. Int. 37 (2011) 1359–1365.

[6] R. Shankar, R.K. Srivastava, S.G. Prakash, Study of dark-conductivity and photoconductivity of ZnO nano structures synthesized by thermal decomposition of zinc oxalate, Electron. Mater. Lett. 9 (2013) 555–559.

[7] G.N. Dar, A. Umar, S.A. Zaidi, A.A. Ibrahim, M. Abaker, S. Baskoutas, M.S. Al-Assiri, Ce-doped ZnO nanorods for the detection of hazardous chemical, Sensors Actuators B Chem. 173 (2012) 72–78.

[8] W. Water, Y.S. Yan, Characteristics of strontium-doped ZnO films on love wave filter applications, Thin Solid Films. 515 (2007) 6992–6996.

[9] T. Dietl, H. Ohno, F. Matsukura, J. Cibert, e D. Ferrand, Zener model description of ferromagnetism in zinc-blende magnetic semiconductors, Science. 287 (2000) 1019–1022.

[10] M.K. Gupta, N. Sinha, B.K. Singh, B. Kumar, Synthesis of K-doped p-type ZnO nanorods along (100) for ferroelectric and dielectric applications, Mater. Lett. 64 (2010) 1825–1828.

[11] Y.C. Yang, C.F. Zhong, X.H. Wang, B. He, S.Q. Wei, F. Zeng, F. Pan, Room temperature multiferroic behavior of Cr-doped ZnO films, J. Appl. Phys. 104 (2008) 64102.

[12] G. Srinet, R. Kumar, V. Sajal, High Tc ferroelectricity in Ba-doped ZnO nanoparticles, Mater. Lett. 126 (2014) 274–277.

[13] S.D. Bukkitgar, N.P. Shetti, R.M. Kulkarni, S.T. Nandibewoor, Electro-sensing base for mefenamic acid on a 5% barium-doped zinc oxide nanoparticle modified electrode and its analytical application, RSC Adv. 5 (2015) 104891–104899.

[14] Z. Jia, D. Ren, L. Xu, Generalized preparation of metal oxalate nano/submicro-rods by facile solvothermal method and their calcined products, Mater. Lett. 76 (2012) 194–197.

[15] M.V.V.S. Reddy, K. V Lingam, T.K.G. Rao, Radical studies in oxalate systems: E.S.R. of CO_2^- in irradiated potassium oxalate monohydrate, Mol. Phys. 42 (1981) 1267–1269.

[16] B. Małecka, E. Drozdz-Cieśla, A. Małecki, Mechanism and kinetics of thermal decomposition of zinc oxalate, Thermochim. Acta. 423 (2004) 13–18.

[17] V. Kornienko, Influence of cation nature on the thermal decomposition of oxalates, Ukr. Chem. J. 23 (1957) 159–167.

[18] C. Hu, J. Mi, S. Shang, J. Shangguan, The study of thermal decomposition kinetics of zinc oxide formation from zinc oxalate dihydrate, J. Therm. Anal. Calorim. 115 (2014) 1119–1125.

[19] R. Majumdar, P. Sarkar, U. Ray, M. Roy Mukhopadhyay, Secondary catalytic reactions during thermal decomposition of

oxalates of zinc, nickel and iron(II), Thermochim. Acta. 335 (1999) 43–53.

[20] J. Mu, D.D. Perulmutter, Thermal Decomposition of carbonates, carboxylates, oxalates, acetates, formates, and hydroxides, Thermochim. Acta. 49 (1981) 207–218.

[21] K. Sabira, K. Muraleedharan, Exploration of the thermal decomposition of zinc oxalate by experimental and computational methods, J. Therm. Anal. Calorim. (2020). https://doi.org/10.1007/s10973-019-09169-6.

[22] A. Patterson, The Scherrer Formula for X-Ray Particle Size Determination, Phys. Rev. 56 (1939) 978-982.

[23] T. Ozawa, A New Method of Analyzing Thermogravimetric Data, Bull. Chem. Soc. Jpn. 38 (1965) 1881–1886.

[24] L.A.Wall. J.H. Flynn, A quick, direct method for the determination of activation energy from thermogravimetric data, Polym. Lett. 4 (1966) 323–328.

[25] H.E. Kissinger, Reaction Kinetics in Differential Thermal Analysis, Anal. Chem. 29 (1957) 1702–1706.

[26] C. Wang. W. Tang, Y. Liu, H. Zhang, New approximate formula for Arrhenius temperature integral, Thermochim. Acta. 408 (2003) 39–43.

[27] M.J. Starink, The Determination of Activation Energy from Linear Heating Rate Experiments: A Comparison of the Accuracy of Isoconversion Methods, Thermochim. Acta. 404 (2003) 163–176.

SUMMARY AND FUTURE OUTLOOK

The thesis deals with the solid-state thermal decomposition studies of zinc oxalate and the effect of some additives on its thermal decomposition. Among the various synthetic approaches for the preparation of metal oxides, the thermal decomposition of metal oxalates is valuable, primarily due to the simplicity and ease of synthesis and the phase purity, composition, *etc*., of the resulting decomposition products. Mixed metal oxide nanoparticles play important roles in several areas of chemistry and physics and these hetero metal oxide nanoparticles can be synthesized by the co-precipitation method using suitable metal oxalate as the precursor and followed by its thermal decomposition. A highly beneficial aspect of the thermal decomposition of oxalate to oxide is that it produces metal oxide particles without any interfering solid by-products. The decomposition study functions as the most useful tool for gaining insight into the mechanism of solid-state decomposition of oxalate based materials leading to metal oxides.

In the very first beginning of the study, zinc oxalate dihydrate was prepared, characterized, and thermally decomposed. The decomposition products were also characterized and found that spherical zinc oxide nanoparticles were formed. The dehydration of zinc oxalate dihydrate and the thermal decomposition behavior of anhydrous zinc oxalate were examined by non- isothermal DSC technique in flowing N_2 atmosphere and carried out the theoretical study to understand the electronic structure and bonding properties in view of the

DFT strategy utilizing Gaussian09W simulation package. The DSC data were analyzed by modern kinetic investigation procedures such as model free isoconversional methods *viz*., FWO, KAS, Tang, Starink, Boswell using multi heating rates to find out the activation energies of the thermal decomposition and the values are found to be compatible with each other. The changes in the activation energy with the conversion function for all the isoconversional methods studied reflect the complexity of the reaction and changing mechanism during the reaction. The theoretical investigation and the bond length values suggested that during the thermal decomposition process, first, one of the Zn-O bond breaks then C-C bond breaks with the elimination of CO_2, and finally C-O bond breaks by evolving CO and ZnO exist as the final decomposition product.

The study then presents the effect of some additives on the kinetics of the thermal decomposition reaction of zinc oxalate dihydrate. Ce^{3+} is selected as an additive aliovalent atom for zinc oxalate lattice with cerium concentrations 0.1, 1, and 5 mol% and examined the kinetics of thermal dehydration and decomposition reactions of Ce added zinc oxalate dihydrate in two different atmospheres, nitrogen and air using non-isothermal DSC and TGA techniques. The thermoanalytical data were analyzed by using different model free isoconversional methods using multi heating rates. The synthesized Ce-ZnO nanoparticles are in spherical in shape and the particle size is reduced with increasing cerium loading. The value of activation energy for the dehydration reaction as well as decomposition reaction is regularly decreasing with an increase in Ce ion concentration in N_2.

There is no regular trend in the decrease of activation energy for the dehydration reaction in the air but the E_a values are decreasing for the decomposition reaction with an increase in Ce ion concentration in the air similar to that of N_2. The value of activation energy for dehydration as well as decomposition reaction is higher in the air than the nitrogen atmosphere. The effect of the addition of cerium on the lowering of activation energy is more pronounced in the nitrogen atmosphere. From the kinetic analysis performed in two different atmospheres, it can be concluded that the decomposition atmosphere has a positive role in determining the activation energy of thermal reactions.

The study also includes the synthesis and characterization of Sr containing (concentration of Sr: 0.1, 1, 2, and 5 mol%) zinc oxalate and the kinetics of its thermal decomposition using non-isothermal DSC technique in flowing N_2. The kinetic analysis of zinc-strontium oxalates using model free isoconversional methods using multiple heating rates shows a decrease in the value of activation energy with an increase in the concentration of strontium ion for the decomposition reaction. The variation in the value of E_a with the conversion function reflects the complexity of the reaction. The addition of strontium into zinc oxalate also cause to alter the mechanism of the thermal decomposition reaction. Pure zinc oxalate obeys Avrami-Erofeev equation and all the strontium containing samples follow the Mampel equation during thermal decomposition reaction.

Subsequently we have synthesized Ba containing zinc oxide nanoparticles (concentration of Ba: 2, 3, 4, and 5 mol%) through a simple, low cost, oxalate co-precipitation route followed by the thermal decomposition. The band gap is found to be increased by the

addition of barium. The activation energy for the dehydration reaction of barium containing zinc oxalate was calculated by using different model free isoconversional methods using non-isothermal DSC in N_2 and TG in air and found that all Ba containing samples have a lower value of E_a than pure ZnOx in nitrogen and the air, all samples except $BZOx_5$ have a lower value of E_a than pure ZnOx. The dehydration reaction is favorable in the nitrogen atmosphere than in air since the value of activation energy in the N_2 atmosphere is smaller than that of air. It is also found that the value of E_a for the decomposition reaction in the N_2 atmosphere of all the barium added samples are higher than that of pure ZnOx except $BZOx_5$.

The study can be extended to investigate the effect of other elements as additives on the kinetics of thermal decomposition of zinc oxalate dihydrate which in the future may help for the development of a theory. These studies provide a starting point for the exploitation of the particular oxalates for the growing industrial world. The first principle calculation using Gaussian or VASP for the synthesized hetero metal oxalate can be done to enlighten the reaction mechanism during thermal decomposition. The synthesized hetero metal oxide of zinc can be tested for various applications like photocatalytic degradation of organic contaminants, sensing for detecting numerous toxic and dangerous gasses, piezoelectric sensors, electro-luminescent material, magnetic material, actuator, antibacterial and antimicrobial activities, and cosmetic ingredients.

PUBLICATIONS

Sl. No.	Journal name, Volume, Year, Page number	Title of the article	Publisher	IF
1	Journal of Thermal Analysis and Calorimetry, 142 (2020), 1315-1327	Exploration of the thermal decomposition of zinc oxalate by experimental and computational methods	Springer, ISSN 1388-6150	2.731
2.	Computational Biology and Chemistry, 77 (2018) 154–166	QSAR classification-based virtual screening followed by molecular docking studies for identification of potential inhibitors of 5-lipoxygenase	Elsevier, ISSN 1476-9271	1.85
3.	Computational Biology and Chemistry, 80 (2019) 66-78	DFT and QTAIM based investigation on the structure and antioxidant behavior of lichen substances atranorin, evernic acid and diffractaic acid	Elsevier, ISSN 1476-9271	1.85
4.	Journal of Thermal Analysis and Calorimetry, (Under revision)	A study on the effect of Ce (III) additives on the kinetics of thermal dehydration and decomposition of zinc oxalate dihydrate	Springer, ISSN 1388-6150	2.731
5.	Thermochimica Acta, (Submitted)	Effect of addition of strontium ion on the kinetics of thermal decomposition of zinc oxalate	Elsevier, ISSN 0040-6031	2.762
6.	Journal of Analytical and Applied Pyrolysis, (Submitted)	Impact of barium addition on the kinetics of thermal dehydration and decomposition of zinc oxalate dihydrate	Elsevier, ISSN 0165-2370	3.905

Book Chapter

1. Kinetic analysis of the formation of barium-zinc oxide nanoparticles from their oxalate precursors, **K. Sabira**, Tinu Lowerence, K. Muraleedharan, Advanced Nanomaterials (Submitted).

Seminar Participation

International

1. Kinetics of thermal decomposition of zinc oxalate in N_2 atmosphere by DSC technique, **K. Sabira**, K. Muraleedharan, MESKVM College, Valanchery, International Conference on Applied Science and Innovative Technology (ICASIT 2018).

National

1. DFT study on the antioxidant capacity of ailanthone from *Ailanthus altissima*, **K. Sabira**, T.K. Shameera Ahamed, K. R. Vijisha, K. Muraleedharan, KSCSTE National Seminar on Organic Chemistry and Computational Chemistry, Morning Star College, Angamaly, 2019.

2. Effect of strontium addition on the kinetics of thermal decomposition of zinc oxalate, **K. Sabira**, P. Nufaila and K. Muraleedharan, National Seminar on Recent Trends in Material Science (NSRTMS- 2019), Govt. College, Chittur, Palakkad.